

22 January 2010 | \$10

# Science





“The fastest separations and  
the gold standard method.  
That’s **electroforward**  
thinking.”



Next-generation precast gels.  
No special buffers required.

Introducing long shelf life Mini-PROTEAN™ TGX (Tris-Glycine eXtended) Gels from Bio-Rad. The innovative TGX formulation delivers consistent, linear separation without the need for expensive, specialized buffers.

Get results faster with:

- Run times as short as 15 minutes
- Transfer in as little as 15 minutes
- New bottom-opening cassette design for faster setup and less handling for downstream applications

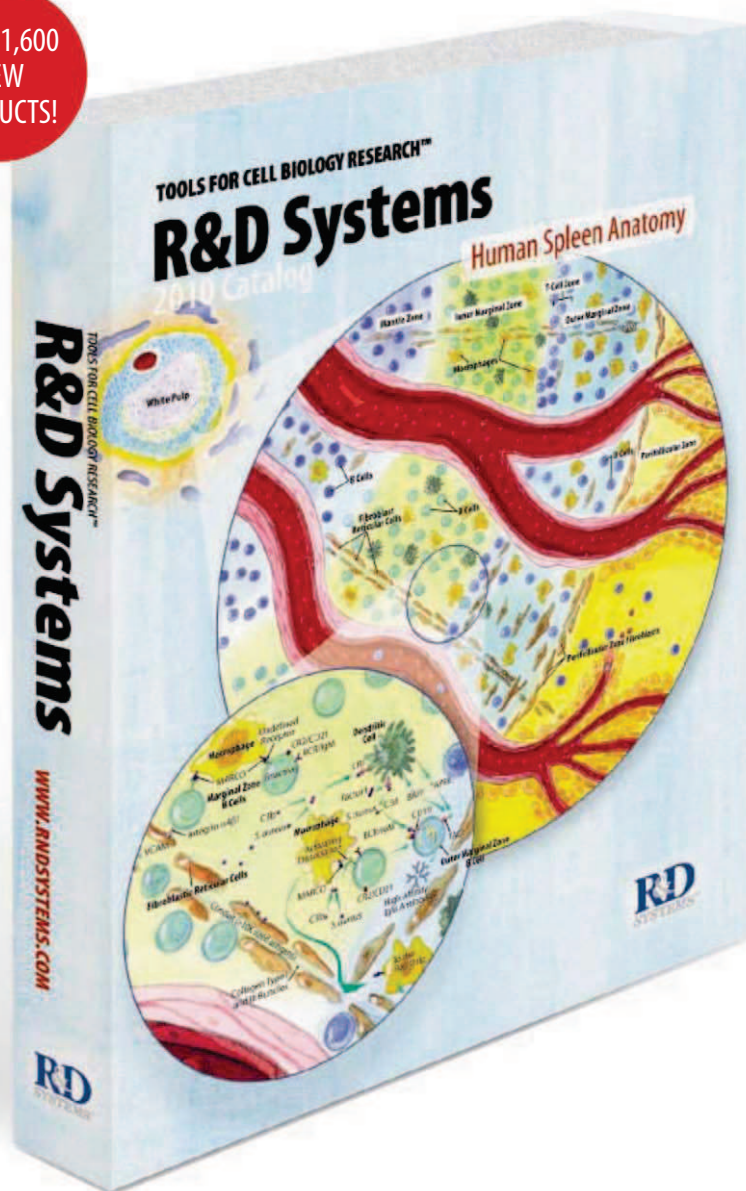
Gel with us at [www.miniprotean.com](http://www.miniprotean.com).

**Research. Together.**

# R&D SYSTEMS 2010 CATALOG AVAILABLE NOW!

R&D Systems is a leading supplier of cell biology reagents with over 20 years of experience serving the research community. More than 97% of the products supplied by R&D Systems are developed and manufactured at our own facilities. This enables us to maintain strict manufacturing and quality control standards, ensuring that our reagents meet the high levels of performance and consistency expected by our customers.

OVER 1,600  
NEW  
PRODUCTS!



OFFERING MORE THAN  
**15,000**  
QUALITY PRODUCTS  
including:

Proteins  
Antibodies  
ELISAs  
Multiplex Immunoassays  
Stem Cell Products  
& More!

Request a catalog online:  
[www.RnDSystems.com/go/Catalog](http://www.RnDSystems.com/go/Catalog)

**R&D Systems Tools for Cell Biology Research™**

USA & Canada **R&D Systems, Inc.** Tel: (800) 343-7475 [info@RnDSystems.com](mailto:info@RnDSystems.com)

Europe **R&D Systems Europe, Ltd.** Tel: +44 (0)1235 529449 [info@RnDSystems.co.uk](mailto:info@RnDSystems.co.uk)

China **R&D Systems China Co., Ltd.** Tel: +86 (21) 52380373 [info@RnDSystemsChina.com.cn](mailto:info@RnDSystemsChina.com.cn)

Selection expanding weekly—visit [www.RnDSystems.com/go/request](http://www.RnDSystems.com/go/request) to sign up for weekly new product updates.



# See more See beyond

For years, scientists have relied on ImageQuant™ and Typhoon™. Now we can offer a new standard of performance with the Typhoon FLA 9000, Typhoon FLA 7000, ImageQuant 4000, and ImageQuant 4000 mini. Covering the full spectrum of imaging methods including quantitative Westerns, UV, IR, visible fluorescence, phosphorimaging, and 2-D DIGE, the new imagers provide exceptional sensitivity, speed, and versatility.

At GE Healthcare, our focus is on helping scientists achieve more, faster. However simple or complex your imaging needs, you can depend on us for quantitative imaging that's quantifiably better.

To find out more about our new range of imagers, contact us today.

Visit [www.gelifesciences.com/imaging](http://www.gelifesciences.com/imaging)

| ÄKTA | Amersham | Biacore | IN Cell Analyzer | Whatman | GE Service |



imagination at work

ÄKTA, Amersham, Biacore, ImageQuant, Typhoon and Whatman are trademarks of GE Healthcare companies.  
© 2010 General Electric Company - All rights reserved.  
GE Healthcare Bio-Sciences AB, Björkgatan 30, 751 84 Uppsala, Sweden  
GE01-10. First published January 2010.



## EDITORIAL

- 393 Improving Access to Research  
*Paul N. Courant et al.*

## NEWS OF THE WEEK

- 398 Foreshadowing Haiti's Catastrophe
- 399 Models Foresee More-Intense Hurricanes in the Greenhouse  
*>> Report p. 454*
- 400 African Physicists Set Their Sights on Mammoth Scope
- 401 Killing of Professor Sparks Fight Over His Science and His Politics
- 401 From *Science's* Online Daily News Site
- 402 Google Plots Exit Strategy As China Shores Up 'Great Firewall'
- 402 Under Fire From Pharma, Institute May Lose Its Director
- 403 From the *Science* Policy Blog

## NEWS FOCUS

- 404 The Tangled Roots of Agriculture  
*>> Science Podcast*
- 407 Trends Document China's Prowess
- 408 Fall Meeting of the American Geophysical Union  
Flows on Mars But No Water Magnetics Point to Magma 'Ocean' at Io Antarctic Glacier Off Its Leash Snapshots from the Meeting

## LETTERS

- 410 Studying Extant Species to Model Our Past  
*A. Whiten et al.*  
Response  
*C. O. Lovejoy et al.*  
Carbon Accounting a Tricky Business  
*A. J. Friedland and K. T. Gillingham*  
East German Institutes Stand Tall  
*E. Th. Rietschel*

## BOOKS ET AL.

- 413 Questioning Collapse  
*P. A. McAnany and N. Yoffee, Eds., reviewed by K. Lewis*
- 414 Pink Brain, Blue Brain  
*L. Eliot, reviewed by A. S. Henderson*

## POLICY FORUM

- 415 Accessible Reproducible Research  
*J. P. Mesirov*

## PERSPECTIVES

- 417 Subversion from the Sidelines  
*N. Argarwal and W. R. Bishai*  
*>> Report p. 466*
- 418 Drylands in the Earth System  
*D. S. Schimel*  
*>> Report p. 451*
- 419 Amoeba-Inspired Network Design  
*W. Marwan*  
*>> Report p. 439*
- 420 And Then There Were None?  
*R. G. Roberts and B. W. Brook*
- 422 Adjusting the Solar System's Absolute Clock  
*J. N. Connelly*  
*>> Report p. 449*
- 423 Epitaxial Growth Writ Large  
*T. L. Einstein and T. J. Stasevich*  
*>> Report p. 445*

## RESEARCH ARTICLE

- 425 The Genetic Landscape of a Cell  
*M. Costanzo et al.*  
A genome-wide interaction map of yeast identifies genetic interactions, networks, and function.

CONTENTS continued >>



page 404



page 414



## COVER

Hurricane Ike caused extensive damage throughout the Caribbean and Gulf of Mexico regions in September 2008, as shown here at Pinar del Rio in western Cuba. A state-of-the-art computer model projects that global warming should cause an increase in the frequency of the most intense western Atlantic hurricanes, like Ike, during the 21st century. See page 454.

Photo: Claudia Daut/Reuters/Landov

## DEPARTMENTS

- 391 This Week in *Science*
- 394 Editors' Choice
- 396 *Science* Staff
- 397 Random Samples
- 478 New Products
- 479 *Science* Careers

# Choose QIAGEN for detection

Detection platforms, assays,  
and analysis software  
by QIAGEN



Use QIAGEN® solutions from sample to result,  
and benefit from sensitive and reliable detection systems:

- Quantitative, real-time PCR detection
- Automated analysis of DNA fragments and RNA
- Pyrosequencing® sequence-based DNA detection and quantification
- Optimized, ready-to-use assays and reagents

Making improvements in life possible — [www.qiagen.com](http://www.qiagen.com)



Sample & Assay Technologies



# Qs & AAAS



**[www.sciencedigital.org/subscribe](http://www.sciencedigital.org/subscribe)**

For just US\$99, you can join AAAS TODAY and  
start receiving *Science* Digital Edition immediately!

# Qs & AAAS



**[www.sciencedigital.org/subscribe](http://www.sciencedigital.org/subscribe)**

For just US\$99, you can join AAAS TODAY and  
start receiving *Science* Digital Edition immediately!



## REPORTS

- 432** Formation of Iapetus' Extreme Albedo Dichotomy by Exogenically Triggered Thermal Ice Migration  
*J. R. Spencer and T. Denk*

- 435** Iapetus: Unique Surface Properties and a Global Color Dichotomy from Cassini Imaging  
*T. Denk et al.*

Thermal migration of water ice explains the observed color asymmetry of Saturn's unusual moon, Iapetus.

- 439** Rules for Biologically Inspired Adaptive Network Design  
*A. Tero et al.*

Human municipal transportation engineers might learn design strategies from the lowly slime mold.

>> *Perspective p. 419*

- 442** Measurement of Universal Thermodynamic Functions for a Unitary Fermi Gas  
*M. Horikoshi et al.*

Cold Fermi gases are used to study resonant fermion-fermion interactions.

- 445** Direct Measurements of Island Growth and Step-Edge Barriers in Colloidal Epitaxy  
*R. Ganapathy et al.*

Multilayer film deposition and the templating of colloidal particles exhibit growth kinetics analogous to epitaxial growth.

>> *Perspective p. 423*

- 449**  $^{238}\text{U}/^{235}\text{U}$  Variations in Meteorites: Extant  $^{247}\text{Cm}$  and Implications for Pb-Pb Dating  
*G. A. Brennecka et al.*

Variable abundances of meteorite isotopes may require correcting the lead-based age of the solar system by 5 million years.

>> *Perspective p. 422*

- 451** Contribution of Semi-Arid Forests to the Climate System  
*E. Rotenberg and D. Yakir*

Semi-arid forests could cool climate by sequestering  $\text{CO}_2$ , but could also warm it by reducing Earth's albedo.

>> *Perspective p. 418*

- 454** Modeled Impact of Anthropogenic Warming on the Frequency of Intense Atlantic Hurricanes  
*M. A. Bender et al.*

Global warming may increase the frequency of intense hurricanes in the western Atlantic region during the 21st century.

>> *News story p. 399; Science Podcast*

- 459** Requirement of Prorenin Receptor and Vacuolar  $\text{H}^+$ -ATPase-Mediated Acidification for Wnt Signaling  
*C.-M. Cruciat et al.*

A dual-function protein acts as an adaptor in a major developmental signaling pathway.

- 463** Identification of RACK1 and Protein Kinase C $\alpha$  as Integral Components of the Mammalian Circadian Clock  
*M. S. Robles et al.*

Rhythmic activation of signaling occurs by core components of the biological clock mechanism.

- 466** Tuberculous Granuloma Induction via Interaction of a Bacterial Secreted Protein with Host Epithelium  
*H. E. Volkman et al.*

Epithelial cells play a role in tubercular granuloma formation and mycobacterial virulence.

>> *Perspective p. 417*

- 469** Evolution of MRSA During Hospital Transmission and Intercontinental Spread  
*S. R. Harris et al.*

By tracing the microevolution of a pathogen, high-throughput genomics reveals person-to-person transmission events.

- 474** Impact of Spikelets on Hippocampal CA1 Pyramidal Cell Activity During Spatial Exploration  
*J. Epsztein et al.*

Bursts of small voltage spikes coordinate neuron firing in the brain during spatial exploration.

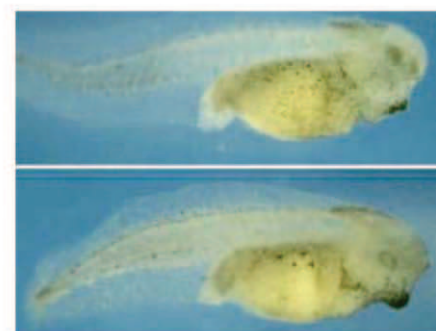
**CONTENTS continued >>**



page 415



pages 432 & 435



page 459

# Rare Mutation Matters!

Find it by deep sequencing of whole exome or candidate genes

## BGI'S GENOMICS BAR



Would 60 Gb/day sequencing capacity, 50 TFLOPS, 5 P storage, 200 bioinformaticians and the use of cutting-edge software programs developed by BGI satisfy your taste?

One of the world's biggest genome centers is looking for collaborators !



tech@genomics.cn  
www.genomics.cn  
86-755-25273395



## SCIENCEONLINE

## SCIENCEXPRESS

[www.sciencexpres.org](http://www.sciencexpres.org)

### Repulsion of Superinfecting Virions: A Mechanism for Rapid Virus Spread

V. Doceul et al.

Early in infection, vaccinia virus exploits the actin cytoskeleton to promote rapid cell-to-cell spread.  
10.1126/science.1183173  
>> *Science Podcast*

### The *Lmo2* Oncogene Initiates Leukemia in Mice by Inducing Thymocyte Self-Renewal

M. P. McCormack et al.

Expression of an oncogene confers self-renewal activity to committed T cells in the thymus long before disease onset.  
10.1126/science.1182378

### Climate-Modulated Channel Incision and Rupture History of the San Andreas Fault in the Carrizo Plain

L. Grant Ludwig et al.

10.1126/science.1182837

### Slip in the 1857 and Earlier Large Earthquakes Along the Carrizo Plain, San Andreas Fault

O. Zielke et al.

The historical behavior of the San Andreas fault may have been dominated by smaller, more frequent slip events.

10.1126/science.1182781

## SCIENCENOW

[www.sciencenow.org](http://www.sciencenow.org)

Highlights From Our Daily News Coverage

### Fish May Not Have Evolved Gills to Breathe

New study suggests a surprising reason for adaptation.

### Radiocarbon Daters Tune Up Their Time Machine

Researchers can now peer back 50,000 years with accuracy.

### Hang Christiaan Huygens! Here's a Better Suspension Bridge

They may be pretty, but simple swooping bridge cables are not the best design.

## SCIENCE SIGNALING

[www.sciencesignaling.org](http://www.sciencesignaling.org)

The Signal Transduction Knowledge Environment

### EDITORIAL GUIDE: Focus Issue—External and Internal Regulators of Immune Responses

J. F. Foley and N. R. Gough

Host defense mechanisms are modulated by host-derived and pathogen-derived factors.

### RESEARCH ARTICLE: Distinct Signal Codes Generate Dendritic Cell Functional Plasticity

K. Arima et al.

The cytokine TSLP triggers distinct signals in dendritic cells that program a T helper 2 (T<sub>H</sub>2)-type response.

### RESEARCH ARTICLE: Attenuation of Rabies Virulence—Takeover by the Cytoplasmic Domain of Its Envelope Protein

C. Préhaud et al.

Survival of rabies virus-infected neurons depends on a single amino acid in the PDZ-binding site of a viral protein.

### PERSPECTIVE: TAK-1 IKK Activation— "Ub" the Judge

S. M. Wuerzberger-Davis and S. Miyamoto

IL-1 $\beta$ -dependent activation of NF- $\kappa$ B occurs in two distinct stages.

### REVIEW: What Is the Function of the Dendritic Cell Side of the Immunological Synapse?

J. L. Rodríguez-Fernández et al.

The immunological synapse organizes signaling responses in dendritic cells, as well as in T cells.

### CONNECTIONS MAP OVERVIEW: Interleukin-1 (IL-1) Pathway

A. Weber et al.

IL-1 $\alpha$  and IL-1 $\beta$  orchestrate the proinflammatory response by multiple tightly controlled mechanisms.

### CONNECTIONS MAP OVERVIEW: Interleukin-1 $\beta$ (IL-1 $\beta$ ) Processing Pathway

A. Weber et al.

The NALP3 inflammasome pathway controls processing and release of interleukin-1 $\beta$ .

## SCIENCE CAREERS

[www.sciencereers.org/career\\_magazine](http://www.sciencereers.org/career_magazine)

Free Career Resources for Scientists

### SPECIAL QUANTITATIVE BIOMEDICINE ISSUE Quantitative Biomedical Careers

S. Gaidos

Physicists and mathematicians are finding new ways to apply quantitative skills to biomedical sciences.

### Informatics Careers Take Shape in Translational and Clinical Research

B. Vastag

Electronic patient data and research repositories mean new opportunities in medical informatics.

### Statistics Serving Biomedicine

E. Pain

Spanish statistician David Rossell supports other biomedical scientists while pursuing his own research.

## SCIENCE TRANSLATIONAL MEDICINE

[www.sciencetranslationalmedicine.org](http://www.sciencetranslationalmedicine.org)

Integrating Medicine and Science

### PERSPECTIVE: Optimizing the Delivery of Cancer Drugs that Block Angiogenesis

Y. Cao and R. Langer

Optimizing antiangiogenic therapy requires the development of new drug delivery systems.

### COMMENTARY: Meeting the Governance Chal- lenges of Next-Generation Biorepository Research

S. M. Fullerton et al.

Requisites for biorepository governance need to keep pace with developments in translational science.

### RESEARCH ARTICLE: Vaccines with MF59 Adjuvant Expand the Antibody Repertoire to Target Protec- tive Sites of Pandemic H5N1 Influenza Virus

S. Khurana et al.

An oil-based adjuvant improves the efficacy of an H1N1 vaccine.

### RESEARCH ARTICLE: Identification of a Class of HCV Inhibitors Directed Against the Nonstructural Protein NS4B

N.-J. Cho et al.

A newly discovered activity in hepatitis C virus gives rise to a distinct class of antiviral compounds.

## SCIENCE PODCAST

[www.sciencemag.org/multimedia/podcast](http://www.sciencemag.org/multimedia/podcast)

Free Weekly Show

Download the 22 January *Science* Podcast to hear about the impact of global warming on Atlantic hurricanes, a mechanism for rapid virus spread, the ancient Natufians, and more.

## SCIENCE INSIDER

[blogs.sciencemag.org/scienceinsider](http://blogs.sciencemag.org/scienceinsider)

Science Policy News and Analysis

SCIENCE (ISSN 0036-8075) is published weekly on Friday, except the last week in December, by the American Association for the Advancement of Science, 1200 New York Avenue, NW, Washington, DC 20005. Periodicals Mail postage (publication No. 484460) paid at Washington, DC, and additional mailing offices. Copyright © 2010 by the American Association for the Advancement of Science. The title SCIENCE is a registered trademark of the AAAS. Domestic individual membership and subscription (51 issues): \$146 (\$74 allocated to subscription). Domestic institutional subscription (51 issues): \$910; Foreign postage extra: Mexico, Caribbean (surface mail) \$55; other countries (air assist delivery) \$85. First class, airmail, student, and emeritus rates on request. Canadian rates with GST available upon request, GST #1254 88122. Publications Mail Agreement Number 1069624. Printed in the U.S.A.

Change of address: Allow 4 weeks, giving old and new addresses and 8-digit account number. Postmaster: Send change of address to AAAS, P.O. Box 96178, Washington, DC 20090-6178. Single-copy sales: \$10.00 current issue, \$15.00 back issue prepaid includes surface postage; bulk rates on request. Authorization to photocopy material for internal or personal use under circumstances not falling within the fair use provisions of the Copyright Act is granted by AAAS to libraries and other users registered with the Copyright Clearance Center (CCC) Transactional Reporting Service, provided that \$20.00 per article is paid directly to CCC, 222 Rosewood Drive, Danvers, MA 01923. The identification code for Science is 0036-8075. Science is indexed in the Reader's Guide to Periodical Literature and in several specialized indexes.



ADVANCING SCIENCE. SERVING SOCIETY.

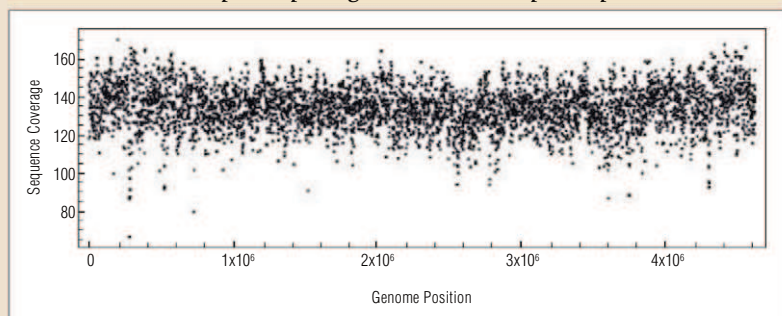


## STUNNING QUALITY

### Reagents for Sample Preparation from New England Biolabs

Introducing NEBNext™, a series of highly pure reagents that facilitate sample preparation for downstream applications such as next generation sequencing and expression library construction. Available in sets, master mixes and modules, these robust reagents undergo stringent quality controls and functional validation, ensuring maximum yield, convenience and value.

#### Sequencing coverage map of the *E. coli* genome after using NEBNext™ DNA Sample Prep Reagent Set 1 for Sample Preparation



*E. coli* strain MG1655 gDNA was prepared with NEBNext DNA Sample Prep Reagent Set 1 and sequenced on an Illumina Genome Analyzer II.

For more information about NEBNext, including customized solutions, please contact [NEBNext@neb.com](mailto:NEBNext@neb.com).

**Now available:**  
**NEBNext™ dsDNA Fragmentase™**  
an enzyme-based solution for the  
fragmentation of DNA

CELEBRATING  
35  
YEARS

NEW ENGLAND  
**BioLabs** Inc.  
enabling technologies in the life sciences

CLONING & MAPPING

DNA AMPLIFICATION  
& PCR

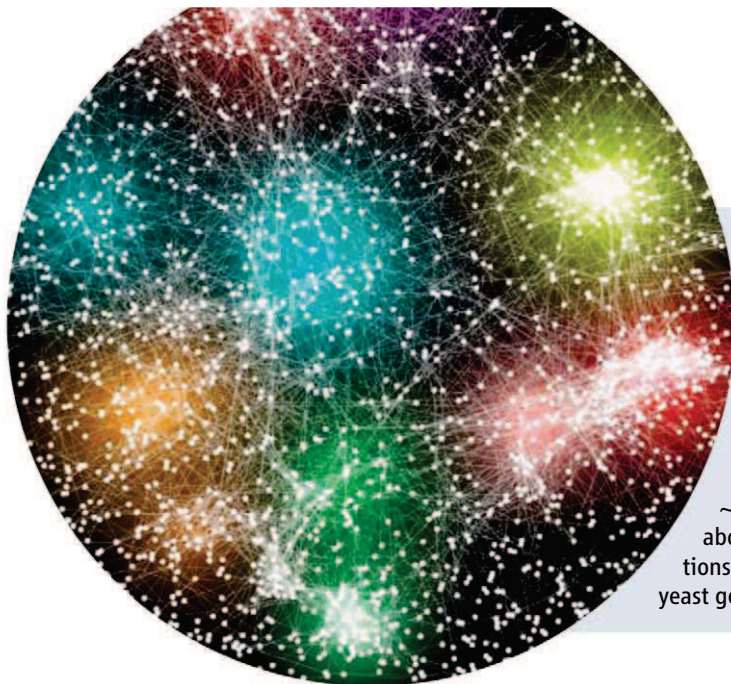
RNA ANALYSIS

PROTEIN EXPRESSION &  
ANALYSIS

GENE EXPRESSION  
& CELLULAR ANALYSIS

[www.neb.com](http://www.neb.com)





## << Making Connections

Genetic interaction profiles highlight cross-connections between bioprocesses, providing a global view of cellular pleiotropy, and enable the prediction of genetic network hubs. **Costanzo *et al.*** (p. 425) performed a pairwise fitness screen covering approximately one-third of all potential genetic interactions in yeast, examining 5.4 million gene-gene pairs and generating quantitative profiles for ~75% of the genome. Of the pairwise interactions tested, about 3% of the genes investigated interact under the conditions tested. On the basis of these data, a reference map for the yeast genetic network was created.

## Iapetus Revealed

The striking appearance of Saturn's moon Iapetus—half black and half white—has puzzled astronomers for over three centuries. Now **Spencer and Denk** (p. 432, published online 10 December) present an explanation for this asymmetry: A thermally controlled runaway migration of water ice triggered by exogenic deposition of dark material on the moon's leading darker side, which faces the direction of motion of the moon in its orbit around Saturn. This mechanism is unique to Iapetus because it rotates slowly enough to allow large temperature variations to arise, it is small enough to allow long-range migration of water, and there is a source of dust to trigger the process. In a related paper, **Denk *et al.*** (p. 435, published online 10 December) present data derived from the Cassini Imaging Science Subsystem that reveal that both dark and bright materials on the leading side of Iapetus are redder than their trailing-side counterparts. This asymmetry results from the deposition of dust and debris from other moons in the saturnian system—the very same process that initiates the thermal segregation proposed above.

## Miniature Transport Engineers

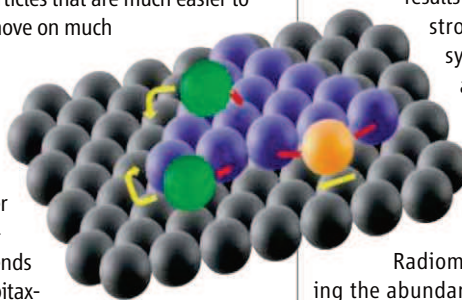
In its vegetative phase, the slime mold *Physarum polycephalum* "slimes" its way through the world seeking food. As it explores, it links previously found food sources with tubular structures. **Tero *et al.*** (p. 439) report that if food sources are deposited on a plate in a pattern corresponding in miniature to the positions of the cities that surround Tokyo, the resulting network of *Physarum* tubules that develops is rather similar in structure to the railroad network that

connects the Japanese cities. A model was produced that describes the adaptive network development displayed by the slime mold. This biologically inspired model might provide insight into how to implement properties like resistance of transport systems to local failures into similar human-designed systems.

## Colloids as Models

Colloids are often used as analogs for atoms in order to study crystallization kinetics or glassy dynamics using particles that are much easier to observe and that move on much slower time scales.

**Ganapathy *et al.*** (p. 445; see the Perspective by **Einstein and Stasevich**) consider whether the analogous behavior extends to the growth of epitaxial films, a technique that is used in manufacturing. Controlling the rate of addition of the colloidal particles allowed the mapping of diffusional pathways during film nucleation and growth on a patterned substrate. The same relationships used to describe atomistic growth could be applied to the colloidal systems, but certain growth barriers such as those found at step edges and corners were controlled by diffusion rather than energetics.



actions give rise to different forms of matter. In the strongly interacting resonant regime, however, fermionic systems have thermodynamic properties that depend only on the interparticle spacing and scaled temperature. **Horikoshi *et al.*** (p. 442; see the Perspective by **Marwan**) precisely characterize the thermodynamics in this universal regime for a system of ultracold fermionic lithium atoms. Analysis of a large number of trapped-gas density profiles confirms that the results depend neither on trap geometry nor the absolute temperature of the gas. The results are relevant to studies of all strongly interacting fermionic systems, including neutron stars and nuclear matter.

## How to Get a Date

Radiometric dating relies on measuring the abundance of a radioactive isotope and/or its decay products. By knowing a decay rate and an isotopic starting abundance—both assumed to be constant—an age is determined. Using high-resolution mass spectrometry, **Brennecka *et al.*** (p. 449, published online 31 December; see the Perspective by **Connelly**) show that the known starting abundance of  $^{238}\text{U}$  and  $^{235}\text{U}$  isotopes in meteorites, which decay into  $^{206}\text{Pb}$  and  $^{207}\text{Pb}$ , respectively, is actually quite variable. Trace amounts of  $^{247}\text{Cm}$  in the early solar system may have unexpectedly contributed additional  $^{235}\text{U}$ , skewing the ratio. Pb-Pb dating, the method commonly used to date early solar system materials, may thus need a correction of up to 5 million years.

## Dissecting Fermion Interactions

Electrons, protons, and other building blocks of our universe belong to a class of particles we call fermions. Different interfermion inter-

*Continued on page 392*

## Science Careers in Translation



Want to build relationships with clinical or basic scientists? Get advice on the best way to conduct a clinical and translational science career? There's no better place to explore these ideas, and to build new scientific relationships, than CTSciNet, the new online community from *Science*, *Science Careers*, and AAAS made possible by the Burroughs Wellcome Fund.

There's no charge for joining, and you'll enjoy access to:

- Practical and specific information on navigating a career in clinical or translational research
- Opportunities to connect with other scientists including peers, mentors, and mentees
- Access to the resources of the world's leading multidisciplinary professional society and those of our partner organizations

Connect with CTSciNet now at:  
[Community.ScienceCareers.org/CTSciNet](http://Community.ScienceCareers.org/CTSciNet)

**CTSciNet**  
Clinical and Translational Science Network

Presented by

**AAAS**

**Science**  
AAAS

**Science Careers**  
From the Journal Science AAAS

## This Week in *Science*

Continued from page 391

### Stormy Weather

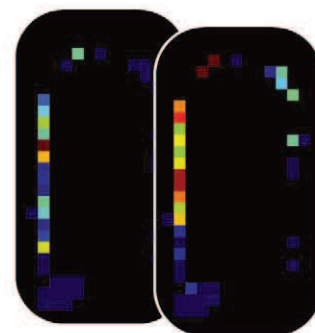
One of the most active questions about the effects of global warming is whether, and how, it might affect the frequency and the strength of hurricanes. Some studies have suggested that warming will bring fewer, and less energetic, hurricanes, while others have claimed that we can expect more intense storms. **Bender *et al.*** (p. 454; see the news story by **Kerr**) explore the influence of global warming on hurricane dynamics over the Atlantic Ocean with a state-of-the-art hurricane prediction model. The model predicts that the annual total number of hurricanes in the 21st century will be less than now, but also that the number of the most intense storms per year will increase. The largest increase of the most intense hurricane frequency is predicted in the western Atlantic, which suggests that Hispaniola, the Bahamas, and the Southeast coast of the United States could be at greater risk.

### Late-Running Clock Components

Many mammalian cells contain a well-characterized biological clock with a 24-hour cycle. In the latter part of the day, transcription mediated by one of the clock components, the transcription factor made up of the CLOCK and BMAL1 proteins, is inhibited, but the mechanism of inhibition has been unclear. **Robles *et al.*** (p. 463) used mass spectrometry to identify proteins that RACK1 (receptor for activated C kinase-1), a scaffold protein that brings protein kinase C- $\alpha$  (PKC $\alpha$ ) into contact with its substrates, caused to be associated with BMAL1 at the time of day when its transcription-activating function was inhibited. Further studies implicated PKC $\alpha$  and RACK1 as integral components of the clock, without which the clock's free-running period was shortened.

### Space and Spikelets

In neurons, spikelets are voltage fluctuations of small amplitude with a spike-like waveform. Spikelets are difficult to detect with extracellular techniques traditionally used to record neuronal activity in freely moving animals. **Epsztein *et al.*** (p. 474) used head-anchored whole-cell recordings to analyze spikelet activity during spatial exploration in freely moving rats. A high incidence of spikelets was often followed by action potentials. Like action potentials, spikelets were all-or-none, but had different kinetics and amplitude, and were clearly distinct from excitatory postsynaptic potentials and occurred to a different extent in different cells. In cells with clear place fields, spikelets had similar spatial firing preferences, as did regular action potentials. Thus, spatially modulated spikelets may be involved in information processing in cortical neuronal networks.



### Garnering Information on Granulomas

In tuberculosis, the tuberculous granuloma has been viewed traditionally as a host-protective structure that serves to "wall off" mycobacteria. However, recent work in the zebrafish embryo showed that mycobacteria convert the nascent granuloma into a vehicle for bacterial expansion and dissemination. Thus, intercepting granuloma formation could provide a strategy for treating tuberculosis, an urgent public health goal in light of the epidemic of extensively drug-resistant tuberculosis. Now **Volkman *et al.*** (p. 466, published online 10 December; see the Perspective by **Agarwal and Bishai**) present the molecular pathway by which mycobacteria induce granulomas in zebrafish. Inhibition of this pathway attenuates infection by reducing granuloma formation, suggesting a therapeutic target for tuberculosis treatment.

### MRSA, Close and Personal

Methods for differentiating pathogen isolates are essential for understanding their evolution and spread, as well as for the formulation of effective clinical strategies. Current typing methods for bacterial pathogens focus on a limited set of characteristics providing data with limited resolving power. **Harris *et al.*** (p. 469) used a high-throughput genome sequencing approach to show that isolates of methicillin-resistant *Staphylococcus aureus* (MRSA) are precisely differentiated into a global geographic structure. The findings suggest that intercontinental transmission has occurred for nearly four decades. The method could also detect individual person-to-person transmission events of MRSA within a hospital environment.

CREDIT: EPSZTEIN ET AL.

Paul N. Courant is  
University Librarian and  
Professor of Economics  
and Public Policy at the  
University of Michigan,  
Ann Arbor, MI.

James J. O'Donnell  
is Professor of  
Classics and Provost at  
Georgetown University,  
Washington, DC.

Ann Okerson is  
Associate University  
Librarian at  
Yale University,  
New Haven, CT.

Crispin B. Taylor is  
Executive Director of  
the American Society  
of Plant Biologists,  
Rockville, MD.

## Improving Access to Research

UNLESS YOU SIT ON YOUR INSTITUTION'S LIBRARY ADVISORY COMMITTEE, A PROFESSIONAL SOCIETY'S publications committee, or a journal editorial board, you may have paid only passing attention to the debate over public access to scientific research, which has been swirling through these communities ever since science journals started publishing online 15 years ago. That is about to change. Last week, the U.S. House Science and Technology Committee's Roundtable on Scholarly Publishing (on which we served along with 10 others) released a report\* arguing that journal articles derived from federal research funding should be made publicly available as quickly as practicable—generally in a year or less after publication—and in ways that will improve scholarship by maximizing the scope for interoperability across articles, among disciplines, and internationally. Currently, there is no consistency regarding which version of an article is freely available. In contrast, the roundtable's report recommends that access policies aim toward making the “Version of Record” (the final version of an article in its published form) publicly available. And the report also asserts that any successful scheme for public access must provide methods for permanent public access.

The scholarly communications enterprise resembles a global ecosystem, comprising a complex interdependent web of relationships. This enterprise is subject to a remarkable pace of change in its underpinning technologies, so that the notion of what constitutes an article, how it is structured, and where and how it is read continues to evolve very rapidly, in the same sort of way as your 2-year-old cell phone no longer quite meets your needs. The report therefore eschews prescriptive solutions to achieve public access, and it favors no particular business model. Instead, it focuses on principles to guide federal policy and practice going forward, in particular the critical role of peer review, the need for continued engagement among stakeholders, and the importance of fostering innovation.

Most notably, to replace the recent heated discourse marked by anger and ideological hard lines, the report recommends a collaborative, nuanced, and flexible approach, believing that this will effectively and quickly achieve the goals of still broader access to a greater scope of scholarly literature. This is a centrist perspective, perhaps, but one that is progressive and reflective of what we see as an increasing convergence among the range of views regarding public access.

So how will the goals of broader access and richer scholarship actually be achieved? The report calls for each U.S. funding agency to develop public access policies that make the best sense in each particular academic niche. Thus, for instance, an agency might choose to work with its stakeholder communities to provide robust public access to journal articles on publisher Web sites, rather than constructing and paying for a centrally operated repository. The report envisions a coordinating and guiding role for the U.S. Office of Science and Technology Policy, through the establishment of an advisory group including researchers, publishers, librarians, university administrators, and the public. It also calls for the development of technological standards that would allow researchers and others to search across distributed networks of information sources, thereby facilitating discovery and the generation of new knowledge.

What next? Clearly the progress of scholarship and electronic publishing and their extraordinary scientific and social benefits will require continuing adaptations by professional societies, libraries, funding agencies, governmental entities representing the public interest, and others. Despite the fact that 2 of our 14 committee members were unable to endorse the report in its entirety,\* we are optimistic that broad middle grounds in the respective stakeholder communities will recognize the wisdom of the roundtable's recommendations, and that the process of engagement through which they were developed represents a sensible and workable path toward an increasingly unfettered and useful body of knowledge.

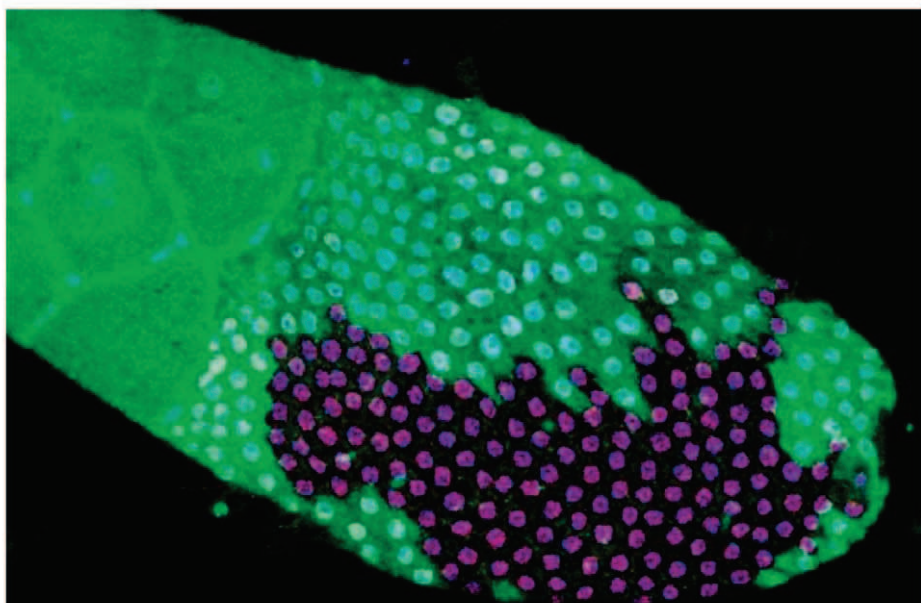
— Paul N. Courant, James J. O'Donnell, Ann Okerson, Crispin B. Taylor

10.1126/science.1186933



\*<http://science.house.gov/press/PRArticle.aspx?NewsID=2710>





## MOLECULAR BIOLOGY

# Untranslated Regulators

A variety of short noncoding RNA molecules—microRNAs, small interfering RNAs, and Piwi-interacting RNAs (piRNAs)—play regulatory roles in eukaryotes. Many piRNAs are derived from transposon-related sequences and, through complementary sequence interactions and a “ping-pong” amplification process, act to silence those selfish and potentially mutagenic elements in germline cells.

However, Robine *et al.* show that a substantial population of piRNAs found in a *Drosophila* somatic ovarian cell line are in fact derived from a distinct subset of genes, and also that the bulk of these piRNAs arise directly from the 3′ untranslated regions (3′ UTRs) of the sense strands. This suggests that the complementary targets of these piRNAs may not be the parental transcripts. Ping-pong amplification is not required for the generation of these 3′ UTR piRNAs, nor does it appear as if they are aberrant products of the primary piRNA processing pathway. Furthermore, Saito *et al.* have found that the *Drosophila* gene *traffic jam* (*tj*) gives rise to 3′ UTR piRNAs and that one of its targets is the *fasciclin III* gene transcript, and Robine *et al.* note that the subset of functional categories of mRNAs that gives rise to the 3′ UTR piRNAs is broadly conserved between fruit flies and mice. — GR

*Curr. Biol.* **19**, 2066 (2009); *Nature* **461**, 1296 (2009).

## PHYSICS

# A Second Second Sound?

Superfluids, such as <sup>4</sup>He below its transition temperature around 2 K, make for a great science demonstration: They flow without viscosity through tiny holes, creep up vertical walls, and refuse to boil. This last property arises because heat, which normally propagates by diffusion, travels through a superfluid following a wave equation (often referred to as the “second sound”), resulting in extremely high thermal conductivity. Meppelink *et al.* realize an analog of this phenomenon in a weakly interacting

Bose-Einstein condensate of sodium atoms by physically separating the condensed (superfluid) from the thermal (normal) portion of the gas. They then cause out-of-phase oscillations of the two components during which the center of mass remains stationary, much as in the case of the second sound. The amplitude of these oscillations is damped as the condensate passes through the thermal cloud, leading to energy exchange between the two (Landau damping). The damping rate is measured as a function of the temperature and confinement of the gas. In the collisionless regime (gas cloud size smaller than the mean free path), the Landau damping

mechanism explains the results, whereas in the hydrodynamic regime the experiments suggest another, collision-dependent mechanism, which lacks a thorough theoretical description. — JS

*Phys. Rev. Lett.* **103**, 265301 (2009).

## CANCER

# Unfaithful Encounters

Chromosomal translocations, whereby nonadjacent regions of chromosomes are inappropriately joined, are a hallmark of several different types of cancer. They can result in the generation of fusion proteins that bypass normal control mechanisms and can wreak havoc in cells. It has been assumed that translocation events occur randomly; whether more ordered processes are involved has been unclear.

The androgen receptor is a transcription factor that regulates gene expression during prostate development. Fusions between an androgen receptor target gene and genes encoding members of the ETS family of transcription factors place ETS proteins under the control of androgen and are associated with prostate cancer. Using androgen-responsive prostate cells, Lin *et al.* could produce cancer-specific gene fusions by inducing genotoxic stress and adding androgen. The activation of the androgen receptor promoted encounters between physically separate genes in the nuclei of prostate cells, and genotoxic stress induced double-stranded breaks in intronic regions of these genes. Furthermore, androgen and genotoxic stress recruited proteins involved in sensing DNA breaks and mediating chromosomal rearrangements. — HP

*Cell* **139**, 1069 (2009).

## CHEMISTRY

# Jumping off the Page

Few marriages of analytical methods have been as successful as that of chromatography and



mass spectrometry; together they can tease out the chemical composition of extraordinarily complex mixtures. A typical apparatus incorporates a gas or liquid chromatograph, in which analytes travel through a separation column, and a

downstream detector where their masses are measured. An early, no-frills variant of chromatography involved spotting samples on paper, an inexpensive and highly portable support medium. Wang *et al.* now show that this simple material can also be used as an ionization platform for introducing samples into mass spectrometers. Samples such as blood are spotted on the paper, which is then cut to a sharp triangular point. The paper is wet with a methanol-water solution, and a high positive bias (4.5 kV) is applied to the paper relative to the nearby inlet of a tandem mass spectrometry under ambient conditions; the precise mechanism for ion release remains somewhat unclear. The authors demonstrate the detection of drugs such as Gleevec in blood, as well as picogram quantities of cocaine swabbed from a surface. Chromatographic methods can also be used to separate components in a sample along the paper, which can then be cut into separate pieces for further analysis. — PDS

*Angew. Chem. Int. Ed.* **49**, 10.1002/anie.200906314 (2010).

## CLIMATE SCIENCE

## Model Behavior

Most of what we believe about how climate will change in the future is based on projections made by sophisticated climate models. There are currently multiple highly complex mathematical representations of the climate system, and although most of them generally make similar predictions about the future course of climate, they differ significantly in many particulars. Because it is not normally clear which models' scenarios are likely to be the most realistic, the question arises of which specific models to believe and why. Knutti *et al.* discuss some major sources of differences between models, how their predictive skill can be evaluated, and how confidence in their projections can be improved by combining the results of multiple models. As climate models become more complex, and the amount of data from them increases, it becomes even more important to have quantitative methods available through which to extract and synthesize information needed to guide climate policy decisions. — HJS

*J. Clim.* 10.1175/2009JCLI3361.1 (2009).

## BIOCHEMISTRY

## Uninhibited Mimicry

*Helicobacter pylori* is a pathogen that causes gastric disease and is associated epidemiologically with gastric cancer. This bacterium injects its protein CagA into epithelial cells lining the

stomach in order to disrupt cellular functions, and a domain of CagA that contains contiguous repeats acts to inhibit the PAR1-MARK family of protein serine-threonine kinases.

Nešić *et al.* describe the 2.2 Å crystal structure of the human kinase MARK2 in complex with a 120-residue repeat-containing subdomain of CagA. Unusually, the kinase adopts an active conformation even though there is no magnesium or ATP present, and a 14-residue CagA segment was observed to occupy the MARK2 substrate-binding site. This peptide appeared to promote and stabilize the active conformation of MARK2 by mimicking conserved features of the host substrates of this protein kinase family in a fashion reminiscent of the inhibition of the cAMP-dependent protein kinase by the endogenous peptide PKI. — VV

*Nat. Struct. Mol. Biol.* **17**, 130 (2010).

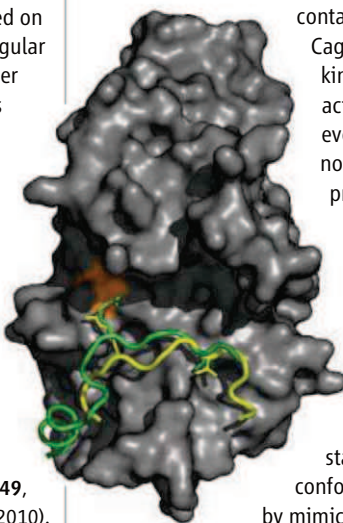
## BIOMEDICINE

## Calculating Unmeasurables

In assessing an epidemic, it would be helpful to know how many people were being infected each day. The objective data, however, are more likely to reflect how many people either became ill or died on a given day, time-lagged tallies that represent subgroups of the total infected population. For latent infections that simmer for years before producing symptoms, such as HIV, or for acute infections where time to death is variable, derivations of the desired incidence curve can be uncertain.

Goldstein *et al.* apply a mathematical method that was originally used for the purpose of extracting images from blur. Information about the time to death and the deaths per day was combined to calculate the incidence distribution, and the authors applied their approach to the influenza epidemic that struck Philadelphia in 1918. Their analysis suggests that in the few days between when the size of the epidemic became clear and when the city enacted closure of public gathering places, the spread of influenza was already being slowed significantly, probably by changes in individual behavior. — PJH

*Proc. Natl. Acad. Sci. U.S.A.* **106**, 21825 (2009).



Hit2LEAD.com™

URL: <http://www.hit2lead.com>



CHEMBRIDGE CORPORATION'S  
ONLINE CHEMICAL STORE

SEARCH  
FIND  
BUY

SCREENING COMPOUNDS  
and BUILDING BLOCKS



- Over 800,000 screening compounds available from stock in 1-100mg amounts.
- Over 12,000 building blocks available from stock in 1-100g amounts.
- Online real-time availability and pricing.
- One-week delivery worldwide. 24-48 hour delivery for rush orders.
- Discounted online prices and cumulative pricing discounts.
- Search by structure, sub-structure, similarity, ID searches, etc.
- Over 95% purity by NMR & LCMS guaranteed on all building blocks.
- Both purchase orders and credit cards are accepted for online order processing.



San Diego, CA

Toll Free: 800-964-6143

Tel: 858-451-7400, Option#4

Fax: 858-451-7401

[www.hit2lead.com](http://www.hit2lead.com)



1200 New York Avenue, NW  
Washington, DC 20005

Editorial: 202-326-6550, FAX 202-289-7562  
News: 202-326-6581, FAX 202-371-9227

Bateman House, 82-88 Hills Road  
Cambridge, UK CB2 1LQ  
+44 (0) 1223 326500, FAX +44 (0) 1223 326501

**SUBSCRIPTION SERVICES** For change of address, missing issues, new orders and renewals, and payment questions: 866-434-AAAS (2227) or 202-326-6417, FAX 202-422-1065. Mailing addresses: AAAS, P.O. Box 96178, Washington, DC 20090-6178 or AAAS Member Services, 1200 New York Avenue, NW, Washington, DC 20005

**INSTITUTIONAL SITE LICENSES** please call 202-326-6755 for any questions or information

**REPRINTS:** Author Inquiries 800-635-7181

Commercial Inquiries 803-359-4578

**PERMISSIONS** 202-326-7074, FAX 202-682-0816

**MEMBER BENEFITS** AAAS/Barnes&Noble.com bookstore www.aaas.org/bn; AAAS Online Store www.apisource.com/aaas/ code MKB6; AAAS Travels: Betchart Expeditions 800-252-4910; Apple Store www.apple.com/epstore/aaas; Bank of America MasterCard 1-800-833-6262 priority code FAA3YU; Cold Spring Harbor Laboratory Press Publications www.cshlpress.com/affiliates/aaas.htm; GEICO Auto Insurance www.geico.com/landingpage/go51.htm?logo=17624; Hertz 800-654-2200 CDP#343457; Office Depot https://bsd.officedepot.com/portal/login.do; Seabury & Smith Life Insurance 800-424-9883; Subaru VIP Program 202-326-6417; VIP Moving Services www.vipmayflower.com/domestic/index.html; Other Benefits: AAAS Member Services 202-326-6417 or www.aaasmember.org.

science\_editors@aaas.org (for general editorial queries)  
science\_letters@aaas.org (for queries about letters)  
science\_reviews@aaas.org (for returning manuscript reviews)  
science\_bookrevs@aaas.org (for book review queries)

Published by the American Association for the Advancement of Science (AAAS), *Science* serves its readers as a forum for the presentation and discussion of important issues related to the advancement of science, including the presentation of minority or conflicting points of view, rather than by publishing only material on which a consensus has been reached. Accordingly, all articles published in *Science*—including editorials, news and comment, and book reviews—are signed and reflect the individual views of the authors and not official points of view adopted by AAAS or the institutions with which the authors are affiliated.

AAAS was founded in 1848 and incorporated in 1874. Its mission is to advance science, engineering, and innovation throughout the world for the benefit of all people. The goals of the association are to: enhance communication among scientists, engineers, and the public; promote and defend the integrity of science and its use; strengthen support for the science and technology enterprise; provide a voice for science on societal issues; promote the responsible use of science in public policy; strengthen and diversify the science and technology workforce; foster education in science and technology for everyone; increase public engagement with science and technology; and advance international cooperation in science.

## INFORMATION FOR AUTHORS

See pages 352 and 353 of the 15 January 2010 issue or access www.sciencemag.org/about/authors

EDITOR-IN-CHIEF **Bruce Alberts**

EXECUTIVE EDITOR

**Monica M. Bradford**

NEWS EDITOR

**Colin Norman**

MANAGING EDITOR, RESEARCH JOURNALS **Katrina L. Kelner**

DEPUTY EDITORS **R. Brooks Hanson, Barbara R. Jasny, Andrew M. Sugden**

**EDITORIAL SENIOR EDITORS/COMMENTARY** Lisa D. Chong, Brad Wible; **SENIOR EDITORS** Gilbert J. Chin, Pamela J. Hines, Paula A. Kiberstis (Boston), Marc S. Lavine (Toronto), Beverly A. Purnell, L. Brian Ray, Guy Riddihough, H. Jesse Smith, Phillip D. Szuroni (Tennessee), Valda Vinson, Jake S. Yeston; **ASSOCIATE EDITORS** Kristen L. Mueller, Jelena Stajic, Nicholas S. Wigginton, Laura M. Zahn; **RESEARCH ASSOCIATE** Alexis Wynne Mogul; **ONLINE EDITOR** Stewart Wills; **ASSOCIATE ONLINE EDITORS** Robert Frederick, Tara S. Marathe; **WEB CONTENT DEVELOPERS** Martyn Green, Andrew Whitesell; **BOOK REVIEW EDITOR** Sherman J. Suter; **ASSOCIATE LETTERS EDITOR** Jennifer Sills; **EDITORIAL MANAGER** Cara Tate; **SENIOR COPY EDITORS** Jeffrey E. Cook, Cynthia Howe, Harry Jach, Barbara P. Ordway, Trista Wagoner; **COPY EDITORS** Chris Filiatreau, Lauren Kmeck; **EDITORIAL COORDINATORS** Carolyn Kyle, Beverly Shields; **PUBLICATIONS ASSISTANTS** Ramatoulaye Diop, Joi S. Granger, Jeffrey Hearn, Lisa Johnson, Scott Miller, Jerry Richardson, Jennifer A. Seibert, Brian White, Anita Wynn; **EDITORIAL ASSISTANTS** Emily Guise, Michael Hicks, Patricia M. Moore, Miriam Weinberg; **EXECUTIVE ASSISTANT** Sylvia S. Kihara; **ADMINISTRATIVE SUPPORT** Maryrose Madrid; **EDITORIAL FELLOW** Melissa R. McCartney; **NEWS DEPUTY NEWS EDITORS** Robert Coontz, Eliot Marshall, Jeffrey Mervis, Leslie Roberts; **CONTRIBUTING EDITORS** Elizabeth Culotta, Polly Shulman; **NEWS WRITERS** Yudhijit Bhattacharjee, Adrian Cho, Jennifer Couzin, David Grimm, Constance Holden, Jocelyn Kaiser, Sam Kean, Richard A. Kerr, Eli Kintisch, Greg Miller, Elizabeth Pennisi, Robert F. Service (Pacific NW), Erik Stokstad, Jue Wang; **INTERNS** Lauren Schenkmann; **CONTRIBUTING CORRESPONDENTS** Jon Cohen (San Diego, CA), Daniel Ferber, Ann Gibbons, Robert Koenig, Andrew Lawler, Mitch Leslie, Charles C. Mann, Virginia Morell, Gary Taubes; **COPY EDITORS** Linda B. Felaco, Melvin Gatling, Melissa Raimondi; **ADMINISTRATIVE SUPPORT** Scherraine Mack; **BUREAUS** San Diego, CA: 760-942-3252, FAX 760-942-4979; Pacific Northwest: 503-963-1940

**PRODUCTION DIRECTOR** James Landry; **SENIOR MANAGER** Wendy K. Shank; **ASSISTANT MANAGER** Rebecca Doshi; **SENIOR SPECIALISTS** Steve Forrester, Chris Redwood; **SPECIALIST** Anthony Rosen; **PREFLIGHT DIRECTOR** David M. Tompkins; **MANAGER** Marcus Spiegler; **SPECIALIST** Jason Hillman

**ART DIRECTOR** Yael Kats; **ASSOCIATE ART DIRECTOR** Laura Creveling; **SENIOR ILLUSTRATORS** Chris Bickel, Katharine Sutliff; **ILLUSTRATOR** Yana Greenman; **SENIOR ART ASSOCIATES** Holly Bishop, Preston Huey, Nayomi Kevitiyagala; **ART ASSOCIATES** Jessica Newfield, Matthew Twombly; **PHOTO EDITOR** Leslie Blizard

## SCIENCE INTERNATIONAL

**EUROPE** (science@science-int.co.uk) **EDITORIAL:** INTERNATIONAL MANAGING EDITOR Andrew M. Sugden; **SENIOR EDITOR/COMMENTARY** Julia Fahrenkamp-Uppenbrink; **SENIOR EDITORS** Caroline Ash, Stella M. Hurlley, Ian S. Osborne, Peter Stern; **ASSOCIATE EDITOR** Maria Cruz; **LOCUM EDITOR** Helen Pickersgill; **EDITORIAL SUPPORT** Deborah Dennison, Rachel Roberts, Alice Whaley; **ADMINISTRATIVE SUPPORT** John Cannell, Janet Clements, Louise Moore; **NEWS:** EUROPE NEWS EDITOR John Travis; **DEPUTY NEWS EDITOR** Daniel Clery; **CONTRIBUTING CORRESPONDENTS** Michael Balter (Paris), John Bohannon (Vienna), Martin Eserink (Amsterdam and Paris), Gretchen Vogel (Berlin)

**LATIN AMERICA CONTRIBUTING CORRESPONDENT** Antonio Regalado

**ASIA** Japan Office: Asca Corporation, Tomoko Furusawa, Rustic Bldg. 7F, 77 Tenjin-cho, Shinjuku-ku, Tokyo 162-0808, Japan; +81 3 6802 4616, FAX +81 3 6802 4615, inquiry@sciencemag.jp; **ASIA NEWS EDITOR** Richard Stone (Beijing: rstone@aaas.org); **CONTRIBUTING CORRESPONDENTS** Dennis Normile [Japan: +81 (0) 3 3391 0630, FAX +81 (0) 3 5936 3531; dnormile@gol.com]; Hao Xin [China: +86 (0) 10 6307 4439 or 6307 3676, FAX +86 (0) 10 6307 4358; cindyhao@gmail.com]; Pallava Bagla [South Asia: +91 (0) 11 2271 2896; pbagla@vsnl.com]

EXECUTIVE PUBLISHER **Alan I. Leshner**

PUBLISHER **Beth Rosner**

**FULFILLMENT SYSTEMS AND OPERATIONS** (membership@aaas.org); **DIRECTOR** Waylon Butler; **SENIOR SYSTEMS ANALYST** Nomuna Nyamaa; **CUSTOMER SERVICE SUPERVISOR** Pat Butler; **SPECIALISTS** Latoya Casteel, LaVonda Crawford, Vicki Linton, April Marshall; **DATA ENTRY SUPERVISOR** Cynthia Johnson; **SPECIALISTS** Shirlene Hall, Tarrika Hill, William Jones

**BUSINESS OPERATIONS AND ADMINISTRATION DIRECTOR** Deborah Rivera-Wienhold; **ASSISTANT DIRECTOR, BUSINESS OPERATIONS** Randy Yi; **MANAGER,**

**BUSINESS ANALYSIS** Eric Knott; **MANAGER, BUSINESS OPERATIONS** Jessica Tierney; **FINANCIAL ANALYST** Priti Pamnani, Celeste Troxler; **RIGHTS AND PERMISSIONS:** ADMINISTRATOR Emilie David; **ASSOCIATE** Elizabeth Sandler;

**MARKETING DIRECTOR** Ian King; **MARKETING MANAGERS** Allison Pritchard, Alison Chandler, Julianne Wiegla; **MARKETING ASSOCIATES** Aimee Aponte, MaryEllen Crowley, Wendy Wise; **MARKETING EXECUTIVE** Jennifer Reeves;

**DIRECTOR, SITE LICENSING** Tom Ryan; **DIRECTOR, CORPORATE RELATIONS** Eileen Bernadette Moran; **PUBLISHER RELATIONS, @RESOURCES SPECIALIST** Kiki Forsythe; **SENIOR PUBLISHER RELATIONS SPECIALIST** Catherine Holland;

**PUBLISHER RELATIONS, EAST COAST** Phillip Smith; **PUBLISHER RELATIONS, WEST COAST** Philip Tsolakidis; **FULFILLMENT SUPERVISOR** Iquo Edim; **FULFILLMENT**

**COORDINATOR** Carrie MacDonald; **MARKETING MANAGER** Christina Schlecht;

**MARKETING ASSOCIATE** Mary Lagnaoui; **ELECTRONIC MEDIA: MANAGER**

Lizabeth Harman; **PROJECT MANAGER** Trista Snyder; **ASSISTANT MANAGER** Lisa Stanford; **SENIOR PRODUCTION SPECIALISTS** Ryan Atkins, Christopher Coleman, Walter Jones; **PRODUCTION SPECIALISTS** Nichele Johnston, Kimberly Oster;

**DIRECTOR, WEB AND NEW MEDIA** Will Collins

**ADVERTISING DIRECTOR, WORLDWIDE AD SALES** Bill Moran

**COMMERCIAL EDITOR** Sean Sanders; 202-326-6430

**PROJECT DIRECTOR, OUTREACH** Brianna Blaser

**PRODUCT** (science\_advertising@aaas.org); **MIDWEST/W. CANADA** Rick Bongiovanni: 330-405-7080, FAX 330-405-7081; **EAST COAST/E. CANADA** Laurie Faraday: 508-747-9395, FAX 617-507-8189; **WEST COAST** Lynne Stickrod: 415-931-9782, FAX 415-520-6940; **UK/EUROPE/ASIA** Roger Gonçalves: TEL/FAX +41 43 243 1358; **JAPAN** ASCA Corporation, Nanako Ide +81 (0) 3 6802 4616, FAX +81 (0) 3 6802 4615; ads@sciencemag.jp; **SENIOR TRAFFIC ASSOCIATE** Deandra Simms

**WORLDWIDE ASSOCIATE DIRECTOR OF SCIENCE CAREERS** Tracy Holmes +44 (0) 1223 326525, FAX +44 (0) 1223 326532

**CLASSIFIED** (advertise@sciencemag.org); **U.S.: SALES MANAGER**

Daryl Anderson: 202-326-6543; **MIDWEST** Tina Burks:

202-326-6577; **EAST**

**COAST** Alexis Fleming: 202-326-6578; **WEST/SOUTH CENTRAL** Nicholas Hintibidze: 202-326-6533; **SALES COORDINATORS** Rohan Edmonson,



ADVANCING SCIENCE. SERVING SOCIETY

## SENIOR EDITORIAL BOARD

**John I. Brauman**, Chair, Stanford Univ.  
**Richard Losick**, Harvard Univ.  
**Linda Partridge**, Univ. College London  
**Michael S. Turner**, University of Chicago

## BOARD OF REVIEWING EDITORS

**Adriano Aguzzi**, Univ. Hospital Zürich  
**Takuzo Aida**, Univ. of Tokyo  
**Joanna Aizenberg**, Harvard Univ.  
**Sonia Altizer**, Univ. of Georgia  
**David Altshuler**, Broad Institute  
**Arturo Alvarez-Buylla**, Univ. of California, San Francisco  
**Richard Amazeing**, Univ. of Wisconsin, Madison  
**Angelika Anton**, MIT  
**Meinert A. Andreae**, Max Planck Inst., Mainz  
**Kristi S. Anseth**, Univ. of Colorado  
**John A. Bargh**, Yale Univ.  
**Cornelia I. Bargmann**, Rockefeller Univ.  
**Ben Barres**, Stanford Medical School  
**Marisa Bartolomei**, Univ. of Penn. School of Med.  
**Facundo Batista**, London Research Inst.  
**Ray H. Baughman**, Univ. of Texas, Dallas  
**Yasmine Belkaid**, NIAID, NIH  
**Stephen J. Benkovic**, Penn State Univ.  
**Ton Bisseling**, Wageningen Univ.  
**Mina Bissell**, Lawrence Berkeley National Lab  
**Peer Bork**, EMBL  
**Robert W. Boyd**, Univ. of Rochester  
**Paul M. Brakerfield**, Leiden Univ.  
**Joseph A. Burns**, Cornell Univ.  
**William P. Butz**, Population Reference Bureau  
**Mats Carlsson**, Univ. of Oslo  
**Peter Carmeliet**, Univ. of Leuven, VIB  
**Mildred Cho**, Stanford Univ.  
**David Clapham**, Children's Hospital, Boston  
**David Clary**, Oxford University  
**J. M. Claverie**, CNRS, Marseille  
**Jonathan D. Cohen**, Princeton Univ.  
**Andrew Cossins**, Univ. of Liverpool  
**Robert H. Crabtree**, Yale Univ.  
**Wolfgang Cramer**, Potsdam Inst. for Climate Impact Research

**F. Fleming Crim**, Univ. of Wisconsin  
**William C. Cumbland**, Univ. of California, Los Angeles  
**Jeff L. Dangl**, Univ. of North Carolina  
**Stanislav Dehaene**, Collège de France  
**Edward DeLong**, MIT  
**Emmanouil T. Dermizakis**, Univ. of Geneva Medical School  
**Robert Desimone**, MIT  
**Claude Desplan**, New York Univ.  
**Dennis Discher**, Univ. of Pennsylvania  
**Scott C. Doney**, Woods Hole Oceanographic Inst.  
**W. Ford Doolittle**, Dalhousie Univ.  
**Jennifer A. Doudna**, Univ. of California, Berkeley  
**Julian Downward**, Cancer Research UK  
**Dennis Duboule**, Univ. of Geneva/EPFL Lausanne  
**Christopher Dye**, WHO  
**Michael B. Elowitz**, Calif. Inst. of Technology  
**Gerhard Ertl**, Fritz-Haber-Institut, Berlin  
**Mark Estelle**, Indiana Univ.  
**Barry Everitt**, Univ. of Cambridge  
**Paul G. Falkowski**, Rutgers Univ.  
**Ernst Fehr**, Univ. of Zurich  
**Tom Fenchel**, Univ. of Copenhagen  
**Alain Fischer**, INSERM  
**Scott E. Fraser**, Cal Tech  
**Chris D. Frith**, Univ. College London  
**Wulfraam Gerstner**, EPFL Lausanne  
**Charles Godfray**, Univ. of Oxford  
**Diane Griffin**, Johns Hopkins Bloomberg School of Public Health  
**Christian Haass**, Ludwig Maximilians Univ.  
**Steven Hahn**, Fred Hutchinson Cancer Research Center  
**Gregory J. Hannan**, Cold Spring Harbor Lab.  
**Niels Hansen**, Technical Univ. of Denmark  
**Dennis L. Hartmann**, Univ. of Washington  
**Chris Hawkesworth**, Univ. of St Andrews  
**Martin Heimann**, Max Planck Inst., Jena  
**James A. Hendler**, Rensselaer Polytechnic Inst.  
**Ray Hilborn**, Univ. of Washington  
**Michael E. Himmel**, National Renewable Energy Lab.  
**Kei Hirose**, Tokyo Inst. of Technology  
**Ove Hoegh-Guldberg**, Univ. of Queensland  
**Brigid L. M. Hogan**, Duke Univ. Medical Center  
**Ronald R. Hoy**, Cornell Univ.  
**Olli Ikkala**, Helsinki Univ. of Technology  
**Meyer B. Jackson**, Univ. of Wisconsin Med. School

**Stephen Jackson**, Univ. of Cambridge  
**Steven Jacobson**, Univ. of Florida, Los Angeles  
**Peter Jonas**, Universität Freiburg  
**Barbara B. Kahn**, Harvard Medical School  
**Daniel Kahne**, Harvard Univ.  
**Gerard Karsenty**, Columbia Univ. College of P&S  
**Bernhard Keimer**, Max Planck Inst., Stuttgart  
**Elizabeth A. Kellom**, Univ. of Missouri, St. Louis  
**Hanna Kokko**, Univ. of Helsinki  
**Lee Kump**, Penn State Univ.  
**Mitchell A. Lazar**, Univ. of Pennsylvania  
**David Lazer**, Harvard Univ.  
**Virginia Lee**, Univ. of Pennsylvania  
**Olle Lindvall**, Univ. Hospital, Lund  
**Marcia C. Linn**, Univ. of California, Berkeley  
**John Lis, Cornell Univ.**  
**Richard Losick**, Harvard Univ.  
**Ke Lu**, Chinese Acad. of Sciences  
**Laura Machuga**, CNRS Beaulieu Inst. for Cancer Research  
**Andrew P. Mackenzie**, Univ. of St Andrews  
**Rud Madarigay**, Ecole Normale Supérieure, Paris  
**Anne Magurran**, Univ. of St Andrews  
**Charles Marshall**, Harvard Univ.  
**Martin M. Matzuk**, Baylor College of Medicine  
**Virginia Miller**, Washington Univ.  
**Yasushi Miyashita**, Univ. of Tokyo  
**Richard Morris**, Univ. of Edinburgh  
**Edward Moser**, Norwegian Univ. of Science and Technology  
**Sean Munro**, MRC Lab. of Molecular Biology  
**Naoto Nagaosa**, Univ. of Tokyo  
**James Nelson**, Stanford Univ. School of Med.  
**Timothy W. Nilsen**, Case Western Reserve Univ.  
**Helga Nowotny**, European Research Advisory Board  
**Stuart H. Orkin**, Dana-Farber Cancer Inst.  
**Elinor Ostrom**, Indiana Univ.  
**Jonathan T. Overpeck**, Univ. of Arizona  
**P. David Pearson**, Univ. of California, Berkeley  
**John Pendry**, Imperial College  
**Reginald M. Penner**, Univ. of California, Irvine  
**Simon Philpott**, Univ. of Florida  
**Philippe Pouch, CNRS**  
**Colin Renfrew**, Univ. of Cambridge  
**Trevor Robbins**, Univ. of Cambridge  
**Barbara A. Romanowicz**, Univ. of California, Berkeley  
**Jens Rostrup-Nielsen**, Haldor Topsøe

**Edward M. Rubin**, Lawrence Berkeley National Lab  
**Shimon Sakaguchi**, Kyoto Univ.  
**Michael J. Sanderson**, Univ. of Arizona  
**Jürgen Sandkühler**, Medical Univ. of Vienna  
**David W. Schindler**, Univ. of Alberta  
**Paul Schulze-Lefert**, Max Planck Inst., Cologne  
**Christine Seidman**, Harvard Medical School  
**Terrence J. Sejnowski**, The Salk Institute  
**Richard J. Shavelson**, Stanford Univ.  
**David Sibley**, Washington Univ.  
**Joseph Silk**, Univ. of Oxford  
**Montgomery Slatkin**, Univ. of California, Berkeley  
**Davor Solter**, Inst. of Medical Biology, Singapore  
**Joan Steitz**, Yale Univ.  
**Elisbeth Stern**, ETH Zürich  
**Yoshiko Takahashi**, Nara Inst. of Science and Technology  
**Jurg Tschopp**, Univ. of Lausanne  
**Derek van der Kooy**, Univ. of Toronto  
**Bert Vogelstein**, Johns Hopkins Univ.  
**Ulrich H. von Andrian**, Harvard Medical School  
**Bruce D. Walker**, Harvard Medical School  
**Christopher A. Walsh**, Harvard Medical School  
**David A. Wardle**, Swedish Inst. of Agric Sciences  
**Graham Warren**, Max F. Perutz Laboratories  
**Colin Watts**, Univ. of Dundee  
**Detlef Weigel**, Max Planck Inst., Tübingen  
**Jonathan Weissman**, Univ. of California, San Francisco  
**Sebastian Westler**, Univ. of Georgia  
**Ellen D. Williams**, Univ. of Maryland  
**Ian A. Wilson**, The Scripps Res. Inst.  
**Jerry Workman**, Stowers Inst. for Medical Research  
**Xiaoliang Sunney Xie**, Harvard Univ.  
**John R. Yates II**, The Scripps Res. Inst.  
**Jan Zaenen**, Leiden Univ.  
**Huda Zoghbi**, Baylor College of Medicine  
**Maria Zuber**, MIT

## BOOK REVIEW BOARD

**David Aldrich**, Duke Univ.  
**David Bloom**, Harvard Univ.  
**Angela Creager**, Princeton Univ.  
**Richard Sweder**, Univ. of Chicago  
**Ed Wasserman**, DuPont  
**Lewis Wolpert**, Univ. College London

## Surprise in the Y

The traditional thinking about the male Y chromosome is that it is a stagnant part of the genome. But the first comprehensive comparison of the Y chromosome in humans and chimpanzees shows that, in fact, it is a hot spot of evolution.

Since sex chromosomes first evolved 200 million years ago, the Y chromosomes have steadily lost genes, mainly retaining only those needed to determine sex and produce sperm. Because humans and chimps have a 98%

genetic overlap, researchers assumed that their Y's should be nearly identical.

But when geneticist David Page of the Massachusetts Institute of Technology in Cambridge and colleagues sequenced the male-specific region of

the Y (MSY) in chimpanzees (which comprises 95% of the Y) and compared it with the human MSY, they got a big surprise: More than 30% of the DNA differs between the two species.

This suggests that the Y has undergone "extraordinary" remodeling in the 6 million years since humans and chimpanzees split from a common ancestor, says Page. The team found that the chimpanzee Y has lost many genes that are still



the theme of the sea in Maya spiritual life. The show, "Fiery Pool: The Maya and the Mythic Sea," will open on 27 March.

## Watery King

The panel at left depicts the Maya ruler Tajchanahk, or "Torch-Sky-Turtle," seated on a water lily throne. The work, framed by a bubbling stream and foliage, symbolizes the melding of Earth, sea, and cosmos, according to the Peabody Essex Museum in Salem, Massachusetts. The museum will feature 90 works on the

present in humans—which presumably makes humans closer to the common ancestor than chimps are. What's more, the chimpanzee MSY has acquired twice as many palindromes—blocks of DNA in which the sequence of nucleotides is a mirror image of the sequence on its complementary strand—as the human MSY has. These have led to even greater structural changes in the chimp Y, the team reported online in *Nature* last week.

The researchers suggest that one cause of these changes is the competitive advantage an animal gains by developing new genes for sperm production. In chimps in particular, many males mate with one fertile female, so natural selection favors those with more (or better) sperm.

The discovery of so much variation in the Y chromosome is stunning researchers. "It's really exciting; it's totally well-documented; it's really dramatic," says population geneticist Andrew Clark of Cornell University.

## Doggy OCD

High-energy Doberman pinschers are a breed particularly susceptible to developing compulsive behaviors—such as incessant licking of flanks or sucking on blankets. Now researchers have used Dobermans to make what Nicholas Dodman of Tufts University Cummings School of Veterinary Medicine in North Grafton, Massachusetts, calls "the first discovery of a really robust psychiatric gene."

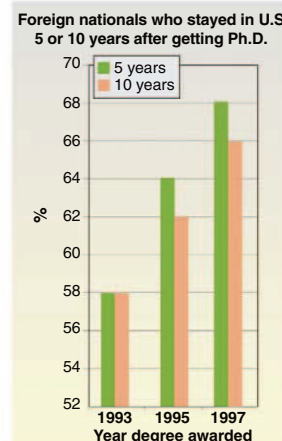
Dodman and his colleagues say canine compulsive disorder (CCD)—analogous to human obsessive-compulsive disorder—is seen in 2% to 5% of dogs brought to the vet. The scientists did a genome-wide association study of 94 Dobermans with CCD, compared with 73 healthy controls. They report in this month's issue of *Molecular Psychiatry* a "highly significant" association with a mutation in neural cadherin-2, a gene involved in central nervous system development, on chromosome 7. Sixty percent of the highest-risk dogs had the mutation, almost three times the rate in the unaffected dogs.

Dennis Murphy, a psychiatrist at the National Institute of Mental Health in Bethesda, Maryland, says an informal consortium of researchers plans to explore the gene further. "It gives us a specific target to look at for compulsive behaviors in humans," he says.

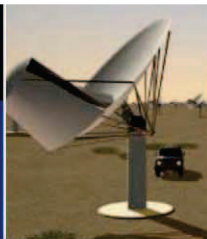


## Foreign Brains Sticking

Several prominent Chinese-born U.S. scientists have recently announced plans to return to their native country. But contrary to many reports, foreign Ph.D.s are not flocking home in droves, Michael Finn of the Oak Ridge Institute for Science and Education in Tennessee reports in a study prepared for the U.S. National Science Foundation. The study finds that 2-year "stay rates" have hovered at about 70% for the past decade. Chinese and Indians, who make up the largest number of foreign doctoral students in the United States, have the highest stay rates.







Angling for  
radioastronomy's  
big prize

400



Google and  
China's Internet

402

## SEISMOLOGY

# Foreshadowing Haiti's Catastrophe

To seismologist William McCann, last week's tragic earthquake in Haiti was a horror foreseen. In 1979, he and a colleague had drawn up a global map titled "Seismic Potential of Major Plate Boundaries." They coded the big fault zones by color—yellows and red denoting the highest probability of rupturing in a big quake. The island of Hispaniola—of which Haiti occupies the western end—was engulfed in red.

"We were concerned because it's been 240 years since the last major earthquake" on the fault that just ruptured, says McCann, who is now an independent consultant with Earth Scientific Consultants in Westminster, Colorado. "Centuries have passed, and this area has been extremely quiet." With the Caribbean tectonic plate to the south straining against the North American plate on the north, quiet was a bad sign. Stress had to be building, but no big quakes were relieving it. When a section of the plate boundary finally did rupture, it did so with devastating fury.

When the east-west, San Andreas-like fault ruptured, tens of thousands likely perished in what may be the Western Hemisphere's worst disaster in a century. Residents of Port-au-Prince felt "very strong" shaking, according to early estimates by the U.S. Geological Survey. Yet at magnitude 7.0, the quake barely qualified as "major." So many people and buildings felt such strong shaking because the epicenter was only 16 kilometers from a city of 2 million inhabitants. And the rupture was shallow, extending upward from a depth of about 10 kilometers. Earthquakes like the one that rocked Sumatra in 2004 break tens of kilometers down and are somewhat muffled as a result.

By seismologists' rule of thumb, that shaking meant "moderate potential damage" in Port-au-Prince, but such projections can't take account of local conditions, note seismic engineers. The capital city is built on sediments, not bedrock, McCann says, so the whole valley would shake like a bowl of jelly. Haiti, the

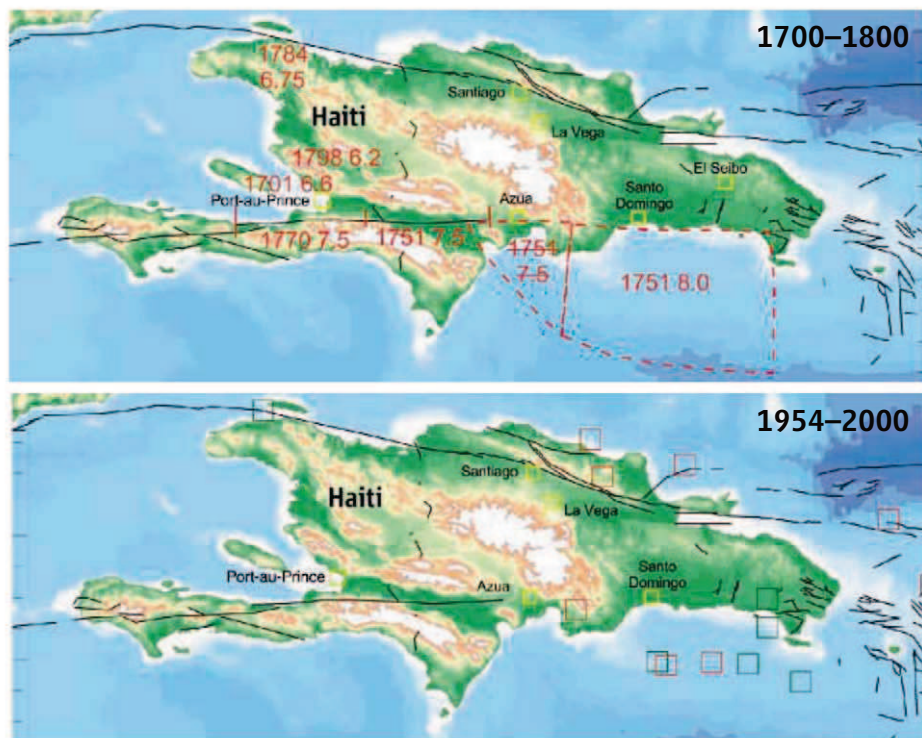
poorest country in the Western Hemisphere, "lacks a reasonable building code" to help structures resist shaking, he says, and "has almost no enforcement" of what code it has.

Last week's quake ruptured only a part of the fault segment that broke in 1770 in a quake since estimated at magnitude 7.5, about five times more powerful. For all the damage it caused, "this quake is not really big," McCann says. Around Hispaniola, "they can get up to magnitude 8," 32 times more powerful. That's because the island—with the Dominican Republic occupying the eastern two-thirds and Puerto Rico and Cuba nearby—is caught in a tectonic fix. The clash of tectonic plates has been a messy business across Hispaniola. Rather than a single, clean plate boundary running east-west across the island, there are two parallel fault systems that are generating quakes with the "Hispaniola microplate" caught between them.

This doubled plate boundary has produced plenty of quakes, though not many big ones lately. For a 2001 meeting on seismic risk reduction in the Caribbean region, McCann compiled historical, geologic, and seismic records of quakes going back centuries, some dramatic. The magnitude 7.5 in 1770—after which 30,000 people died of sickness and hunger—was something of an aftershock to the century's main event, a magnitude 8.0 in 1751 along the southeastern coast where the Caribbean plate dives beneath the Dominican Republic rather than sliding by as it does in the west. Another magnitude 7.5 broke the central part of the southern fault system a few months later. Then in the 19th century, a magnitude 8.0 hit the north coast of Haiti on the northern fault system. The 20th century was far calmer. In the first half, four magnitude 7s hit the Dominican Republic's north coast, but Haiti was disquietingly devoid of larger quakes throughout.

"The last couple of generations have been lucky," says McCann, but "we may be coming out of the quiet time we've had." Stress is always building on a plate-bounding fault, but when that stress is released in a quake, it can transfer stress to its neighbors. That can push them to failing one after another, as seems to have happened in 1751. The faults of Hispaniola may be coming out of their slumber, McCann warns, and it's now only clearer what havoc they can wreak.

—RICHARD A. KERR



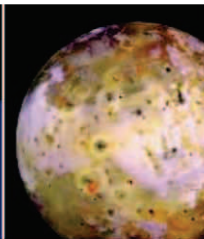
**Rolling thunder, quiet, ...** On Hispaniola, quakes were large and frequent in the 18th century but smaller in the late 20th century (year and magnitude in red, *top*; magnitude 6 quakes, larger squares, *bottom*).

CREDIT: W. R. MCCANN/EARTH SCIENTIFIC CONSULTANTS INC.



The enigma  
of the Natufians

404



Io's  
magma ocean

408

## GLOBAL WARMING

# Models Foresee More-Intense Hurricanes in the Greenhouse

Fewer but fiercer and more-destructive hurricanes will sweep the Atlantic Basin in the 21st century as climate change continues, a new modeling study by U.S. government researchers suggests. The results, reported on page 454, bear out tentative forecasts from earlier studies, although the researchers caution that this is still far from the last word.

"The models seem to be converging," says tropical meteorologist James Kossin of the National Climate Data Center's office at the University of Wisconsin, Madison, who was not involved in the work. Plenty of uncertainties remain, Kossin notes, but compared with earlier studies, this one "is more credible; ... it's important."

What makes the new study more realistic is its sharper picture of the atmosphere. In low-resolution models such as global climate models, the fuzzy rendition of the atmosphere can't generate any hurricanes, much less the intense ones that account for most of the damage hurricanes cause. The high-resolution models used by the U.S. National Weather Service to forecast hurricane growth and movement do produce a realistic mix of both weak and strong storms, but those models can't simulate global warming.

So climate modeler Morris Bender of the National Oceanic and Atmospheric Administration's Geophysical Fluid Dynamics Laboratory in Princeton, New Jersey, and his colleagues used a technique sometimes called "double-downscaling." The group started with the average of atmospheric and oceanic conditions forecast for the end of the century by 18 global climate models. They transferred those averaged conditions into a North Atlantic regional model detailed enough to generate a realistic number of hurricanes,

although still too sketchy to get their intensities right. Finally, the team transferred the regional model's storms to an even higher-resolution hurricane forecast model capable of simulating which ones would develop into category 3, 4, and 5 storms.

The first downscaling showed an 18% decline in the total number of hurricanes. In

and inhibit the formation of new storms.

The group calculates that although the overall number of hurricanes would decline in a warmer world, they would still cause more damage, according to the modeling. Category 3 to 5 hurricanes have accounted for 86% of all U.S. damage despite constituting only 24% of U.S. landfalls, the group notes. That's because

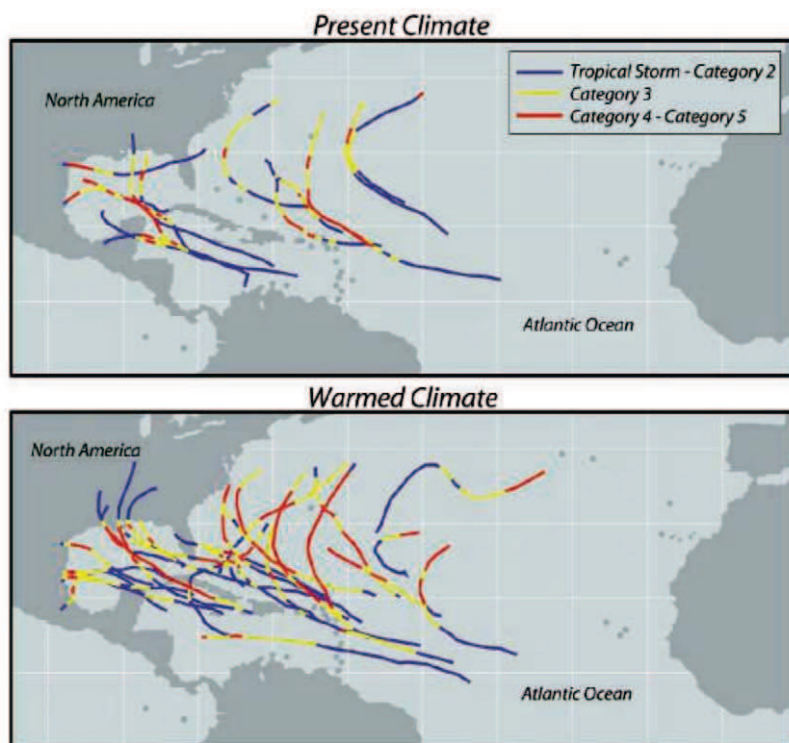
when storms move up from one category to the next, the potential damage roughly doubles. The group finds that in the models, the increase in the rare, most intense storms dominates, leading to a net increase in potential damage of roughly 30%.

The researchers note that the new modeling offers no support for claims that global warming has already noticeably affected hurricane activity. In the real world, the number of Atlantic hurricanes observed during the past 25 years has doubled; in the model, global warming would cause a slight decline in the number over the same period. Given that the mid-resolution model used by the group duplicates the observed rising trend, it may be natural. And the group estimates—very roughly—that so far any effect greenhouse

warming has had on hurricane intensity should still be unrecognizable amid natural variations in hurricane activity.

"It's a good step, a big step forward," says tropical meteorologist Peter Webster. "They've done about as much as you can do with downscaling, [but] it's not the final step." As ever, researchers are looking for yet more computer power and higher resolution to boost the realism of simulations. If the models continue to converge as realism increases, the monster storms that seemed to be already upon us would be removed to decades hence.

—RICHARD A. KERR



**More big blows in the greenhouse.** Computer simulation of the most intense hurricanes shows an increase from today (top) to a warmer world at the end of the century (bottom).

the second downscaling, that decline in the number of storms was limited to moderate-strength storms. Category 4 and 5 storms, with maximum winds of 216 kilometers per hour and above, about doubled in frequency by the end of the century; the strongest storms, with winds of 234 kilometers per hour and above, more than tripled. The results generally matched those of earlier studies that took different approaches to coping with limited resolution. They were also consistent with longstanding theory that as ocean temperatures rise, the additional water vapor driven into the atmosphere can both intensify existing storms



## SCIENTIFIC COOPERATION

# African Physicists Set Their Sights on Mammoth Scope

**DAKAR**—At times, it has looked more like a scene from the movie *Braveheart* than a science conference. “Together we are stronger!” intoned Charles McGruder III to a room packed with physicists from across Africa, who applauded and pumped their fists in the air. McGruder, an astronomer from Western Kentucky University in Bowling Green and a past president of the U.S. National Society of Black Physicists (NSBP), was calling on the scientists here to show a united front in Africa’s bid to host what would be the world’s largest scientific instrument, the Square Kilometre Array (SKA) radio telescope. Last week’s meeting\* in the Senegalese capital not only was the first physics conference spanning the continent but also became a rally for African science, including the establishment of a new African Physical Society.

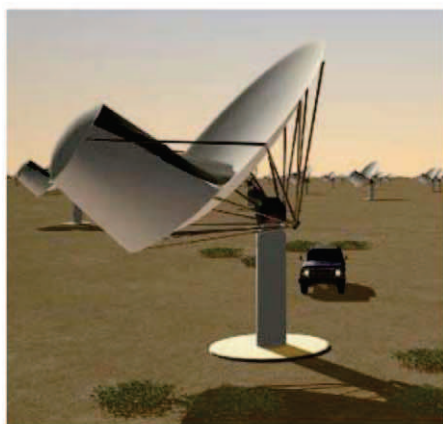
On the minds of many here was SKA, a next-generation radio telescope that will probe gas clouds in the early universe with a collecting area 100 times that of the Very Large Array in Socorro, New Mexico. A lengthy site-selection process has already eliminated China and South America, leaving just Africa and Australia (*Science*, 29 September 2006, p. 1871), with a final decision by the 19 SKA member states due in 2012. “Five years ago, everyone assumed that Australia was sure to get the SKA,” says Phil Charles, director of the Southern African Large Telescope (SALT), an 11-meter optical instrument in Sutherland, South Africa. Australia has long been “a giant” of radio astronomy, he says, whereas Africa had almost no radio telescopes.

But then in 2006, the government of South Africa committed \$250 million to constructing an array of radio dishes as a precursor to the African SKA. Seven of the planned 80 dishes of the array—known as MeerKAT—have now been built. “Now people are taking our bid seriously,” Charles says. Meanwhile, Australia is building up its own seed array of dishes, called ASKAP.

The African bid faces unique political challenges. Whereas Australia would host the entire tele-

scope within its own borders, in Africa the massive array of dishes would be spread across nine countries, with the core in South Africa. Coordinating its construction, use, and maintenance across those borders would require unprecedented regional scientific cooperation. Civil wars and border disputes are serious hurdles. “I put the chances at 50–50” for the African bid, says physicist Cingo Ndimiso, manager of South Africa’s National Laser Centre. “The biggest problem is putting the legal framework in place in each state” so that information and researchers can move freely.

But the benefits of building SKA in Africa far outweigh the difficulties, argues McGruder: “Just the construction alone of the SKA will improve Internet access and help Africa enter the knowledge economy.”



**Continental reach.** The Square Kilometre Array will require thousands of dishes like the one depicted (top), arranged in 30 stations. A possible African configuration is shown above.

McGruder hopes that such arguments will help African researchers persuade their governments to work together to win the SKA bid.

The scientists at the meeting took a first step by founding the African Physical Society. An African Astronomical Society is now in the works. Having pan-African scientific organizations will be “crucial” for reducing governmental red tape, says the conference organizer, Ahmadou Wagué, a physicist at the University of Dakar. “Mobility is a huge problem. This has been the first time that many of us scientists have met each other face to face” due to visa difficulties. McGruder adds that having pan-African science groups will also help with finances. “Funding from outside for African science currently goes through the African Union,” he says. “Scientists need to have control of that money.”

In spite of the good will at the meeting, there was no consensus on the African bid’s chances of success, nor even of SKA’s benefits. “I worry that it would worsen the problem of brain drain from the other African countries to South Africa,” says a European physicist at the meeting, who did not want to be identified because of his collaborations in Africa. Others dismissed such worries. “This meeting makes it clear that Africa has achieved the critical mass of scientists,” says Sune Svanberg, a physicist at Lund University in Sweden. “The SKA belongs here.”

Between now and 2012, the lobbying will be intense. The total construction cost for SKA is estimated at more than \$2 billion, says McGruder, and the United States may provide one-third of that. Because of this, McGruder’s influence could be pivotal, says SALT’s Charles. Where SKA ends up will be largely determined by “the people with the deepest pockets,” he says. McGruder adds that “bringing the SKA to Africa is [the] top priority” of NSBP. “We have a real kinship.”

The ultimate lobbying moment could come this summer when South Africa hosts the World Cup football tournament. “If Obama comes for a visit, we’re going to take him to SALT and MeerKAT,” says Charles with a twinkle in his eye. “We want him to see cutting-edge African astronomy for himself.”

—JOHN BOHANNON

\*The IAM International Workshop on Optics and Lasers in Science and Technology, Dakar, 11–16 January 2010.

IRAN

# Killing of Professor Sparks Fight Over His Science and His Politics

As the first Iranian to receive a physics Ph.D. from a domestic university, Masoud Alimohammadi was a source of pride to his country. In 1989, when Pakistani Nobelist Abdus Salam inaugurated the doctoral program at the Sharif University of Technology, Alimohammadi's mentors touted him as proof that Iran could now produce the next Salam. In 2008, the government picked Alimohammadi, by then a professor of theoretical physics at the University of Tehran, to be its representative for an international scientific facility being built in Jordan called SESAME, Synchrotron-light for Experimental Science and Applications in the Middle East.

Last week, Alimohammadi was assassinated by a remote-controlled motorcycle bomb outside of his apartment. And the country's guardians clutched him even tighter to their bosom. Iranian authorities characterized the killing as an attempt by U.S. and Israeli intelligence agencies to rein in Iran's nuclear program. But colleagues and others believe that the government may actually be the culprit. They point to recent actions by Alimohammadi both before and after the controversial reelection of President Mahmoud Ahmadinejad last June as evidence that the physicist favored political changes and that his death was a warning to other academics who supported the reform movement.

One thing is clear: Alimohammadi was not a nuclear scientist. Trained as a theoretical particle physicist, he had spent years studying string theory and, more recently, dark energy. "His scientific contributions to the Iranian physics community cannot be replaced in the foreseeable future," says Hessamaddin Arfaei, a physicist at Sharif University who was Alimohammadi's thesis adviser.

Alimohammadi was one of 240 Tehran professors who had declared their support for Ahmadinejad's main opponent, Mir-Hossein Mousavi. A more recent example of his activism—and something that reformers say made him a target—occurred just a week before he was killed.

According to Ali Nayeri, an Iranian-born physicist at Chapman University in Orange, California, who first met him at Sharif University, Alimohammadi criticized the regime and urged open dialogue at a 5 January forum held at his department. Speaking to a gathering of students, he said he knew that fear of



**Slain scientist.** Masoud Alimohammadi was a theoretical physicist, not a nuclear scientist.

reprisals kept many more on campus from attending the event. "I too was instructed not to come," he said, according to Nayeri, who translated the talk—posted on YouTube—for *Science*. Frequently interrupted by audience members, some of whom wanted to hear him talk about fraud in the presidential election, Alimohammadi urged students to press on with the reform movement without descending into chaos.

Nayeri, a sympathizer of the reformist movement, says he and many students he has talked to believe that Alimohammadi paid a price for his activism. "His killing was masterminded by the Islamic Republic," Nayeri alleges. "The message to academics is, 'Don't meddle in the political sphere.'"

But another former colleague from the Institute for Studies in Theoretical Physics and Mathematics—where Alimohammadi was a research fellow in the early 1990s—says it's not implausible that the killing was planned by a foreign power. Reza Mansouri, who was deputy minister for research under Ahmadinejad's predecessor, Mohammad Khatami, says the disappearance last year of an Iranian nuclear scientist, Shohram Amiri, during a pilgrimage to Saudi Arabia has reinforced rumors that some foreign intelligence agencies would like to see some Iranian physicists dead. Maybe Alimohammadi was "targeted based on a wrong interpretation of his expertise," he says.

Last week's state funeral featured a confrontation between reformers and government supporters, with each side claiming the allegiance of the slain physicist. Meanwhile, more than 100 academics of Iranian origin around the world have demanded that the Iranian government investigate the murder and bring the assassins to justice. **—YUDHIJIT BHATTACHARJEE**

**ScienceNOW.org**

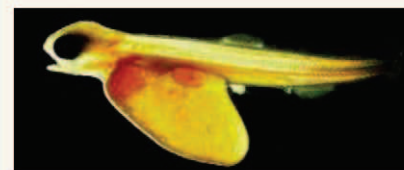
## From *Science's* Online Daily News Site

### Time Machine Tune Up

It took nearly 30 years and a lot of heated debate, but a team of researchers has finally produced what archaeologists, geologists, and other scientists have long been waiting for: a calibration curve that allows radiocarbon dating to achieve its full potential. The new curve, which now extends back 50,000 years, could help researchers work out key questions in human evolution, such as the effect of climate change on human adaptation and migrations. <http://bit.ly/radiocalibration>

### A Better Suspension Bridge

A bit of bridge-building wisdom that dates back to 17th century Dutch polymath Christiaan Huygens needs a rethink, reports a team of structural engineers. Following Huygens's lead, engineers have assumed that the best design for a suspension bridge relies on simple cables that hang between towers in an elegant curve. A more-complicated design uses less material and is therefore more efficient, according to the new work. But it's not likely to appear on roads. <http://bit.ly/suspensionbridge>



### Why Did Fish Evolve Gills?

If you said, "to breathe," then you probably passed Biology 101. But you—and the textbooks—may not be right. A new study argues that the structures really emerged to help keep fish in chemical balance with their environment. <http://bit.ly/fishgills>

### Oil Drop Navigates Complex Maze

Lab rats, watch your back. Scientists have found a way to make simple droplets of oil navigate complex labyrinths with the same skill as laboratory rodents. The advance could help researchers devise better ways to solve other mazelike problems, from rooting out cancer in the body to mapping paths through traffic jams. <http://bit.ly/oildrop>

Read the full postings, comments, and more on [scienconow.sciencemag.org](http://scienconow.sciencemag.org).



## ACADEMIC FREEDOM

# Google Plots Exit Strategy As China Shores Up 'Great Firewall'

**BEIJING**—Google's declaration last week that it will no longer play ball with Chinese censors has inflamed tensions between backers of the free flow of information and advocates of China's increasingly assertive efforts to cleanse the Internet of offensive material.

Much more is at stake than the possible demise of a single Web site, Google.cn. "Any effort to block open access to the Internet would hurt the Chinese academic community and the long-term interests of China," says Rao Yi, life sciences dean at Peking University. In recent weeks, however, China has slapped new controls on Web content and commerce. For example, last month the Ministry of Industry and Information Technology (MIIT) issued rules intended to "weed out pornography" on Web sites that provide content to cell-phone users. And authorities have imposed an Internet blockade on an entire region of western China, where people now can access only a few sites within China.

It's unclear whether Google's defiance will

affect scientists. If the government were to retaliate by adding Google.com to its roster of forbidden sites, access could be cut off to Gmail and two research tools, Google Scholar and Google Earth. It wouldn't be a total loss: PubMed, for instance, could compensate in part for the loss of Scholar. And some see the upheaval as a blessing in disguise. In the long term, argues Zhu Yong-Guan, director of the Institute of Urban Environment in Xiamen, "Google's pullout will in a way stimulate China's own innovation."

Google's operations in China were fraught from the start. When the company launched Google.cn in January 2006, it took flak for agreeing to censor search results, as Microsoft's MSN and other sites do. In that sense, Google was merely obeying the law. A State Council decree in 2000 bans Web content that—among other things—harms security, subverts state power, destroys national unity, incites ethnic hatred, disturbs social order, or spreads obscenity.

Google's relations with authorities soured last summer, after government-run CCTV accused Google.cn of suggesting obscene associations when search terms like "mother" and "son" were entered. The government shuttered the Web site temporarily. Then last month, Google uncovered a "highly sophisticated" attack targeting Gmail accounts of human-rights activists, according to Senior Vice President David Drummond in a 12 January post to Google's official blog. In response, he wrote, "We have decided we are no longer willing to continue censoring our results on Google.cn." Google was expected to meet with Chinese officials this week to, as Drummond says, discuss "the basis on which we could operate an unfiltered search engine within the law, if at all."

Of paramount importance to scientists here is not Google.cn's fate but whether access to information in China will be further restricted. Apparently realizing that innovation requires freedom to explore new ideas, censors are not deaf to pleas from the academic community. When researchers recently complained about some pages of the Massachusetts Institute of Technology's Web site being blocked, according to an official with the China Education and Research Network, a national academic network under

## GERMANY

# Under Fire From Pharma, Institute May Lose Its Director

A long-running feud between pharmaceutical companies and the German institute that evaluates the effectiveness of medical treatments could cost the institute director his job. Although the post is supposed to be apolitical, members of Germany's new coalition government have called for Peter Sawicki, founding director of the Institute for Quality and Efficiency in Health Care (known by its German acronym IQWiG), to be replaced with someone who is friendlier to the pharmaceutical industry. As *Science* went to press, the institute's board of directors was expected to decide on 20 January whether Sawicki, a clinical researcher and diabetes expert, will be replaced when his contract runs out later this year.

Sawicki's supporters say the move would endanger the institute's reputation for impartial and rigorous science, and earlier this month a petition signed by 600 doctors and clinical researchers called on the health minister and the board to keep Sawicki on. Gerd Antes, director of the German Cochrane



**Looking for work?** Peter Sawicki heads a German institute that has drawn the ire of drug companies for how it evaluates medical treatments.

Centre in Freiburg, a not-for-profit organization that analyzes health care effects, says that replacing Sawicki would significantly undermine IQWiG and its work. Antes views the anti-Sawicki push as "part of the political game to soften and to weaken rigorous pro-

cedures for new drugs and medical devices in Germany."

IQWiG, based in Cologne, was started in 2004 as part of a reform of the German health care system. With a function similar to the U.K.'s National Institute for Health and Clinical Excellence (NICE), IQWiG's reports inform the panel that decides which treatments are covered by Germany's publicly funded insurance plans. Sawicki has tussled with drug companies over access to their unpublished studies and over reports from the institute, such as the one that found "no evidence" that a new product was superior to older synthetic human insulin. Industry groups, especially the German organization of research-based pharmaceutical companies, VFA, have been highly critical of IQWiG, saying, for example, that IQWiG is too selective in deciding which studies to include in its evaluations.

Big pharma's attacks have even come from outside Germany. In March 2009, the Pharmaceutical Research and Manufacturers of America petitioned the Obama Administra-

CREDIT: IQWiG



**Closing shop?** Attacks on Gmail accounts were the last straw for Google China.

the education ministry, access was restored.

But last July's riots in Xinjiang Uyghur Autonomous Region strengthened the hand of Chinese officials who favor tighter Internet curbs. After claiming that social networking sites were used to orchestrate the violence, authorities cut off the region's

Internet access, complicating scholars' lives (*Science*, 11 December 2009, p. 1471). Late last month, access was restored to many local sites, but so far only four outside Xinjiang. Elsewhere in mainland China, Internet access is much freer—although Facebook, YouTube, and major blog sites are blocked.

Across China, more restrictions are coming on line to cope with the skyrocketing number of people who use cell phones to access the Net: 60.8% of the country's 384 million Internet users. Ostensibly to fight the spread of porn, MIIT and other organs are working to better monitor content originating from cell phones and to "speed up pilot projects for discovering harmful information" on wireless Internet, according to MIIT's Web site. As the ministry tightened up, Google abruptly postponed this week's planned release of its new mobile phone technology in China, offering no information on whether the launch would be rescheduled.

In an interview posted to the State Council's Web site last week, the council's information director, Wang Chen, stated that "China's Internet is entering an important stage of development, confronting both rare opportunities and severe challenges." That's one sentiment both proponents and critics of the Great Firewall can agree on.

—RICHARD STONE AND HAO XIN

tion to put Germany on a trade and intellectual property "priority watch list" chiefly because of IQWiG's influence on the German drug market. The petition complained that the institute has "inadequately taken into account the value of innovative pharmaceuticals," among other complaints. The Obama Administration declined to put Germany on its watch list.

Sawicki acknowledges that it is difficult for new drugs or techniques to make the grade. "We have introduced a method based on patient-relevant outcomes: morbidity, mortality, and quality of life," he says, while avoiding what he calls "invalid surrogates," such as cholesterol levels or bone density. "You can lower cholesterol and increase mortality. You can lower blood pressure and increase heart failure," he says. Second, he says, "we are looking for progress" rather than just effectiveness, which means that an innovation is not compared with a placebo but with the current standard of care. "We are trying to answer the question, 'Is it better?'" Sawicki says he has some sympathy for the drugmakers: "It is very difficult to produce something better than what we already had."

Industry complaints about the institute have found some support among German

politicians. In the October agreement forming Germany's new governing coalition, the parties stated their intention to examine IQWiG's methods, with the goal of "increasing the acceptance of the institute's findings among patients, caregivers, and producers." In late November, German media reported that recommendations circulated among top health policymakers called for Sawicki to be replaced and for the institute to be made more industry-friendly. Sawicki is also facing an ethics inquiry, which he says he requested after a new finance director found irregularities in expense accounts. Specifics of the inquiry, involving a leased Audi as an official car and business-class domestic flights, leaked earlier this week.

The institute's work is bound to be controversial, says Antes. Similar research in the United States has also attracted criticism (*Science*, 27 November 2009, p. 1183). Although Sawicki's term hasn't been flawless, Antes says, he has been instrumental in getting the institute up and running. "He never gives in. He has a very strong spine. In 5 years, they have established an institute with a good international reputation."

—GRETCHEN VOGEL

## ScienceInsider

### From the Science Policy Blog



The World Health Organization (WHO) is defending itself from Wolfgang Wodarg, a German physician who has called **the H1N1 swine flu pandemic** "fake" because the virus isn't very different from existing strains. WHO has dismissed Wodarg's suggestion that big pharma coaxed WHO into declaring a pandemic so that it could produce and sell more vaccine. <http://bit.ly/8ZiYL2>

Scientists at the helm of the Intergovernmental Panel on Climate Change are discussing steps to **respond to issues raised by e-mails** uncovered at the University of East Anglia after a theft by a presumed hacker in November. IPCC says none of the e-mails suggest malfeasance, but it is nonetheless considering outside reviews and training for authors to deal better with outside pressures. <http://bit.ly/70COJT>

French science minister Valérie Pécresse has chosen **Alain Fuchs**, now head of Chimie ParisTech, to lead the **National Centre for Scientific Research**, a €3.4 billion agency whose 12,000 scientists study everything from archaeology to astronomy. <http://bit.ly/7EK0go>

A 150-page **report on minority faculty at the Massachusetts Institute of Technology** tiptoes around the question of racism in trying to understand the low numbers of underrepresented minorities—2.7% of MIT's science faculty and only 3.4% of the hires in the past 20 years. Its recommendations, embraced by senior administrators pledging to do better, include improved mentoring, training in hidden biases, and cluster hires as well as closer monitoring of current practices. <http://bit.ly/5yUnDQ>

A diverse group of scientific publishers, librarians, and university officials think that all U.S. research agencies should require their grantees to **make their papers freely available** as soon as possible, in line with the policy of the National Institutes of Health. <http://bit.ly/7EKncf>





# The Tangled Roots of Agriculture

**A once-popular view that climate change led the Near East's ancient Natufians to begin domesticating plants and animals is under increasing attack, but alternative paradigms are still being formed**

**PARIS**—About 20,000 years ago, when the last ice age was at its peak, sparse populations of hunter-gatherers roamed the largely treeless steppes of the eastern Mediterranean region in highly mobile bands of perhaps 15 to 50 people. For thousands of years, they eked out a marginal existence, traveling widely to gather tubers and nuts and hunt deer and gazelles. Then, about 14,500 years ago, the climate warmed suddenly. Woodlands of pistachio, olive, and oak, along with lush fields of wild wheat and barley, began to take over the steppes. Just as suddenly, hunter-gatherers in what is now Israel, Jordan, Syria, and Lebanon began doing things they had rarely, if ever, done before. Although they continued to hunt, they built permanent houses of stone and wood, and buried their dead in and around them with elaborate rituals. They ground up wild cereals with mortars and pestles, made tools and art objects from animal bones, and perhaps even practiced Shamanism. And they gathered in sedentary or semisedentary communities of up to several hundred people.

These were the Natufians, a culture so different from what came before that archaeologists once thought they were invaders from afar. Their large, socially complex communities “represent a key development in human settlement history,” says archaeologist Phillip Edwards of La Trobe University in Victoria, Australia. In the Near East, Natufian culture was the next-to-last stop on the long road to

farming, and many of its features seem to foreshadow the Neolithic epoch, when the earliest farmers built densely populated villages of stone and mud brick, painted their walls with art, and buried their dead under the floors. “Many of the activities present in the early Neolithic had their roots in the Natufian,” says zooarchaeologist Natalie Munro of the University of Connecticut, Storrs.

But the warmth that ushered in the Natufian era didn't last long. About 13,000 years ago, smack in the middle of the Natufian cultural florescence, a sharp, 1300-year-long cold and dry spell called the Younger Dryas reversed the post-ice age warming. For some archaeologists, the Natufian response to this sudden cooling holds the clues to one of archaeology's central mysteries: why former hunter-gatherers settled down and invented agriculture.

According to a once-popular hypothesis, the Younger Dryas created an environmental crisis that forced the Natufians or whoever replaced them to begin domesticating plants and animals to ensure that they had enough to eat (*Science*, 20 November 1998, p. 1446), thus spurring the world's first experiments with agriculture.

Back in 1989, when archaeologists Ofer Bar-Yosef of Harvard University and

François Valla of the University of Paris in Nanterre convened the world's leading Natufian experts for a meeting, the Younger Dryas model was well on its way to becoming a leading paradigm for agricultural origins. But when Bar-Yosef and Valla called the Natufian mavens back together for a meeting in Paris last fall,\* opinions had shifted. In talks and recent journal articles, many researchers rejected the idea that the Younger Dryas forced Near Eastern hunter-gatherers to become farmers—or that the Natufians themselves were precocious farmers, as some had suggested.

“Agriculture was not driven by climate change,” says Lisa Maher, an archaeologist at the University of Cambridge in the United Kingdom. Nor, says Arlene Rosen, a geoarchaeologist at University College London (UCL), was Natufian culture simply a way station on the road to farming: “The Natufians were not on a trajectory to agriculture. In fact, they carried on ... for 1300 years as successful foragers during the Younger Dryas.” Nevertheless, researchers say, the Natufians' successful adaptations to what nature threw at them, and their many cultural innovations, may have helped make agriculture possible when the weather was more conducive to it.

## Follow the lunate

The Natufians were discovered and named in 1928 by the legendary British archaeologist Dorothy Garrod. At Shuqba Cave north

\*The Natufian Culture in the Levant II, Paris, 7–11 September 2009.

Online  
sciencemag.org



Podcast interview  
with author  
Michael Balter.

**First farm?** The excavators of Abu Hureyra in Syria think rye was domesticated there.

east of Jerusalem and at el-Wad Cave on Mount Carmel, Garrod unearthed distinctive, crescent-shaped flint tools called lunates, as well as grinding stones and mortars, figurines and jewelry, the remains of stone buildings, and burials of dozens of individuals.

Today, about 60 Natufian sites are known, ranging from larger, villagelike “base camps” to smaller “mobile camps.” Archaeologists divide the culture—often identified by the presence of the lunates, probably used as arrowheads and for cutting plants—into two periods: a more sedentary Early Natufian, characterized by larger encampments and elaborate group burials adorned with ochre and jewelry; and a more mobile Late Natufian, with smaller camps and undecorated, individual burials.

Archaeologists agree that the milder, post-ice age climate conditions helped transform mobile hunter-gatherers into the more sedentary Natufians. In the early years of Natufian research, archaeologists had only a rough idea how old their sites were, in part because of the lack of a suitable radiocarbon calibration curve (*Science*, 15 September 2006, p. 1560). But new dating shows that the Natufians appeared right around the time of the Bølling-Allerød interstadial warm period, which began 14,500 years ago and lasted until the beginning of the Younger Dryas. “There is clearly a striking correlation between the emergence of the larger-scale Natufian settlements and the beginning of the warm and moist Bølling-Allerød,” says UCL archaeologist Andrew Garrard. During colder times, this region was mostly a treeless steppe dotted with shrubs and grasslands, and new forests expanded rapidly, presumably providing the Natufians with nuts and other calorie-rich plant resources and encouraging them to settle down.

Nevertheless, researchers have had little evidence on Natufian use of plants, which preserve poorly in the Mediterranean’s wet winters and hot, dry summers. “We have had almost no direct data on plant use in this period,” says Garrard.

New research at Dederiyeh Cave in northwest Syria is helping to fill that gap. In unpublished work presented here, archaeologist Yoshihiro Nishiaki of the University of Tokyo reported the remains of stone buildings occupied between 14,000 and 13,000 years ago, one of which was heavily burnt, charring and preserving many plant remains. So far, archaeobotanist Ken-ichi Tanno of Japan’s Research Institute for Humanity and Nature in Kyoto has found that nearly 90% of the 12,000 plant fragments he studied come from pistachio and almond trees. Tanno also found significant amounts of wild wheat, one of the main cereals domesticated in the region during the later Neolithic period. The finds at Dederiyeh show that Natufian plant use was “intensive, knowledgeable, and complex,” says Maher. But there’s no sign that the Natufians actually cultivated plants at Dederiyeh rather than simply collecting them wild.

There is also plentiful evidence of Natufian hunting, particularly of the mountain gazelle. Just outside el-Wad Cave, for example, where archaeologist Mina Weinstein-



**Spirit world.** This 12,000-year-old burial at Hilazon Tachtit in Israel might have been that of a shaman woman.

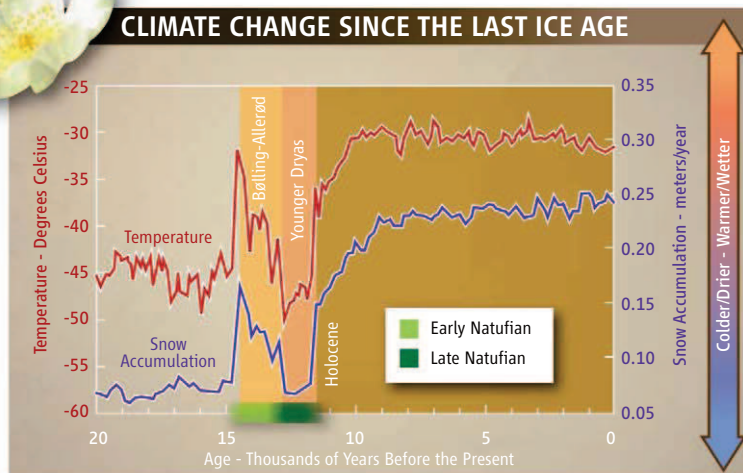
hunting continued unabated during the Younger Dryas, according to studies by Bar-Oz, Munro, and others, a finding they say is inconsistent with decreases in the Natufian population.

### A paradigm gone dry?

The Younger Dryas, named for the sudden return to more southern latitudes of the cold-adapted plant *Dryas octopetala*, has been precisely dated from isotopic ratios of oxygen, nitrogen, and other elements in the Greenland ice cores, which vary with changes in temperature and moisture. These records indicate that the Younger Dryas stretched from 12,900 to 11,600 years ago;

pollen cores and other proxy climate indicators suggest that at least parts of the Near East also experienced this cold, dry spell. The Younger Dryas dates correspond closely to the calibrated dates for the Late Natufian, thought to have begun about 13,000 years ago. This period, archaeologists agree, is marked by at least a partial return to the more mobile lifestyle that preceded the sedentary Early Natufian. Beginning in the late 1980s, Bar-Yosef, Anna Belfer-Cohen of The Hebrew University of Jerusalem, and other researchers argued influentially that the Late

Natufian culture was a response to the cold, dry conditions, which shrank the resource-rich forests and made wild cereals such as wheat and barley more scarce. They argued that the region’s hunter-gatherers turned to agriculture, planting and cultivating fields of the now-precious grains, in a hypothesis often repeated in journal articles and popular books, not to mention on Wikipedia.



**Stormy weather.** Records from Greenland ice cores suggest that the Late Natufians of the Near East had little trouble surviving the cold and dry Younger Dryas (named after the arctic plant *Dryas octopetala*, inset, top).

Evron of the University of Haifa in Israel has led renewed excavations since the mid-1990s, Haifa zooarchaeologist Guy Bar-Oz found that gazelle made up about 75% of the animal bones. Moreover, some researchers say that the pattern of gazelle hunting argues against the idea that a harsh climate during the Younger Dryas caused Natufian population levels to crash. The intensity of gazelle

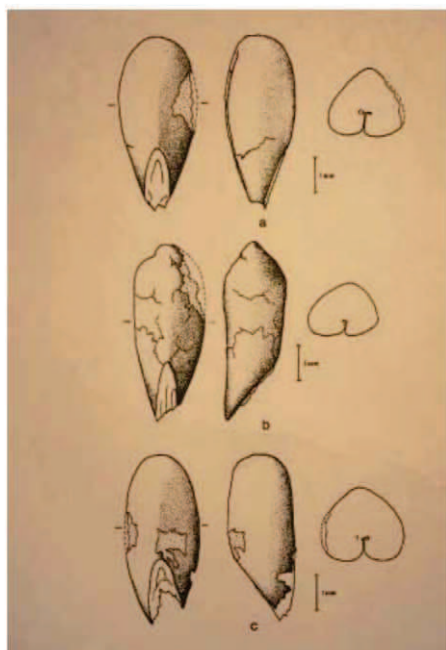


The strongest evidence for this idea comes from the site of Abu Hureyra in Syria, excavated during the 1970s by a team led by archaeologist Andrew Moore, now at the Rochester Institute of Technology in New York state. They found plump rye seeds, which suggested to them that humans had selected over time for large grains. Based on this and other lines of evidence, Moore and UCL archaeobotanist Gordon Hillman argued that rye and perhaps other cereals were domesticated at Abu Hureyra about 13,000 years ago, roughly at the beginning of the Younger Dryas. If true, that would make it the earliest evidence of farming in the world. Supporting evidence came from indications that the Late Natufians intensified their processing of plants. For example, a 2004 study of three Natufian sites in Israel by archaeologist Laure Dubreuil of Trent University in Peterborough, Canada, found more grinding stones in the Late than Early Natufian, as well as evidence from use wear that the stones were increasingly used to grind cereals and legumes. However, the grinding stones could also have been used for working animal hides and grinding ochre for ritual burials, according to a follow-up study published in *Antiquity* late last year by Dubreuil and archaeologist Leore Grosman of Hebrew University.

Despite the Younger Dryas's 20-year run as a leading explanation for the rise of agriculture, many scientists remained skeptical, and the idea has come under increasing attack. "The so-called impact of the Younger Dryas was always a matter of belief, not a matter of science," says Valla. Archaeobotanist George Willcox of the Archéorient research center in Jalès, France, says that "there is only one site where [the younger Dryas explanation] could possibly work, and that's not enough." That site is Abu Hureyra, but Willcox isn't convinced that the nine fat rye seeds reported there really represent domesticated grain. "There are so few of them," he says, adding that "the general consensus is that plump grains are not good evidence for domestication."

Other archaeologists see little evidence that the Late Natufians actually faced an environmental crisis. Archaeologist Nicholas Conard of the University of Tübingen in Germany and his co-workers have found considerable evidence at Baaz rock shelter in Syria that Natufians ate freshwater fish, which points "to the presence of stable sources of flowing water at a time when we are supposed to be in an environmental crisis due to aridity."

And newer calibrated radiocarbon dating suggests that the Natufians did reasonably



**Rounded rye.** The Abu Hureyra team argues that these plump rye grains were domesticated.

well during the entire Younger Dryas, Grosman argued in a talk here. The calibrated dates now stretch the Natufian period from about 2300 uncalibrated years to well over 3000 calibrated years and make the Late Natufian even longer than the Early Natufian. To have survived the return to harsh conditions for so long, Rosen says, the Late Natufians must have had a "stable adaptation" to the Younger Dryas. Moreover, Munro says, the increased mobility of the Late Natufian was not a likely "trigger for agriculture" and may have in fact postponed it.



**Galloping gazelle.** Natufians probably hunted their favorite prey using lunates (inset) as arrowheads.

Some Younger Dryas advocates are not convinced by this logic. Bar-Yosef argues that many of the first Neolithic sites, which cropped up just as both the Late Natufian and the Younger Dryas ended about 11,500 years ago, are "more than 10 times as large as the biggest Natufian sites. Where did they come from if food supplies were not improving during the late centuries of the Younger Dryas?" And Moore says that although the Younger Dryas was not the only catalyst for farming, at Abu Hureyra it "provided a key trigger." As evidence he cites not only the rye grains but also other signs, such as a rise in weeds typically found in cultivated fields and an increase in legumes such as lentils, which Moore says could not have survived the dry Younger Dryas unless they were deliberately cultivated. Moore also points to increasing evidence that early farmers engaged in "predomestication cultivation" long before cereals and other plants took on the domesticated morphology that makes them recognizable to archaeobotanists (*Science*, 29 June 2007, p. 1830).

But if the dissenters are right and the Younger Dryas did not trigger the rise of agriculture in the Levant, what did? Many archaeologists have concluded that farming began not during the cold, dry climate that hit Natufian culture at its height, but only later—after warm, moist conditions were restored 11,600 years ago. In this view, says Rosen, prehistoric peoples were both "pushed" into agriculture by growing populations that fostered renewed sedentism and "pulled" by the increased rainfall and milder climates that made farming more attractive and less risky. Only then, Rosen says, was nature in full "come-hither mode," making agriculture not only possible but also desirable.

Willcox, whose own research suggests that both cultivation and domestication didn't start until the Holocene, says he "agrees 100%" with this viewpoint. But although the Natufians may not have invented agriculture, many archaeologists say, their many cultural innovations—in art, technology, architecture, and possibly experimentation with wild plant cultivation—probably made later developments possible. In a sense, says anthropologist Donald Henry of the University of Tulsa in Oklahoma, the Natufians were "preadapted" for farming—even if, as Valla puts it, "they had no clue what was to follow."

—MICHAEL BALTER

CREDITS (TOP TO BOTTOM): A.M.T. MOORE; VILLAGE ON THE EUPHRATES, OXFORD UNIVERSITY PRESS, 2000; © ABED AL HAFIZ HASHLAMOUN/EPA/CORBIS; (INSET) PHILLIP EDWARDS/LA TROBE UNIVERSITY

## SCIENCE INDICATORS

## Trends Document China's Prowess

New report shows how a decade of investment in science and technology has moved the world's most populous nation into the front ranks on key global indicators

China has arrived. But the rest of the world has not left the building. That's the message from the 2010 edition of *Science and Engineering Indicators*, the newly released biennial collection of data on the global scientific enterprise from the U.S. National Science Foundation ([www.nsf.gov/nsb/sei](http://www.nsf.gov/nsb/sei)).

"I don't think we've ever seen another country in which S&T spending has risen by 20% annually for more than a decade,"

explains NSF's Rolf Lehming, who oversees the statistical compendium. "The results show up everywhere: percent of GDP devoted to research, undergraduate degrees, the value of knowledge-intensive products." The 2010 volume reflects "a consolidation" of what's been taking place for years, he adds, "and we don't see a flattening of these trends."

Yet China's rise doesn't mean that other

countries aren't also continuing to invest in research and education. Here is a sampling of global metrics featured in this year's *Indicators*—which fails to capture the international economic crisis of 2008–09—plus a snapshot of the current job market for U.S. scientists.

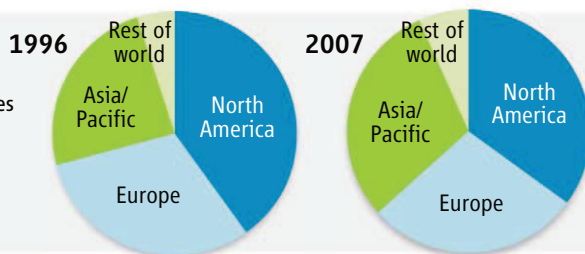
—JEFFREY MERVIS

## SPENDING

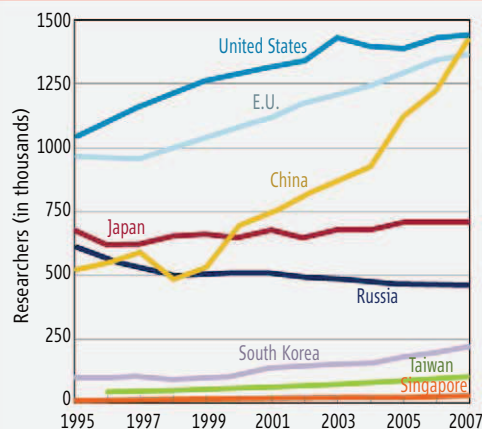
## Trilateral powers.

The annual research expenditures of the United States, Asia, and Europe are almost the same.

SOURCES: OECD; UNESCO; NSF



## WORKFORCE



SOURCE: OECD, MAIN SCIENCE AND TECHNOLOGY INDICATORS (2009)

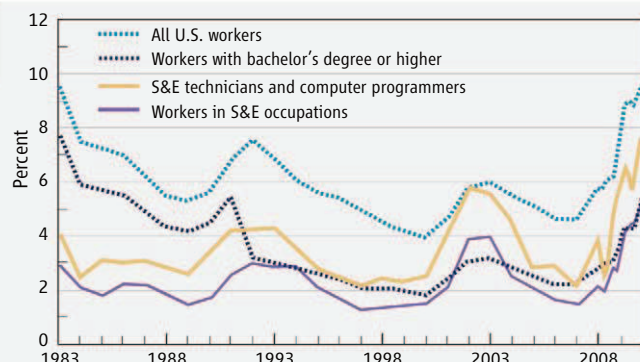


**Staffing up.** The size of China's scientific workforce now equals that of the United States and the European Union, although it still trails in the number per 1000 workers.

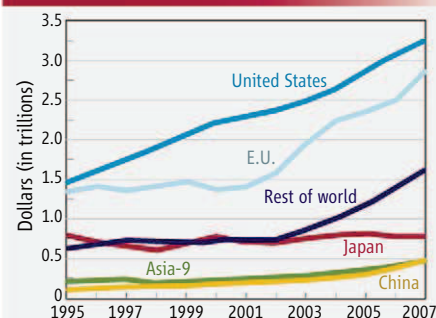
## UNITED STATES JOBLESS RATE

**Working on it.** The scientific sector is still much better off than the rest of the U.S. economy, although unemployment rates have risen to levels not seen in nearly 30 years.

SOURCES: OECD; UNESCO; NSF



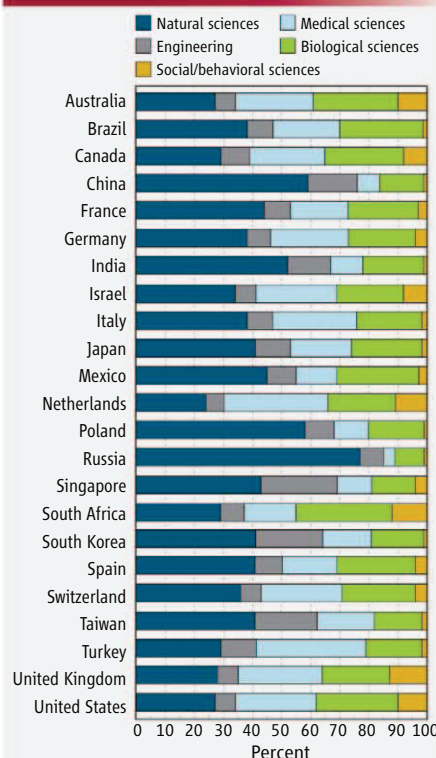
## COMMERCE



**The payoff.** Asian nations still lag in their ability to create what NSF calls "knowledge-intensive commercial services," a sector that includes business and financial services and communications.

SOURCES: IHS GLOBAL INSIGHT; WORLD INDUSTRY SERVICE

## PUBLICATIONS, BY FIELDS



**Paper trail.** Countries differ greatly in their research interests, as measured by their overall publication record across various fields.

SOURCES: THOMSON REUTERS, SCIENCE CITATION INDEX AND SOCIAL CITATION INDEX; THE PATENT BOARD; NSF



## Flows on Mars But No Water

Finding liquid water on Mars would open the possibility of present-day life on the frigid, forbidding planet. So when planetary scientists reported in 2006 that they had photographic evidence that liquid water had flowed on the martian surface twice in recent years, astrobiologists in particular took notice (*Science*, 8 December 2006, p. 1528).

Now researchers operating the next-generation camera orbiting Mars have found eight more of the steep gullies where it looks as if

The dry explanation came in back-to-back talks at the meeting by planetary scientists Serina Diniega and Colin Dundas—both of the University of Arizona, Tucson—with their UA colleagues Alfred McEwen and Shane Byrne. Looking at images taken from orbit during the past 9 years (4.5 martian years), including those from the HiRISE camera on board Mars Reconnaissance Orbiter, they searched for discernible changes from one imaging pass to the next.

Diniega and her colleagues focused on gullies cut into sand dunes. The selected gullies have a classic form: an upper alcove eaten into the dune, a narrow channel cut by sand draining from the alcove, and an apron of sand deposited at the channel's lower end. They found 17 gullies where changes had occurred: Aprons had grown, channels had widened, or whole new channels had formed. These active dune gullies were located between 45°S and 52°S, where it gets cold enough for part of the carbon dioxide atmosphere to freeze and form centimeters-thick frost layers on the ground. All 17 of the changes appeared to happen during the early southern spring, when any frost would be thickest and temperatures were just beginning to rise.

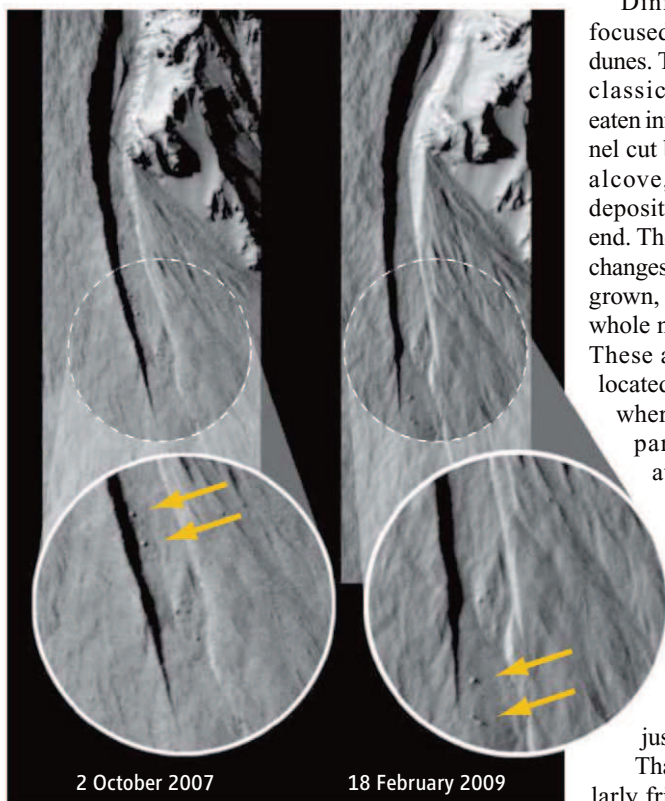
That combination of particularly frigid latitudes and spring-time warming suggests that carbon dioxide frost was essential to the recent flows, Diniega said. Perhaps the weight of the frost

triggers small avalanches, she said. Then the frost might turn into gas that makes sand into a free-flowing fluid, transforming a tiny avalanche into a big, erosive one.

Dundas and his colleagues concentrated on classically shaped gullies on crater walls. They found eight new examples of changes—a lighter or darker tone to gully deposits or changes in gully shape. The eight cases out of 10 known whose timing could be constrained tended to occur in winter and never in sum-

mer, Dundas said, consistent with the timing of dune gully changes. And the crater gully changes were not always superficial; in one case (see figure), meter-scale boulders appear to have been moved.

“What impressed the heck out of me was the boulders moving down the slope,” says applied physicist Michael Hecht of the Jet Propulsion Laboratory in Pasadena. “There’s a significant amount of material being moved.” Aharonson sees a role for carbon dioxide frost in triggering flows down both dune and crater gullies, at least the higher-latitude ones reported here. And frost is “a good candidate” for creating dune gullies in the first place, he says. Forming crater-wall gullies is another matter. Flowing liquid water—perhaps in an earlier, warmer era—is still in the running for that more demanding chore.



**Mars evolving.** The camera aboard Mars Reconnaissance Orbiter has caught recent changes in a gully, including boulders (arrows) that a dry debris flow may have carried downhill.

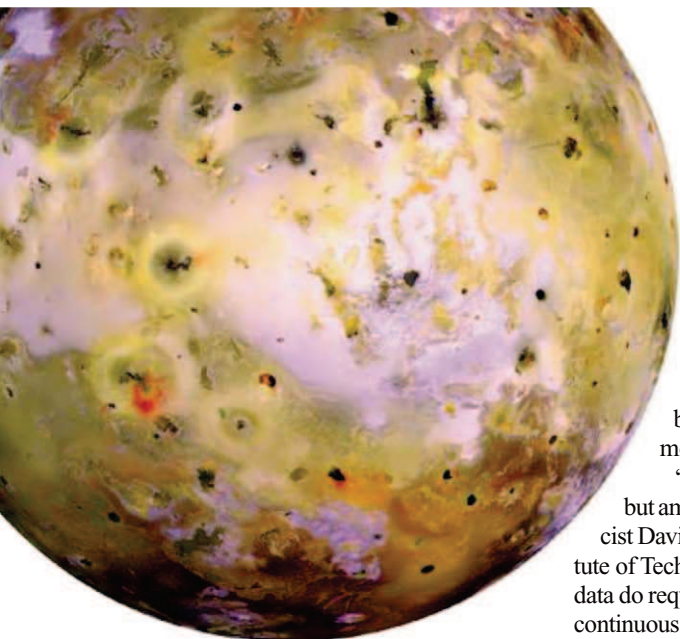
water recently gushed downhill. But the timing and geographic distribution of the flows point not to liquid water but to bone-dry flows of debris somehow facilitated by a ground frosting of frozen carbon dioxide. “I think they have a very compelling case that [the flows] are carbon dioxide-related,” says planetary scientist Oded Aharonson of the California Institute of Technology in Pasadena. The next question is whether the same dry process could have actually created the gullies.

## Magnetics Point to Magma ‘Ocean’ at Io

Three of Jupiter’s large moons have global salty oceans under kilometers of ice, but the fourth, Io, is just a ball of rock. Nevertheless, space physicist Krishan Khurana of the University of California, Los Angeles, and colleagues presented evidence at the meeting for a global ocean tens of kilometers beneath the volcano-pocked surface of Io. This one, however, would be mostly molten rock, harkening back to the solar system’s very earliest days when most big, rocky bodies sported a magma ocean.

Planetary geologist Alfred McEwen of the University of Arizona, Tucson, says the new findings “definitely support the idea of significant [magma] in Io’s mantle” and possibly a full-blown magma ocean. At a minimum, much of Io’s rocky innards is likely more molten mush than solid rock.

Planetary scientists have long wanted to probe Io’s interior for a magma ocean. In 1979, theorists predicted a fiery surface on Io and a magma ocean within it. Jupiter’s gravity raises tides in Io, they noted, kneading the solid rock of the moon and generating heat in the interior. Spacecraft immediately found more volcanic activity on Io than in the rest of the solar system combined. And planetary geologists eventually found at least a few of Io’s 100 known volcanic hot spots to be hundreds of degrees hotter than the hottest lavas on Earth, suggesting a crystal-laden “mushy magma ocean”



**Hot.** A lot of molten rock lies beneath Io's volcano-pocked surface.

would have reversed the poles of any induced field. Sure enough, it was flipped. To produce the observed induced field in a model, the group had to assume that rock about 50 kilometers beneath the surface was completely molten or nearly so.

"Khurana's result is very interesting but ambiguous," says planetary geophysicist David Stevenson of the California Institute of Technology in Pasadena. The magnetic data do require substantial melting of rock in a continuous layer around Io, he says, but sorting out the nature and geometrical arrangement of Io's deep magma ocean or global mush will require an Io orbiter.

(*Science*, 3 December 1999, p. 1827).

But when space physicists tried to probe Io's interior, they encountered an engulfing cloud of confounding debris. In the case of the other three satellites, Jupiter's powerful magnetic field sweeps through the salty ocean and induces an electrical current. That current generates a moon-centered magnetic field that spacecraft flying by could detect. Molten rock would work similarly, but Io's high-flying volcanic debris becomes electrically charged and would tend to mask any weak magnetic field induced in a magma ocean.

But in the course of preparing a proposal to return to Io, Khurana and colleagues went back to magnetic-field data gathered near Io by the Galileo spacecraft. They removed the masking interference as best as they could, leaving what appeared to be an induced field recorded during one flyby. To prove that their first try wasn't a fluke, they corrected magnetic data from a second flyby when Jupiter's magnetic field swept through at a different angle, which

## Antarctic Glacier Off Its Leash

An unmanned autonomous submarine has discovered a sea-floor ridge that may have been the last hope for stopping the now-accelerating retreat of the Pine Island Glacier, a crumbling keystone of the West Antarctic Ice Sheet. The ridge appears to have once protected the glacier, but no more. The submarine found the glacier floating well off the ridge and warmer, ice-melting water passing over the ridge and farther under the ice. And no survey, underwater or airborne, has found another such glacier-preserving obstacle for the next 250 kilometers landward.

The Pine Island and adjacent Thwaites glaciers are key to the fate of West Antarctic

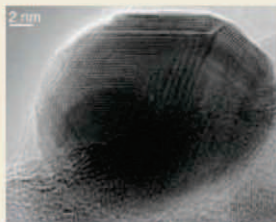
ice, says glaciologist Richard Alley of Pennsylvania State University, University Park, in an e-mail. And West Antarctica is key to how fast and far sea level will rise in a warming world. "To a policymaker, I suspect that the continuing list of [such] ice-sheet surprises is not reassuring," he writes.

At the meeting, glaciologist Adrian Jenkins of the British Antarctic Survey in Cambridge and colleagues described how the instrument-laden Autosub3 cruised for 94 hours along 510 kilometers of track beneath the floating portion of the Pine Island Glacier in January 2009. The sub found a 300-meter-high ridge across the ocean cavity formed by the floating end of the glacier. Deep, warmer water was overtopping the ridge and passing through the gap between floating ice and the ridge top on its way to melting back more of the glacier. That gap has been growing, Jenkins said, perhaps since the 1970s. An aerial photograph from 1973 shows a bump in the ice where the ridge is now known to be, suggesting that the ice was then resting on the ridge and no warmer water could have been getting through.

Although the last physical obstacle to continued melting and retreat of the Pine Island Glacier has been breached, the ice's fate remains murky, says glaciologist David Holland of New York University in New York City. That's because glaciologists aren't sure what got the glacial retreat started in the first place, he notes. It wasn't the greenhouse simply warming the ocean, researchers agree. Instead, shifting winds around Antarctica in recent decades may have driven warmer waters up to the ice and dislodged it from its perch on the ridge. But what caused the winds to shift? Global warming? The ozone hole? Random variability? Glaciologists—and policymakers—would like to know. —**RICHARD A. KERR**

## Snapshots from the Meeting >>

**Still no mammoth-killer.** Nanodiamonds really do litter the sedimentary record at the geologic moment that the mammoths disappeared, geochemist Philippe Claey's of the Free University of Brussels and his colleagues reported at the meeting. A group of researchers has argued that the collision of a 4-kilometer-wide hypervelocity asteroid or comet created the minuscule jewels 12,900 years ago while wiping out all manner of megafauna (*Science*, 2 January 2009, p. 26). "There's really no doubt the nanodiamonds are there," says Claey's. The problem is that they look just like the nanodiamonds found in modern soils in Belgium and Germany. And "a deliberate and detailed hunt" for the type of nanodiamond that forms only under the extreme conditions of an



**What a rock.** Nanodiamonds mark the mammoth extinction, but they don't signify an impact.

impact turned up nothing. So Claey's and colleagues—along with most researchers—still see no clear evidence for an impact.

**Teach them, and they will flee.** The hugely disastrous Sumatran tsunami of 2004 prompted the expansion of warning systems around the world, but that didn't do residents of the Samoan islands any good last September when a nearby earthquake shook them. More than 180 people died before any official warning could reach them. Even so, "there's no doubt training saved lives," says oceanographer Walter Dudley of the University of Hawaii, Manoa, who—with his colleagues—interviewed survivors. The number of saved lives "is certainly in the hundreds, if not the thousands," says Dudley. In preceding months, many islanders had received training from the Department of Homeland Security in how to respond to strong ground shaking. In one reported case, the shaking prompted more than 800 children and adults at a coastal school to evacuate safely to higher ground. In minutes, the tsunami destroyed their school. Says Dudley: "Our experience is, when people know what to do, they won't be victims." —**R.A.K.**





## LETTERS

edited by Jennifer Sills

## Studying Extant Species to Model Our Past

THE COVER CAPTION FOR THE SPECIAL SECTION ON *ARDIPITHECUS RAMIDUS* (2 OCTOBER 2009, p. 60; cover caption, p. 5) echoed a conclusion threaded among the Research Articles: *Ar. ramidus* appears to be so different from *Pan* that “extant great apes are poor models for our last common ancestor.” We are concerned that oversimplistic interpretations of such remarks will devalue exciting progress in synthesizing diverse sources of evidence about our past (1–3). Studies of extant species are yielding important information about behavior and cognition that the fossil record lacks (3–5). Of course, naively projecting the chimpanzee into the past would provide an incomplete model of human origins, given that modern chimpanzees are not our

ancestors. However, extant species play vital roles in several types of contemporary analyses. One of these methods is strategic modeling (6), in which data on extant species are used to derive general principles. This approach is revealing the sociological or ecological correlates of sexual dimorphism, which are being used to interpret the available fossil evidence. Another overlooked method is cladistic analysis, in which features shared by a family of related taxa, such as the great apes (including humans), are identified and parsimoniously attributed to a common ancestor (7, 8). Furthermore, refined referential models, for both single and multiple species, offer behavioral proxies for long-dead forms (9). It would be tragic and illogical if any departures from “chimpaniness” in *Ar. ramidus* were seen as clashing with the integration of recent findings from primatology and paleoanthropology (1–3).

ANDREW WHITEN,<sup>1\*</sup> WILLIAM C. MCGREW,<sup>2</sup> LESLIE C.AIELLO,<sup>3</sup> CHRISTOPHE BOESCH,<sup>4</sup> ROBERT BOYD,<sup>5</sup> RICHARD W. BYRNE,<sup>1</sup> ROBIN I. M. DUNBAR,<sup>6</sup> TETSUROMATSUZAWA,<sup>7</sup> JOAN B. SILK,<sup>5</sup> MICHAEL TOMASELLO,<sup>4</sup> CAREL P. VAN SCHAIK,<sup>8</sup> RICHARD WRANGHAM<sup>9</sup>

<sup>1</sup>Scottish Primate Research Group, University of St. Andrews, St. Andrews, KY16 9JP, UK. <sup>2</sup>Leverhulme Centre for Human Evolutionary Studies, University of Cambridge, CB2 1QH, UK. <sup>3</sup>Wenner-Gren Foundation, 470 Park Avenue South, New York, NY 10016, USA. <sup>4</sup>Max-Planck Institute for Evolutionary Anthropology, Deutscher Platz 6, Leipzig 04103, Germany. <sup>5</sup>Department of Anthropology, University of California, Los Angeles, Los Angeles, CA 90024, USA. <sup>6</sup>Institute of Cognitive and Evolutionary Anthropology, University of Oxford, Oxford OX2 6PN, UK. <sup>7</sup>Primate Research Institute, Kyoto University, Inuyama, Aichi 484, Japan. <sup>8</sup>Anthropological Institute and Museum, University of Zurich, CH8057, Zurich, Switzerland. <sup>9</sup>Department of Anthropology, Harvard University, Cambridge, MA 02138, USA.

\*To whom correspondence should be addressed. E-mail: aw2@st-andrews.ac.uk

## References

1. M. Haslam *et al.*, *Nature* **460**, 339 (2009).
2. W. C. McGrew, R. Foley, Eds., special issue on *Paleoanthropology Meets Primatology*, *J. Hum. Evol.* **57** (2009).
3. R. Boyd, J. B. Silk, Eds., *How Humans Evolved*, 5th Edition (Norton & Company, London, 2009).
4. A. Whiten, C. P. van Schaik, *Philos. Trans. R. Soc. London Ser. B* **362**, 603 (2007).
5. P. Kappeler, J. Silk, Eds., *Mind the Gap: Tracing the Evolution of Human Universals* (Springer-Verlag, Berlin, 2009).
6. J. Tooby, I. deVore, in *The Evolution of Human Behavior: Primate Models*, W. G. Kinzey, Ed. (SUNY Press, New York, 1987), pp. 183–237.
7. R. W. Wrangham, in *The Evolution of Human Behavior: Primate Models*, W. G. Kinzey, Ed. (SUNY Press, New York, 1987), pp. 51–71.
8. R. W. Byrne, *The Thinking Ape: Evolutionary Origins of Intelligence* (Oxford Univ. Press, Oxford, 1995).

## Response

WHITEN *ET AL.* IMPLY THAT WE UNDERVALUED extant species. We find this perplexing. We never stated that studies of extant chimpanzees are unimportant. Our conclusions were based on intensive review of homologous anatomical traits in other primates. Indeed, to understand hominid origins, we must now instead rely on “fundamental evolutionary theory,” which Whiten *et al.* refer to as “strategic modeling.” Increasingly relevant is a vast and still growing knowledge of ecological, locomotor, social, and reproductive interrelationships of not just chimpanzees, but other primates and a wide variety of other vertebrates. In fact, using “data on extant species...to derive general principles” was exactly our approach—the majority of the 108 citations in the final *Ardipithecus* paper referenced such studies. We expressly advocated more intensive reliance on additional living species (beyond *Pan*) because these promise a more comprehensive understanding of social structure in advanced K primates (e.g., *Brachyteles* and other atelines), creation and use of tools (e.g., *Cebus*), and even neuroendocrinology (voles and several primates).

A broad comparative base is equally imperative for accurate phylogenetic analyses, particularly those involving cladistics. The potential of the latter methods to accurately “recover” ancestral phenotypes by parsimony relies on the presence and density of taxa (both extinct and extant) surrounding the nodes of interest. This has been empirically shown with morphological data sets (1) and certainly also applies to behaviors. For example, cladistic analysis of extant species may retrieve the locomotor behavioral trait of knuckle-walking, as the

## Letters to the Editor

Letters (~300 words) discuss material published in *Science* in the previous 3 months or issues of general interest. They can be submitted through the Web ([www.submit2science.org](http://www.submit2science.org)) or by regular mail (1200 New York Ave., NW, Washington, DC 20005, USA). Letters are not acknowledged upon receipt, nor are authors generally consulted before publication. Whether published in full or in part, letters are subject to editing for clarity and space.

# Qs & AAAS



**[www.sciencedigital.org/subscribe](http://www.sciencedigital.org/subscribe)**

For just US\$99, you can join AAAS TODAY and  
start receiving *Science* Digital Edition immediately!



# Qs & AAAS



**[www.sciencedigital.org/subscribe](http://www.sciencedigital.org/subscribe)**

For just US\$99, you can join AAAS TODAY and  
start receiving *Science* Digital Edition immediately!

nodal phenotype for the *Pan/Homo* common ancestor, but the *Ardipithecus* forelimb shows that this inference is simplistic and almost certainly incorrect. Indeed, *Ardipithecus* and other Miocene hominoids establish that extant chimpanzees are poor models for our last common ancestor with chimpanzees. Contrary to Whiten *et al.*'s assertions, this conclusion was informed, and should be further extended, by general principles established from all relevant species. All great ape species merit study and conservation, but despite their genomic proximity, none of them should be interpreted as anatomically or behaviorally "living fossils" or "time machines."

C. OWEN LOVEJOY,<sup>1\*</sup> GEN SUWA,<sup>2</sup> T. D. WHITE<sup>3</sup>

<sup>1</sup>Department of Anthropology, School of Biomedical Sciences, Kent State University, Kent, OH 44240-0001, USA. <sup>2</sup>The University Museum, the University of Tokyo,

Hongo, Bunkyo-ku, Tokyo 113-0033, Japan. <sup>3</sup>Human Evolution Research Center, and Department of Integrative Biology, 3101 Valley Life Sciences Building, University of California, Berkeley, CA 94720, USA.

\*To whom correspondence should be addressed. E-mail: olovejoy@aol.com

#### Reference

1. D. S. Strait, F. E. Grine, *J. Hum. Evol.* **47**, 399 (2004).

## Carbon Accounting a Tricky Business

THE POLICY FORUM "FIXING A CRITICAL CLIMATE accounting error" (23 October 2009, p. 527), in which T. D. Searchinger *et al.* describe the error of assigning biofuel carbon emissions as zero, is long overdue. The heat-trapping potential of carbon dioxide from a

modern carbon source is exactly the same as that from a fossil carbon source. The only way biofuel carbon emissions will have no net effect on the global energy balance is if the modern carbon released during biofuel combustion were removed from the atmosphere and quickly incorporated into a carbon sink. The need to count "changes in emissions from land use when biomass for energy is harvested or grown" is vital, but Searchinger *et al.* minimize the difficulty in determining what those emission changes are.

The land-use changes that may occur due to the widespread use of biofuels such as ethanol are highly variable (1–3). Both forest and abandoned or reclaimed agricultural land have potentially large stores of deep mineral soil carbon. We are just beginning to understand the extent of carbon release associated with conversion to bioenergy cultivation [e.g., (4–6)]. The state of the science related to soil carbon dynamics is not developed enough to allow proper carbon accounting of land-use change.

Furthermore, land-use decisions are a dynamic process based on a variety of factors, many unrelated to biofuels. To fully attribute land-use change emissions to biofuels would require determining what would

## Innovation has its Rewards

The Alternatives Research & Development Foundation, a U.S. leader in the funding and promotion of alternatives to the use of laboratory animals in research, testing, and education, is currently soliciting research proposals for its 2010 Alternatives Research Grant Program. Preference will be given to proposals that address the goals of the 2007 National Academy of Sciences report, *Toxicity Testing in the 21st Century: A Vision and A Strategy*.

- Up to \$40,000 in funding.
- Downloadable application and instructions at [www.ardf-online.org](http://www.ardf-online.org).
- Deadline: March 30, 2010.
- Recipients notified: May 20, 2010



Alternatives Research & Development  
FOUNDATION

801 Old York Rd., #316  
Jenkintown, PA 19046  
phone: (215)887-8076  
[www.ardf-online.org](http://www.ardf-online.org)  
[grants10@ardf-online.org](mailto:grants10@ardf-online.org)

## Call for Applications

Applications are now being accepted for the **2010 NASA Space Radiation Summer School**, a three-week course designed to offer graduate students, postdoctoral fellows, and faculty an integrated curriculum of radiation biology, radiation chemistry, and physics culminating in hands-on accelerator-based experiments using the synchrotron facility at the NASA Space Radiation Laboratory. Up to 15 students will be selected for the course, tentatively scheduled for **May 20 – June 11, 2010** at the Brookhaven National Laboratory (BNL) on Long Island, New York. Topics will include DNA damage and repair, genotoxicity measurements, cell cycle checkpoints and apoptosis, the bystander effect, genomic instability, neurodegeneration, tissue remodeling, and the relationships of these processes to carcinogenesis and late degenerative effects following exposure to space radiation, as well as the space radiation environment, physics and biochemistry of charged particle interaction with condensed matter, ionizing radiation dosimetry, and accelerator operations. Course faculty consists of leading university and national laboratory biologists and physicists actively engaged in NASA space radiation research and BNL experts in heavy ion experimentation and methods.

Application instructions are available online at  
[www.dsls.usra.edu/spacerad/2010/](http://www.dsls.usra.edu/spacerad/2010/)

Application Deadline - 11:59 p.m. CT, Sunday, February 28, 2010

U.S. citizens and foreign nationals may apply. All selected students must satisfy BNL/DOE safety and security requirements in order to be admitted. Selected students must also demonstrate oral and written proficiency in the English language. Travel expenses in the U.S. and room and board will be covered for selected participants. Successful applicants from outside the U.S. must provide for their travel to/from New York/Long Island. Course sponsors are the NASA Space Radiation Program, Pacific Northwest National Lab, U.S. Dept of Energy, Brookhaven National Lab, and Universities Space Research Association.



have happened in the absence of biofuels. With the complex land-use transitions that may occur—perhaps from cultivation for crops to bioenergy to pasture—it will be exceedingly difficult to ascribe a given land-use history solely to agricultural or bioenergy production. Thus, the science of soil carbon and the difficulty of assigning land use are just two of the many complexities that will further confound adequate carbon accounting—pointing to a need for both further research and careful analysis.

ANDREW J. FRIEDLAND<sup>1</sup>\* AND  
KENNETH T. GILLINGHAM<sup>2</sup>

<sup>1</sup>Environmental Studies Program, Dartmouth College, Hanover, NH 03755, USA. <sup>2</sup>Management Science and Engineering, Stanford University, Stanford, CA 94305, USA.

\*To whom correspondence should be addressed. E-mail: andy.friedland@dartmouth.edu

#### References

1. T. D. Searchinger *et al.*, *Science* **319**, 1238 (2008).
2. M. Wise *et al.*, *Science* **324**, 1183 (2009).
3. K. T. Gillingham *et al.*, *Mitig. Adapt. Strategies Glob. Change* **13**, 675 (2008).
4. S. Fontaine *et al.*, *Nature* **450**, 277 (2007).
5. A. Diochon *et al.*, *For. Ecol. Manag.* **257**, 413 (2009).
6. A. Diochon, L. Kellman, *Geophys. Res. Lett.* **35**, L14402 (2008).

## East German Institutes Stand Tall

THE NEWS FOCUS STORY “AUFBAU OST: MAX Planck’s East German experiment” (G. Vogel, 6 November 2009, p. 788) claims that “Aufbau Ost” (building up the East) is a project of Max Planck Society. In fact, the term “Aufbau Ost” refers to all government-funded projects to rebuild infrastructure in the former German Democratic Republic. Moreover, our scientific system consists of more than one organization: Others include the Fraunhofer Society, Helmholtz Association, and Leibniz Association. All of these organizations contributed to the scientific “Aufbau Ost.” In fact, in the early years the Max Planck Society indicated that it would not interfere.

The complex process of evaluation and restructuring the East German institutes resulted in more than 40 institutes of the Leibniz Association in the eastern part of Germany employing nearly 7000 people, several large-scale research facilities of the Helmholtz Association, and more than 20 institutes of Fraunhofer Society. None of these was men-

tioned in the story. In nearly all of these institutes, researchers who received their training in East Germany are still working today. These “inherited researchers” have proven to be a crucial support and an important source of innovative ideas for our institutes. They were in no way a burden, as insinuated in the story.

Hans-Peter Hiepe, who administers the German science ministry’s programs for the former East, says in the News Focus story that “[s]cience is really successful when researchers can see their research reflected in the regional economy.” This has already materialized in cases such as Greifswald, Potsdam, Jena, and Berlin-Adlershof.

More astonishing is the quote of Hiepe that the foundation of the research landscape in East Germany “is made of matchsticks.” After nearly 20 years of highly successful work and a number of follow-up evaluations by internationally renowned experts—many with outstanding results—my experience is that we have built our excellent scientific institutions and research infrastructure on a sound basis.

ERNST TH. RIETSCHEL

President of the Leibniz Association, Berlin, 10117, Germany. E-mail: rietschel@leibniz-gemeinschaft.de

WHERE THE BASIC SCIENCE

WORLD

MEETS THE

WORLD

OF MEDICINE

Science

AAAS

www.ScienceTranslationalMedicine.org

## Submit your work to *Science Translational Medicine* today!

On October 7, AAAS and *Science* launched *Science Translational Medicine*, a new journal focused on applications of basic research knowledge that will improve human health.

The journal’s goal is simple: to help the scientific community harness decades of progress in research at the basic level and translate these biological discoveries into medical advances. Take this opportunity to have your work recognized in this groundbreaking new journal.

Papers in the following areas will be reviewed and considered for publication:

- Animal & Human Studies
- Applied Physical Sciences
- Behavior
- Bioengineering
- Biomarkers
- Cancer
- Cardiovascular Disease
- Cell Culture
- Chemical Genomics/Drug Discovery
- Data Mining
- Drug Delivery
- Gene Therapy/Regenerative Medicine
- Imaging
- Immunology/Vaccines
- Infectious Diseases
- Medical Informatics
- Medical Nanotechnology
- Metabolism/Diabetes/Obesity
- Neuroscience/Neurology/Psychiatry
- Pharmacogenetics
- Policy
- Toxicology and Pharmacokinetics
- And other interdisciplinary approaches to medicine



INTEGRATING MEDICINE AND SCIENCE

## ANTHROPOLOGY

# Did They Fail? Could They Choose?

Krista Lewis

**Q**uestioning *Collapse: Human Resilience, Ecological Vulnerability, and the Aftermath of Empire* began as a conference session at the 2006 annual meetings of the American Anthropological Association, where scholars came together to discuss the massive popular appeal of Jared Diamond's *Guns, Germs, and Steel* and *Collapse* (1, 2). Their discussion expanded and developed into a volume that brings together archaeologists, cultural anthropologists, and historians to reanalyze and reinterpret Diamond's case studies and conclusions.

In many cases the authors, all prominent scholars in the time periods, areas, and topics they write about, are able to identify and correct an array of errors in Diamond's data. *Questioning Collapse*, however, is not a collection of indignant scholars dwelling on factual inaccuracies or "Diamond-bashing." The volume presents lively debate, critique, and engagement not only with Diamond's theses but, more importantly, directly with the serious issues he raises and the roles serious scholars should take. The authors contribute positively to critical public discussions about understanding what the past has to offer us as we move toward an increasingly global, environmentally fragile future. Their chapters were written for the wider public rather than being narrowly focused at specialists and yet also have much of value for professionals in the authors' disciplines.

The studies in *Questioning Collapse* make clear that environment is not the only issue that societies must deal with in order to make "civilizations" sustainable. None of the authors disagree with Diamond's claim that understanding past human-environment interactions is important to our future. But they do caution that we need to make certain that studies and arguments are very carefully constructed, methodologically rigorous, and conscious of all possible nuances and facets of the issue. The contributors show how this can

be done for the societies they study, and they explain the implications of Diamond's troubling propensity to overlook the real and powerful influences of cultural ideologies on the paths that civilizations take.

Diamond conjures a sense of crisis, defining collapse in dramatic ways that ignore how societies also choose to be resilient, to adapt and change in ways that can even include abandoning places in favor of new settlements or strategies that better fit their environmental, economic, religious, or other cultural needs. Who is to say that a society such as Norse Greenland, which existed for 450 years,

was a failure because its inhabitants eventually decided for a variety of reasons that life could be better elsewhere? Or that the Maya abandoning their monumental Classic period religious centers was a collapse rather than a political and social shift that was a good decision at the time?

Notably, the authors pay attention to the living descendants of the supposedly failed, collapsed societies that Diamond profiles. The volume does something largely long missing (at least in literature easily accessible to the public), which is to reject historical amnesia by bridging the gap between ancient "lost" societies and the cultural inheritors of these traditions who are still among us. Several chapters highlight the continued existence of communities such as native Easter Islanders, the Maya of Central America, Native North Americans, and Aboriginal Australians and what they have to say about their supposed disappearances. These people have not in fact vanished, but what have been obscured by narratives such as Diamond's (and, admittedly, by archaeological and popular romanticism) are their cultural histories and perspectives. One nice feature of the book is the inclusion of short profiles of

living individuals from the areas in question, whose words and faces represent the human reality of their diverse perspectives.

Diamond intended *Collapse* as an environmental wake-up call but missed the crucial fact, clearly argued in this volume, that proposed solutions to our global environmental problems cannot succeed without grappling with the complex issues of history, colonization, and social injustice that have brought us to our current state of fragility and crises. Several chapters raise the bitter truth that many societies do not have the entirely free choice about how they deal with their environment that Diamond assumes. Especially today, societies are increasingly constrained by being interlaced into complex global social and economic networks. Who are we, from our positions of power and influence, to suggest that the people of Papua New Guinea, for example, should forbid logging or mining on their land when the alternatives available to them also will not sustain or improve their lives and those of their children?

We cannot ease our current global environmental crises without understanding their complex histories and equitably addressing the socioeconomic problems that create

**Questioning Collapse**  
Human Resilience,  
Ecological Vulnerability,  
and the Aftermath of Empire

Patricia A. McAnany and  
Norman Yoffee, Eds.

Cambridge University Press,  
Cambridge, 2010. 390 pp. \$90,  
£55. ISBN 9780521515726.  
Paper, \$29.99, £17.99.  
ISBN 9780521733663.



**Icons of collapse.** Moai left standing close to the quarry at Rano Raraku, Rapa Nui (Easter Island).

and sustain them, and that cannot be done without many difficult shifts in perspective, including about how we define and assign blame for societal collapse. Stepping into someone else's shoes is easy to recommend, but the actual shedding of subconscious cultural ideas about what constitutes "common sense" and practicality in order to do so is much more difficult. Even more challenging may be the creation and maintenance

The reviewer is at the Department of Sociology and Anthropology, University of Arkansas, Little Rock, AR 72204, USA. E-mail: kxlewis@ualr.edu



of socioeconomic systems that value those diverse perspectives, share control and interpretation of heritage, and (most important of all) alleviate problems of social justice. However, such actions are not entirely impossible, and the suggestions the authors of *Questioning Collapse* make about how we can move in those directions are valuable contributions to the effort.

#### References

1. J. Diamond, *Guns, Germs, and Steel: The Fates of Human Societies* (Norton, New York, 1987).
2. J. Diamond, *Collapse: How Societies Choose to Fail or Succeed* (Viking, New York, 2005); reviewed in (3).
3. T. Flannery, *Science* **307**, 45 (2005).

10.1126/science.1184327

## PSYCHOLOGY

# Unsex the Brain

A. Scott Henderson

Does the brain have a sex? Until recently, most investigators considered this question a silly one—the answer was no. But advances in neuroscience, behavioral genetics, and technology—especially magnetic resonance imaging and positron emission tomography—have cast this query in a different light. With increasing confidence, scholars and commentators have cataloged putative differences between male and female brains. These presumed differences have panicked gender-conscious parents, prompted redesigned schools, and provided entrepreneurs with substantial profits.

Amid a rising din of claims and counterclaims concerning this topic, Lise Eliot offers a work of serious and highly persuasive scholarship. A neuroscientist at the Rosalind Franklin University of Medicine and Science, Eliot focuses on a question that lies at the heart of the male-female brain debate: Why do boys and girls perform differently on certain cognitive tasks? Arguing that environmental factors are more influential than intrinsic ones, she repudiates claims made by several popularizers of sex differ-

ences, including Leonard Sax (the physician-psychologist founder of the National Association for Single Sex Public Education) and Michael Gurian (the family therapist turned social philosopher who coined the phrase “boy crisis”).

Summarizing an exhaustive survey of existing research, Eliot concludes that the brains of boys and girls are extremely similar, differing significantly only in their size and maturation rate, neither of which has a demonstrable impact on cognitive functions. In evaluating a range of other traits, she emphasizes their difference value ( $d$ ), a statistic that measures the gap between male and female performance (1). For most cognitive and behavioral traits,  $d$  is small (around 0.2), which means that males and females perform almost equally as well (or as poorly). This makes generalizing about certain characteristics difficult unless one concentrates on the extremes of a distribution curve, where even small differences can add up—for example, the disproportionate number of boys who have dyslexia or girls who suffer from anxiety disorders. Eliot astutely notes that it is this headline-grabbing focus on extremes that typifies claims made by Sax, Gurian, and others.

If, as Eliot maintains, there are so few hard-wired differences between male and female brains, why do the cognitive abilities and interests of boys and girls diverge by mid-to-late adolescence? Why, for instance, do boys typically outperform girls by 35 to 40 points on the math section of the Scholastic Aptitude Test (SAT)? According to Eliot, this can be partially explained by

demographic factors. Significantly more girls than boys who take the SAT come from low socioeconomic backgrounds, the variable that has the greatest influence on standardized test results. Eliot also discusses how test takers can be affected by stereotype threat—the tendency for individuals who are negatively stereotyped to underperform on various tests. Thus, at least some of the performance differences identified by researchers are more apparent than real.

Nevertheless, Eliot acknowledges that



bona fide cognitive “gaps” do exist between boys and girls. These gaps are initially quite small—girls begin talking a couple of months earlier, for example; boys tend to have better spatial reasoning skills by age five. These differences quickly lead to positive feedback loops: Children enjoy, and therefore practice, skills and activities they are good at, and this practice

results in improved performance. As Eliot phrases it, the brain wires itself “in large measure according to the experiences in which it is immersed from prenatal life through adolescence.” Parents and teachers, however, are frequently ignorant of these dynamics, misinterpreting the ever-widening boy-girl achievement gaps as the basis for self-fulfilling prophecies and stereotypes.

Only two weaknesses detract from the book’s many strengths. The title—perhaps chosen for marketing appeal—misleadingly suggests the opposite of Eliot’s thesis. More problematic, Eliot mentions her own children throughout the book, sometimes to illustrate substantive points. This kind of anecdotal evidence is at odds with her otherwise scrupulous marshalling of experimental data, and it also raises the ethical issue of whether children are truly able to give permission for having their lives revealed in a book written by one of their parents.

Eliot’s pedagogical prescriptions are straightforward and logical. She sees few merits and several disadvantages to single-gender classrooms and schools. Instead—given her contention that virtually all skills can be learned—she urges parents and educators to take advantage of the brain’s plasticity by providing children with a wealth of experiences, especially ones that will stretch them beyond their natural aptitudes. Considering the nonsense already in print (much of it erroneously presented as scientific fact), *Pink Brain, Blue Brain* should be required reading for anyone who wants a more thoughtful consideration of how the brains of boys and girls do—but mostly do not—differ.

#### References and Notes

1. The difference value is given by the mean score of males less the mean score of females divided by the standard deviation of both groups.

10.1126/science.1185957

CREDIT: N. CARY/SCIENCE

**Pink Brain, Blue Brain**  
How Small Differences Grow  
into Troublesome Gaps—and  
What We Can Do About It

by Lise Eliot

Houghton Mifflin Harcourt,  
Boston, 2009. 432 pp. \$25.  
ISBN 9780618393114.

The reviewer is in the Department of Education, Furman University, 3300 Poinsett Highway, Greenville, SC 29613–1134, USA. E-mail: Scott.Henderson@Furman.edu

## COMPUTER SCIENCE

# Accessible Reproducible Research

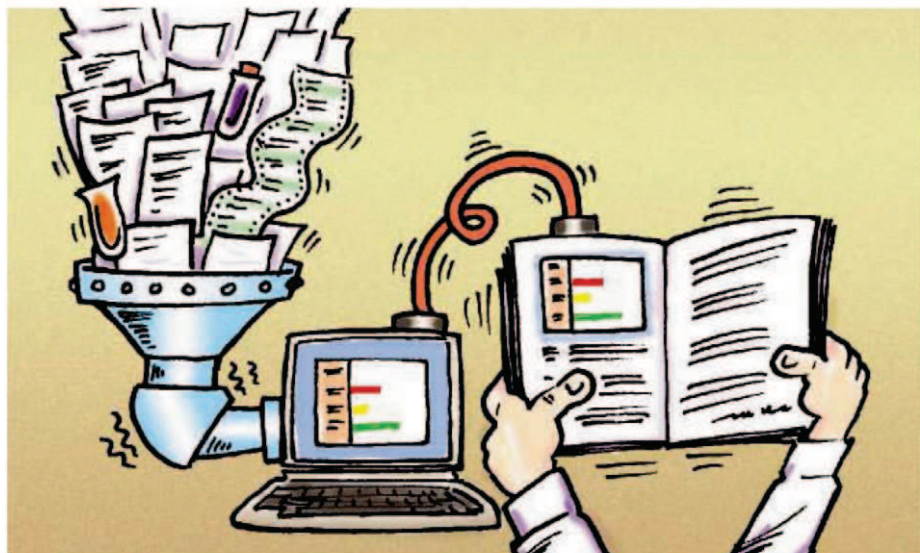
Jill P. Mesirov

Scientific publications have at least two goals: (i) to announce a result and (ii) to convince readers that the result is correct. Mathematics papers are expected to contain a proof complete enough to allow knowledgeable readers to fill in any details. Papers in experimental science should describe the results and provide a clear enough protocol to allow successful repetition and extension.

Over the past ~35 years, computational science has posed challenges to this traditional paradigm—from the publication of the four-color theorem in mathematics (1), in which the proof was partially performed by a computer program, to results depending on computer simulation in chemistry, materials science, astrophysics, geophysics, and climate modeling. In these settings, the scientists are often sophisticated, skilled, and innovative programmers who develop large, robust software packages.

More recently, scientists who are not themselves computational experts are conducting data analysis with a wide range of modular software tools and packages. Users may often combine these tools in unusual or novel ways. In biology, scientists are now routinely able to acquire and explore data sets far beyond the scope of manual analysis, including billions of DNA bases, millions of genotypes, and hundreds of thousands of RNA measurements. Similar issues may arise in other fields, such as astronomy, seismology, and meteorology. While propelling enormous progress, this increasing and sometimes “indirect” use of computation poses new challenges for scientific publication and replication. Large data sets are often analyzed many times, with modifications to the methods and parameters, and sometimes even updates of the data, until the final results are produced. The resulting publication often gives only scant attention to the computational details. Some have suggested these papers are “merely the advertisement of scholarship whereas the computer programs, input data, parameter values, etc. embody the scholarship itself” (2). However, the actual code or software “mashup” that gave rise to the final analysis may be lost or unrecoverable.

For example, colleagues and I published a computational method for distinguishing



between two types of acute leukemia, based on large-scale gene expression profiles obtained from DNA microarrays (3). This paper generated hundreds of requests from scientists interested in replicating and extending the results. The method involved a complex pipeline of steps, including (i) preprocessing of the data, to eliminate likely artifacts; (ii) selection of genes to be used in the model; (iii) building the actual model and setting the appropriate parameters for it from the training data; (iv) preprocessing independent test data; and finally (v) applying the model to test its efficacy. The result was robust and replicable, and the original data were available online, but there was no standardized form in which to make available the various software components and the precise details of their use.

## Reproducible Research

This experience motivated the creation of a way to encapsulate all aspects of our *in silico* analyses (3) in a manner that would facilitate independent replication by another scientist

(4). Computer and computational scientists refer to this goal as “reproducible research” (5), a coinage attributed to the geophysicist Jon Claerbout in 1990, who imposed the standard of makefiles for construction of all the figures and computational results in papers published by the Stanford Exploration Project (6). Since that time, other approaches have been proposed (7–14), including the ability to insert active scripts within a text document (15) and the use of a markup lan-

As use of computation in research grows, new tools are needed to expand recording, reporting, and reproduction of methods and data.

guage that can produce all of the text, figures, code, algorithms, and settings used for the computational research (16). Although these approaches may accomplish the goal, they are not practical for many nonprogramming experimental scientists using other groups’ or commercial software tools today.

A similar challenge was encountered more than 20 years ago when scientists wanting to access data from remote computers had to write their own retrieval programs. The solution was the invention of the World Wide Web (17), together with the concept of “Web browsers” such as MOSAIC (18) and its successors. The approach was so effective that we now take it for granted.

In the same spirit, we need a paradigm that makes it simple, even for scientists who do not themselves program, to perform and publish reproducible computational research. Toward this end, we propose a Reproducible Research System (RRS), consisting of two components. The first element is a Reproducible Research Environment (RRE) for doing the computational work. An RRE provides computational tools together with the ability to automatically track the provenance of data, analyses, and results and to package them (or pointers to persistent versions of them) for redistribution. The second element is a Reproducible Research Publisher (RRP), which is a document-preparation system, such as standard word-processing software, that provides an easy link to the RRE. The RRS thus makes it easy to perform analyses and then to embed them directly into a



paper. A reader can readily reproduce the analysis and, in fact, can extend it within the document itself by changing parameters, data, filters, and so on.

A simple form of this concept is embedded in most word processors: When one “clicks” on a spreadsheet embedded in a document, an active spreadsheet will “pop up,” which allows the reader to fill in new numbers, propagate formulas, and create new charts, all without leaving the document. This can be thought of as a rudimentary RRS, involving linkage between an RRE (the spreadsheet program) and an RRP (the word processor).

### GenePattern-Word RRS

In collaboration with researchers at Microsoft, my coauthors and I (4) conceived and created a user-friendly version of an RRS. The RRE is the GenePattern computational genomics environment (19), and the RRP is an adaptation of Microsoft Word that can link to GenePattern (20). Other “quantitative programming environments” (8) might serve as the RRE, and other document preparation environments could, with appropriate modification, serve as the RRP (21).

GenePattern is an environment that allows analysis of genomic data sets by (i) creating pipelines by “connecting” modules, from a large library of over 120 tools; (ii) defining parameters for analysis; and (iii) specifying the data sets to be used. These “analytic workflows” can be created through a user-friendly, graphical user interface without writing any computer code; they can then be executed on a GenePattern server running on the researcher’s desktop, a larger departmental machine, or a high-performance compute farm. GenePattern automatically tracks the versions of modules and pipelines, captures the history of users’ analytic sessions, and can generate the corresponding pipelines (including parameters and input data files) from user output files, as well as package them for redistribution. In this way, a nonprogramming scientist can create fully reproducible *in silico* research.

The combined GenePattern-Word RRS embeds the functionality of GenePattern pipelines within a Microsoft Word document (figs. S1 to S4). By using a menu in the word processor, an author can link text, tables, and figures to previously executed GenePattern pipelines comprising the entire analysis and data that yielded those results (22). Pipelines and data can then be stored in their entirety within the document or (for space or runtime considerations) as a pointer to their location on the Web.

Similarly, a reader of the document can open a dashboard within the word processor

to view the GenePattern pipelines. When one selects a table or figure, the word processor displays the pipeline that produced it. Just as with opening a spreadsheet, the reader can directly connect to a GenePattern server to rerun the calculation, change parameters, or apply the method to other data. The reader can save the exploratory results within the document, along with their provenance (for replication) and annotated text. The document can then be sent to a colleague.

### Conclusion

The GenePattern-Word RRS system described here is intended as an example. Scientists who employ stochastic simulations would benefit from RRSs designed to capture simulations, including the initialization parameters. Commercial vendors of software packages used by the research community could (and should) develop RRS versions of their codes. Critical to a robust RRS is the automated tracking and maintaining of code versions so that, as methods evolve, the computations can still be repeated. High-performance codes may involve special requirements for processing and storage. Equally important may be the hardware configuration, operating system version, compiler version, and so on for full provenance of a complex piece of software. Although we have focused here on new software systems as a foundation for reproducible research, it is important to note that data integrity and persistence are also critical concerns (23).

The centrality of the role of computation in science—from molecular biology to the social sciences (24)—calls out for a new model for the way we publish our results. Just as it is routine to include references in our papers, we should also include our complete computational methods. Journals can play a key role in making this a requirement for publication. To facilitate this, we need simple, intuitive ways to both capture and embed our computational work directly into our papers. The value of such tools goes beyond mere documentation. They will encourage the next generation of scientists to become “active” consumers of scientific publications—not just looking at the figures and tables, but running computational experiments to probe the results as they read the paper.

### References and Notes

1. K. Appel, W. Haken, *Discrete Math.* **16**, 179 (1976).
2. M. Schwab, M. Karrenbach, J. Claerbout, *Comput. Sci. Eng.* **2**, 61 (2000).
3. T. R. Golub *et al.*, *Science* **286**, 531 (1999).
4. M. Reich *et al.*, *Nat. Genet.* **38**, 500 (2006).
5. Reproducible research in this context refers to the ability to repeat the calculations for analyzing the data and obtaining the computational results rather than independent validation by another algorithm or

6. The Stanford Exploration Project (<http://sepwww.stanford.edu>) is a 25-year-old project in seismic imaging. To achieve his reproducibility goal, Claerbout leveraged the work of Feldman (25), who developed the Make program in the 1980s for maintaining and building executable programs from source code.
7. Special Issue on Reproducible Results, *Comput. Sci. Eng.* **11**, 3 (2009).
8. J. Buckheit, D. Donoho, in *Wavelets and Statistics*, A. Antoniadis, Ed. (Springer-Verlag, Berlin, 1995), pp. 55–81.
9. R. Gentleman, *Stat. Appl. Genet. Mol. Biol.* **4**, 25 (2005).
10. R. Gentleman, D. Temple Lang, *J. Comput. Graph. Statist.* **16**, 1 (2007).
11. Sweave processing of Open Document Format (ODF) files, <http://cran.r-project.org/web/packages/odfWeave/index.html>.
12. *Notebook Basics*, Wolfram Research, <http://reference.wolfram.com/mathematica/guide/NotebookBasics.html>.
13. *Using Notebook to Publish to Microsoft Word*, [www.mathworks.com/access/helpdesk/help/techdoc/matlab\\_env/brgdb8.html](http://www.mathworks.com/access/helpdesk/help/techdoc/matlab_env/brgdb8.html).
14. *Scripting Platform Plug-Ins*, <http://inference.us/Solution-Platform/Scripting%20Platform%20Plug-Ins.aspx>.
15. A script is a programming language interpreted or carried out by another program. Examples of the approach of embedding active scripts in text include (12–14).
16. This approach leverages the work of Knuth and his typesetting system TeX (26), as well as his notion of literate programming, introduced in the early 1980s, where a single file produces both source code (“tangle” command) and documentation (“weave” command) (27).
17. T. Berners-Lee *et al.*, *Commun. ACM* **37**, 76 (1994).
18. M. Andreessen, “NCSA Mosaic Technical Summary” (National Center for Supercomputing Applications, 1993).
19. GenePattern, [www.broadinstitute.org/genepattern](http://www.broadinstitute.org/genepattern).
20. The GenePattern-Word RRS is a freely available open source add-in to the Microsoft Office application; <http://genepatternwordaddin.codeplex.com>. A technical description and a video of a user session are in the Supporting Online Material.
21. Key features of an RRE are automated provenance tracking and easy packaging of the computational analysis for redistribution. Packages like geWorkbench, MeV, Galaxy, and Accelrys Software’s Pipeline Pilot have varying amounts of this functionality and might be modified to add the rest. They do not require the user to script or program. Examples of alternative document preparation software include, Open Office’s Writer, Corel’s WordPerfect, and Apple’s Pages. It is highly unlikely that any one piece of software would support all of science. But providing scientists who use computation with the means to capture the history of their analyses and to embed them into their documents in an easy and accessible manner should encourage a more thorough and interactive manner of publication.
22. An easy, straightforward method to provide reproducibility of the analysis associated with a scientific result increases the probability that authors will adopt it. It takes only a minute or two to link each executed pipeline to the document.
23. Committee on Science, Engineering, and Public Policy. *Ensuring the Integrity, Accessibility, and Stewardship of Research Data in the Digital Age* (National Academies Press, Washington, DC, 2009).
24. G. King, *PS: Polit. Sci. Polit.* **39**, 119 (2006).
25. S. I. Feldman, *Bell Lab.* **9**, 255 (1979).
26. D. E. Knuth, *TEX and METAFONT: New Directions in Typesetting* (American Mathematical Society, Providence, RI, 1979).
27. D. E. Knuth, *Comput. J.* **27**, 97 (1984).
28. Thanks to C. Mundie, R. Hinrich, and T. Hey at Microsoft for funding the development of the Word add-in; to Infusion Development and Persistent Systems for software implementation; to GenePattern team members P. Tamayo, M. Reich, T. Liefeld, H. Thorvaldsdottir, B. Hill, and H. Keuhn; to B. Gross and E. Lander; and to Broad Institute testers.

### Supporting Online Material

[www.sciencemag.org/cgi/content/full/327/5964/415/DC1](http://www.sciencemag.org/cgi/content/full/327/5964/415/DC1)

10.1126/science.1179653

## MICROBIOLOGY

## Subversion from the Sidelines

Nisheeth Agarwal and William R. Bishai

**M***ycobacterium tuberculosis*, which kills 1.7 million people annually, is a pathogen that proliferates within macrophages of the immune system. The granuloma—the hallmark lesion of tuberculosis—forms from repeated waves of macrophages that arrive at the site of infection to combat the pathogen, only to be themselves infected by bacteria multiplying within their dying predecessors. A central tenet in the characterization of tuberculosis has been that the granuloma represents a host defense response that contains the infection. But could the beneficiary of granuloma formation be the pathogen itself rather than the host? On page 466 in this issue, Volkman *et al.* show that a secreted bacterial peptide and secreted host cell protein are key to stimulating early granuloma development and maintaining the infection (1). The simplest interpretation is that the pathway constitutes a deliberate pro-granulomatous virulence mechanism that benefits the bacteria.

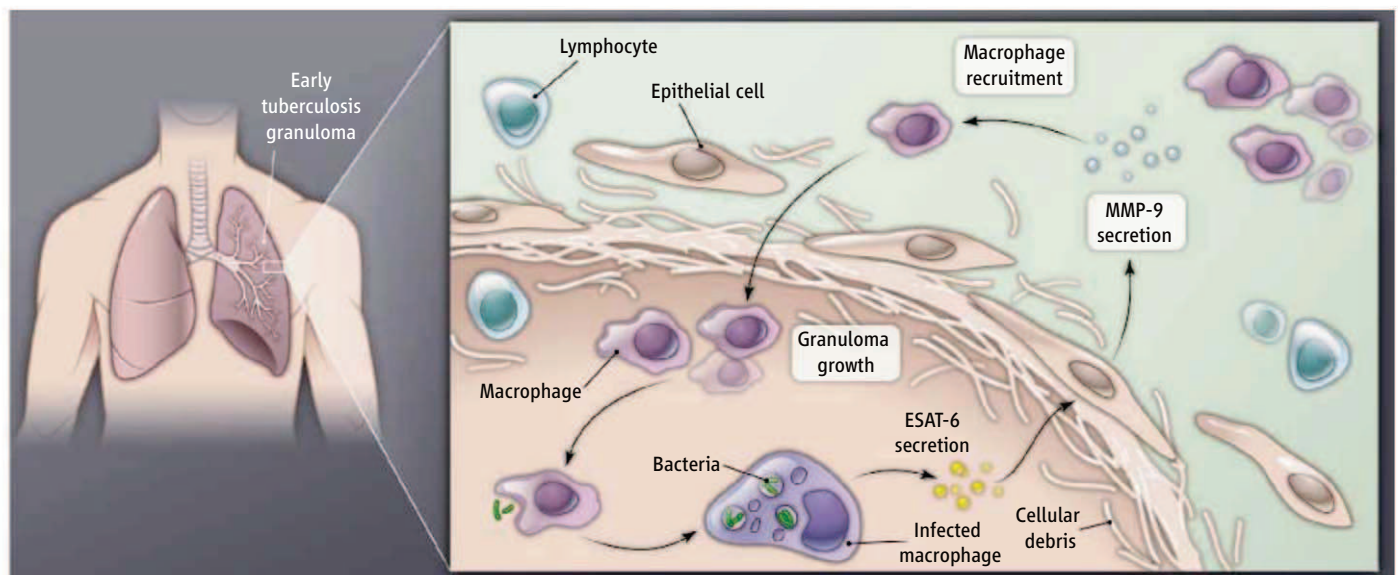
To evaluate the early events of granuloma formation, Volkman *et al.* used the natural host-pathogen pair, *Mycobacterium marinum* and the zebrafish model organism. The authors engineered a strain of *M. marinum* lacking a genomic region called the region of

difference-1 (RD1) locus, thus rendering the bacterium akin to the tuberculosis live-attenuated vaccine strain, bacille Calmette-Guérin (BCG). The RD1 locus encodes two key proteins—early secretory antigen-6 (ESAT-6) and culture filtrate protein-10—as well as a putative apparatus that may facilitate their secretion; the absence of this locus in the vaccine strain accounts for some of its attenuated phenotype (2, 3). Volkman *et al.* observed reduced expression of the enzyme matrix metalloproteinase-9 (MMP-9) in zebrafish infected with the RD1 deletion strain. MMP-9 belongs to a superfamily of over 20 matrix-modifying proteases. Although they are important for the pathogenesis of tuberculous meningitis and pleurisy, and are candidate effectors in the pathogenesis of lung cavities in tuberculosis (4), a role for these proteases in early granuloma formation has been largely eclipsed by attention on proinflammatory cytokines released from macrophages and T cells in the granuloma itself. MMP-9 expression was detected mainly in epithelial cells located near the edge of granulomas. Although in vitro models of tuberculosis infection have detected MMP-9 expression in epithelial cells (5), Volkman *et al.* demonstrate that inhibiting MMP-9 in infected zebrafish embryos both reduced granuloma formation and reduced bacterial proliferation, thus showing a causal role for the protease in disease pathogenesis.

A bacterial peptide subverts epithelial cells, resulting in a remodeling that promotes the early progression of tuberculosis.

Earlier findings that the RD1 deletion strain of *M. marinum* does not elicit normal granuloma formation and survives poorly in the zebrafish host (6) suggested that the ability to induce granuloma development enhances survival of the bacteria. Similarly, an *M. tuberculosis* mutant (lacking an adenylate cyclase enzyme) yielded an infection with deficient granuloma formation and enhanced bacterial survival in mice (7). Until now, data such as these formed the basis of a chicken-and-egg debate: Are such bacterial mutants innately attenuated, leading to reduced granulomatous immune responses? Or do the wild-type strains of these bacteria possess deliberate virulence factors (e.g., RD1-associated proteins and adenylate cyclase) that promote granuloma formation because granulomas benefit the microbe's pathogenesis plan?

Volkman *et al.* determined that the bacterial virulence factor ESAT-6, generated by bacteria that have been engulfed by macrophages, elicits the secretion of a noncytokine host factor (MMP-9), and that both elements are required for granuloma formation (see the figure). Even more remarkably, the MMP-9 comes primarily from bystander epithelial cells peripheral to the granuloma, not from macrophages or other cells within it. The injection of purified ESAT-6 into granulomas in zebrafish induced MMP-9 expression in surrounding epithelial cells. Thus, the two secreted proteins comprise



**Peripheral participants.** The findings of Volkman *et al.* suggest a scenario of tuberculosis development in which mycobacteria that have been engulfed by macrophages at the initial site of infection release ESAT-6. ESAT-6 stimulates

bystander epithelial cells on the periphery of the infection site to produce MMP-9, which attracts naïve macrophages. Recruited macrophages become infected, resulting in bacterial proliferation and granuloma expansion.



a virulence mechanism that benefits the bacteria early in granuloma formation. This may permit an early, synergistic phase of unimpeded bacterial proliferation, whereas later in the infection, the pathogen must face the host's acquired cell-mediated immune response, which is bacteriostatic.

Further work will need to confirm that ESAT-6-mediated induction of MMP-9 secretion can be reproduced in other systems, including cultured epithelial cells *in vitro*. It is also unclear how ESAT-6 reaches the epithelial cells. If ESAT-6 migrates extracellularly, this would provide a point of vulnerability because neutralizing antibodies might interrupt the pathogenic signal. However, ESAT-6-based tuberculosis vaccines have not shown dramatic effectiveness in animal models (8). Clearly, the findings from the *M. marinum*–zebrafish system must be translated to *M. tuberculosis* and mammalian models.

With case rates of multidrug-resistant and extensively drug resistant tuberculosis at 5 and 0.5%, respectively, there is an urgent need for new drugs (9). Importantly, the results of Volkman *et al.* reveal at least two new therapeutic opportunities. Whereas traditional antimicrobial compounds kill bacteria, a new antivirulence approach would inhibit or neutralize crit-

ical microbial virulence factors. Examples of antivirulence strategies include antitoxin therapies for diphtheria, botulism, and tetanus, and a small molecule that blocks cholera pilus and toxin expression (10). ESAT-6 may be just such an antivirulence target; though clearly dispensable for bacterial viability, the granuloma program of the pathogen is crippled without it.

A second therapeutic avenue may be host-directed therapy. Although routinely used for managing infectious diseases such as pediatric meningitis (with corticosteroids and antibiotics) and hepatitis C (with the cytokine interferon- $\alpha$ -2b and antivirals), the concept of correcting host responses that are subverted by pathogen virulence strategies has not been fully exploited. The findings of Volkman *et al.* point to MMP-9 as a host target to inhibit in tuberculosis. Inhibitors of these proteases are already being developed as therapeutics for common noninfectious diseases such as osteoarthritis, chronic obstructive pulmonary disease, cirrhosis, metastatic cancer, and myocardial infarction. Indeed, there is evidence that MMP-9-deficient mice may be naturally resistant to *M. tuberculosis* (11). Moreover, host-directed therapies would not be plagued by the emergence of rapid resistance due to overuse, as is the case with drug-resistant staphylo-

cocci, enterococci, and mycobacteria.

Sixteen years ago, "Remodeling schemes of intracellular pathogens" (12) highlighted the finding that once engulfed by a macrophage (and internalized into the cell's phagosome compartment), *M. tuberculosis* modifies its intracellular environment to facilitate its survival and proliferation (13). Volkman *et al.* show that beyond altering its intracellular environment, this pathogen harbors a sinister scheme to remodel its tissue environment as well.

#### References and Notes

1. H. E. Volkman *et al.*, *Science* **327**, 466 (2010); published online 10 December 2009 (10.1126/science.1179663).
2. T. Hsu *et al.*, *Proc. Natl. Acad. Sci. U.S.A.* **100**, 12420 (2003).
3. A. S. Pym *et al.*, *Nat. Med.* **9**, 533 (2003).
4. P. T. Elkington, J. S. Friedland, *Thorax* **61**, 259 (2006).
5. P. T. Elkington *et al.*, *Am. J. Respir. Dis. Crit. Care Med.* **37**, 431 (2007).
6. J. M. Davis, L. Ramakrishnan, *Cell* **136**, 37 (2009).
7. N. Agarwal *et al.*, *Nature* **460**, 98 (2009).
8. N. Ganguly *et al.*, *Tuberculosis (Edinb.)* **88**, 510 (2008).
9. A. Wright *et al.*, *Lancet* **373**, 1861 (2009).
10. D. T. Hung *et al.*, *Science* **310**, 670 (2005).
11. J. L. Taylor *et al.*, *Infect. Immun.* **74**, 6135 (2006).
12. P. L. Small *et al.*, *Science* **263**, 637 (1994).
13. S. Sturgill-Koszycki *et al.*, *Science* **263**, 678 (1994).
14. The support of NIH awards AI 30036, 37856, and 36973 is gratefully acknowledged.

10.1126/science.1185569

#### CLIMATE

## Drylands in the Earth System

David S. Schimel

**A**rid regions (or drylands) cover about 45% of Earth's land surface; in most classifications of ecosystem types, they constitute the largest biome on the planet. Yet the global change literature is dominated by other ecosystems, particularly the humid tropics, with high deforestation rates and high biodiversity levels, and the Arctic regions, with high rates of warming and huge stocks of vulnerable carbon. Drylands are less studied because they seem to have low rates of biological activity and sparse biota. On page 451 of this issue, Rotenberg and Yakir (1) present evidence that contradicts this received wisdom. The dryland Yatir Forest in Israel takes up carbon at rates similar to those of pine forests in continental Europe.

For the past decade, Yakir and co-workers have studied carbon, water, and energy exchange in one of the world's driest forests.

Rotenberg and Yakir now analyze how the Yatir Forest maintains productivity despite severe temperature and water stress. They argue that an adjustment of forest metabolism to ambient conditions reduces the impact of climate on carbon flux. Yatir's net carbon uptake [2.3 metric tons per hectare (t/ha)] is slightly higher than that of the average European pine forest (2 t/ha) and only slightly lower than the mean for all pine forests globally (2.5 t/ha).

How does a forest growing in a hot, dry environment sustain such high rates of carbon uptake? Several mechanisms contribute to the high levels of activity. First, although photosynthesis rates in this system are moderate relative to the range of fluxes observed globally, respiration is low (possibly because low soil moisture inhibits decomposition), resulting in a carbon storage efficiency 60% higher than the average of global data.

A second explanation lies in the timing of biological activity. The rates of carbon exchange in the Yatir Forest peak early in the spring, when temperatures are far below their

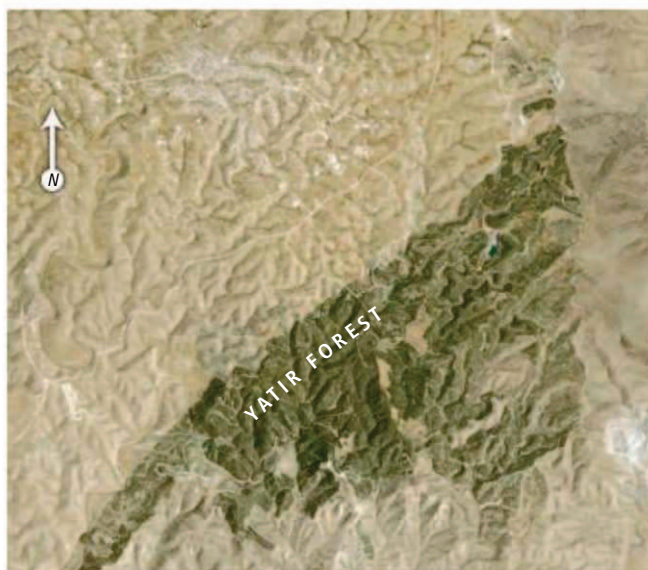
A study of one of the world's driest forests elucidates the climatic effects of drylands.

midsummer highs. The local vegetation is adapted to achieve peak photosynthesis rates at springtime temperatures around 14°C and to be relatively dormant during the midsummer highs of 25°C and above. A series of sites from high northern latitudes through southern Europe also had peak carbon exchange rates at similar temperatures (16° to 18°C) [data cited in (1)]. However, in most ecosystems, peak photosynthesis rates occur near maximal temperatures.

Peak rates of carbon uptake are a key control over annual uptake; the other key control is the length of the growing season (when the system gains carbon) relative to the dormant season (when the system loses carbon) (2). The displacement of peak growth to early spring in the Yatir Forest results in a growing season length similar to other coniferous forest ecosystems, also contributing to Yatir's carbon uptake.

Rotenberg and Yakir expose an important set of emergent controls over carbon metabolism globally. The work reinforces the need to conduct research in extreme and marginal envi-

National Ecological Observatory, Inc., 5340 Airport Boulevard, Boulder, CO 80301, USA. E-mail: dschimel@naeoinc.org



**The Yatir Forest from space.** The dark color of the forest contrasts with the surrounding, desertified landscapes. The Yatir, which covers about 30 km<sup>2</sup>, warms its local environment by absorbing incoming solar radiation, whereas the surrounding bright desert landscapes reflect more of the incoming radiation to space. Today, the Yatir shows up as a green anomaly in a vast desert landscape, but in biblical times, this entire region was forested.

report a real-world analog to this computer-enabled thought experiment.

Desertification exposes the bright soil surface, which reflects sunlight, much as in the boreal simulation. At the same time, increased convection over dryland forests such as the Yatir cools the surface, reducing outgoing thermal radiation but increasing the radiative forcing on the overlying regional

atmosphere and likely increasing air temperatures aloft. Whereas desert surfaces are hotter than vegetated ones, the atmosphere overlying the desert cools with altitude more quickly and is cooler overall. Paradoxically, desertification has thus likely contributed local cooling to offset the global warming from the carbon release that occurs when dryland forests are cleared.

Although modern humanity has a hard time realizing it, the climate system has never been unchanging. Human activities have long been a driver of change in the Earth system and will continue to be for the foreseeable future (4). Rotenberg and Yakir's study of the arid Yatir Forest shows how recent desertification has affected local temperatures and global climate. It also provides a perspective on how humans and the cli-

mate system have interacted over millennia.

More than 3000 years ago, at the dawn of the human modification of the Earth system, the Israelites entered Canaan (modern-day Lebanon, Israel, and the Palestinian territories) and were commanded by Joshua to "go up into the forest country and clear an area for yourselves there" [Joshua 17:15; see also (5)]. Those early settlers released carbon as they cleared forests, thereby changing the albedo, affecting the surface energy balance, and altering the local climate. The modern-day Yatir Forest was planted in 1964 by the Jewish National Fund and—as Rotenberg and Yakir document—has substantially modified the local climate. A global program of dryland reforestation may initially cause regional warming as these new forests modify the surface energy balance, but will pay dividends in the long term as these forests become substantial global carbon sinks.

#### References

1. E. Rotenberg, D. Yakir, *Science* **327**, 451 (2010).
2. G. Churkina, D. S. Schimel, B. H. Braswell, X. M. Xiao, *Glob. Change Biol.* **11**, 1777 (2005).
3. G. B. Bonan, D. Pollard, S. L. Thompson, *Nature* **359**, 716 (1992).
4. G. B. Bonan, *Ecological Climatology: Concepts and Applications* (Cambridge Univ. Press, Cambridge, ed. 2, 2008).
5. D. Hillel, *The Natural History of the Bible: An Environmental Exploration of the Hebrew Scriptures* (Columbia Univ. Press, New York, 2006).

10.1126/science.1184946

ronments to expand the scale over which processes are observed.

The authors extend their analysis to consider other pathways through which forests influence climate and to elucidate the role of drylands in the overall surface energy budget of Earth's land surface. Since Bonan *et al.*'s seminal 1992 study (3), it has been known that tree cover affects the local radiation balance, with important consequences for climate. Forests are dark and absorb incoming solar radiation, converting it into energy for photosynthesis and heat and thereby causing local warming. Bonan *et al.*'s computer simulation explored eliminating the dark boreal forest cover and thereby exposing the bright, highly reflective snow. The bright surface reflects more of the incoming sunlight, cooling the surface. Rotenberg and Yakir now

## SYSTEMS BIOLOGY

# Amoeba-Inspired Network Design

Wolfgang Marwan

The ability to self-optimize is one of the fundamental properties of living organisms. Adaptive self-optimization in the course of biological evolution is an obvious phenomenon, although it occurs on a time scale of millions of years. On page 439 of this issue, Tero *et al.* (1) describe a model system where self-optimization of cell morphology in response to a chosen experimental situation can be directly observed and mathematically

quantified as it occurs on a time scale of hours to a few days. These living cells display adaptive behavior of the sort that may be desired for scalable, multicomponent networks that are supposed to function robustly in the absence of central control mechanisms. Self-organization, self-optimization, and self-repair as it naturally occurs in the slime mold *Physarum polycephalum* are capabilities that may be required for technological systems such as mobile communication networks or networks of dynamically connected computational devices.

The *Physarum* microorganism (a plasmodium) used by Tero *et al.* is a multinucleate

Computational models of biological self-organizing systems may have real-world applications for optimizing dynamic technological networks.

single cell that continually grows as long as nutrition is available. During growth, multiple nuclear divisions occur but the growing cell does not divide, so that all nuclei remain suspended in a single contiguous cytoplasmic volume. When the plasmodium grows on a nutrient-rich substratum, it covers the surface as a coherent layer (like a pancake). If nutrition becomes limited, it forms fenestrae and finally transforms into a network of interconnected veins that enclose the entire cytoplasmic volume (see the figure). Each vein is a gel-like tube covered by a cell membrane and contains a core of fluid cytoplasm.





**Adaptive network formation.** The slime mold *Physarum polycephalum* is a single-cell organism that forms a veined network that explores the available space and connects food sources (left). Understanding the formation and behavior of this type of biological adaptive network may inform the development of real-world dynamic technological networks such as mobile communication networks or transportation systems, such as the Tokyo rail system (right).

By rhythmic contraction of its cytoskeleton, cytoplasm is continually pumped through these veins, and this continuous mixing seems to be the reason why all nuclei proceed synchronously through the cell division cycle. The network architecture is highly dynamic. Veins change in thickness, they may form and vanish again, and the plasmodium as a whole can crawl over its substratum, moving over centimeters in a couple of hours. Plasmodia usually do not dissociate. If food sources are spatially separated, such as oat flakes scattered over a wet surface, the plasmodial veins attempt to connect these food sources along the shortest possible pathways, even finding optimized paths through a maze (2). How this optimization is performed in terms of molecular mechanisms remains a challenging question.

Tero *et al.* present a surprisingly simple mathematical model for the development of a network of veins connecting multiple purposefully placed food sources. In their experiment, cities around Tokyo were represented as oat flakes on a wet surface that was inoculated with *Physarum*. Plasmodial veins connected these oat flakes by forming an optimized network closely approaching the purposefully designed Tokyo railway system.

Networks of plasmodial veins form without any central control mechanism that might instruct the organism about the relative position of the oat flakes or tell it how to connect them. The self-optimization algorithm that drives this morphogenesis works equally efficiently for networks with few or many nodes (oat flakes). The absence of central control mechanisms inspired Tero *et al.* to design a corresponding computational model capable of adaptive network design. Using a simple and robust algorithm, the model generates *in silico* networks that closely resemble those formed by the plasmodium. It is essentially based on feedback loops between the thickness of each tube and the cytoplasmic flow through the respective tube, where streaming

rate positively influences tube diameter and thus its transport capacity for cytoplasm. The dynamics and adaptability of the network structure are the direct results of the iteration of these local rules. The described algorithm or similar ones may provide general solutions for developing real-world, fault-tolerant networks without the need of a centralized control system.

In addition to inspiring next-generation engineering solutions, the work of Tero *et al.* offers a new approach to systems biology. It provides a simple mathematical model for a complex biological phenomenon—adaptive plasmodial shape control—involving growth,

morphogenesis, and homeostasis coordinated with maintenance, self-optimization, and self-repair of morphological and functional structures, the molecular and mechanistic bases of which are completely unclear. Even though the mathematical model has no basis in any specific molecular mechanism, it is nonetheless beautifully useful. It quantitatively mimics phenomena that are fundamental to any living system—phenomena that can be neither captured nor quantified by verbal description alone. Because the model has a number of tunable parameters that can be determined by computational fitting of experimental data, it provides objective readouts (e.g., to search for mutants that display quantitative alterations). Are there genes specifically involved in self-optimization, self-organization, or self-repair? Can molecular circuits be identified, and if so, how are they built, how do they function, and how are they linked to other regulatory systems at the single-cell level? Addressing these questions may lead to yet undiscovered fundamental functionalities in living cells and unravel their molecular basis.

#### References

1. A. Tero *et al.*, *Science* **327**, 439 (2010).
2. A. Tero *et al.*, *J. Theor. Biol.* **244**, 553 (2007).

10.1126/science.1185570

#### PALEONTOLOGY

## And Then There Were None?

Richard G. Roberts<sup>1</sup> and Barry W. Brook<sup>2</sup>

Direct dating of fossils of the putative last survivors of the Australian megafauna supports claims that they were extinct by 40 thousand years ago and not later.

Giant marsupials, reptiles, and flightless birds once inhabited Australia (see the first figure). But 23 of the 24 genera of these megafauna disappeared in the late Pleistocene (~125 to ~12 thousand years ago). Most Australian megafauna appear to have survived until 51 to 40 thousand years ago, with human impact by hunting or vegetation change proposed as the extinction drivers (1–4). Yet, one site has stood out as an anomaly: Cuddie Springs in interior New South Wales. Persistent claims have been made that this site contains megafauna fossils associated with stone tools in sediments deposited

40 to 30 thousand years ago (5–7), thus indicating prolonged overlap between people and megafauna. These claims have been challenged (2, 8) based on concerns about possible reworking of fossils from older deposits. To resolve this conundrum, Grün *et al.* (9) have now directly dated the fossils themselves. The results provide no evidence for the late survival of megafauna at the site.

Cuddie Springs is an ephemeral lake in the Australian semiarid zone. Fossils were originally discovered when digging wells for water. Many more have since been exhumed from the claypan, including the remains of the giant bird *Genyornis newtoni*, the three-ton *Diprotodon optatum* (the largest marsupial ever to roam Australia), and a range of supersized kangaroos. The fossils found in the same sedimentary layers as stone tools (stratigraphic unit SU6; see the second fig-

<sup>1</sup>Centre for Archaeological Science, School of Earth and Environmental Sciences, University of Wollongong, Wollongong, NSW 2522, Australia. <sup>2</sup>The Environment Institute, School of Earth and Environmental Sciences, University of Adelaide, Adelaide, SA 5005, Australia. E-mail: rgrob@uow.edu.au; barry.brook@adelaide.edu.au

ure) have attracted most recent attention. The lack of preserved collagen has prevented these fossils from being dated directly by radiocarbon methods (8). Instead, their antiquity has been inferred from radiocarbon dating of charcoal fragments and from optical dating of quartz grains found alongside the bones and stones. The ages range from 40 to 30 thousand years ago, but show no pattern of increasing age with depth. Optical dating of individual sand grains revealed that some were incorporated in the past 12,000 years, indicating recent intrusion of sediment into SU6 (2). Immediately below the lowest artifacts, but separated in time by several tens of millennia, is a geological discontinuity, which represents a former land surface.

Sidestepping the question of whether the fossils are associated with the dated charcoal and sediment grains, Grün *et al.* (9) directly date the teeth of several species of extant and extinct fauna with electron spin resonance (ESR) and uranium-series methods. Both methods are sensitive to the postdepositional history of uranium uptake by the dental tissues, but to varying extents. Minimum ages can be determined by assuming that all the uranium was absorbed soon after burial; tighter constraints can be made for teeth with sufficient uranium by modeling its uptake to obtain combined uranium-series/ESR ages.

Using this multifaceted strategy, Grün *et al.* found that none of the dated megafauna in SU6 were younger than 50 thousand years; even the remains of extant taxa were older than 40 thousand years (see the second figure). SU6 also contained three teeth that dated to the middle Pleistocene (~780 to ~125 thousand years ago). Clearly, at least some of the megafauna teeth in SU6 are derived from older deposits, possibly due to well-digging or lateral displacement.

While making these measurements, Grün *et al.* also discovered a flaw in a geochemical argument used previously to support the hypothesis that the Cuddie fossils have not been redeposited (5). This interpretation was based on the similarity in the rare earth element chemistry of the bones and surrounding sediments. From their profiling of uranium and thorium concentrations in bone, Grün *et al.* conclude that the rare earth element signatures do not reflect the



**Past Australian megafauna.** Animals that once called Australia home include (clockwise from top left) *Genyornis*; *Diprotodon*; *Procoptodon* (the largest-ever kangaroo); the thylacine (which survived in Tasmania until 1936); *Thylacoleo* (the biggest marsupial carnivore); and the giant lizard, *Megalania*.

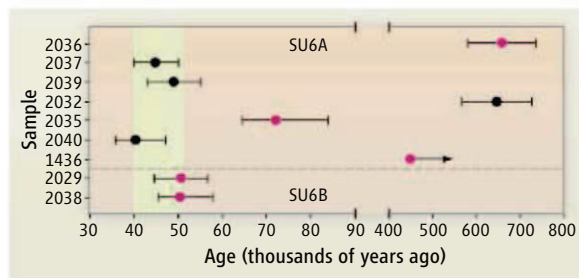
composition of the bone itself. Instead, these signatures mirror the geochemistry of the surface coatings and dirt trapped in cracks and pores, which could have formed long after the bones had been eroded from the sedimentary layers that originally contained them, and redeposited in SU6.

This redating of the Cuddie Springs fossils (9) brings the site into agreement with the 51- to 40-thousand-year extinction interval that captures the last survivors elsewhere in Australia (1–4, 10, 11). Claims for sites containing younger megafauna—such as Nombe Rockshelter, Seton Rockshelter, and Cloggs

Cave (6, 7)—should be considered suspect, pending dating using modern methods, preferably on the fossils themselves, as applied elsewhere (1, 4, 10, 11). Reliable ages for redeposited remains can be determined only by direct dating.

So what brought down the Australian megafauna? Given that people arrived in Australia sometime between 60 and 45 thousand years ago, human impact was likely the decisive factor. Humans may have caused the demise of the megafauna in two main ways: hunting—possibly of juveniles at rates as low as one kill per person per decade, termed “imperceptible overkill” (12)—and habitat disturbance, most likely by burning vegetation (3). Vegetation change seems to have accompanied the downfall of *Genyornis* in central Australia (1, 3), but not necessarily elsewhere (4, 13). Climate change—specifically increased aridity—may have reinforced the human impact, but the Australian megafauna were well adapted to dry conditions (13), having survived repeated droughts before succumbing during a period of comparatively benign climate (2, 4, 11, 14).

Recent findings on the North America megafauna may have implications for the earlier Australian extinctions. Using spores of a dung fungus





to track megafauna abundance, Gill *et al.* (15) showed that herbivore populations collapsed shortly before the onset of vegetation change and increased fire. The same chain of events may have occurred earlier in Australia, but over a time span too fine to be resolved by current dating methods. Recovery of ancient DNA from sediments has also revealed that mammoths and horses survived much later in North America than indicated by the fossil record, owing to the improbability of finding and dating fossils of the last survivors, especially in dwindling populations (16). Application of these types of approaches in Australia

may further refine the timing of the events leading up to extinction and provide sharper insights into the likely drivers of this ecological catastrophe.

#### References and Notes

1. G. H. Miller *et al.*, *Science* **283**, 205 (1999).
2. R. G. Roberts *et al.*, *Science* **292**, 1888 (2001).
3. G. H. Miller *et al.*, *Science* **309**, 287 (2005).
4. C. S. M. Turney *et al.*, *Proc. Natl. Acad. Sci. U.S.A.* **105**, 12150 (2008).
5. C. N. G. Trueman, J. H. Field, J. Dortch, B. Charles, S. Wroe, *Proc. Natl. Acad. Sci. U.S.A.* **102**, 8381 (2005).
6. J. Field, M. Fillios, S. Wroe, *Earth-Sci. Rev.* **89**, 97 (2008).
7. M. Fillios, J. Field, B. Charles, *Quat. Int.* **211**, 123 (2010).
8. R. Gillespie, B. W. Brook, *Archaeol. Oceania* **41**, 1 (2006).

9. R. Grün *et al.*, *Quat. Sci. Rev.*, published online 1 December 2009; 10.1016/j.quascirev.2009.11.004.
10. R. Grün *et al.*, *Aust. J. Earth Sci.* **55**, 917 (2008).
11. L. K. Ayliffe *et al.*, *Quat. Sci. Rev.* **27**, 1784 (2008).
12. B. W. Brook, C. N. Johnson, *Alcheringa* (Special Issue 1), 39 (2006).
13. G. J. Prideaux *et al.*, *Proc. Natl. Acad. Sci. U.S.A.* **106**, 11646 (2009).
14. G. J. Prideaux *et al.*, *Geology* **35**, 33 (2007).
15. J. L. Gill *et al.*, *Science* **326**, 1100 (2009).
16. J. Haile *et al.*, *Proc. Natl. Acad. Sci. U.S.A.* **106**, 22352 (2009).
17. The authors thank the artist, P. Trusler, and the Australian Postal Corporation for permission to reproduce the painting shown in the first figure. The original work is held in the National Philatelic Collection.

10.1126/science.1185517

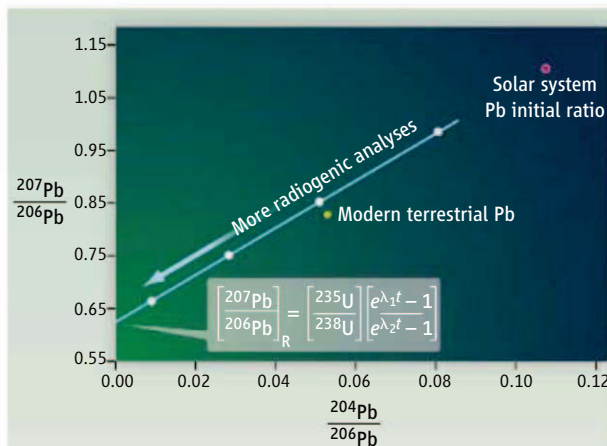
#### GEOCHEMISTRY

## Adjusting the Solar System's Absolute Clock

J. N. Connelly

Meteorites and their components provide the only means to study the circumstances and processes that gave rise to our solar system. But the task of unraveling our origins is by no means straightforward. A single undifferentiated meteorite—a chondrite—typically contains matrix and inclusions formed over a wide range of conditions and time before eventually being accreted into a single body. Understanding this complex assemblage, especially over the critical first 10 million years, allows the formulation of models of the spatially and temporally evolving thermochemical conditions that gave rise to the solar system. Geochronology—the determination of ages of events recorded by meteorites—provides the requisite temporal information. Although advances have been made over the past decade in this field, on page 449 of this issue, Brennecka *et al.* (1) present data suggesting that a basic assumption for the use of the U-Pb chronometer in geochronology, the golden spike for deep time, may be incorrect.

Two types of chronometers are used to measure the ages of ancient meteorites. So-called relative chronometers are based on the rapid decay [half-lives <10 million years (My)] of now extinct, short-lived radioiso-



The recent demonstration that a basic assumption in using isotope decay to measure the age of meteorites is incorrect has profound implications for dating the early solar system.

**Setting a date.** In the inverse Pb-Pb diagram, the radiogenic  $^{207}\text{Pb}/^{206}\text{Pb}$  ratio [ $(^{207}\text{Pb}/^{206}\text{Pb})_R$ ] can be calculated by projecting a line through data points with variable mixtures of radiogenic Pb and initial Pb to the y intercept, where the initial Pb is theoretically zero. This variability is created by strategically analyzing related fragments, minerals, or acid leachates with variable U/Pb ratios. (Subscript R refers to radiogenic;  $\lambda_1$  and  $\lambda_2$  represent the decay constants of  $^{235}\text{U}$  and  $^{238}\text{U}$ , respectively; and  $t$  represents time.)

topes that were created either just before or during the formation of the solar system. These relative chronometers, such as  $^{41}\text{Ca}$ – $^{41}\text{K}$ ,  $^{26}\text{Al}$ – $^{26}\text{Mg}$ ,  $^{53}\text{Mn}$ – $^{53}\text{Cr}$ ,  $^{60}\text{Fe}$ – $^{60}\text{Ni}$ , and  $^{182}\text{Hf}$ – $^{182}\text{W}$ , require that the initial abundances of the parent radioisotope are known and that it was homogeneously distributed throughout the solar system. The short half-lives of these extinct nuclides have the potential to provide the most precise age estimates for the first 10 My. But the recent discovery of large-scale isotopic variability of nucleosynthetic origin for elements of contrasting volatility among different meteorite groups (2) casts doubts on the assumption of homogeneous distribution of short-lived radioisotopes.

Absolute chronometers are based on long-lived radioisotopes so that the present-day parent-daughter ratio in a sample provides an

age in years before present with no assumptions necessary regarding the initial inventory of the parent radioisotope or its homogeneous distribution. Of the absolute chronometers, only the U-Pb system has half-lives and systematics suitable for resolving events in the first 10 My of the solar system. In addition to its high resolution, the U-Pb system is unique in a second way. Two isotopes of U,  $^{235}\text{U}$  and  $^{238}\text{U}$ , break down spontaneously at different rates (half-lives of 0.704 and 4.47 billion years) to produce  $^{207}\text{Pb}$  and  $^{206}\text{Pb}$ , respectively.

If it is accepted (and it has been) that the  $^{238}\text{U}/^{235}\text{U}$  of all objects is 137.88, then one may calculate an absolute age knowing only the ratio of radioactively produced  $^{207}\text{Pb}$  and  $^{206}\text{Pb}$  (see the figure). This so-called Pb-Pb method is advantageous, if not necessary, because late alteration and/or laboratory treatment to remove ubiquitous contaminant terrestrial Pb typically alters the U/Pb ratio so that the measured parent-daughter

Centre for Star and Planet Formation, Natural History Museum of Denmark, University of Copenhagen, Copenhagen 1350 Denmark. E-mail: connelly@snm.ku.dk

ratios do not reflect those of a closed system. Because the Pb isotopic ratios remain unaffected by late alteration or laboratory treatment, the Pb-Pb age remains accurate despite any shifts in the U/Pb ratio that may have recently occurred.

It has long been assumed that the solar system inherited a fixed inventory of galactically derived  $^{238}\text{U}$  and  $^{235}\text{U}$  that was homogeneously distributed in the protosolar molecular cloud and that they were not measurably fractionated in natural systems. All ages reported in the literature today are based on this assumed fixed  $^{238}\text{U}/^{235}\text{U}$  ratio. The isotopic composition of U is typically not measured in samples owing to the technical challenge of measuring the extreme  $^{238}\text{U}/^{235}\text{U}$  ratio of small amounts of U sufficiently precisely and the lack of evidence, despite prior attempts (3), that this ratio varies measurably in meteorites. But Brennecka *et al.* demonstrate that this assumption of a fixed U ratio is incorrect for some of the solar system's oldest solids, calcium-aluminum-rich inclusions (CAIs), and that the ratio may vary up to 3000 parts per million from the accepted value of 137.88. This translates into a potential age offset of 5 My for a given radiogenic ratio ( $^{207}\text{Pb}/^{206}\text{Pb}$ )<sub>r</sub>—or about 50% of the life span of the solar protoplanetary disk. They attribute this heterogeneity to the variable fractionation of short-lived  $^{247}\text{Cm}$  that

decays to  $^{235}\text{U}$ , by using Nd as a geochemical proxy for the now extinct Cm.

Ages from a relative chronometer can be mapped into absolute time in the past when a single object is found to be suitable for both a Pb-Pb age and a relative age. For example, CAIs anchor the  $^{26}\text{Al}$ - $^{26}\text{Mg}$  system (4), whereas the differentiated basaltic angrite LEW 86010 provides the anchor for the  $^{53}\text{Mn}$ - $^{53}\text{Cr}$  system (5, 6). If the short-lived nuclides were homogeneous and the  $^{238}\text{U}/^{235}\text{U}$  ratio was consistent, all ages from different chronometers for samples that behaved as a closed system should be concordant. But they are not. For example, age offsets of up to 3 My exist between Pb-Pb ages and the available relative chronometers for some rapidly cooled volcanic meteorites (7).

Homogeneity of short-lived nuclides in the disk has commonly been singled out as the least robust assumption in geochronology, from which one can infer that the relative chronometers are most likely in error. But it is now possible that variations in the  $^{238}\text{U}/^{235}\text{U}$  ratio in meteorites and their components may, at least in part, be to blame for the discordances. However, so far the offsets in the  $^{238}\text{U}/^{235}\text{U}$  ratio of CAIs reported by Brennecka *et al.* will only make the discordance between Pb-Pb ages and the relative chronometers worse.

With the rapidly growing identifications of planets that orbit distant stars, and the tan-

talizing perspective of discovering an Earth-like world, understanding the sequence of events leading to the formation of the planetary bodies in our solar system has never been so relevant. Brennecka *et al.* convincingly relate for the first time the important discovery that U is isotopically variable in CAIs, implying that the currently accepted age for the formation of the solar system's first solids (4) may be incorrect. At the same time, they have defined a new benchmark for high precision and accurate geochronology: All future Pb-Pb studies must include  $^{238}\text{U}/^{235}\text{U}$  ratios. Only then can we be certain that we have an internally consistent Pb-Pb chronometric database and a correct temporal framework within which to interpret meteorites and, in turn, understand the origins of our solar system.

## References

1. G. Brennecka *et al.*, *Science* **327**, 449 (2010); published online 31 December 2009 (10.1126/science.1180871).
2. A. Trinquier *et al.*, *Science* **324**, 374 (2009).
3. C. Stirling, A. N. Halliday, D. Porcelli, *Geochim. Cosmochim. Acta* **69**, 1059 (2005).
4. Y. Amelin, A. N. Krot, I. D. Hutcheon, A. A. Ulyanov, *Science* **297**, 1678 (2002).
5. D. P. Glavin, A. Kubny, E. Jagoutz, G. W. Lugmair, *Meteorit. Planet. Sci.* **39**, 693 (2004).
6. Y. Amelin, *Geochim. Cosmochim. Acta* **72**, 221 (2008).
7. J. N. Connelly, M. Bizzarro, K. Thrane, J. A. Baker, *Geochim. Cosmochim. Acta* **72**, 4813 (2008).

10.1126/science.1183755

## MATERIALS SCIENCE

# Epitaxial Growth Writ Large

Theodore L. Einstein<sup>1</sup> and Timothy J. Stasevich<sup>2</sup>

The performance of semiconductors in device applications often depends on their crystallinity—the grain boundaries and defects of a polycrystalline material interfere with transport of charge carriers. Single crystalline layers can be grown through epitaxy: Atoms are deposited from the gas phase on top of an existing crystal to form new layers. However, if the growth process is not well controlled or is too rapid, unwanted surface features, such as mounds, may form. Thus, the fabrication process relies heavily on monocrystalline growth of a single element. Models to find optimal

conditions for this process have been studied for a long time (1, 2) and have had to become increasingly sophisticated (3, 4). Insights from related processes involving molecules or even larger particles can test our understanding of how epitaxy works and can be easier to observe directly. On page 445 of this issue, Ganapathy *et al.* (5) describe epitaxial growth with colloidal spheres some four orders of magnitude larger than atoms. Models developed for atomic epitaxy can describe these processes, despite colloid-colloid attractions arising in a way very different from atomic interactions.

Models of epitaxial growth must account for how adsorbed atoms, called adatoms, interact with each other and the surface template, as well as the effects of different incoming fluxes  $F$  of atoms and different growth temperatures. Adatoms are trapped by attrac-

The technological goal of optimizing the controlled deposition of atomic monolayers is simplified by studying models of deposition of larger colloids.

tive forces in wells of the corrugated surface potential but move when they have enough energy to “hop” over these barriers (see the figure, panel A). A minimal model describing how adatoms move requires attractions between neighboring atoms (such as chemical bonds) to create the potential wells and energy barriers to describe the hopping process. Analysis of the energy barriers helps in estimating the thermal surface diffusion coefficient  $D$ . The model must also account for the greater difficulty of atoms dropping over a step edge, because they must break even more bonds. In the simplest picture, this leads to the so-called “Ehrlich-Schwoebel” (ES) barrier (see the figure, panel B) (6, 7).

For colloidal particles, attractive forces arise from a “depletion interaction.” Smaller surrounding polymer “depletants” have a hard time getting between closely spaced colloids,

<sup>1</sup>Department of Physics, University of Maryland, College Park, MD 20742, USA. <sup>2</sup>Fluorescence Imaging Group, Laboratory of Receptor Biology and Gene Expression, National Cancer Institute, National Institutes of Health, Bethesda, MD 20892, USA. E-mail: einstein@umd.edu; stasevich@mail.nih.gov



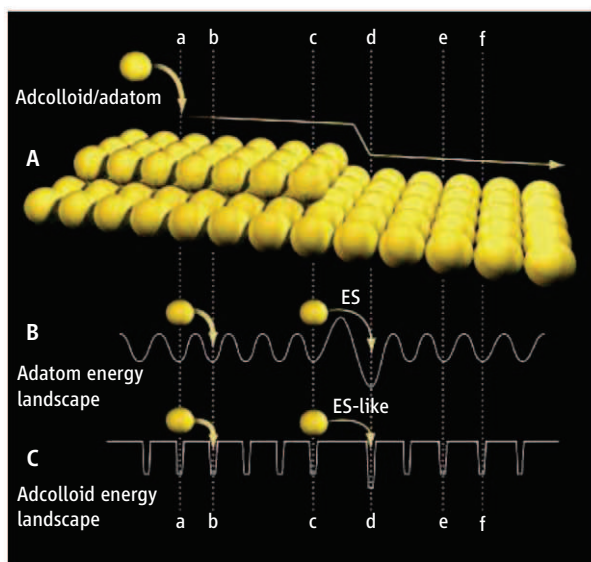
and the depletion layer creates a pressure imbalance that pushes the colloids together (8), creating an effective bond. This bond is broken when an adsorbed colloid, or adcolloid, hops between neighboring sites. Unlike adatoms, the bond is very short range (relative to the size of the adcolloid), and the energy landscape is nearly flat for most of the hop (see the figure, panel C). Thus, once the initial detachment is taken into account, the remaining part of the hopping time (inverse rate) is proportional to the path length of the hop alone and does not depend on barrier height. Because this length is greater for hops over steps or around the corners of disconnected regions of the same layer (called “islands”), colloids spend more time at these locations, just as atoms spend more time overcoming an ES barrier.

This ES-like barrier leads to a great simplification compared with atomic systems.

The energy or time associated with a mobile colloid crossing over step edges, going around corners or kinks, and other common routes, can be computed in terms of path length alone. For example, there should be simple relations between the barriers for colloidal deposition on square and triangular templates. The motion of atoms on a surface involves subtle relaxations, as well as long-range or multiautom interactions, that would confound similar computations.

Unlike atomic systems, where bond strengths are largely fixed, the colloid-colloid bond can be tuned by varying the depletant concentration. Thus, a key parameter for describing epitaxial growth, the ratio  $D/F$ , can be adjusted independently from  $10^{-1}$  to  $10^4$ . This range overlaps substantially with that accessible to atomic systems and should allow for many useful comparisons.

For example, the coalescence of islands is important because unwanted domain walls between islands can form. Ganapathy *et al.* show that for a given  $D/F$ , there is a critical concentration  $n_c$  of disconnected colloidal islands that marks the end of an initial growth period. The number of islands then decays as further growth causes islands to coalesce, just as in atomic systems (4, 9). The scaling of  $n_c$  approaches  $(D/F)^{-1/3}$ , just as classical nucle-



**Colloidal versus atomic epitaxy.** (A) The physical landscape for epitaxial growth is depicted. The colloids in the system described by Ganapathy *et al.* are 10,000 times as large as atoms, but their epitaxial dynamics are remarkably similar because both types of adsorbed particles—adatoms or adcolloids—encounter a step-edge barrier (ES or ES-like) for downward hops (c→d). The energy landscape for adatoms (B) undulates more robustly than its mesa-like adcolloidal counterpart (C) because colloidal bonds are too short to produce similar barriers. Because the segment lengths *cd* are greater than those for *ab* and *ef*, a colloid trying to move from *c* to *d* will have a smaller chance than one diffusing between *a* and *b* or *e* and *f*. Like atoms, colloids tend to settle at site *d* because of its higher coordination.

ation theory would predict. Mound formation during multilayer growth of atoms would also be expected in colloidal systems because of the ES-like barrier at step edges that inhibits the completion of a lower layer. Meandering instabilities—to-and-fro step oscillations—that can prevent the step-flow growth of atoms in device fabrication should also occur on a series of colloidal steps.

Another important concept is the size of the smallest island that is stable to decay—the critical nucleus. This quantity determines the distribution of the sizes of islands (4, 9) and of their capture zones (4, 10)—the areas around an island in which surrounding adatoms will likely attach to the island. The distribution of capture zones was only recently argued to be related to the critical nucleus size (11). For colloids, this number is 2 (dimers are stable), so colloidal systems can be used to test this concept directly.

Although it will certainly be instructive to compare colloidal and atomic epitaxy, there are many aspects of growth that will be difficult to realize in colloidal systems. For example, colloidal growth lacks the control over deposition angles available with atomic beams that can cause shadowing effects (12) and growth asymmetries when atoms impinge obliquely.

Colloidal epitaxy as described by Ganapathy *et al.* should still prove to be a useful model for many complex systems. For example, colloids of different sizes could model heteroepitaxy, which is used to grow compound semiconductors such as gallium arsenide. In contrast to such covalently bonded systems, where the crystalline structure arises from orbital hybridization, here the ratio of the larger to the smaller radius of the two spheres can be important. In ionic materials, transitions from sodium chloride to cesium chloride to zincblende structures, with 6, 8, and 4 nearest neighbors, respectively, occur as this ratio increases. For colloids, the challenge will be avoiding the formation of amorphous structures, because the ordering in atomic systems stems in part from differences in charge as well as size.

Similarly, colloids of different sizes can be used to explore the role of surfactants and step decoration on the controlled growth of surface structures; for example, the decoration of colloidal islands by colloids of a different size should predictably alter island shape (13). Finally, colloids may even prove to be useful models of biological systems, where depletion attractions still play an unappreciated role (8). Nonspherical colloids could model the epitaxy of antifreeze proteins (14) and kidney stones (15). Indeed, a wide range of interesting epitaxial systems should quite literally come into focus when modeled with colloids.

## References and Notes

1. A. Pimpinelli, J. Villain, *Physics of Crystal Growth* (Cambridge Univ. Press, Cambridge, 1989).
2. T. Michely, J. Krug, *Islands, Mounds and Atoms* (Springer, Berlin, 2004).
3. A. Voigt, Ed., *Multiscale Modeling in Epitaxial Growth* (Birkhäuser, Basel, 2005).
4. J. W. Evans, P. A. Thiel, M. C. Bartelt, *Surf. Sci. Rep.* **61**, 1 (2006).
5. R. Ganapathy, M. R. Buckley, S. J. Gerbode, I. Cohen, *Science* **327**, 445 (2010).
6. G. Ehrlich, F. G. Hudda, *J. Chem. Phys.* **44**, 1039 (1966).
7. R. L. Schwoebel, E. J. Shipsey, *J. Appl. Phys.* **37**, 3682 (1966).
8. D. Marenduzzo, K. Finan, P. R. Cook, *J. Cell Biol.* **175**, 681 (2006).
9. J. G. Amar, F. Family, P.-M. Lam, *Phys. Rev. B* **50**, 8781 (1994).
10. J. A. Blackman, P. A. Mulheran, *Phys. Rev. B* **54**, 11681 (1996).
11. A. Pimpinelli, T. L. Einstein, *Phys. Rev. Lett.* **99**, 226102 (2007).
12. Y. Shim, J. G. Amar, *Phys. Rev. Lett.* **98**, 046103 (2007).
13. T. J. Stasevich, C. Tao, W. G. Cullen, E. D. Williams, T. L. Einstein, *Phys. Rev. Lett.* **102**, 085501 (2009).
14. J. A. Raymond, P. Wilson, A. L. DeVries, *Proc. Natl. Acad. Sci. U.S.A.* **86**, 881 (1989).
15. S. R. Qiu *et al.*, *Proc. Natl. Acad. Sci. U.S.A.* **101**, 1811 (2004).
16. Work at the University of Maryland was supported by the NSF Materials Research Science and Engineering Center under grant DMR 05-20471.

10.1126/science.1184947

# The Genetic Landscape of a Cell

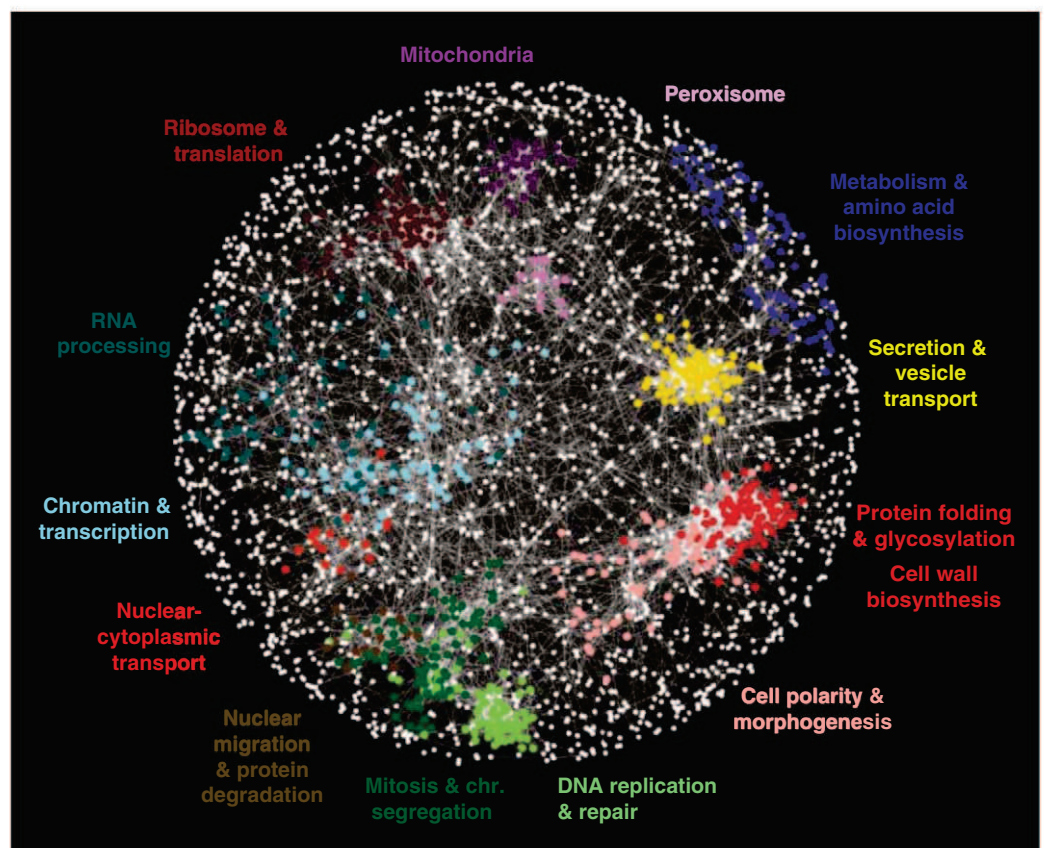
Michael Costanzo,<sup>1,2\*</sup> Anastasia Baryshnikova,<sup>1,2\*</sup> Jeremy Bellay,<sup>3</sup> Yungil Kim,<sup>3</sup> Eric D. Spear,<sup>4</sup> Carolyn S. Sevier,<sup>4</sup> Huiming Ding,<sup>1,2</sup> Judice L.Y. Koh,<sup>1,2</sup> Kiana Toufighi,<sup>1,2</sup> Sara Mostafavi,<sup>1,5</sup> Jeany Prinz,<sup>1,2</sup> Robert P. St. Onge,<sup>6</sup> Benjamin VanderSluis,<sup>3</sup> Taras Makhnevych,<sup>7</sup> Franco J. Vizeacoumar,<sup>1,2</sup> Solmaz Alizadeh,<sup>1,2</sup> Sondra Bahr,<sup>1,2</sup> Renee L. Brost,<sup>1,2</sup> Yiqun Chen,<sup>1,2</sup> Murat Cokol,<sup>8</sup> Raamesh Deshpande,<sup>3</sup> Zhijian Li,<sup>1,2</sup> Zhen-Yuan Lin,<sup>9</sup> Wendy Liang,<sup>1,2</sup> Michaela Marback,<sup>1,2</sup> Jadine Paw,<sup>1,2</sup> Bryan-Joseph San Luis,<sup>1,2</sup> Ermira Shuteriqi,<sup>1,2</sup> Amy Hin Yan Tong,<sup>1,2</sup> Nydia van Dyk,<sup>1,2</sup> Iain M. Wallace,<sup>1,2,10</sup> Joseph A. Whitney,<sup>1,5</sup> Matthew T. Weirauch,<sup>11</sup> Guoqing Zhong,<sup>1,2</sup> Hongwei Zhu,<sup>1,2</sup> Walid A. Houry,<sup>7</sup> Michael Brudno,<sup>1,5</sup> Sasan Ragibizadeh,<sup>12</sup> Balázs Papp,<sup>13</sup> Csaba Pál,<sup>13</sup> Frederick P. Roth,<sup>8</sup> Guri Giaever,<sup>2,10</sup> Corey Nislow,<sup>1,2</sup> Olga G. Troyanskaya,<sup>14</sup> Howard Bussey,<sup>15</sup> Gary D. Bader,<sup>1,2</sup> Anne-Claude Gingras,<sup>9</sup> Quaid D. Morris,<sup>1,2,5</sup> Philip M. Kim,<sup>1,2</sup> Chris A. Kaiser,<sup>4</sup> Chad L. Myers,<sup>3†</sup> Brenda J. Andrews,<sup>1,2†</sup> Charles Boone<sup>1,2†</sup>

A genome-scale genetic interaction map was constructed by examining 5.4 million gene-gene pairs for synthetic genetic interactions, generating quantitative genetic interaction profiles for ~75% of all genes in the budding yeast, *Saccharomyces cerevisiae*. A network based on genetic interaction profiles reveals a functional map of the cell in which genes of similar biological processes cluster together in coherent subsets, and highly correlated profiles delineate specific pathways to define gene function. The global network identifies functional cross-connections between all bioprocesses, mapping a cellular wiring diagram of pleiotropy. Genetic interaction degree correlated with a number of different gene attributes, which may be informative about genetic network hubs in other organisms. We also demonstrate that extensive and unbiased mapping of the genetic landscape provides a key for interpretation of chemical-genetic interactions and drug target identification.

The relation between an organism's genotype and its phenotype are governed by myriad genetic interactions (1). Although

a complex genetic landscape has long been anticipated (2), exploration of genetic interactions on a genome-wide level has been limited.

**Fig. 1.** A correlation-based network connecting genes with similar genetic interaction profiles. Genetic profile similarities were measured for all gene pairs by computing Pearson correlation coefficients (PCCs) from the complete genetic interaction matrix. Gene pairs whose profile similarity exceeded a PCC > 0.2 threshold were connected in the network and laid out using an edge-weighted, spring-embedded, network layout algorithm (7, 8). Genes sharing similar patterns of genetic interactions are proximal to each other; less-similar genes are positioned farther apart. Colored regions indicate sets of genes enriched for GO biological processes summarized by the indicated terms.



Systematic deletion analysis in the budding yeast, *Saccharomyces cerevisiae*, demonstrates that the majority of its ~6000 genes are individually dispensable, with only a relatively

<sup>1</sup>Banting and Best Department of Medical Research, Terrence Donnelly Centre for Cellular and Biomolecular Research, University of Toronto, Toronto, Ontario M5S 3E1, Canada.

<sup>2</sup>Department of Molecular Genetics, Terrence Donnelly Centre for Cellular and Biomolecular Research, University of Toronto, Toronto, Ontario M5S 3E1, Canada. <sup>3</sup>Department of Computer Science and Engineering, University of Minnesota, Minneapolis, MN 55455, USA. <sup>4</sup>Department of Biology, Massachusetts Institute of Technology, Cambridge, MA 02142, USA.

<sup>5</sup>Department of Computer Science, University of Toronto, Toronto, Ontario M5S 2E4, Canada. <sup>6</sup>Department of Biochemistry, Stanford Genome Technology Center, Stanford University, Palo Alto, CA 94304, USA. <sup>7</sup>Department of Biochemistry, University of Toronto, Toronto, Ontario M5S 1A8, Canada.

<sup>8</sup>Department of Biological Chemistry and Molecular Pharmacology, Harvard Medical School, Boston, MA 02115, USA.

<sup>9</sup>Samuel Lunenfeld Research Institute, Mount Sinai Hospital, 600 University Avenue, Toronto, Ontario M5G 1X5, Canada.

<sup>10</sup>Department of Pharmacy, University of Toronto, Toronto, Ontario M5S 3E1, Canada. <sup>11</sup>Department of Biomolecular Engineering, University of California, Santa Cruz, CA 95064, USA.

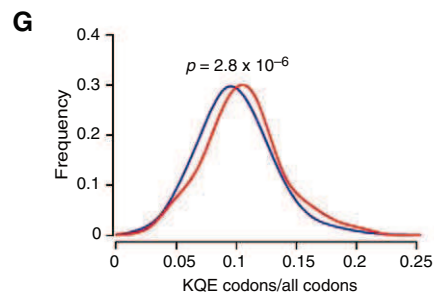
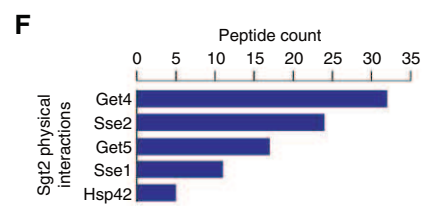
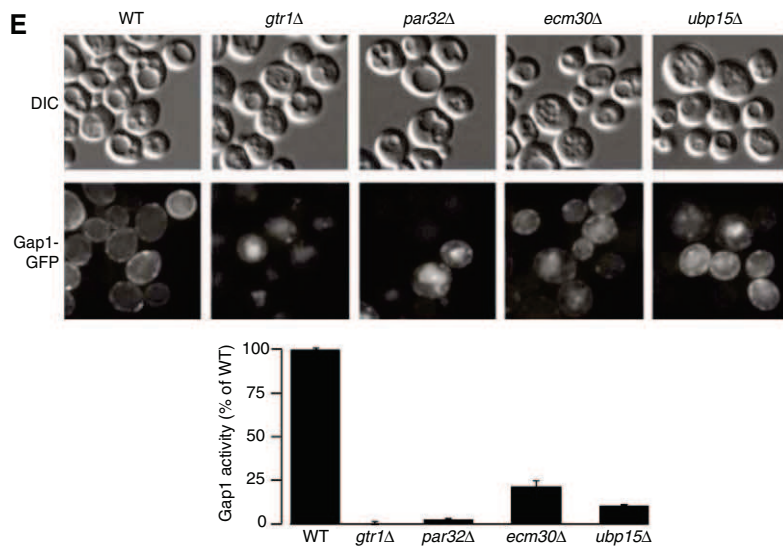
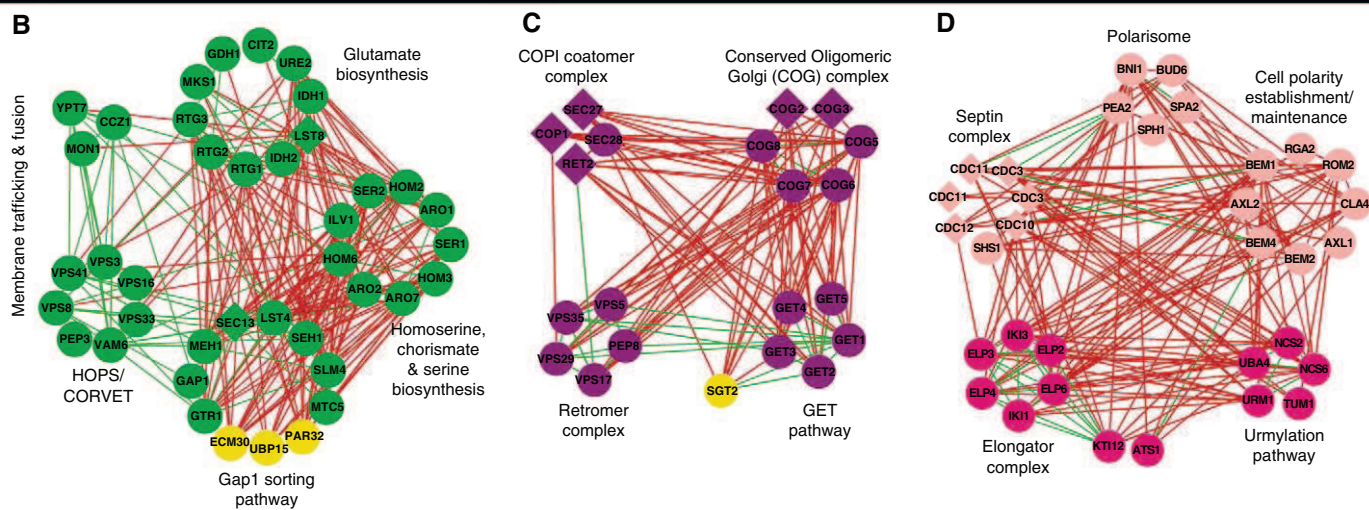
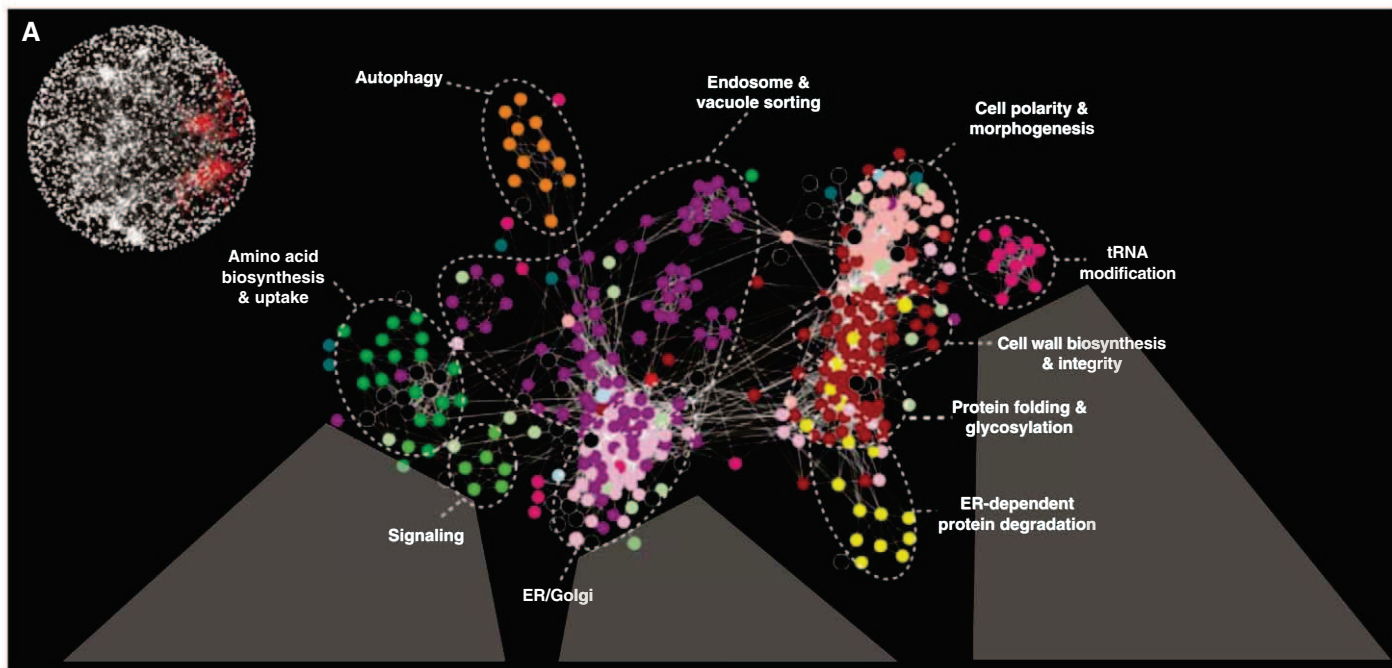
<sup>12</sup>S&P Robotics, Inc., 1181 Finch Avenue West, North York, Ontario M3J 2V8, Canada. <sup>13</sup>Institute of Biochemistry, Biological Research Center, H-6701 Szeged, Hungary.

<sup>14</sup>Department of Computer Science, Lewis-Sigler Institute for Integrative Genomics, Carl Icahn Laboratory, Princeton University, Princeton, NJ 08544, USA. <sup>15</sup>Biology Department, McGill University, Montreal, Quebec H3A 1B1, Canada.

\*These authors contributed equally to this work.

†To whom correspondence should be addressed. E-mail: cmyers@cs.umn.edu (C.L.M.); brenda.andrews@utoronto.ca (B.J.A.); charlie.boone@utoronto.ca (C.B.)





small subset (~20%) required for viability (1), which suggests the evolution of extensive buffering against genetic perturbations (3). Genome-scale screens for genetic interactions that affect the fitness of a cell or organism can chart the genetic network underlying functional redundancy (1). In particular, synthetic genetic array (SGA) methodology (4) enables the systematic mapping of synthetic lethal genetic interactions through an automated form of genetic analysis that produces high-density arrays of double mutants (5). Here, we report construction of a functionally unbiased genetic interaction map for a eukaryotic cell.

**Genome-scale, quantitative analysis of genetic interactions.** We consider a digenic interaction as a double mutant that shows a significant deviation in fitness compared with the expected multiplicative effect of combining two single mutants (6). Negative interactions refer to a more severe fitness defect than expected, with the extreme case being synthetic lethality; positive interactions refer to double mutants with a less severe fitness defect than expected. To quantitatively score genetic interactions in large-scale SGA screens, we developed a model to estimate fitness defects directly from double-mutant colony sizes (7, 8) (fig. S1A). We screened 1712 *S. cerevisiae* query genes, including 334 conditional or hypomorphic alleles of essential genes, for a total of ~5.4 million gene pairs spanning all biological processes (fig. S1, B and C) (7, 8). These queries were selected randomly with respect to function; however, preference was given to mutants exhibiting fitness defects (7, 8). Comparing fitness estimates of single mutants with their corresponding double-mutant phenotypes identified ~170,000 interactions, a threefold increase over all previously reported genetic interaction data (fig. S1, D and E). Our data captured ~35% of previously reported negative genetic interactions (7, 8) (fig. S1D) and exhibited significant correlation ( $r = 0.89$ ) (fig. S1F) with genetic interactions identified by high-resolution liquid growth profiles (7–9), which confirmed the accuracy of our measurements (fig. S1F). Thus, our approach enabled assembly of a quantitative fitness-based profile of genetic interactions on a genome-wide scale.

We determined false-negative and false-positive rates at a defined confidence threshold ( $|\epsilon| > 0.08$ ,  $P < 0.05$ ) (fig. S2A) (7, 8) and used this filtered data set for all analyses. Data evaluation, by several different measures (7, 8), indicated that interactions that corresponded to specific confidence levels were functionally informative (fig. S2, B and C). In particular, enrichment for Gene Ontology (GO) coannotated gene pairs was correlated with the significance and magnitude of genetic interaction (fig. S2B), as well as with genetic profile similarity (fig. S2C) (7, 8). Notably, we found about twice as many negative interactions as positive genetic interactions (fig. S1B). Moreover, negative genetic interactions tended to be more informative for identifying physical interactions and GO coannotated gene pairs than positive interactions (fig. S2C).

**A functional map of the cell.** Genes belonging to the same pathway or biological process tend to share similar profiles of genetic interactions (5). We exploited this property to construct a global network, grouping genes with similar interaction patterns together: Nodes in this network represent genes, and edges connect gene pairs that share common sets of genetic interactions or similar interaction profiles (Fig. 1). This network highlights genetic relations between diverse biological processes and the inherent functional organization of the cell. Genes displaying tightly correlated profiles form discernible clusters corresponding to distinct bioprocesses, and the relative distance between distinct clusters appears to reflect shared functionality (Fig. 1). For example, the role of the microtubule cytoskeleton in bridging nuclear chromosomal- and actin cytoskeleton-based functions is illustrated by the close proximity and relative positioning of clusters corresponding to genes annotated with roles in cell polarity and morphogenesis, mitosis and chromosome segregation, and DNA replication and repair (Fig. 1). Despite screening only ~30% of the genome as query genes, we recovered genetic interactions for ~75% of the genome because partial genetic interaction profiles were generated for nearly all nonessential genes in the genome. Our data were able to precisely predict known gene functions (GO biological process annotations), as well as or

better than all other genome-scale data sets (fig. S2D), and assigned a substantial amount of unique functional information for the genes not captured by previous genetic interaction studies (fig. S2D).

**Predicting function and relations.** Although complex, the genetic interaction network contains functional information at multiple levels of resolution. The interrogation of the genetic map at higher resolution enabled the dissection of broad biological processes into distinct, yet interdependent, gene cohorts (Fig. 2) [supporting data file S8 (8)]. In even more detail, we can also visualize networks in which genes are connected by edges that correspond to genetic interactions directly. Indeed, gene clusters that are correlated by negative (red) and positive (green) genetic interactions reveal network organization reflecting biological pathways and/or protein complexes and their functional integration with one another (Fig. 2, B to D). The genetic interactions occurring between different pathways and complexes were often monochromatic, as predicted previously (10), such that they were composed almost exclusively of a single type of genetic interaction, either all negative or all positive.

Genetic clusters were used to predict function for uncharacterized genes on the basis of network connectivity (Fig. 2, A to D). Three genes, *PAR32*, *ECM30*, and *UBP15*, had interaction profiles similar to those of members of the Gap1-sorting module (Fig. 2B), and consistent with a role in this process, all three genes led to Gap1 sorting and transport defects when deleted (Fig. 2E). Additional experimental results (fig. S3) (11) suggest that Par32 may function in target of rapamycin (TOR)-dependent regulation of the Gln3, Gat1, Rtg1, and Rtg3 transcription factors (12), whereas Ecm30 forms a stoichiometric complex with the Ubp15 ubiquitin protease (7, 8) that may modulate Gap1 localization, perhaps by controlling its ubiquitination state.

In another example, similar genetic interaction profiles suggested a strong functional relation between the GET pathway and the poorly characterized gene, *SGT2* (Fig. 2C). Consistent with a role in endoplasmic reticulum (ER)-dependent membrane targeting (13) or protein folding (14), we found that Sgt2 physically interacts with Get4, Get5, and heat shock 70

**Fig. 2.** Magnification of the functional map better resolves cellular processes. (A) A subnetwork corresponding to a region of the global map described in Fig. 1 is indicated in red (inset). Node color corresponds to a specific biological process: dark green, amino acid biosynthesis and uptake; light green, signaling; light purple, ER-Golgi; dark purple, endosome and vacuole sorting; yellow, ER-dependent protein degradation; red, protein folding and glycosylation, cell wall biosynthesis and integrity; fuchsia, tRNA modification; pink, cell polarity and morphogenesis; orange, autophagy; and black, uncharacterized. Individual genetic interactions contributing to genetic profiles revealed by (A) are illustrated for three specific subnetworks in (B) to (D). (B to D) Subsets of genes belonging to amino acid biosynthesis and uptake, ER-Golgi, and tRNA modification regions of the network were selected, and, in some cases, additional genes were included from the complete network shown in Fig. 1. Nodes are grouped according to profile similarity, and edges represent negative (red) and positive (green)

genetic interactions ( $|\epsilon| > 0.08$ ,  $P < 0.05$ ). Nonessential (circles) and essential (diamonds) genes are colored according to the biological process indicated in (A), and uncharacterized genes are depicted in yellow. (E) *PAR32*, *ECM30*, and *UBP15* are required for plasma membrane localization (micrographs) and activity (histogram) of the Gap1 amino acid permease. DIC, differential interference contrast; GFP, green fluorescent protein. (F) Sgt2 physically interacts with components of the GET pathway and members of the Hsp70 chaperone family. Proteins identified with high confidence as specific interactors for tandem affinity purification (TAP)-tagged Sgt2 (Sgt2-TAP) are shown in decreasing order of spectral counts. (G) Distribution of the Elp and Urm modified codon usage among synthetic sick or lethal interaction partners. The fraction of Elp and Urm modified codons (lysine, glutamine, and glutamic acid) relative to all codons was measured for all negative interactors with genes in the Elp or Urm complex (red) relative to the background usage of all genes (blue).



(Hsp70) protein family members (Fig. 2F), and, similarly to GET pathway mutants (13), deletion of *SGT2* results in mislocalization of the tail-anchored protein, Pex15 (fig. S4).

**Deciphering complex regulatory relations from the global genetic network.** Because the global genetic interaction map represents a broad functional survey, it should provide insights into the regulatory wiring diagram of the cell. For example, synthetic lethal interactions between genes encoding the elongator (Elp) complex and those of the urmylation (Urm) pathway suggested that the Urm pathway collaborates with the Elp complex in the modification of specific transfer RNAs (tRNAs) (15) (Fig. 2D). In addition to their synthetic lethal relation, Elp and Urm pathway genes shared highly similar genetic interaction profiles; notably, these interactions were enriched for cell polarity and secretion genes ( $P < 10^{-3}$ ) (Fig. 2D), which reflects a specific cell polarity defect associated with Elp pathway mutants (16).

The elongator tRNA modification machinery has been postulated either to broadly affect the translation of a suite of mRNAs whose genes have cell polarity roles or to selectively influence the activity of a key polarity regulatory gene (17). We were intrigued by the finding that the subset of Elp-Urm negative interactors, as well as cell polarity and secretion genes, in general, encode proteins that are significantly enriched for the amino acids that charge Elp- and Urm-modified tRNAs (Fig. 2G) (7, 8). These findings suggest

that Elp and Urm pathways may be biased toward the regulation of a functionally specific subset of cellular proteins. *ELP1* is a highly conserved gene whose human ortholog, inhibitor of kappa light polypeptide gene enhancer in B cells, kinase complex-associated protein (IKBKAP), is associated with a neurological disorder, familial dysautonomia, which leads to disruption of cytoskeletal organization when mutated (18, 19). Thus, it is possible that disease manifestation may involve impaired IKBKAP-dependent translation of a set of human genes belonging to a specific functional group.

**Genetic network connectivity.** Consistent with the degree distribution of other biological networks (1), the majority of genes have few interactions, whereas a small number are highly connected and serve as network hubs (Fig. 3A). We found subsets of genes that showed a strong bias in their interaction type. About 2% of array genes exhibited more than eight times as many negative interactions as positive ones, whereas a smaller set containing ~1% of all array genes showed four times as many positive as negative interactions (Fig. 3B). Genes displaying this behavior were functionally distinct. Specifically, a bias toward negative interaction was observed for genes required for normal progression of the cell division cycle ( $P < 10^{-8}$ ), which highlights the central role of checkpoints in maintaining viability in dividing cells. Predominantly positive interactions were indicative of genes involved in translation, ribosomal

RNA processing, and mRNA decay ( $P < 10^{-5}$ ), which may suggest that defects in the translation machinery somehow mask phenotypes that would otherwise be expressed in normal cells.

**Genetic interaction degree, fitness, multifunctionality, and pleiotropy.** Genetic interaction hubs show a clear association with several fundamental physiological and evolutionary properties (Fig. 3C), which may be predictive of genetic interactions in other organisms. In particular, we uncovered a strong correlation between genetic interaction degree and single-mutant fitness ( $r = 0.73$ ). Single mutants with increasingly severe fitness defects tended to exhibit an increased number of both negative and positive interactions (Fig. 3C and fig. S5, A and B) (7, 8). This relation was also observed for essential genes where the average number of interactions involving a temperature-sensitive mutant allele was inversely proportional to allele fitness at a given semipermissive temperature (fig. S5B). The increased connectivity of genes with fitness defects when singly mutated was not due to nonspecific interactions derived from a generally compromised cell or experimental noise; interactions with these genes were found to overlap with known functional relationships just as frequently as other interactions (fig. S5C).

In addition to the correlation with single-mutant fitness defects, genetic interaction hubs showed a high degree of pleiotropy. Specifically, the number of genetic interactions for a particular hub was significantly correlated with the number

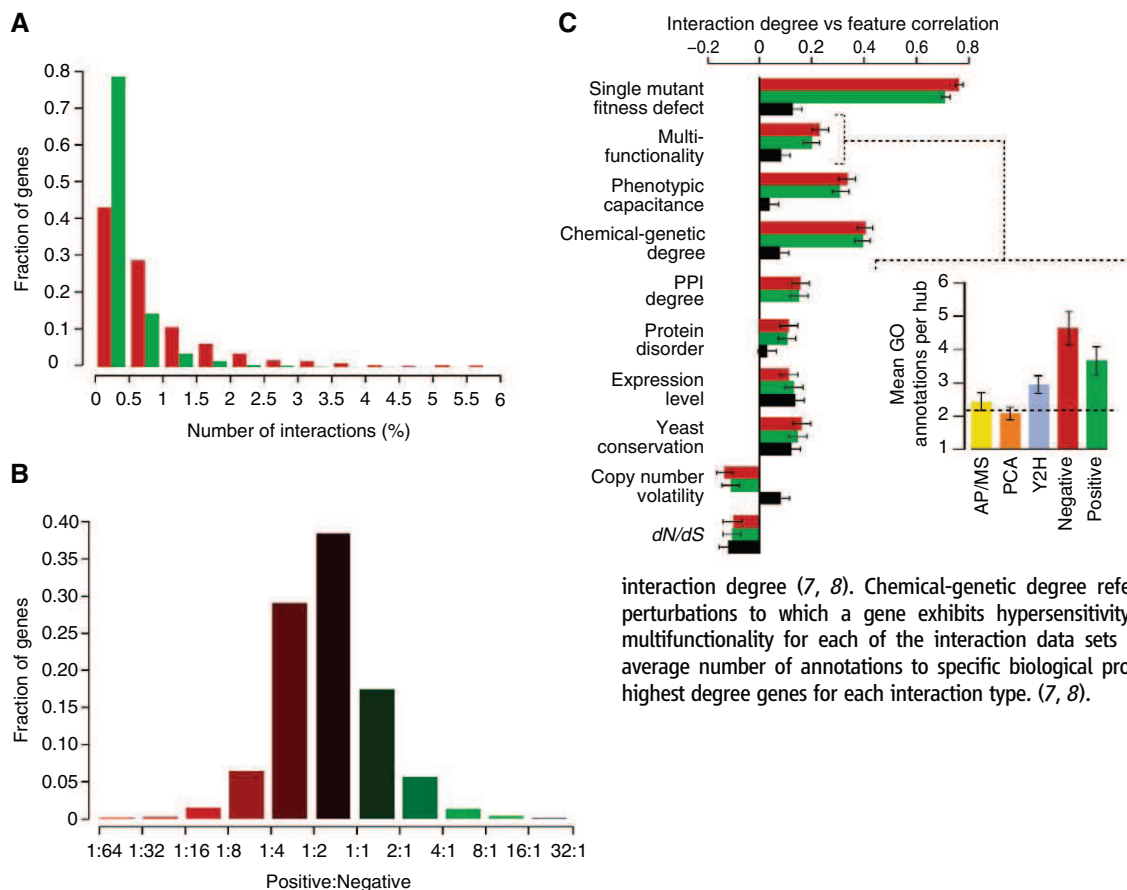


**Fig. 3.** Positive and negative genetic interactions on the basis of a defined confidence threshold ( $|r| > 0.08$ ,  $P < 0.05$ ) (7, 8). **(A)** The distribution of genetic interaction network degree for negative (red) and positive (green) interactions involving query genes. **(B)** The ratio of positive to negative interactions for each gene varies across the genome. **(C)** Pearson correlation between genetic interaction degree (derived from the array mutant strains) and physiological and evolutionary properties was measured for positive (green), negative (red) and protein-protein (black)

interaction degree (7, 8). Chemical-genetic degree refers to the number of chemical perturbations to which a gene exhibits hypersensitivity. (Inset) The relation to gene multifunctionality for each of the interaction data sets is illustrated by measuring the average number of annotations to specific biological process GO terms for the top 1% highest degree genes for each interaction type. (7, 8).

of distinct annotated functions (multifunctionality) for that gene (Fig. 3C and inset). This connection between network hubs and pleiotropy was further reflected by the rich variation associated with hub mutant phenotypes and increased phenotypic capacitance, the number of different morphological phenotypes linked to a specific gene as defined quantitatively (Fig. 3C) (20). This relation suggests that genetic network hubs play key roles in the integration and execution of morphogenetic programs.

It is noteworthy that these correlations persisted after we controlled for fitness defects of single mutants (fig. S5D). Furthermore, these

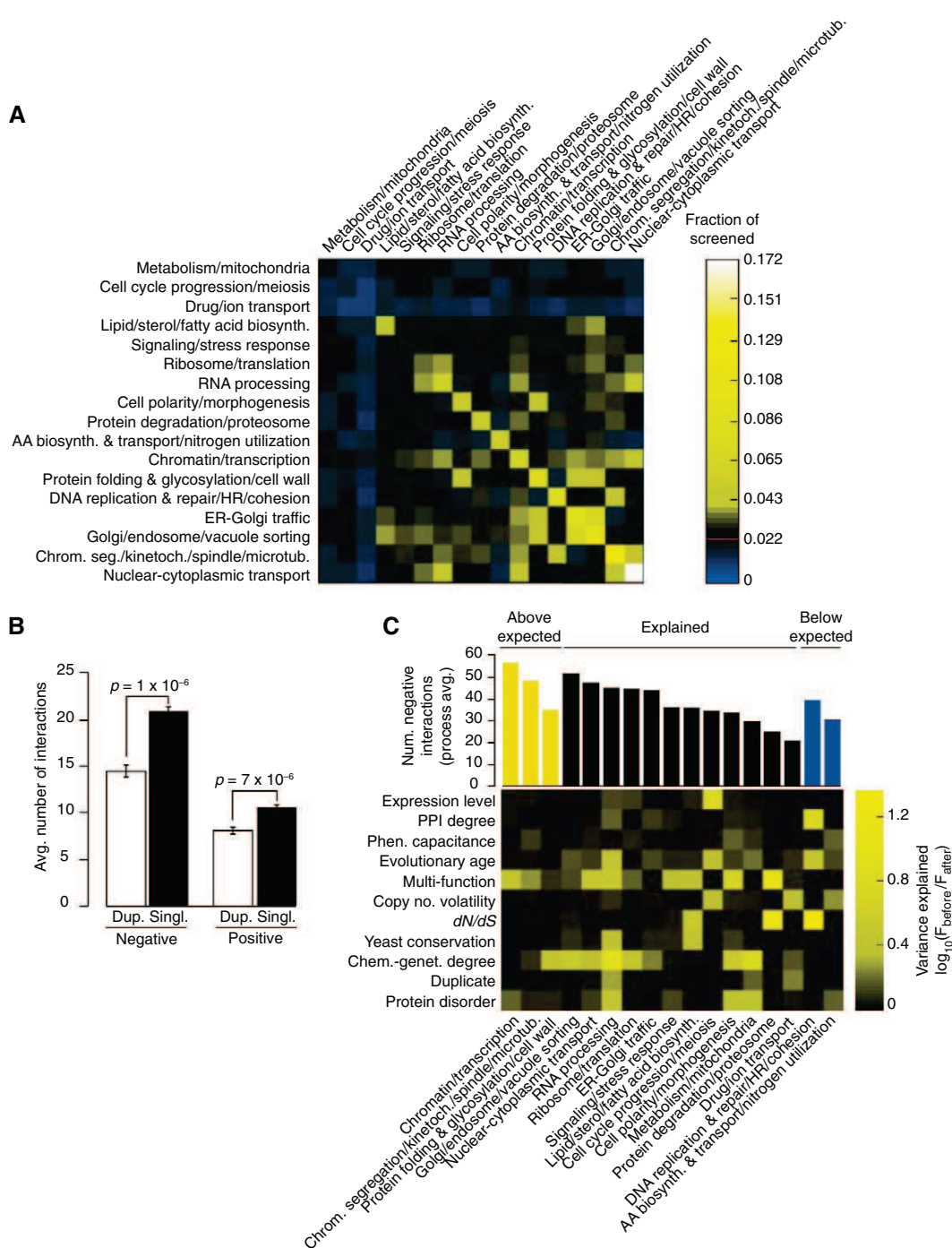
trends reveal characteristics that distinguish genetic network hubs from hubs on the physical interaction network (Fig. 3C). Notably, the correlation to both fitness and multifunctionality was several fold stronger for genetic interaction degree (Fig. 3C). This likely reflects the ability of genetic perturbation analysis to identify broad phenotypic connections that cannot be captured in networks subject to physical constraints and suggests that large-scale genetic interaction networks will be of wide utility for defining the functional wiring diagrams of cells and organisms.

Although there are several distinguishing characteristics of genetic interaction hubs, we

measured a significant correlation ( $r \sim 0.2$ ) between the genetic and physical interaction degree for any given gene (Fig. 3C). Similar to protein-protein interaction hubs (21–23), we found that genetic network hubs tend to be expressed at higher mRNA levels. In comparison with the whole-genome sequences of 23 different Ascomycota fungi species, we found that genetic interaction degree correlated positively with gene conservation and negatively with copy number volatility, which indicates that they tend to be lost or duplicated less frequently. Genes showing more genetic interactions evolved ( $dN/dS$ ) more slowly than genes

**Fig. 4. (A)** Frequency of synthetic lethal/sick (negative) genetic interactions within and across biological processes. The fraction of screened gene pairs exhibiting negative interactions was measured for 17 broadly defined functional gene sets (7, 8). A color was assigned to each process-process element reflecting the fraction of interaction (blue, below the frequency of random pairs; black, statistically indistinguishable from the random background of interactions; and yellow, above the frequency of random pairs), with the diagonal representing within-process interactions. The red line in the color scale bar indicates random background.

**(B)** Genetic interaction frequency of duplicate genes. T bars, SEM. **(C)** Gene-specific factors explaining the variation in number of negative interactions across biological processes. (Top) The average number of interactions across each process with the color indicating processes that have more interactions than expected (yellow,  $P < 0.05$ ); processes whose interaction degree is explained by the factors indicated on the y axis; and those with fewer interactions than expected (blue,  $P < 0.05$ ). The influence of each gene-specific factor in explaining the number of interactions observed was measured by plotting the ratio of  $F$  statistics of the bioprocess factor before and after incorporating the additional gene-specific factor. This ratio is indicated by the corresponding column in the heat map (7, 8). (AA, amino acids; chrom. seg., chromosome segregation; HR, homologous recombination; kinetoch., kinetochore)





with few interactions (Fig. 3C), which suggests that genetic hubs generally tend to be evolutionarily constrained. However, a subset of genetic interaction hubs appears to behave differently. Despite their tendency to evolve faster (fig. S5F) (24), proteins with higher levels of native disorder tend to exhibit a large number of genetic interactions, which suggests that genes encoding disordered proteins may represent a distinct class of genetic interaction hub.

**Distribution of genetic interactions by bioprocess.** We assessed the distribution of genetic interactions across different cellular processes for both negative (Fig. 4A) and positive (fig. S6A) (7, 8) interactions. The heat map identified functions enriched (yellow) or depleted (blue) for genetic interactions relative to the expected frequency of a random gene set. As expected, genes involved in similar biological processes were enriched for negative interactions; however, we also observed genetic interactions bridging bioprocesses (Fig. 4A). Specifically, genes involved in chromatin, transcription, ER-Golgi transport, and Golgi-endosome transport showed a significant number of interactions that bridge diverse functions, which suggests that many of these genes are interconnected or pleiotropic. These bioprocess-level

findings concur with individual gene analyses, which indicated that genes involved in processes related to chromatin structure and transcription ( $P < 10^{-14}$ ), as well as secretion and vesicle transport ( $P < 10^{-9}$ ), were among the most highly connected genes in our network. The central role for chromatin- and transcription-related processes identified in the yeast genetic network is consistent with large-scale genetic network mapping in *Caenorhabditis elegans* (25), and the bridging function for secretory pathway genes emphasizes their role as communication conduits for the cell. In contrast to genetic interactions, protein-protein interactions connect relatively fewer bioprocesses, and thus, although highly informative of local pathway architecture, physical interactions fail to provide a complete picture of multifunctionality or interconnections between cellular processes (fig. S6A). Reduced interactions in particular gene sets, such as meiosis, drug or ion transport, and metabolism or mitochondrial genes (blue in Fig. 4A), may arise because some processes are more buffered than others and require more complex genetic analysis to uncover their interactions (5), whereas others may function only under certain environmental conditions (26).

Because variation was observed in the average number of genetic interactions for genes across

different bioprocesses, we tested whether gene-specific properties (Fig. 3C) were predictive of this variation. For example, we found that gene duplicates exhibited fewer interactions when surveyed across the entire genome (Fig. 4B) (7, 8), and therefore, we asked if bioprocesses with relatively few genetic interactions could be explained by specific factors, such as a high percentage of duplicated genes. An analysis of covariance (ANCOVA) (Fig. 4C) (7, 8) showed that a linear model including the gene-specific properties predictive of genetic interaction hubs (Fig. 3C) was sufficient to explain the number of negative (12 out of 17) (Fig. 4C) and positive (13 out of 17) (fig. S6B) genetic interactions for the majority of bioprocesses. For example, the relatively few genetic interactions seen for genes with roles in drug and ion transport are explained by a combination of a high rate of gene duplication (~50 to 60%) and copy number volatility among genes annotated to this process. This is consistent with the tendency of genes encoding protein pumps to undergo numerous duplication events (27), which confirms that extensive redundancy associated with large gene families complicates the identification of digenic interactions. Three bioprocesses had significantly more negative interactions than predicted (Fig. 4C) ( $P < 0.05$ ),

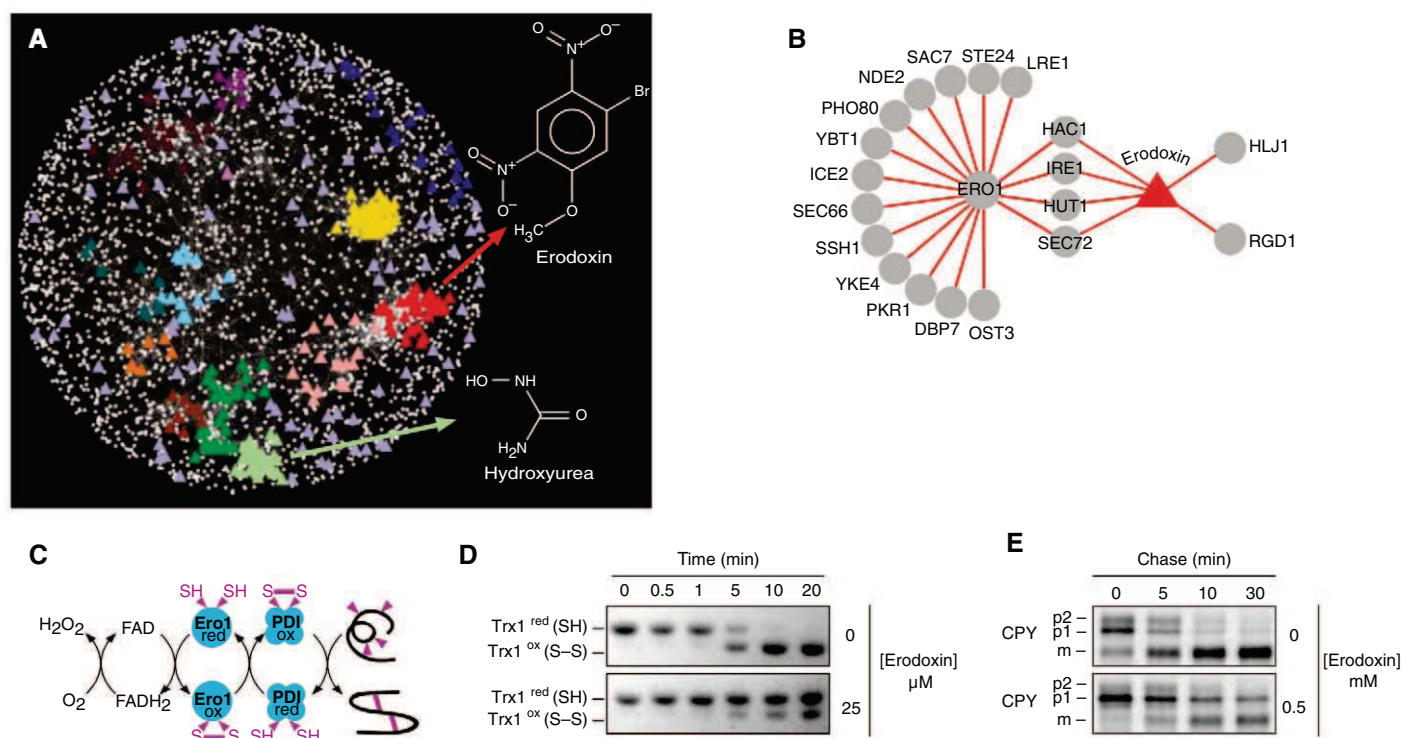


**Fig. 5.** (A) A chemical-genetic interaction map is shown in which colored triangles represent chemical compounds and white nodes correspond to genes. Compounds were positioned on the map by highlighting the gene node whose genetic interaction profile most closely resembles the chemical genetic profile of the compound derived from three sources (7, 8). Compounds tightly correlated to genes positioned within functional clusters (Fig. 1) were colored accordingly to the color of the cluster as in Fig. 1. The chemical-genetic profile of hydroxyurea clustered with genes involved in DNA replication and repair, whereas that of erodoxin clustered

with genes involved in protein folding, glycosylation, and cell wall biosynthesis. Compounds positioned outside functional clusters are colored light purple. (B) Network displaying overlap between ERO1 negative genetic interactions and genes resulting in growth inhibition when deleted in the presence of erodoxin. (C) ERO1-dependent pathway for oxidative protein-folding pathway. (D) Erodoxin inhibits Ero1-dependent oxidation of Trx1 in vitro. (E) Erodoxin inhibits CPY processing to the vacuolar form in vivo. ER (p1), Golgi (p2), and vacuolar (m) forms of CPY are indicated.

including those that show functional enrichment for genetic interaction hubs (Fig. 4A). Conversely, DNA replication and repair and amino acid biosynthesis showed significantly fewer negative interactions than predicted ( $P < 0.05$ ), which suggested that either more genetic interactions remain to be found for these genes under different environmental conditions or that these genes are more buffered and thus are inherently less connected on the digenic network.

**Overlap between the genetic and the protein-protein interaction networks.** We observed genetic interactions overlapping with 10 to 20% of protein-protein interaction pairs, depending on the physical interaction mapping methodology (fig. S7), which is significantly higher than expected randomly (~3%). Considering the global yeast physical interaction network as defined by affinity purification–mass spectrometry (28, 29), yeast two-hybrid protocol (30), or protein-fragment complementation assay (PCA) (31), roughly an equivalent number of physical interactions overlapped with negative and positive genetic interaction pairs: ~7% of protein-protein interacting pairs shared a negative genetic interaction, whereas ~5% shared a positive interaction. Conversely, considering our genetic interaction network, only a small fraction of gene pairs that show a genetic interaction (0.4% negative and 0.5% positive) are also physically linked. These findings suggest that the vast majority of both positive and negative interactions occurs between, rather than within, complexes and pathways, connecting those that presumably work together or buffer one another, respectively.

**Navigating from genetic to chemical-genetic interaction networks.** The set of ~4700 viable yeast deletion mutants has been exposed to hundreds of different chemical compounds (26). We quantified the chemical-genetic degree for each gene by counting the number of chemical (environmental) perturbations for which the corresponding gene deletion mutant showed hypersensitivity. We found a significant correlation ( $r = 0.4$ ,  $P < 10^{-5}$ ) between genetic interaction and chemical-genetic degree (Fig. 3C). These observations suggest that hubs on a chemical-genetic network are predictive of hubs on the genetic interaction network and can be used to link environmental capacitance and genetic robustness. Furthermore, our data suggest that the same genes buffer the cell against both environmental and genetic insults. It is not known whether natural selection favors genetic robustness (32), but the positive correlation between genetic interaction degree and environmental capacitance suggests that genetic and environmental robustness may coevolve (33).

Because chemical perturbations mimic genetic perturbations, the genetic network should be useful for predicting the cellular targets of bioactive molecules (34). We identified genetic interaction profiles that are significantly correlated to a chemical-genetic profile of a particular com-

pound (7, 8, 26, 34) and showed that compounds often clustered to dense regions of the genetic network indicative of specific bioprocesses (Fig. 5A). For example, hydroxyurea, a compound that inhibits ribonucleotide reductase and blocks DNA synthesis, clusters with the gene cohort annotated with roles in DNA replication and repair (Fig. 5A). These results demonstrate that clustering of chemical-genetic and genetic interaction profiles complements haploinsufficiency profiling, which has the potential to identify drug targets directly (26). We used this network approach to examine the previously uncharacterized compound, 0428-0027, which we have subsequently named erodoxin (Fig. 5A). Erodoxin clustered with genes associated with protein folding, glycosylation, and cell wall biosynthesis functions (Fig. 5A) because the erodoxin chemical-genetic profile most closely resembled the genetic interaction profile of *ERO1* (Fig. 5B and fig. S8A), an essential gene involved in oxidative protein folding (Fig. 5C) (35). Two additional lines of evidence suggested that Ero1 is the target of erodoxin. First, *ero1Δ* and *fad1Δ* heterozygotes were the most hypersensitive mutants identified from haploinsufficiency profiling (fig. S8B) (7, 8). Second, we found that erodoxin leads to inhibition of Trx1 oxidation (Fig. 5D) and delayed carboxy peptidase Y (CPY) processing (Fig. 5E), which suggests that it inhibits Ero1 activity both in vitro and in vivo.

**Exploring the universe of genetic interactions.** Unbiased, systematic, and quantitative analysis of digenic loss-of-function perturbations assigns a rich phenotypic profile to each gene and enables construction of a functional map of the cell, organizing genes and higher-order bioprocesses according to their related roles (Fig. 1). The functional connections defined by genetic interactions complement the information derived from networks based upon physical interactions, which links previously uncharacterized genes to specific pathways and complexes and reveals connections between pathways and complexes. The global mapping of genetic networks is becoming feasible in more complex cells and metazoans because of the growing availability of whole-genome sequences and large-scale sets of gene-knockdown reagents (1). Although negative genetic interactions can be conserved from yeast to worms and from yeast to human cells, the extent to which individual genetic interactions are conserved over large evolutionary distances remains unclear (1). The conservation of the genetic map may also occur at various levels of resolution. For example, overall network topology (Fig. 1) and properties (Fig. 3C) may be more highly conserved than particular genetic interactions because they reflect the fundamental architecture of the cell. The ability to integrate genetic and chemical-genetic perturbation data offers the potential to link bioactive compounds to their targets (Fig. 5), to identify genetic interaction hubs through chemical perturbations (Fig. 3C), to design synthetic lethal

therapies for targeting genetically defined tumors (36), and to understand the mechanistic basis of drug synergy (37). Finally, genetic interaction maps provide a model for understanding the link between genotype and phenotype and for outlining the general principles of complex genetic interaction networks, which play a key role in governing inherited phenotypes, including human disease (3).

## References and Notes

1. S. J. Dixon, M. Costanzo, A. Baryshnikova, B. Andrews, C. Boone, *Annu. Rev. Genet.* **43**, 601 (2009).
2. C. H. Waddington, *The Strategy of the Gene* (Allen & Unwin, London, 1957).
3. L. Hartwell, *Science* **303**, 774 (2004).
4. A. H. Tong et al., *Science* **294**, 2364 (2001).
5. A. H. Tong et al., *Science* **303**, 808 (2004).
6. R. Mani, R. P. St. Onge, J. L. Hartman 4th, G. Giaever, F. P. Roth, *Proc. Natl. Acad. Sci. U.S.A.* **105**, 3461 (2008).
7. Materials and methods are available as supporting material on Science Online.
8. See supplementary information at <http://drygin.ccrb.utoronto.ca/~costanzo2009>.
9. R. P. St. Onge et al., *Nat. Genet.* **39**, 199 (2007).
10. D. Segrè, A. Deluna, G. M. Church, R. Kishony, *Nat. Genet.* **37**, 77 (2005).
11. A. Huber et al., *Genes Dev.* **23**, 1929 (2009).
12. E. J. Chen, C. A. Kaiser, *J. Cell Biol.* **161**, 333 (2003).
13. M. C. Jonikas et al., *Science* **323**, 1693 (2009).
14. M. B. Metzger, S. Michaelis, *Mol. Biol. Cell* **20**, 1006 (2009).
15. S. Leidel et al., *Nature* **458**, 228 (2009).
16. P. B. Rahl, C. Z. Chen, R. N. Collins, *Mol. Cell* **17**, 841 (2005).
17. A. Esberg, B. Huang, M. J. Johansson, A. S. Byström, *Mol. Cell* **24**, 139 (2006).
18. T. Naumanen, L. D. Johansen, E. T. Coffey, T. Kallunki, *Cell Adh. Migr.* **2**, 236 (2008).
19. L. D. Johansen et al., *J. Cell Sci.* **121**, 854 (2008).
20. S. F. Levy, M. L. Siegal, A. Levchenko, *PLoS Biol.* **6**, e264 (2008).
21. P. M. Kim, L. J. Lu, Y. Xia, M. B. Gerstein, *Science* **314**, 1938 (2006).
22. H. B. Fraser, D. P. Wall, A. E. Hirsh, *BMC Evol. Biol.* **3**, 11 (2003).
23. C. Pál, B. Papp, L. D. Hurst, *Genetics* **158**, 927 (2001).
24. P. M. Kim, A. Sboner, Y. Xia, M. Gerstein, *Mol. Syst. Biol.* **4**, 179 (2008).
25. B. Lehner, C. Crombie, J. Tischler, A. Fortunato, A. G. Fraser, *Nat. Genet.* **38**, 896 (2006).
26. M. E. Hillenmeyer et al., *Science* **320**, 362 (2008).
27. M. J. Dunham et al., *Proc. Natl. Acad. Sci. U.S.A.* **99**, 16144 (2002).
28. A. C. Gavin et al., *Nature* **440**, 631 (2006).
29. N. J. Krogan et al., *Nature* **440**, 637 (2006).
30. H. Yu et al., *Science* **322**, 104 (2008).
31. K. Tarassov et al., *Science* **320**, 1465 (2008).
32. J. A. de Visser et al., *Evolution* **57**, 1959 (2003).
33. C. D. Meiklejohn, D. L. Hartl, *Trends Ecol. Evol.* **17**, 468 (2002).
34. A. B. Parsons et al., *Nat. Biotechnol.* **22**, 62 (2004).
35. C. S. Sevier et al., *Cell* **129**, 333 (2007).
36. P. C. Fong et al., *N. Engl. J. Med.* **361**, 123 (2009).
37. J. Lehar, B. R. Stockwell, G. Giaever, C. Nislow, *Nat. Chem. Biol.* **4**, 674 (2008).
38. We thank S. Dixon, T. Hughes, P. Jorgensen, and M. Tyers for critical comments. Supported by Genome Canada through the Ontario Genomics Institute (2004-OGI-3-01) and the Canadian Institutes of Health Research (GSP-41567) (C.B., B.A.), the University of Minnesota Biomedical Informatics and Computational Biology program (J.B., R.D.), and a seed grant from the Minnesota Supercomputing Institute (J.B., B.V.).

**Supporting Online Material** [www.sciencemag.org/cgi/content/full/327/5964/425/DC1](http://www.sciencemag.org/cgi/content/full/327/5964/425/DC1) Materials and Methods  
SOM Text  
Figs. S1 to S8  
References

20 August 2009; accepted 12 November 2009  
10.1126/science.1180823



# Formation of Iapetus' Extreme Albedo Dichotomy by Exogenically Triggered Thermal Ice Migration

John R. Spencer<sup>1\*</sup> and Tilmann Denk<sup>2</sup>

The extreme albedo asymmetry of Saturn's moon Iapetus, which is about 10 times as bright on its trailing hemisphere as on its leading hemisphere, has been an enigma for three centuries. Deposition of exogenic dark material on the leading side has been proposed as a cause, but this alone cannot explain the global shape, sharpness, and complexity of the transition between Iapetus' bright and dark terrain. We demonstrate that all these characteristics, and the asymmetry's large amplitude, can be plausibly explained by runaway global thermal migration of water ice, triggered by the deposition of dark material on the leading hemisphere. This mechanism is unique to Iapetus among the saturnian satellites because its slow rotation produces unusually high

The fact that Iapetus is much darker on its leading hemisphere (the hemisphere that faces forward in its orbit around Saturn, centered near longitude 90°W) than on its opposite trailing hemisphere has been known almost since the moon's discovery in 1671 (1). The dark terrain on the leading hemisphere, named Cassini Regio, extends toward the trailing side near the equator, and bright trailing-side terrain extends over the poles onto the leading side (2). Albedo varies by a factor of ~10 between the two hemispheres (3).

Most proposed hypotheses for the origin of the global albedo dichotomy can be divided into three categories: (i) A dark debris cloud, produced by a large impact on a body within the Saturn system [Hyperion (4, 5), Iapetus itself (6), a former outer satellite (7), or Titan (8)] was deposited on Iapetus' leading side early in its history. (ii) Interplanetary or circum-saturnian dust gradually alters one hemisphere of Iapetus in a process that may be ongoing today. Four alteration processes have been suggested: leading-side deposition of dark material (9–11); leading-side removal of ice, exposing a dark substrate (12, 13); leading-side enrichment of intrinsic dark material due to impact erosion of ice (14–16), with possible further darkening by chemical or irradiation processes (3); and trailing-side deposition of icy material (17). (iii) Dark material was emplaced onto the surface by endogenic geologic processes (2).

All these models have insurmountable weaknesses. It is impossible to reproduce the elongated shape of Cassini Regio by the deposition of a dark debris cloud or other exogenic infall [e.g., (10, 13)], and the boundaries between Cassini Regio and the bright terrain are very abrupt and irregular on

kilometer scales, which is also inconsistent with simple exogenic infall (18). Endogenic models cannot explain the precise alignment of the dark terrain with the apex of motion of Iapetus (2).

A fourth category of model, which combines exogenic darkening with insolation-controlled thermal sublimation, has unfortunately been overlooked since it was proposed in 1974 (19), despite its successful prediction of increased darkening along the equator and brighter poles, as subsequently observed (20). The original description of this model was brief and qualitative, and is here developed in quantitative detail, constrained by observations made by the Cassini spacecraft.

The mobility of water ice depends strongly on surface temperature, which for a given latitude and distance from the Sun depends primarily on albedo, thermal inertia, and rotation rate. Temperatures on the icy saturnian satellites have been measured directly by Cassini's Composite Infrared Spectrometer (CIRS) instrument (21). Observed spectra are close approximations to blackbodies, and we assume here that the temperature of the best blackbody fit to each spectrum is a reliable proxy for surface temperature. Diurnal temperature variations observed by the CIRS long-wavelength detector FP1 [20 to 600 cm<sup>-1</sup>, field of view (FOV) 4 mrad] yield global albedos and thermal inertias (22) when fitted with a one-dimensional numerical thermal model (23). Thermal inertias are very low, generally between 8 and 25 J m<sup>-2</sup> s<sup>-1/2</sup> K<sup>-1</sup>, indicating an unconsolidated surface. Subsolar temperatures on Iapetus, which are crucial to determining H<sub>2</sub>O stability, were observed at higher spatial resolution near the leading/trailing boundary with CIRS' shorter-wavelength detector FP3 (600 to 1100 cm<sup>-1</sup>, FOV 0.3 mrad) during the close flyby on 10 September 2007 (Fig. 1). There is a strong inverse correlation between daytime temperature and albedo. Spatial resolution is sufficient to resolve the largest dark and bright areas, re-

vealing peak dark- and bright-terrain temperatures of 129 and 113 K, respectively. Thermal model fits to these temperatures, using thermal inertias from (22), yield dark- and bright-terrain albedos of 0.04 and 0.39, respectively. The bright-terrain albedo is substantially higher than the 0.31 value determined from the FP1 data (which have lower spatial resolution), probably because those data included some dark terrain within the bright-terrain measurements.

Diurnal thermal models, constrained by measured thermal inertias and albedos (22), yield diurnally averaged upward H<sub>2</sub>O sublimation rates for the icy saturnian satellites (Fig. 2A), using the known vapor pressure dependence on temperature (24). Iapetus' long rotation period (79 days) yields substantially higher daytime temperatures for a given albedo than on the other saturnian satellites, because there is more time for temperatures to equilibrate with sunlight and a smaller fraction of the absorbed sunlight is reradiated from the night side. The low albedo of the leading side further increases temperatures there. Because of the extreme temperature dependence of sublimation rates, mean sublimation is determined largely by maximum diurnal temperature rather than mean temperature, so ice on Iapetus with the low albedo of the leading side has by far the highest sublimation rate of ice on any saturnian satellite, equivalent to >100 m of sublimation in a billion years if unimpeded by the formation of a lag deposit.

Impact gardening competes with sublimation, mixing lag deposits or recondensed frosts back into the subsurface. Gardening rates on Iapetus are unknown, but the Moon provides a useful analog (25) (Fig. 2B). Unless saturnian satellite gardening rates differ drastically from lunar rates, it is clear that for Rhea and all colder objects, H<sub>2</sub>O sublimation is negligible, whereas sublimation dominates on Iapetus' dark side, and the interplay of the two processes is more complex on Phoebe and the bright side of Iapetus.

Many synchronously rotating outer-planet satellites exhibit color, albedo, or textural differences between their leading and trailing hemispheres (26–28), due primarily to differing exposures of the two hemispheres to exogenic effects such as impact gardening, deposition of exogenic material, or magnetospheric effects. With the exception of Iapetus, the highest-amplitude leading/trailing asymmetries among icy satellites are for Dione and Europa, with disk-integrated leading/trailing brightness ratios of 1.45 and 1.33, respectively (29, 30).

We suggest that exogenic deposition of dark material from either a heliocentric source or (more probably) from Saturn's outer retrograde satellites results in a moderate darkening and reddening of the leading hemisphere of Iapetus (18), raising leading-hemisphere temperatures and H<sub>2</sub>O sublimation rates, as previously proposed (19). Sublimating molecules follow ballistic trajectories because Iapetus' atmosphere is negligible. The median molecule jump distance before re-impacting the surface is a large fraction of Iapetus' 734-km radius for likely surface

<sup>1</sup>Southwest Research Institute, 1050 Walnut Street, Suite 300, Boulder, CO 80304, USA. <sup>2</sup>Freie Universität, Malteserstr. 74-100, 12249 Berlin, Germany.

\*To whom correspondence should be addressed. E-mail: spencer@boulder.swri.edu

temperatures [e.g., 590 km at 125 K and 470 km at 105 K, measured along the surface (31)], so there is efficient transfer of H<sub>2</sub>O from the leading hemisphere to the colder trailing hemisphere and poles. As discussed above, if the initial albedo is comparable to or lower than that of Iapetus' current bright hemisphere, this lag deposit will eventually accumulate faster than it can be remixed into the regolith by impact gardening, and the surface will darken further. The resulting increase in temperatures and sublimation rates produces a runaway process that proceeds until sublimation is cut off by formation of a dark, ice-free lag deposit on the leading hemisphere. This process is similar to the thermal segregation of ice and dark material postulated for the icy Galilean satellites (32) and seen by Galileo (33, 34). On the Galilean satellites the segregation is local rather than global, probably because of the much smaller molecule jump distance [tens of kilometers (35)] and the much larger radii of those satellites.

We have tested this scenario with a series of simplified numerical models of exogenic depo-

sition and H<sub>2</sub>O migration on Iapetus (31). Dark material is deposited at a rate that decreases with distance from the center of the leading hemisphere, and ice then migrates in response to insolation and the exogenic darkening. Figure 3 shows that a range of model parameters can reproduce Iapetus' appearance quite well. Key parameters for models A and B, respectively (31), are a peak leading-side dark-material deposition rate of 3 and 0.3 cm per billion years, surface mixing to a depth of 10 and 1 cm, and power-law and linear relationships between dark-material abundance and albedo. The dependence of exogenic darkening on distance from the center of the trailing hemispheres is also slightly different. A mixing depth of 1 cm is perhaps less plausible than 10 cm, given that ~10 cm of impact gardening occurs in 10<sup>9</sup> years in the lunar regolith (25). In both models, modest initial darkening of the leading hemisphere produces runaway darkening at low latitudes as sublimation becomes important, leading to an equatorial strip of dark, ice-free terrain that expands in latitude and longitude upon further sublimation. On

the trailing hemisphere, there is net deposition of frost due to antipodal focusing of water molecules sublimating from the leading side, but with continued sublimation, the leading-hemisphere dark terrain eventually begins to encroach on the trailing side [(31); table S1 and fig. S3 discuss the parameter dependence of model results].

The model albedo distribution is strongly bimodal and the bright/dark boundary is sharp, consistent with high-resolution Cassini images (18), and the shape of the dark terrain on Iapetus' leading hemisphere is very similar to that in the models. The most important discrepancy is that ice at low latitudes on the trailing side is brighter in the models than on Iapetus (31).

The bright poleward-facing slopes seen at mid-latitudes on Iapetus (18, 36) are also a natural consequence of the water ice mobility predicted by this model. Water molecules deposited at mid-latitudes will preferentially remain on pole-facing slopes and sublime from warmer equator-facing slopes. Similar thermally driven phenomena are seen on Callisto (32) and Ganymede (33). The presence of apparent

**Fig. 1.** Cassini CIRS FP3 measurements of noontime temperatures on Iapetus compared to a Cassini Imaging Science Subsystem map of surface albedos (41). **(Left)** Color-coded (600 to 1100 cm<sup>-1</sup>) brightness temperatures. **(Center)** The area covered by CIRS is outlined in red to reveal the albedo patterns in the region covered. **(Right)** Temperature (color) and albedo (brightness) are superposed. Regions where the dark and bright terrains are fully resolved are shown by red and blue diamonds, respectively; temperatures are 129 K and 113 K in these locations. The yellow star shows the location of the subsolar point. The map uses a longitude system in which 0°W corresponds to the mean sub-Saturn direction.

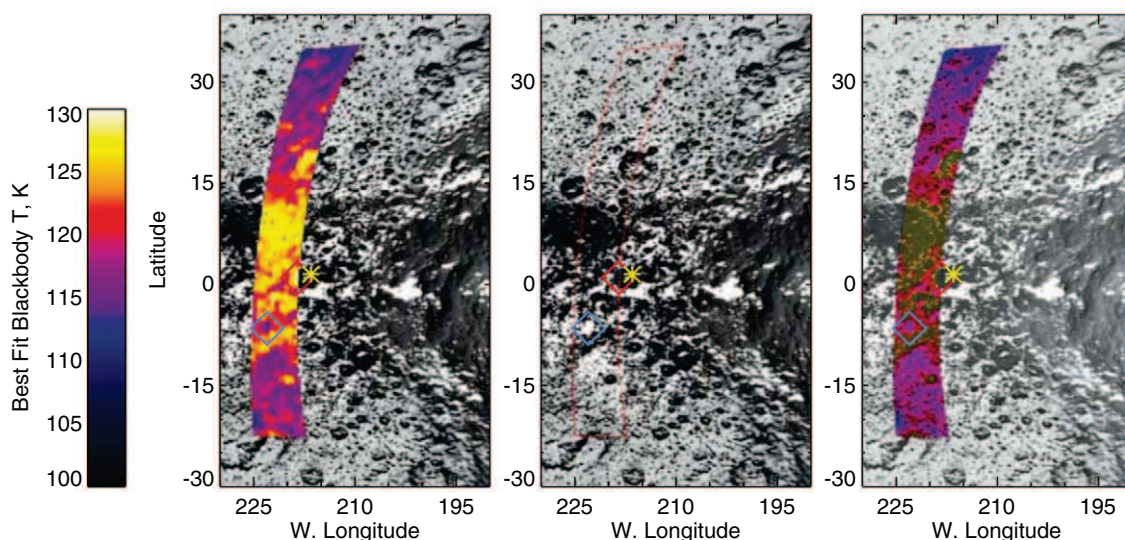


**Fig. 2.** **(A)** Peak temperatures (at mean solar distance) and diurnally averaged upward H<sub>2</sub>O sublimation rates for the equatorial regions of the icy saturnian satellites. Numbers in parentheses give the assumed bolometric albedos and thermal inertias in J m<sup>-2</sup> s<sup>-1/2</sup> K<sup>-1</sup>, from (22) except for Phoebe [from (42)], and the albedo of the bright terrain on Iapetus has been adjusted to 0.39 as described in the text. Unit emissivity is assumed. Sublimation rates for Enceladus are negligible because of its extremely high albedo (0.81). **(B)** Comparison of H<sub>2</sub>O sublimation rates and estimated 50% probability impact gardening depth, for Earth's Moon using a "constant flux" model (25), as a function of time.

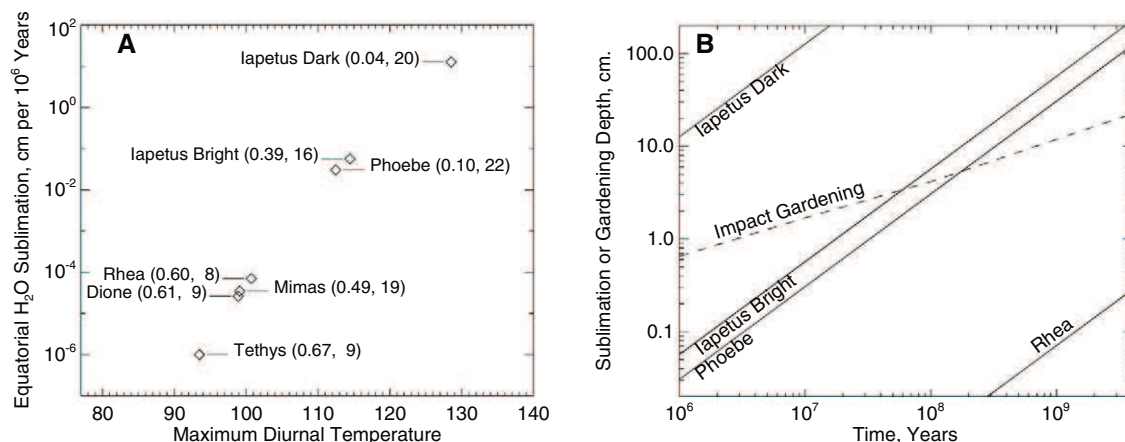


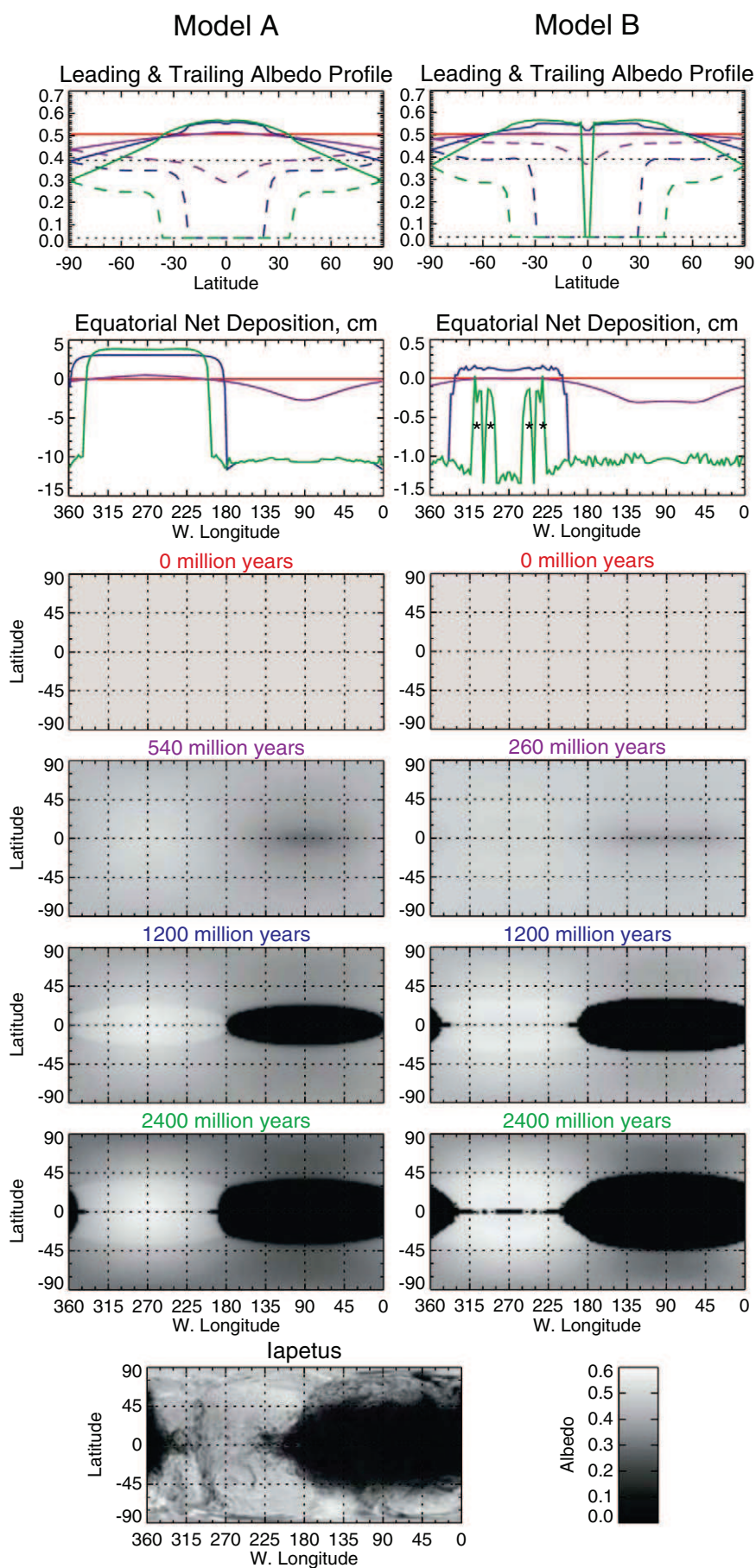


**Fig. 3.** Evolution of surface albedo and frost deposition depth, color-coded by time, for example model runs A and B, with parameters described in the text and detailed in (31). The albedo plots show pole-to-pole profiles in the center of the leading (90°W, dashed lines) and trailing (270°W, solid lines) hemispheres; the dotted horizontal lines show the observed dark-terrain albedo (0.04) and that of the equatorial bright terrain near longitude 220°W (0.39). Stars on the model B net deposition plot indicate albedo instabilities discussed in the text. The bottom panel shows the actual albedo distribution on Iapetus, derived from a mosaic of Cassini images (43). The albedo scale is indicated by the scale bar, although the Iapetus mosaic is not photometrically accurate and is scaled very approximately using the CIRIS bright- and dark-terrain albedos that we determined.

local thermal segregation (32) of bright and dark terrains at low latitudes on Iapetus' trailing hemisphere (18) also points to the importance of insolation-controlled migration of water ice. Analogous temperature/albedo instabilities were seen in the same region in the last time step of model B (Fig. 3), where small differences in ice thickness resulting from numerical noise became greatly exaggerated, because regions with less ice were darker and thus lost their remaining ice faster, depositing it on neighboring bright regions. Although in the model this process was triggered by model artifacts, the instability that exaggerated those artifacts is a real physical process.

A strong prediction of this model is that the dark material of Iapetus' Cassini Region should be essentially ice-free. On Iapetus' dark terrain, with peak daytime temperatures of 129 K, 1 mm of ice should sublime in only 8000 years. Cassini Region shows both a weak H<sub>2</sub>O absorption edge at 160 nm (37) and a strong 3- $\mu$ m H<sub>2</sub>O band (38), but these features may be due to bound water rather than H<sub>2</sub>O ice. The weaker 1.5- and 2.0- $\mu$ m H<sub>2</sub>O bands typically seen in planetary water ice are not seen in Cassini Region, so if ice is present, it must be in micrometer-sized grains. However, micrometer-sized ice grains should sublime away in decades at these temperatures.

The leading-side dark lag deposit, once formed, will thicken with time as impact gardening brings additional ice to the surface (a process not included in our model), and in turn that ice sublimates as well. Any ice within the impact-gardened layer will thus be lost, and the thickness of the dark layer may be comparable to the depth of impact gardening, perhaps several tens of centimeters (Fig. 2B). This is consistent with Cassini images showing small craters within the dark terrain with bright ejecta, rims, and crater floors (18). Here, recent impacts forming craters with diameters on the order of tens of meters and depths on the order of meters have apparently punched through the upper dark-material layer and excavated fresh subsurface ice. The abundance of bright craters may be consistent with sublimation darkening rates (31). Our model is also consistent with Cassini and ground-based radar observations, which suggest that the leading/trailing asymmetry is only tens of centimeters deep (31, 39, 40) (fig. S4).



We suggest that exogenically triggered global thermal segregation of bright and dark material on Iapetus is a likely explanation for both the extreme amplitude and the shape of Iapetus' albedo dichotomy. In our model, the uniqueness of Iapetus is attributable not so much to a unique exogenic darkening mechanism (because the initial darkening may be relatively modest) than to a unique combination of size, heliocentric distance, and rotation rate, which allows global migration of the water ice in response to the exogenic darkening.

## References and Notes

1. J. D. Cassini, *Philos. Trans. R. Soc.* **12**, 831 (1677).
2. B. A. Smith *et al.*, *Science* **215**, 504 (1982).
3. S. W. Squyres, C. Sagan, *Nature* **303**, 782 (1983).
4. R. A. J. Matthews, *Q. J. R. Astron. Soc.* **33**, 253 (1992).
5. S. Marchi, C. Barbieri, A. Dell'Oro, P. Paolucci, *Astron. Astrophys.* **381**, 1059 (2002).
6. R. G. Tabak, W. M. Young, *Earth Moon Planets* **44**, 251 (1989).
7. T. Denk, G. Neukum, *Lunar Planet. Sci. Conf.* **XXXI**, abstr. 1660 (2000).
8. T. C. Owen *et al.*, *Icarus* **149**, 160 (2001).
9. S. Soter, paper presented at the IAU Colloquium 28, Cornell University, Ithaca, NY, 18 to 21 August 1974.
10. J. A. Burns, D. P. Hamilton, F. Mignard, S. Soter, in *Physics, Chemistry, and Dynamics of Interplanetary Dust*, ASP Conference Series 104, B. Å. S. Gustafson, M. S. Hanner, Eds. (Astronomical Society of the Pacific, San Francisco, 1996), pp. 179–182.
11. B. J. Buratti, M. D. Hicks, K. A. Tryka, M. S. Sittig, R. L. Newburn, *Icarus* **155**, 375 (2002).
12. A. F. Cook, F. A. Franklin, *Icarus* **13**, 282 (1970).
13. P. D. Wilson, C. Sagan, *Icarus* **122**, 92 (1996).
14. D. P. Cruikshank *et al.*, *Icarus* **53**, 90 (1983).
15. J. F. Bell, D. P. Cruikshank, M. J. Gaffey, *Icarus* **61**, 192 (1985).
16. B. J. Buratti, J. A. Mosher, *Icarus* **115**, 219 (1995).
17. C. Peterson, *Icarus* **24**, 499 (1975).
18. T. Denk *et al.*, *Science* **10**, (2009).
19. D. A. Mendis, W. I. Axford, *Annu. Rev. Earth Planet. Sci.* **2**, 419 (1974).
20. D. A. Mendis, W. I. Axford, *J. Geophys. Res.* **113**, A11217 (2008).
21. F. M. Flasar *et al.*, *Space Sci. Rev.* **115**, 169 (2004).
22. C. J. A. Howett, J. R. Spencer, J. C. Pearl, M. Segura, *Icarus* 10.1016/j.icarus.2009.07.016 (2009).
23. J. R. Spencer, L. A. Lebofsky, M. V. Sykes, *Icarus* **78**, 337 (1989).
24. C. E. Bryson, V. Cazcarra, L. L. Levenson, *J. Chem. Eng. Data* **19**, 107 (1974).
25. D. E. Gault, F. Hoerz, D. E. Brownlee, J. B. Hartung, in *Proceedings of the Fifth Lunar Science Conference* (Pergamon, New York, 1974), vol. 3, pp. 2365–2386.
26. J. Veverka, in *Planetary Satellites*, J. Burns, Ed. (Univ. of Arizona Press, Tucson, AZ, 1977), p. 171–209.
27. B. J. Buratti, J. Veverka, *Icarus* **58**, 254 (1984).
28. B. J. Buratti, J. A. Mosher, *Icarus* **90**, 1 (1991).
29. B. J. Buratti, J. A. Mosher, P. D. Nicholson, C. A. McGhee, R. French, *Icarus* **136**, 223 (1998).
30. D. Morrison, N. D. Morrison, in *Planetary Satellites*, J. Burns, Ed. (Univ. of Arizona Press, Tucson, AZ, 1977), pp. 363–378.
31. See supporting material on Science Online.
32. J. R. Spencer, *Icarus* **69**, 297 (1987).
33. L. M. Prockter *et al.*, *Icarus* **135**, 317 (1998).
34. J. M. Moore *et al.*, *Icarus* **140**, 294 (1999).
35. N. G. Purves, C. B. Pilcher, *Icarus* **43**, 51 (1980).
36. C. C. Porco *et al.*, *Science* **307**, 1237 (2005).
37. A. R. Hendrix, C. J. Hansen, *Icarus* **193**, 344 (2008).
38. D. P. Cruikshank *et al.*, *Icarus* **193**, 334 (2008).
39. S. J. Ostro *et al.*, *Icarus* **183**, 479 (2006).
40. G. J. Black, D. B. Campbell, L. M. Carter, S. J. Ostro, *Science* **304**, 553 (2004).
41. T. Roatsch *et al.*, *Planet. Space Sci.* **57**, 83 (2009).
42. F. M. Flasar *et al.*, *Science* **307**, 1247 (2005).
43. S. Albers, [http://laps.noaa.gov/albers/sos/saturn/iapetus/iapetus\\_rgb\\_cyl\\_www.jpg](http://laps.noaa.gov/albers/sos/saturn/iapetus/iapetus_rgb_cyl_www.jpg) (2008).
44. We dedicate this paper to the late Steve Ostro, for his invaluable insights into the subsurface structure of Iapetus. We acknowledge the magnificent work by the Cassini project that made possible the observations presented here, and in particular the work of J. Pearl, M. Segura, and other members of the Cassini CIRIS team. Supported by the Cassini project and by NASA grants NNX07AU40G and NNG04GK67G, and by the German Aerospace Center (DLR).

**Supporting Online Material** [www.sciencemag.org/cgi/content/full/science.1177132/DC1](http://www.sciencemag.org/cgi/content/full/science.1177132/DC1) SOM Text Figs. S1 to S4 Table S1 References

1 June 2009; accepted 3 December 2009  
Published online 10 December 2009;  
10.1126/science.1177132  
Include this information when citing this paper.

# Iapetus: Unique Surface Properties and a Global Color Dichotomy from Cassini Imaging

Tilman Denk,<sup>1\*</sup> Gerhard Neukum,<sup>1</sup> Thomas Roatsch,<sup>2</sup> Carolyn C. Porco,<sup>3</sup> Joseph A. Burns,<sup>4</sup> Götz G. Galuba,<sup>1</sup> Nico Schmedemann,<sup>1</sup> Paul Helfenstein,<sup>4</sup> Peter C. Thomas,<sup>4</sup> Roland J. Wagner,<sup>2</sup> Robert A. West<sup>5</sup>

Since 2004, Saturn's moon Iapetus has been observed repeatedly with the Imaging Science Subsystem of the Cassini spacecraft. The images show numerous impact craters down to the resolution limit of ~10 meters per pixel. Small, bright craters within the dark hemisphere indicate a dark blanket thickness on the order of meters or less. Dark, equator-facing and bright, poleward-facing crater walls suggest temperature-driven water-ice sublimation as the process responsible for local albedo patterns. Imaging data also reveal a global color dichotomy, wherein both dark and bright materials on the leading side have a substantially redder color than the respective trailing-side materials. This global pattern indicates an exogenic origin for the redder leading-side parts and suggests that the global color dichotomy initiated the thermal formation of the global albedo dichotomy.

Since 2004, the Imaging Science Subsystem (ISS) (1) onboard the Cassini spacecraft has observed the saturnian moon Iapetus (Fig. 1 and table S1) during multiple campaigns (table S2), including a close, targeted flyby on 10 September 2007 (2). One reason for Iapetus being a primary target for the Cassini instruments was its unique global albedo dichotomy (3), the first surface property ever detected on a planetary moon outside the Earth-Moon system. The roughly elliptical, very dark area on the leading hemisphere (named Cassini Regio) has been

repeatedly observed by Cassini ISS; it covers ~40% of the surface and is precisely centered at the middle of Iapetus' leading side at 0°N, 93.5°W (4). Cassini Regio is found to be homogeneously dark, with two exceptions: small, bright craters deep within the dark terrain and bright, mainly poleward-facing slopes closer to the edges.

We have identified brighter-than-average craters with diameters up to ~200 m within the highest-resolution images; they display features ranging from subtly lightened rims to obvious bright floors and bright-ray systems. The brightest

one, Escremiz (Fig. 2, A and B), is about four times brighter than its surroundings. Only a few percent of these craters are more than twice as reflective as their environs, whereas all others have almost faded to the average albedo of Cassini Regio.

If the darkening process is uniform for all fresh craters, then the brightest craters should be the youngest. With this concept as a guide, we roughly estimated when different craters were formed (5). Figure 2C shows that fresh craters fade very quickly. If a new crater has excavated icy material that is ~10 times brighter than the dark Cassini Regio coating (and, thus, about as bright as icy parts of the trailing side), it is only about half as bright ~10,000 years later. After ~10 million years, it has faded to approximately half of the brightness of the surrounding dark terrain. Extrapolating these data from the observed area to the whole Cassini Regio indicates that the largest bright-ray crater with an age similar to Escremiz should be ~200 m in size and that slightly more than 100 craters similar or larger in size and comparable or younger in age than Escremiz should exist on Iapetus' dark hemisphere.

<sup>1</sup>Institut für Geologische Wissenschaften, Freie Universität Berlin, 12249 Berlin, Germany. <sup>2</sup>Institut für Planetenforschung, Deutsches Zentrum für Luft- und Raumfahrt (DLR), Rutherfordstraße 2, 12489 Berlin, Germany. <sup>3</sup>Cassini Imaging Central Laboratory for Operations (CICLOPS), Space Science Institute, 4750 Walnut Street, Suite 205, Boulder, CO 80301, USA. <sup>4</sup>Department of Astronomy, Cornell University, Space Sciences Building, Ithaca, NY 14853, USA. <sup>5</sup>Jet Propulsion Laboratory (JPL), California Institute of Technology, 4800 Oak Grove Drive, Pasadena, CA 91109, USA.

\*To whom correspondence should be addressed. E-mail: Tilmann.Denk@fu-berlin.de



The visual appearance of crater Escremiz implies that the dark material is, at most, a few meters thick. For a diameter of ~60 m, the crater depth should be on the order of ~10 m (6).

Because Escremiz shows a completely bright crater floor and no indication of layering in the crater walls (Fig. 2B), its dark blanket should be much less thick, consistent with results from

radar experiments that estimate thicknesses of only decimeters (7, 8).

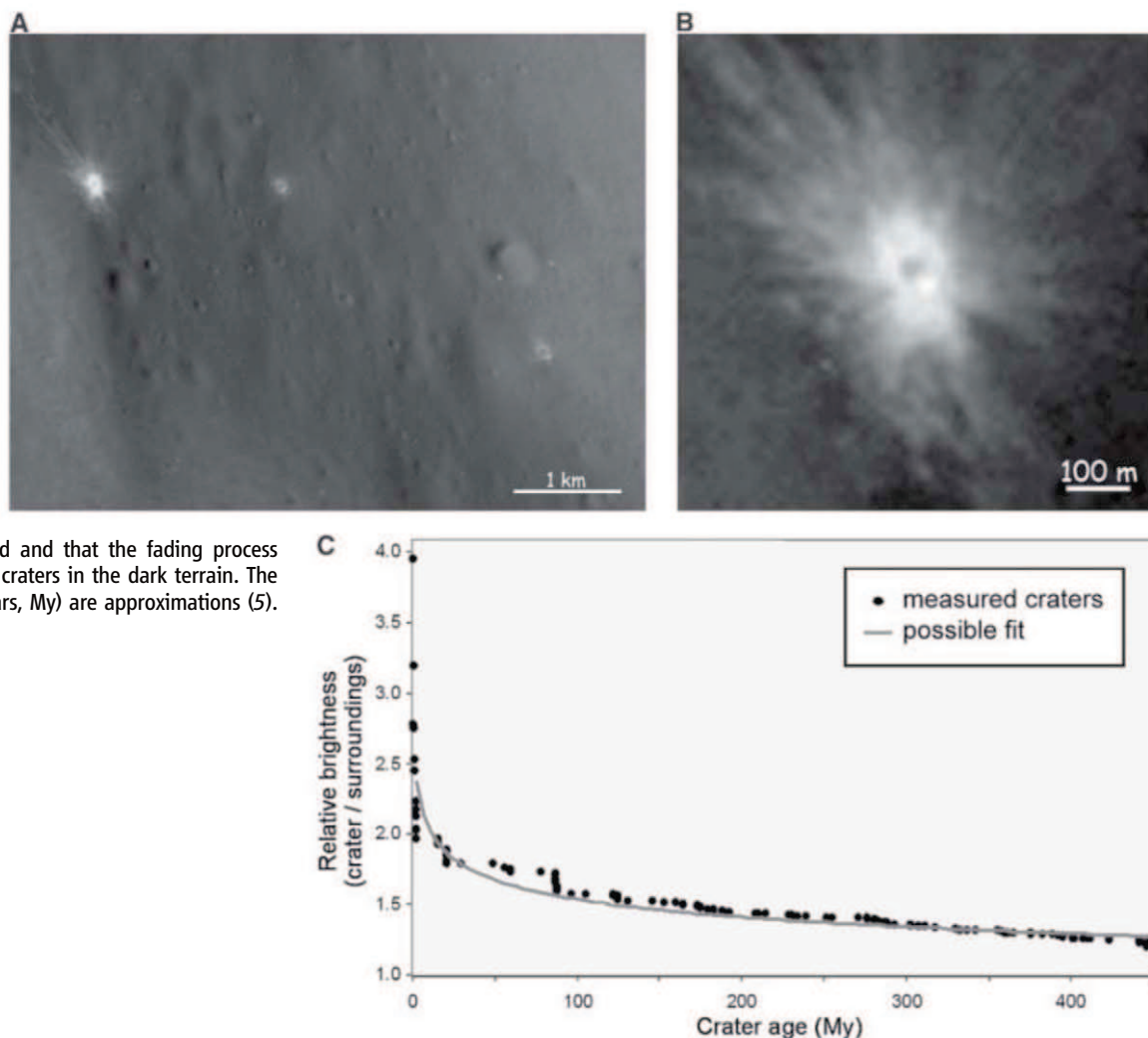
The other exceptions to the observed homogeneity of Cassini Regio are bright, poleward-facing crater walls at mid-latitudes and near the eastern and western boundaries. Above ~28° latitude north or south on Iapetus' leading side, still inside but near the northern or southern edge of Cassini Regio, the observed craters are dark, but the majority of their poleward-facing rims and central peaks is bright and presumably icy (Fig. 1, left, and fig. S1). The strong correlation of the appearance of local dark/bright patches to their planetographic latitude and slope direction suggests that they were formed through runaway temperature-driven water-ice sublimation (9). Whereas areas of lower solar irradiation remain bright, areas of higher irradiation lose their water-ice component, leaving behind the more refractory dark component.

The visual appearance of bright craters with dark, equator-facing walls above ~45° latitude, just outside Cassini Regio (again on the leading side) (fig. S1) (10), is also a strong indication that this temperature-dependent effect takes place. Another possible interpretation, in which these dark slopes result from exogenically infalling material, appears unlikely. In this case, the orientation of the dark



**Fig. 1.** Global views of Iapetus' dark leading side (**left**) (image IDs: N1482859847 to N1482859953) and its bright trailing side (**right**) (image IDs: N1568157586 to N1568160072); north is up. Turgis (17°N, 28°W), with a diameter of ~580 km, is the largest known well-preserved basin on Iapetus and is visible in the dark Cassini Regio at its eastern edge. The prominent basin on the southern trailing side (on the lower left side of the right-hand plot) is Engelier (41°S, 265°W, ~504 km).

**Fig. 2.** (A) Bright craters within the dark terrain, observed during closest approach of the targeted flyby. Bright-ray crater Escremiz (1.6°N, 173.5°W, diameter ~60 m; at the upper left) is the most prominent of the observed craters of this class on Iapetus. Image ID: N1568127660. (B) Enlarged and contrast-enhanced display of Escremiz. (C) Brightnesses of small craters within the dark terrain versus individual crater age, under the assumption that brightness and age are directly correlated and that the fading process acts similarly on all fresh craters in the dark terrain. The crater ages (in million years, My) are approximations (5).



slopes would be point-symmetric about the center of Iapetus' leading side (the apex of motion) and not mirror-symmetric with respect to the equator, as observed by the Cassini camera.

A common property of these local dark/bright variations is sharp albedo boundaries (at pixel scales of several tens to hundreds of meters), both inside and outside Cassini Regio. Discrete dark patches are even observed on the trailing side, far away from Cassini Regio. Near the equator (continuing to  $\sim 20^\circ$  north or south latitude), these patches are often correlated with depressions, especially with dark-floored craters and troughs (fig. S2). At latitudes up to  $\sim 55^\circ$ , dark patches are only seen on equator-facing slopes (fig. S3). At higher latitudes, no dark spot has been imaged on the trailing side.

Besides very small craters and craters with distinct albedo patterns, a large number of regular impact craters of all sizes have shaped Iapetus' landscape. The generally high crater density indicates that both the bright and the dark surface areas of Iapetus are globally ancient. At large sizes, we find old, often degraded basins with diameters nearly reaching Iapetus' radius (11). No other saturnian moon shows so many large basins. In many areas, craters smaller than  $\sim 5$  to  $10$  km follow a  $-2$  power law in the cumulative crater size-frequency diagram, indicating an equilibrium distribution ("crater saturation"). However, there are also regions (for instance, within the large basins) where the smaller-crater frequencies do not lie along the  $-2$  equilibrium distribution. For such terrains, and globally for craters  $>10$  km in size, it is possible to determine the production function (Fig. 3).

Our data also provide clear evidence that earlier hypotheses for the formation of the global albedo dichotomy, postulating infall of interplanetary or circum-saturnian dust as the cause, do not work. The complex mottling that appears along the boundary dividing the albedo dichotomy (fig. S4) prevents all explanations except those involving endogenic geologic activities or thermally driven sublimation processes, as in the thermal-migration model of Spencer and Denk (12). However, to function properly, this model requires a small, continuous nonthermal darkening process on the leading side to initiate the longitudinal thermal asymmetry between the low-latitude terrain on the leading and trailing sides.

A global color and brightness pattern, which is apparent in the ISS data and is distinct from the long-known global albedo dichotomy, could provide this required trigger. The spectral slopes of leading-side surface materials are generally steeper and redder than those of trailing-side materials across both bright and dark terrains at near-infrared wavelengths. At near-ultraviolet wavelengths, the dark material of the leading side has flatter spectra than that of the trailing side (Fig. 4). Unlike the more elliptically shaped albedo dichotomy, this color dichotomy is well separated into two simple hemispheres (Fig. 4 and fig. S6). The approximate boundaries near the sub-Saturn and anti-Saturn meridians are gradual over hundreds of kilometers but are nevertheless

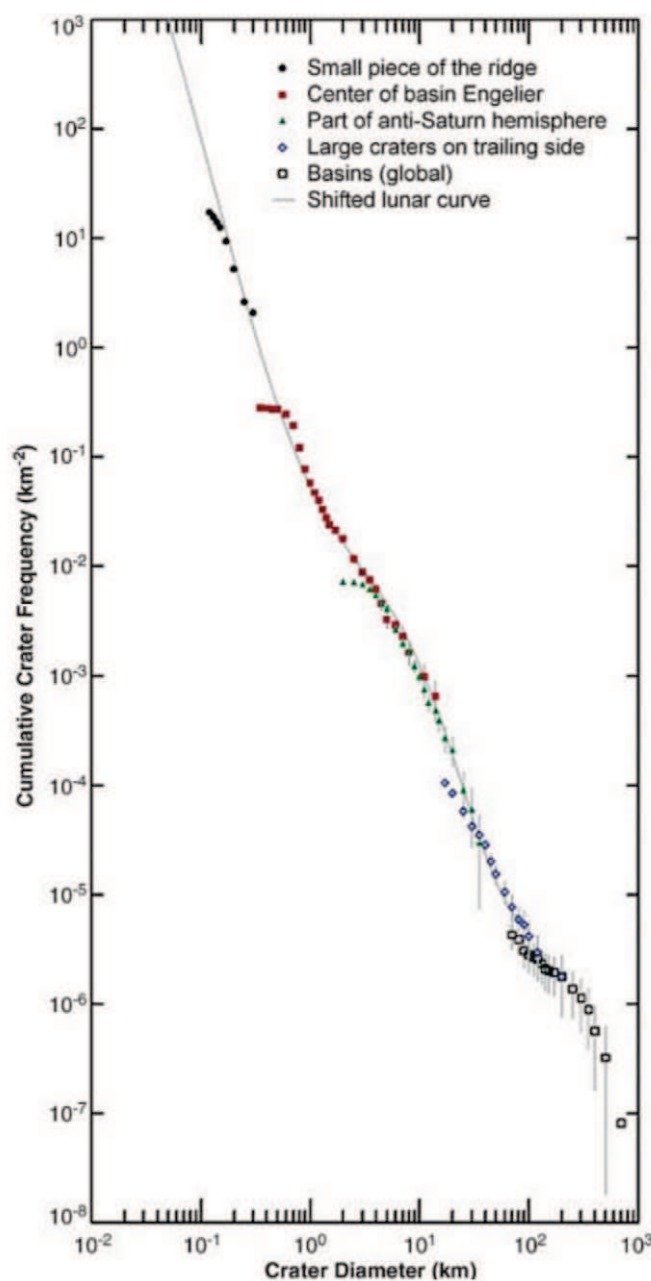
obvious in the images. They are not correlated with the dark terrain; rather, they subdivide even the otherwise (and colorwise) very homogeneous Cassini Regio into two different hues. Similarly, the bright mid-latitude and polar regions on the leading side are redder and darker than their counterparts on the trailing side (figs. S5 and S6).

This hemispheric color pattern suggests an exogenic origin for the color dichotomy. Although rejected as potential causes for the albedo dichotomy, some of the previously proposed hypotheses for the origin of the albedo dichotomy (via ballistic mechanisms) might actually explain the color dichotomy. We reconsider three options: (i) direct impact by interplanetary micrometeoroids (13, 14), (ii) the continuous inflow of reddish dust that originates from the outer saturnian irregular satellites after they are struck by the interplanetary

flux (including macroscopic impacts) (15–19), and (iii) collisions with ejecta formed during a one-time violent impact on Iapetus or another nearby moon (20). The dust in process (i) reaches Iapetus on interplanetary paths, whereas that from processes (ii) and (iii) travels on circumsaturnian orbits. Processes (i) and (ii) would be long-term or ongoing, whereas (iii) would probably have happened early in the history of the solar system.

Saturn's ability to gravitationally focus interplanetary material at Iapetus' orbit is modest (21). Thus, if interplanetary dust darkened and reddened Iapetus' surface as strongly as in mechanism (i), the irregular saturnian moons should also be reddened substantially at visual wavelengths. However, this is not observed; Phoebe is not red (18, 22). Furthermore, closer to Saturn, the dust flux should increase because of gravitational focusing, either

**Fig. 3.** Cumulative crater size-frequency distribution of Iapetus, combining five individual measurements that are identified by different colors and symbols. Crater sizes of  $\sim 300$  to  $\sim 600$  m are missing because no area was observed at sufficient resolution that is young enough to show this part of the production function. Data-point roll-overs at the smaller sizes in each sample occur because of the limited spatial resolution of each of the measured images. The thin line shows the crater size-frequency distribution of Earth's Moon (40), shifted by a factor of  $\sim 5$  toward smaller craters, for comparison. Image IDs from our data: N1568126582, N1568158175, and W1568128142 from the targeted flyby; Iapetus basemap (41).





strongly reddening and darkening Mimas' leading side or, alternatively, its trailing side and poles if plasma drag determines the paths of dust within the saturnian magnetosphere (23). Again, neither is observed (24). Therefore, interplanetary material is not a likely cause of Iapetus' color dichotomy.

An early giant impact [explanation (iii)] that created a debris swarm to later produce the color dichotomy also seems improbable. Cassini images show that Iapetus' leading side is uniformly dark at low latitudes. Without a darkening process that continues at least until the time when the youngest medium-sized crater in Cassini Regio was emplaced, there is no obvious reason why such youthful craters like Malun (fig. S7) should have darkened as well, and Iapetus should exhibit some larger bright-floor and bright-ray craters deep within Cassini Regio. Yet, Cassini images do not show any hints of this.

In hypothesis (ii), impact ejecta lost from the outer satellites must move inward. Solar-radiation pressure and Poynting-Robertson drag have been found to provide plausible mechanisms to spiral in dust along the warped Laplacian plane toward Iapetus' leading side (16, 17, 19). For the gravity and surface area of an irregular moon, sizes on the order of tens of kilometers might provide the optimal dimensions (25). Phoebe (214 km) (10) is larger, Ymir (~18 km) is about right, and the other 27 known retrograde irregular moons (estimated

sizes of ~4 to 8 km) (26) are somewhat undersized. Although the nine known prograde irregular moons (~7 to 40 km) fit better in this size range, they are not candidate sources because impacts of prograde dust on prograde Iapetus occur more or less isotropically with ~0 km/s, whereas impacts of retrograde dust occur head-on into the leading side at ~6.5 km/s and are swept up much more efficiently by Iapetus. The probability of collisions into Iapetus might even increase by more than one order of magnitude for particles coming with inclinations >170° (19), and of the dust released from the respective moons, fractions of more than 20% might collide with Iapetus (17, 19). Substantial amounts of retrograde-orbiting debris might also have been produced by collisions of Phoebe and other retrograde moons with several former irregular moons (27, 28). A debris cloud similar to the one that is required for this model to work appears to have recently been found (29).

Another argument for hypothesis (ii) is the appearance of chaotically tumbling Hyperion, the next known satellite interior to Iapetus. Its unusual reddish color and intermediate albedo (with respect to dark Cassini Regio and the bright icy surfaces of the other saturnian moons) might be a result of the same process that formed Iapetus' color dichotomy (30), whereas Titan fully protects the inner moons from outer dust (17). A prediction of this scenario

is that synchronously rotating, so far undetected, hypothetical moons outside Titan's orbit should show a global asymmetry as well.

However, issues remain even with this hypothesis. For instance, it is not known if a few particular moons provide the bulk of the dust or if all contribute similarly and if these moons even produce dust of the appropriate color. Furthermore, the colors of these moons are more or less unknown, as are processes such as dust grain-size selection by radiation effects. Other unanswered questions concern the sputtering physics of the dust, how impact-heating alters the dust's color, possible magnetospheric influences on the dust transport (especially near the midnight side of Saturn), and potential grain-size selection processes, but none of these appears insurmountable at first glance.

Callisto (fig. S8), the outermost regular moon of Jupiter, and Neptune's moon, Triton, do not exhibit anything similar to the Iapetus color dichotomy in Voyager or Galileo data (31, 32). Because Callisto is located deep within the jovian magnetosphere and Triton possesses a thin atmosphere, their situations are very different from Iapetus'. The two atmosphereless regular moons orbiting permanently or temporarily outside the magnetosphere of Uranus are a better comparison. Indeed, Oberon and Titania revealed substantially redder leading versus trailing sides in Voyager 2 images, whereas the inner moons Umbriel, Ariel, and Miranda did not (33). It is plausible to assume that retrograde dust (with respect to the planetocentric system) from the outer Uranian moons coated the leading sides of those moons that are temporarily or permanently orbiting outside the magnetosphere, similar to the formation of the color dichotomy on Iapetus and the reddening of Hyperion in the saturnian system. This comparison also suggests that dust and debris from outer moons is the most likely cause of the color dichotomy on Iapetus.

#### References and Notes

1. C. C. Porco *et al.*, *Space Sci. Rev.* **115**, 363 (2004).
2. [www.geoinf.fu-berlin.de/projekte/cassini/cassini\\_fu\\_iapetus\\_flyby.php](http://www.geoinf.fu-berlin.de/projekte/cassini/cassini_fu_iapetus_flyby.php) (2007).
3. J. D. Cassini, *Journal des Sçavans* **1677** (issue no. VI), 70 (1677).
4. The mean location of the center of Iapetus' leading side (the hemisphere facing the direction of Iapetus' motion) is not at 90.0°W longitude, but rather at 93.5°W because the surface coordinate system is defined so as to place the crater Almeric at 276.0°W (34).
5. See supporting material on Science Online for a detailed description of the age estimations.
6. C. R. Chapman, W. B. McKinnon, in *Satellites*, J. A. Burns, M. S. Matthews, Eds. (Univ. of Arizona Press, Tucson, AZ, 1986), pp. 492–580.
7. G. J. Black, D. B. Campbell, L. M. Carter, S. J. Ostro, *Science* **304**, 553 (2004).
8. S. J. Ostro *et al.*, *Icarus* **183**, 479 (2006).
9. J. R. Spencer, *Icarus* **69**, 297 (1987).
10. C. C. Porco *et al.*, *Science* **307**, 1237 (2005).
11. B. Giese *et al.*, *Icarus* **193**, 359 (2008).
12. J. R. Spencer, T. Denk, *Science* **327**, 432 (2010); published online 10 December 2009 (10.1126/science.1177132).
13. A. F. Cook, F. A. Franklin, *Icarus* **13**, 282 (1970).
14. P. D. Wilson, C. Sagan, *Icarus* **122**, 92 (1996).
15. S. Soter, paper presented at the IAU Colloquium 28, Cornell University, Ithaca, NY, 18 to 21 August 1974.

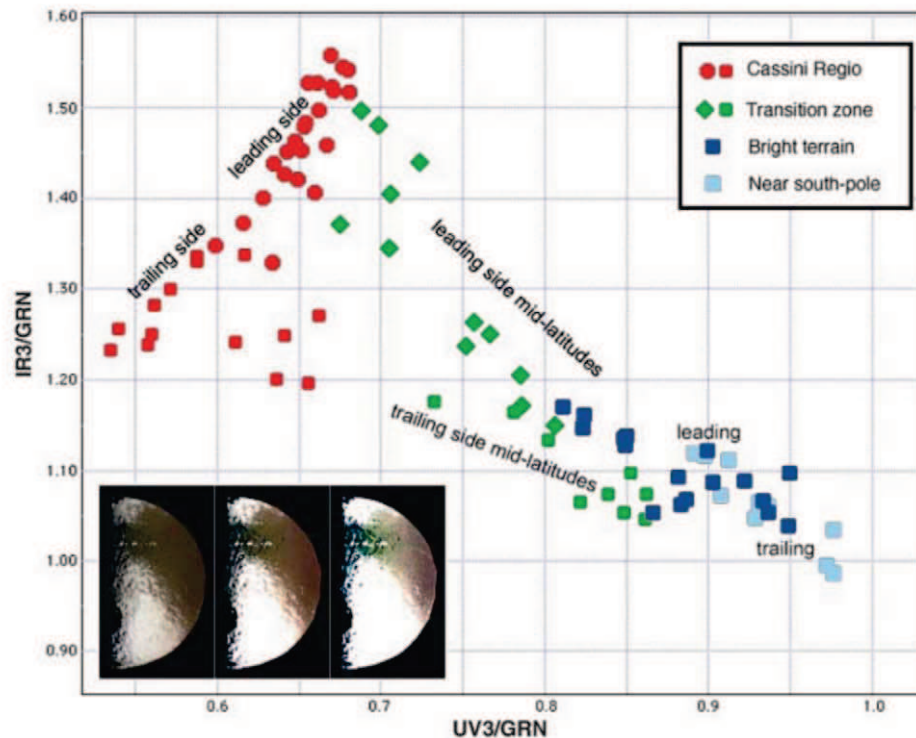


**Fig. 4.** Color-ratio diagram for parts of the anti-Saturn hemisphere of Iapetus, showing the colors of the leading and trailing sides. Each dot represents a slope of a three-color spectrum in a particular, randomly selected location. The left axis displays the long-wavelength ratio [color ratio between images taken in the 953 nm (IR3) and 563 nm (GRN) filters]; the horizontal axis gives the short-wavelength slopes [color ratio between images taken in the 340 nm (UV3) and GRN filters] of the spectra. (Inset) Image from which these color slopes have been measured (image IDs: N1476574148, N1476574185, and N1476574238). (Left) Normal contrast showing the color differences in the bright terrain; (center) enhanced contrast; (right) extreme contrast enhancement, indicating the color differences within the dark terrain.

16. J. A. Burns, P. L. Lamy, S. Soter, *Icarus* **40**, 1 (1979).
17. J. A. Burns, D. P. Hamilton, F. Mignard, S. Soter, in *Physics, Chemistry, and Dynamics of Interplanetary Dust*, ASP Conference Series 104, B. A. S. Gustafson, M. S. Hanner, Eds. (Astronomical Society of the Pacific, San Francisco, 1996), pp. 179–182.
18. B. J. Buratti, M. D. Hicks, K. A. Tryka, M. S. Sittig, R. L. Newburn, *Icarus* **155**, 375 (2002).
19. F. Tosi *et al.*, preprint available at <http://arxiv.org/abs/0902.3591> (2009).
20. Besides Iapetus, Hyperion, Titan, and outer-satellite impacts were suggested; see also (12).
21. Reference (18) mentions an increase of the dust flux by ~20%, whereas (35) finds as much as a factor of 3 for some cases.
22. D. J. Tholen, B. Zellner, *Icarus* **53**, 341 (1983).
23. The leading sides of the moons beyond Mimas and inside Titan should be substantially coated by E-ring particles (24, 36, 37), making them less useful for this argument.
24. B. J. Buratti, J. A. Mosher, T. V. Johnson, *Icarus* **87**, 339 (1990).
25. J. A. Burns *et al.*, *Science* **284**, 1146 (1999).
26. S. S. Sheppard, [www.dtm.ciw.edu/users/sheppard/satellites/satsatdata.html](http://www.dtm.ciw.edu/users/sheppard/satellites/satsatdata.html) (2009).
27. D. Nesvorný, J. L. A. Alvarellos, L. Dones, H. F. Levison, *Astron. J.* **126**, 398 (2003).
28. D. Turrini, F. Marzari, H. Beust, *Mon. Not. R. Astron. Soc.* **391**, 1029 (2008).
29. A. J. Verbiscer, M. F. Skrutskie, D. P. Hamilton, *Nature* **461**, 1098 (2009).
30. This idea was developed in several papers (18, 38, 39), but under the assumption that dust from the outer saturnian moons formed Iapetus' albedo dichotomy.
31. T. V. Johnson *et al.*, *J. Geophys. Res. Solid Earth* **88**, 5789 (1983).
32. T. Denk, R. Jaumann, G. Neukum, in *Lisbon Euroconference Jupiter After Galileo and Cassini*, Abstracts Book 17 to 21 June 2002, Lisbon, Portugal, abstr. no. P-4.1.18, 2002, p. 118.
33. B. J. Buratti, J. A. Mosher, *Icarus* **90**, 1 (1991).
34. M. E. Davies, F. Y. Katayama, *Icarus* **59**, 199 (1984).
35. K. J. Zahnle, P. Schenk, H. Levison, L. Dones, *Icarus* **163**, 263 (2003).
36. K. D. Pang, C. C. Voge, J. W. Rhoads, J. M. Ajello, *J. Geophys. Res. Solid Earth* **89**, 9459 (1984).
37. D. P. Hamilton, J. A. Burns, *Science* **264**, 550 (1994).
38. P. C. Thomas, J. Veverka, *Icarus* **64**, 414 (1985).
39. K. S. Jarvis, F. Vilas, S. M. Larson, M. J. Gaffey, *Icarus* **146**, 125 (2000).
40. G. Neukum, B. A. Ivanov, in *Hazards Due to Comets and Asteroids*, T. Gehrels, Ed. (Univ. of Arizona Press, Tucson, AZ, 1994), pp. 359–416.
41. T. Roatsch *et al.*, *Planet. Space Sci.* **57**, 83 (2009).
42. We acknowledge the individuals at CICLOPS (at the Space Science Institute in Boulder, CO) and JPL (Pasadena, CA), as well as the members and associates of the Imaging Team for the successful conduct of the ISS experiment onboard the Cassini spacecraft. This paper is dedicated to Steve Ostro, whose work helped considerably to explain the nature of Iapetus' dark terrain. This work has been funded by the German Aerospace Center (DLR) and NASA/JPL.

**Supporting Online Material** [www.sciencemag.org/cgi/content/full/science.1177088/DC1](http://www.sciencemag.org/cgi/content/full/science.1177088/DC1) SOM Text Figs. S1 to S8 Tables S1 and S2 References and Notes

1 June 2009; accepted 1 December 2009  
Published online 10 December 2009;  
10.1126/science.1177088  
Include this information when citing this paper.

# Rules for Biologically Inspired Adaptive Network Design

Atsushi Tero,<sup>1,2</sup> Seiji Takagi,<sup>1</sup> Tetsu Saigusa,<sup>3</sup> Kentaro Ito,<sup>1</sup> Dan P. Bebber,<sup>4</sup> Mark D. Fricker,<sup>4</sup> Kenji Yumiki,<sup>5</sup> Ryo Kobayashi,<sup>5,6</sup> Toshiyuki Nakagaki<sup>1,6\*</sup>

Transport networks are ubiquitous in both social and biological systems. Robust network performance involves a complex trade-off involving cost, transport efficiency, and fault tolerance. Biological networks have been honed by many cycles of evolutionary selection pressure and are likely to yield reasonable solutions to such combinatorial optimization problems. Furthermore, they develop without centralized control and may represent a readily scalable solution for growing networks in general. We show that the slime mold *Physarum polycephalum* forms networks with comparable efficiency, fault tolerance, and cost to those of real-world infrastructure networks—in this case, the Tokyo rail system. The core mechanisms needed for adaptive network formation can be captured in a biologically inspired mathematical model that may be useful to guide network construction in other domains.

Transport networks are a critical part of the infrastructure needed to operate a modern industrial society and facilitate efficient movement of people, resources, energy, and information. Despite their importance, most networks have emerged without clear global design principles and are constrained by the priorities imposed at their initiation. Thus, the main motivation historically was to achieve high transport efficiency at reasonable cost, but with correspondingly less emphasis on making systems tolerant to interruption or failure. Introducing robustness inevitably requires additional redundant pathways that are not cost-effective in the short term. In recent years, the spectacular failure of key infrastructure

such as power grids (1, 2), financial systems (3, 4), airline baggage-handling systems (5), and railway networks (6), as well as the predicted vulnerability of systems such as information networks (7) or supply networks (8) to attack, have highlighted the need to develop networks with greater intrinsic resilience.

Some organisms grow in the form of an interconnected network as part of their normal foraging strategy to discover and exploit new resources (9–12). Such systems continuously adapt to their environment and must balance the cost of producing an efficient network with the consequences of even limited failure in a competitive world. Unlike anthropogenic infrastructure systems, these biological networks have been subjected to successive rounds of evolutionary selection and are likely to have reached a point at which cost, efficiency, and resilience are appropriately balanced. Drawing inspiration from biology has led to useful approaches to problem-solving such as neural networks, genetic algorithms, and efficient search routines developed from ant colony optimization algorithms (13). We exploited the slime mold *Physarum polycephalum* to develop a biologically inspired model for adaptive network development.

*Physarum* is a large, single-celled amoeboid organism that forages for patchily distributed food sources. The individual plasmodium initially explores with a relatively contiguous foraging margin to maximize the area searched. However, behind the margin, this is resolved into a tubular network linking the discovered food sources through direct connections, additional intermediate junctions (Steiner points) that reduce the overall length of the connecting network, and the formation of occasional cross-links that improve overall transport efficiency and resilience (11, 12). The growth of the plasmodium is influenced by the characteristics of the substrate (14) and can be constrained by physical barriers (15) or influenced by the light regime (16), facilitating experimental investigation of the rules underlying network formation. Thus, for example, *Physarum* can find the shortest path through a maze (15–17) or connect different arrays of food sources in an efficient manner with low total length (TL) yet short average minimum distance (MD) between pairs of food sources (FSs), with a high degree of fault tolerance (FT) to accidental disconnection (11, 18, 19). Capturing the essence of this system in simple rules might be useful in guiding the development of decentralized networks in other domains.

We observed *Physarum* connecting a template of 36 FSs that represented geographical locations of cities in the Tokyo area, and compared the result with the actual rail network in Japan. The *Physarum* plasmodium was allowed to grow from Tokyo and initially filled much of the available land space, but then concentrated on FSs by thinning out the network to leave a subset of larger, interconnecting tubes (Fig. 1). An alternative protocol, in which the plasmodium was allowed to extend fully in the available space and the FSs were then presented simultaneously, yielded similar results. To complete the network formation, we allowed any excess volume of plasmodium to

<sup>1</sup>Research Institute for Electronic Science, Hokkaido University, Sapporo 060-0812, Japan. <sup>2</sup>PRESTO, JST, 4-1-8 Honcho, Kawaguchi, Saitama, Japan. <sup>3</sup>Graduate School of Engineering, Hokkaido University, Sapporo 060-8628, Japan. <sup>4</sup>Department of Plant Sciences, University of Oxford, Oxford OX1 3RB, UK. <sup>5</sup>Department of Mathematical and Life Sciences, Hiroshima University, Higashi-Hiroshima 739-8526, Japan. <sup>6</sup>JST, CREST, 5 Sanbancho, Chiyoda-ku, Tokyo, 102-0075, Japan.

\*To whom correspondence should be addressed. E-mail: [nakagaki@es.hokudai.ac.jp](mailto:nakagaki@es.hokudai.ac.jp)



accumulate on a large FS outside the arena (LFS in Fig. 2A).

A range of network solutions were apparent in replicate experiments (compare Fig. 2A with Fig. 1F); nonetheless, the topology of many *Physarum* networks bore similarity to the real rail network (Fig. 2D). Some of the differences may relate to geographical features that constrain the rail network, such as mountainous terrain or lakes. These constraints were imposed on the *Physarum* network by varying the intensity of illumination, as the plasmodium avoids bright light (16). This yielded networks (Fig. 2, B and C) with greater visual congruence to the real rail network (Fig. 2D). Networks were also compared with the minimal spanning tree (MST, Fig. 2E), which is the shortest possible network connecting all the city positions, and various derivatives with increasing numbers of cross-links added (e.g., Fig. 2F), culminating in a fully connected Delaunay triangulation, which represents the maximally connected network linking all the cities.

The performance of each network was characterized by the cost (TL), transport efficiency (MD), and robustness (FT), normalized to the corresponding value for the MST to give  $TL_{MST}$ ,  $MD_{MST}$ , and  $FT_{MST}$ . The TL of the Tokyo rail network was greater than the MST by a factor of  $\sim 1.8$  (i.e.,  $TL_{MST} \approx 1.8$ ), whereas the average  $TL_{MST}$  for *Physarum* was  $1.75 \pm 0.30$  ( $n = 21$ ). Illuminated networks gave slightly better clustering around the value for the rail network (Fig. 3A). For comparison, the Delaunay triangulation was longer than the MST by a factor of  $\sim 4.6$ . Thus, the cost of the solutions found by *Physarum* closely matched that of the rail network, with about 30% of the maximum possible number of links in place. The transport performance of the two networks was also similar, with  $MD_{MST}$  of  $0.85$  and  $0.85 \pm 0.04$  for the rail network and the *Physarum* networks, respectively. However, the *Physarum* networks achieved this with marginally lower overall cost (Fig. 3A).

The converse was true for the fault tolerance ( $FT_{MST}$ ) in which the real rail network showed marginally better resilience, close to the lowest level needed to give maximum tolerance to a single random failure. Thus, only 4% of faults in the rail network would lead to isolation of any part, whereas  $14 \pm 4\%$  would disconnect the illuminated *Physarum* networks, and  $20 \pm 13\%$  would disconnect the unconstrained *Physarum* networks. In contrast, simply adding additional links to the MST to improve network performance resulted in networks with poor fault tolerance (Fig. 3B).

The trade-off between fault tolerance and cost was captured in a single benefit-cost measure, expressed as the ratio of  $FT/TL_{MST} = \alpha$ . In general, the *Physarum* networks and the rail network had a benefit/cost ratio of  $\sim 0.5$  for any given  $TL_{MST}$  (Fig. 3B). The relationship between different  $\alpha$  values and transport efficiency (Fig. 3C) highlighted the similarity in aggregate behavior of the *Physarum* network when considering all three performance measures ( $MD_{MST}$ ,  $TL_{MST}$ , and  $FT_{MST}$ ).

**Fig. 1.** Network formation in *Physarum polycephalum*. (A) At  $t = 0$ , a small plasmodium of *Physarum* was placed at the location of Tokyo in an experimental arena bounded by the Pacific coastline (white border) and supplemented with additional food sources at each of the major cities in the region (white dots). The horizontal width of each panel is 17 cm. (B to F) The plasmodium grew out from the initial food source with a contiguous margin and progressively colonized each of the food sources. Behind the growing margin, the spreading mycelium resolved into a network of tubes interconnecting the food sources.

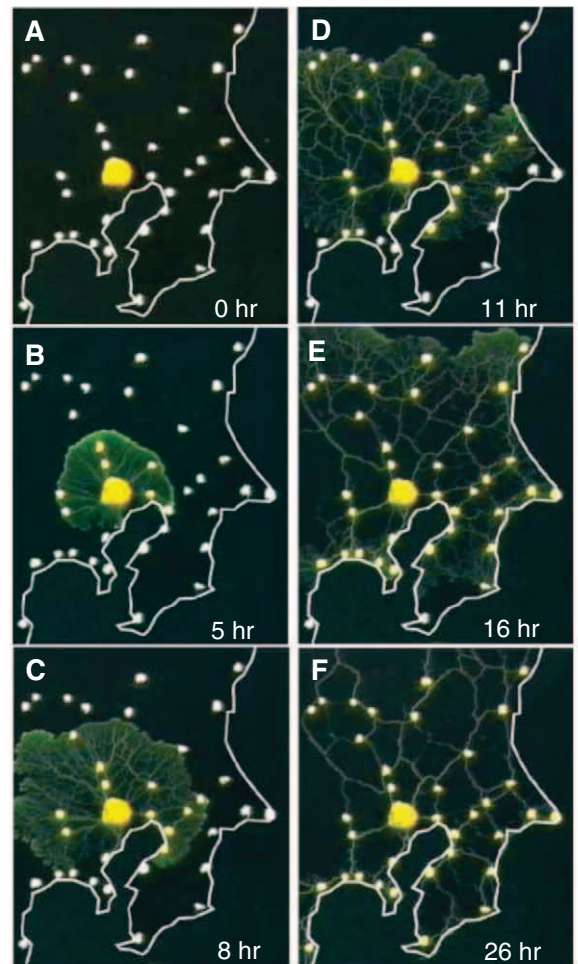


**Fig. 2.** Comparison of the *Physarum* networks with the Tokyo rail network. (A) In the absence of illumination, the *Physarum* network resulted from even exploration of the available space. (B) Geographical constraints were imposed on the developing *Physarum* network by means of an illumination mask to restrict growth to more shaded areas corresponding to low-altitude regions. The ocean and inland lakes were also given strong illumination to prevent growth. (C and D) The resulting network (C) was compared with the rail network in the Tokyo area (D). (E and F) The minimum spanning tree (MST) connecting the same set of city nodes (E) and a model network constructed by adding additional links to the MST (F).

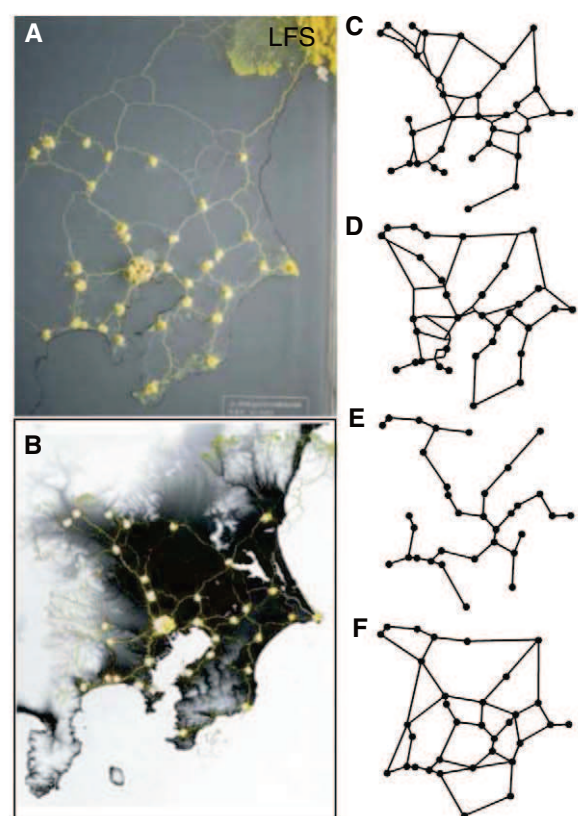
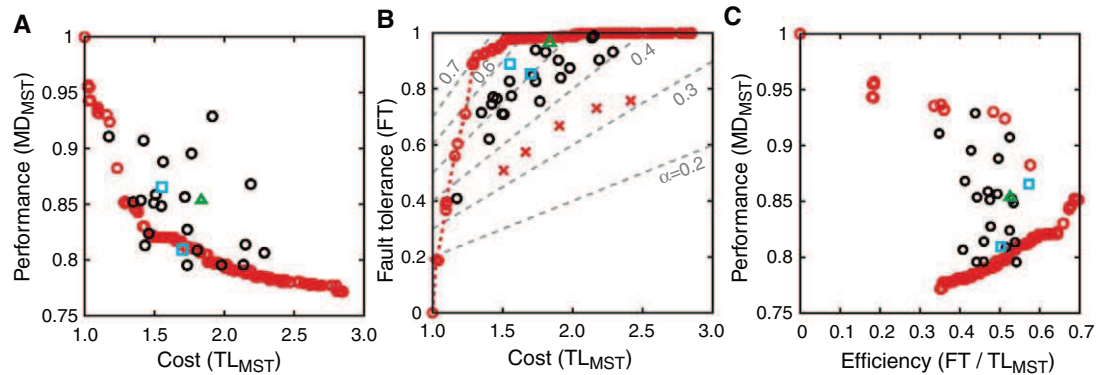
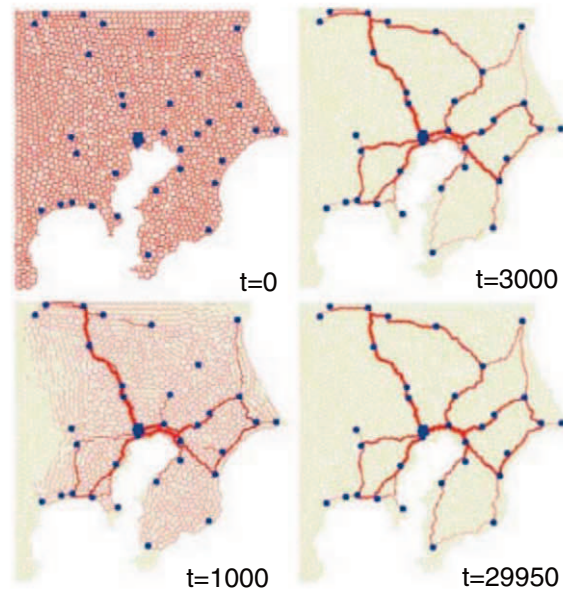


**Fig. 3.** Transport performance, resilience, and cost for *Physarum* networks, model simulations, and the real rail networks. (A) Transport performance of each network, measured as the minimum distance between all pairs of nodes, normalized to the MST ( $MD_{MST}$ ) and plotted against the total length of the network normalized by the MST ( $TL_{MST}$ ) as a measure of cost. Black circles and blue squares represent results obtained from *Physarum* in the absence or presence of illumination, respectively. The green triangle represents the actual rail network. Open red circles represent simulation results as  $I_0$  was varied from 0.20 to 7.19 at a fixed  $\gamma$  ( $= 1.80$ ) and initial random fluctuations of  $D_{ij}$ . (B) Fault tolerance (FT), measured as the probability of disconnecting part of the network with failure of a single link. Crosses represent results for reference networks; other



symbols as in (A). Different values of the benefit/cost ratio,  $\alpha = FT/TL_{MST}$ , are shown as dashed lines. (C) Relationship between  $MD_{MST}$  and  $\alpha$ . Although the overall performance of the experiment and that of the real rail network are clustered together, the simulation model achieves better fault tolerance for the same transport efficiency.

**Fig. 4.** Network dynamics for the simulation model. In this typical time course for evolution of the simulation, time ( $t$ ) is shown in arbitrary units; cities are blue dots. Each city was modeled as a single FS, apart from Tokyo, which was an aggregate of seven FSs to match the importance of Tokyo as the center of the region. At the start ( $t = 0$ ), the available space was populated with a finely meshed network of thin tubes. Over time, many of these tubes died out, whilst a limited number of tubes became selectively thickened to yield a stable, self-organized solution.  $\gamma = 1.80$ ,  $I_0 = 2.00$ .



The rail network was embedded in the cluster of results for the *Physarum* networks with a marginally higher  $\alpha$  value for the same transport efficiency (Fig. 3C).

Overall, we conclude that the *Physarum* networks showed characteristics similar to those of the rail network in terms of cost, transport efficiency, and fault tolerance. However, the *Physarum* networks self-organized without centralized control or explicit global information by a process of selective reinforcement of preferred routes and simultaneous removal of redundant connections.

We developed a mathematical model for adaptive network construction to emulate this behavior, based on feedback loops between the thickness of each tube and internal protoplasmic flow (18–22) in which high rates of streaming stimulate an increase in tube diameter, whereas tubes tend to decline at low flow rates (23). The initial shape of a plasmodium is represented by a randomly meshed lattice with a relatively fine spacing, as shown in Fig. 4 ( $t = 0$ ). The edges represent plasmodial

tubes in which protoplasm flows, and nodes are junctions between tubes. Suppose that the pressures at nodes  $i$  and  $j$  are  $p_i$  and  $p_j$ , respectively, and that the two nodes are connected by a cylinder of length  $L_{ij}$  and radius  $r_{ij}$ . Assuming that flow is laminar and follows the Hagen-Poiseuille equation, the flux through the tube is

$$Q_{ij} = \frac{\pi r_{ij}^4 (p_i - p_j)}{8\eta L_{ij}} = \frac{D_{ij} (p_i - p_j)}{L_{ij}} \quad (1)$$

where  $\eta$  is the viscosity of the fluid, and  $D_{ij} = \pi r_{ij}^4 / 8\eta$  is a measure of the conductivity of the tube. As the length  $L_{ij}$  is a constant, the behavior of the network is described by the conductivities,  $D_{ij}$ , of the edges.

At each time step, a random FS (node 1) is selected to drive flow through the network, so the flux includes a source term  $\sum_j Q_{1j} = I_0$ . A second random FS is chosen as a sink (node 2) with a corresponding withdrawal of  $I_0$  such that  $\sum_j Q_{2j} = -I_0$ . As the amount of fluid must be conserved,

the inflow and outflow at each internal node must balance so that  $i$  ( $i \neq 1, 2$ ),  $\sum_j Q_{ij} = 0$ . Thus, for a given set of conductivities and selected source and sink nodes, the flux through each of the network edges can be computed.

To accommodate the adaptive behavior of the plasmodium, the conductivity of each tube evolves according to  $dD_{ij}/dt = f(|Q_{ij}|) - D_{ij}$ . The first term on the right side describes the expansion of tubes in response to the flux. The second term represents the rate of tube constriction, so that in the absence of flow the tubes will gradually disappear. The functional form  $f(|Q|)$  is given by  $f(|Q|) = |Q|^\gamma / (1 + |Q|^\gamma)$ , which describes a sigmoidal response where  $\gamma$  is a parameter that controls the nonlinearity of feedback ( $\gamma > 0$ ). A typical simulation result with  $I_0 = 2$  and  $\gamma = 1.8$  (Fig. 4) gave a network with features similar to those of both the *Physarum* system and the rail network (Fig. 2, C and D, respectively).

In general, increasing  $I_0$  promoted the formation of alternative routes that improved performance by reducing  $MD_{MST}$  and made the network more fault-tolerant, but with increased cost (Fig. 3, A to C, and fig. S11). Low values of  $\gamma$  also gave a greater degree of cross-linking with an increased number of Steiner points (fig. S2, A and B). Conversely, decreasing  $I_0$  (fig. S1A) or increasing  $\gamma$  (fig. S2I) drove the system toward a low-cost MST (Fig. 2E), but with an inevitable decrease in resilience (Fig. 3B). The final network solution also depended slightly on the stochastic variation assigned to the starting values of  $D_{ij}$ . Judicious selection of specific parameter combinations ( $I_0 = 0.20$ ,  $\gamma = 1.15$ ) yielded networks with remarkably similar topology and metrics to the Tokyo rail network (fig. S2B). However, by increasing  $I_0$  to 2 and  $\gamma$  to 1.8, the simulation model also achieved a benefit/cost ratio ( $\alpha = FT/TL_{MST}$ ) that was better than those of the rail or *Physarum* networks, reaching a value of 0.7 with an almost identical transport efficiency of 0.85 (Fig. 3C). Conversely, the consequence of the increased  $TL_{MST}$  observed in the rail or *Physarum* networks would be to confer greater resilience to



multiple simultaneous failures at the expense of increased cost, rather than tolerance to a single disconnection that is evaluated by  $FT_{MST}$ .

Our biologically inspired mathematical model can capture the basic dynamics of network adaptability through iteration of local rules and produces solutions with properties comparable to or better than those of real-world infrastructure networks. Furthermore, the model has a number of tunable parameters that allow adjustment of the benefit/cost ratio to increase specific features, such as fault tolerance or transport efficiency, while keeping costs low. Such a model may provide a useful starting point to improve routing protocols and topology control for self-organized networks such as remote sensor arrays, mobile ad hoc networks, or wireless mesh networks (24).

#### References and Notes

1. R. Albert, I. Albert, G. Nakarado, *Phys. Rev. E* **69**, 025103R (2004).
2. R. V. Solé, M. Rosas-Casals, B. Corominas-Murtra, S. Valverde, *Phys. Rev. E* **77**, 026102 (2008).
3. R. M. May, S. Levin, G. Sugihara, *Nature* **451**, 893 (2008).
4. J. Kambhu, S. Weidman, N. Krishnan, *Econ. Policy Rev.* **13**, 1 (2007).
5. House of Commons Transport Committee, *The Opening of Heathrow Terminal 5 HC 543* (Stationery Office, London, 2008).
6. *Train Derailment at Hatfield* (Independent Investigation Board, Office of Rail Regulation, London, 2006).
7. R. Albert, H. Jeong, A.-L. Barabási, *Nature* **406**, 378 (2000).
8. R. Carvalho *et al.*, <http://arxiv.org/abs/0903.0195> (2009).
9. D. Bebb, J. Hynes, P. Darrah, L. Boddy, M. Fricker, *Proc. R. Soc. London Ser. B* **274**, 2307 (2007).
10. J. Buhl *et al.*, *Behav. Ecol. Sociobiol.* **63**, 451 (2009).
11. T. Nakagaki, H. Yamada, M. Hara, *Biophys. Chem.* **107**, 1 (2004).
12. T. Nakagaki, R. Kobayashi, Y. Nishiura, T. Ueda, *Proc. R. Soc. London Ser. B* **271**, 2305 (2004).
13. A. Colomi *et al.*, *Int. Trans. Oper. Res.* **3**, 1 (1996).
14. A. Takamatsu, E. Takaba, G. Takizawa, *J. Theor. Biol.* **256**, 29 (2009).
15. T. Nakagaki, H. Yamada, Á. Tóth, *Nature* **407**, 470 (2000).
16. T. Nakagaki *et al.*, *Phys. Rev. Lett.* **99**, 068104 (2007).
17. T. Nakagaki, H. Yamada, Á. Tóth, *Biophys. Chem.* **92**, 47 (2001).
18. A. Tero, K. Yumiki, R. Kobayashi, T. Saigusa, T. Nakagaki, *Theory Biosci.* **127**, 89 (2008).
19. T. Nakagaki, R. Guy, *Soft Matter* **4**, 57 (2008).
20. T. Nakagaki, T. Saigusa, A. Tero, R. Kobayashi, in *Topological Aspects of Critical Systems and Networks: Proceedings of the International Symposium*, K. Yakubo *et al.*, Eds. (World Scientific, Singapore, 2007), pp. 94–100.
21. A. Tero, R. Kobayashi, T. Nakagaki, *J. Theor. Biol.* **244**, 553 (2007).
22. A. Tero, R. Kobayashi, T. Nakagaki, *Physica A* **363**, 115 (2006).
23. T. Nakagaki, H. Yamada, T. Ueda, *Biophys. Chem.* **84**, 195 (2000).
24. I. Akyildiz, X. Wang, W. Wang, *Comput. Netw.* **47**, 445 (2005).
25. Supported by MEXT KAKENHI grants 18650054 and 20300105, Human Frontier Science Program grant RGP51/2007, EU Framework 6 contract 12999 (NEST), and NERC grant A/S/882.

**Supporting Online Material** [www.sciencemag.org/cgi/content/full/327/5964/439/DC1](http://www.sciencemag.org/cgi/content/full/327/5964/439/DC1) Figs. S1 and S2

17 June 2009; accepted 20 November 2009

10.1126/science.1177894

# Measurement of Universal Thermodynamic Functions for a Unitary Fermi Gas

Munekazu Horikoshi,<sup>1\*</sup> Shuta Nakajima,<sup>2</sup> Masahito Ueda,<sup>1,2</sup> Takashi Mukaiyama<sup>1,3</sup>

Thermodynamic properties of matter generally depend on the details of interactions between its constituent parts. However, in a unitary Fermi gas where the scattering length diverges, thermodynamics is determined through universal functions that depend only on the particle density and temperature. By using only the general form of the equation of state and the equation of force balance, we measured the local internal energy of the trapped gas as a function of these parameters. Other universal functions, such as those corresponding to the Helmholtz free energy, chemical potential, and entropy, were calculated through general thermodynamic relations. The critical parameters were also determined at the superfluid transition temperature. These results apply to all strongly interacting fermionic systems, including neutron stars and nuclear matter.

**D**egenerate two-component Fermi systems with large scattering lengths are of great interest in diverse settings such as neutron stars (1–3), quark-gluon plasma (4), high critical temperature ( $T_c$ ) superconductors (5), and resonantly interacting cold Fermi gases near Feshbach resonances (6–18). Even though the temperature of these systems ranges widely from  $10^{-7}$  K for cold atoms to more than  $10^{12}$  K for quark-gluon plasma, they exhibit remarkably similar behavior at the unitarity limit. As the scattering length

diverges, the universal thermodynamics that describes these systems depends only on the particle density,  $n$ , and temperature,  $T$ . This assumption is referred to as the “universal hypothesis (UH)” (19, 20).

In the context of cold atoms, two fermionic alkali elements,  $^6\text{Li}$  and  $^{40}\text{K}$ , have been successfully used to explore the physics of the unitarity limit (6–18). This was possible because of the tunability of the fermion-fermion interaction and the stability of ultracold fermionic gases near Feshbach resonances (21, 22). Recently, a comparison of the entropy-energy relations extracted from experimental measurements on both  $^6\text{Li}$  and  $^{40}\text{K}$  provided evidence of universal thermodynamics at the unitarity limit (23). However, because a unitary Fermi gas is realized in a harmonic trap, the inhomogeneous atomic density distribution causes the thermodynamic quantities to be position-dependent.

Therefore, integration over the entire cloud provides only indirect information on the relationship between each individual thermodynamic quantity and the particle density. To determine the universal thermodynamic functions using such an inhomogeneous system, the thermodynamic

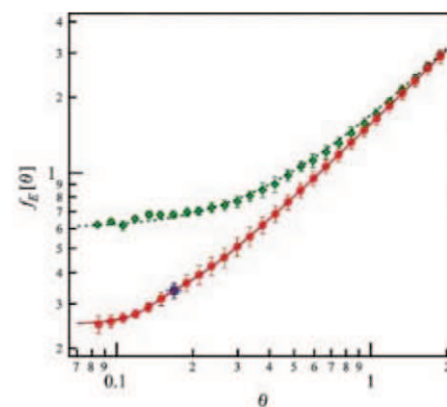


**Fig. 1.** Universal function of the internal energy. Universal functions of the internal energy ( $f_E[0] = E/N\epsilon_F$ ) plotted for an ideal Fermi gas (green diamonds) and for a unitary Fermi gas (red circles). The data are averaged over a suitable temperature range. The error bars show the data spread of one standard deviation originating mainly from statistical errors. The green dashed curve shows the theoretical universal function for the ideal Fermi gas, whereas the red solid curve shows the measured universal function for the unitary Fermi gas. The red solid curve is obtained by fitting the data represented by red circles so that it levels off at  $f_E[0] = 3(1 + \beta)/5 = 0.25$  at the low-temperature limit, where  $\beta$  is the universal parameter (15), and approaches the theoretical value obtained at the high-temperature limit (20). The blue square corresponds to the critical point.

<sup>1</sup>Japan Science and Technology Agency, Exploratory Research for Advanced Technology (ERATO), Macroscopic Quantum Control Project, 2-11-16 Yayoi, Bunkyo-ku, Tokyo 113-8656, Japan.

<sup>2</sup>Department of Physics, University of Tokyo, 7-3-1 Hongo, Bunkyo-ku, Tokyo 113-0033, Japan. <sup>3</sup>Center for Frontier Science and Engineering, University of Electro-Communications, 1-5-1 Chofugaoka, Chofu, Tokyo 182-8585, Japan.

\*To whom correspondence should be addressed. E-mail: hori@sogo.t.u-tokyo.ac.jp

quantities together with the density and temperature must be measured locally.

According to the UH (19, 20), all thermodynamic quantities are universal functions of the Fermi energy,  $\epsilon_F(n) = \hbar^2(3\pi^2n)^{2/3}/2m$ , and the reduced temperature, which is defined as the ratio of the temperature to the Fermi energy,  $\theta(n, T) = k_B T / \epsilon_F(n)$ . Here,  $\hbar$  is Planck's constant divided by  $2\pi$ ,  $m$  is the atomic mass, and  $k_B$  is the Boltzmann constant. Therefore, the internal energy,  $E$ ; Helmholtz free energy,  $F$ ; chemical potential,  $\mu$ ; and entropy,  $S$ , can be expressed simply by  $E = N\epsilon_F(n)f_E[\theta]$ ,  $F = N\epsilon_F(n)f_F[\theta]$ ,  $\mu = \epsilon_F(n)f_\mu[\theta]$ , and  $S = Nk_B f_S[\theta]$ , respectively. Here,  $f_E[\theta]$ ,  $f_F[\theta]$ ,  $f_\mu[\theta]$ , and  $f_S[\theta]$  are the dimensionless universal functions of the reduced temperature,  $\theta$  (11), and  $N$  is the total number of atoms. Because the universal functions are mutually related through thermodynamic relations, it is sufficient to know one of them to reproduce the others.

To determine the universal functions, we start by noting that the local pressure,  $p$ , of a trapped gas is related to the internal energy density,  $\mathcal{E} = n\epsilon_F(n)f_E[\theta]$ , through the equation of state,  $p = 2\mathcal{E}/3$ , at any temperature at the unitarity limit (11, 19). In thermal equilibrium, the mechanical equilibrium is determined by

the balance between the internal force exerted by the gas pressure and the external force attributed to the trapping potential,  $V_{\text{trap}}$  (11), at position  $r$ :

$$\nabla p(r) + n(r)\nabla V_{\text{trap}}(r) = 0 \quad (1)$$

Therefore, the spatial density profiles can be used to determine the local pressure. We solve Eq. 1 to determine the local pressure,  $p(r)$ , from the measured atomic density distribution and the trapping potential. By relating  $f_E(r) = 3p(r)/2n(r)\epsilon_F(r)$  to the reduced temperature,  $\theta(r)$ , at the same position, we can determine the universal function,  $f_E[\theta]$ , in a model-independent manner. In fact, we can determine  $f_E[\theta]$  over a wide range of temperatures from a single density profile because it contains information on the universal function ranging from  $f_E[\theta_0]$  at the cloud center to  $f_E[\infty]$  at the edge of the cloud; here,  $\theta_0$  is the reduced temperature at the center of the cloud.

We prepared a degenerate unitary Fermi gas containing the two lowest spin states of  $^6\text{Li}$  atoms in an optical dipole trap at the Feshbach-resonance magnetic field of 834 G (22). The temperature was controlled by the

final trap depth of the forced evaporative cooling process, and the gas was held until the system reaches thermal equilibrium. The trap frequencies in the  $x$ ,  $y$ , and  $z$  directions of the trapping potential,  $V_{\text{trap}}(\mathbf{r})$ , were precisely measured at several trap depths, and the measured values were interpolated over the entire range of trap depths to determine accurate trap frequencies at each point. The atomic density distribution,  $n(r)$ , was determined from the absorption image taken perpendicular to the axial direction after a 3-ms free expansion at the same magnetic field. From the image, we constructed the in situ three-dimensional atomic density distribution under the assumption of the local density approximation (LDA) [see (24) for a discussion on the validity of LDA], and this distribution was used to determine the universal function (25). The temperature,  $T$ , was determined by using the thermometry applicable to a trapped unitary Fermi gas (15), which allowed us to estimate  $T/T_{F,\text{trap}}$  from  $E_{\text{total}}/E_{F,\text{trap}}$ . Here,  $E_{F,\text{trap}} = k_B T_{F,\text{trap}} = \hbar\bar{\omega}(3N)^{1/3}$  is the Fermi energy in the trap with  $\bar{\omega}$  being the geometric mean of the trap frequencies.  $E_{\text{total}} = 3m\omega_z^2\langle z^2 \rangle$  is the total energy per particle (11), where  $\omega_z$  is the axial trap frequency and  $\langle z^2 \rangle$  is the axial mean square size of the trapped gas. The temperature,  $T$ , is obtained by multiplying the given  $T/T_{F,\text{trap}}$  by  $T_{F,\text{trap}}$ .

To check the validity of our method, we first applied it to an ideal Fermi gas to determine its thermodynamic functions. The thermodynamics of an ideal Fermi gas can also be described by universal functions (different from those of a unitary gas); the equation of state,  $p = 2\mathcal{E}/3$ , and Eq. 1 still hold. We took 50 profiles at 526 G, where the scattering length is zero, and analyzed them according to the procedure described above. Figure 1 plots the experimentally obtained thermodynamic function of the internal energy for an ideal Fermi gas,  $f_E^{\text{ideal}}[\theta]$  (green diamonds), with the theoretical curve superimposed (dashed green curve). They are in close agreement, which indicates that we have successfully determined the thermodynamic function for the ideal Fermi gas from the atomic density distribution.

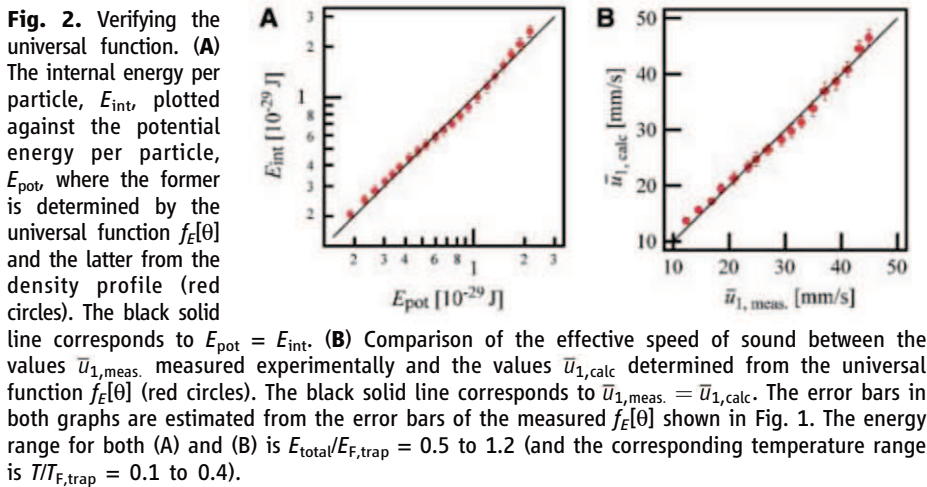


Fig. 2. Verifying the universal function. (A) The internal energy per particle,  $E_{\text{int}}$ , plotted against the potential energy per particle,  $E_{\text{pot}}$ , where the former is determined by the universal function  $f_E[\theta]$  and the latter from the density profile (red circles). The black solid line corresponds to  $E_{\text{pot}} = E_{\text{int}}$ . (B) Comparison of the effective speed of sound between the values  $\bar{u}_{1,\text{meas}}$  measured experimentally and the values  $\bar{u}_{1,\text{calc}}$  determined from the universal function  $f_E[\theta]$  (red circles). The black solid line corresponds to  $\bar{u}_{1,\text{meas}} = \bar{u}_{1,\text{calc}}$ . The error bars in both graphs are estimated from the error bars of the measured  $f_E[\theta]$  shown in Fig. 1. The energy range for both (A) and (B) is  $E_{\text{total}}/E_{F,\text{trap}} = 0.5$  to 1.2 (and the corresponding temperature range is  $T/T_{F,\text{trap}} = 0.1$  to 0.4).

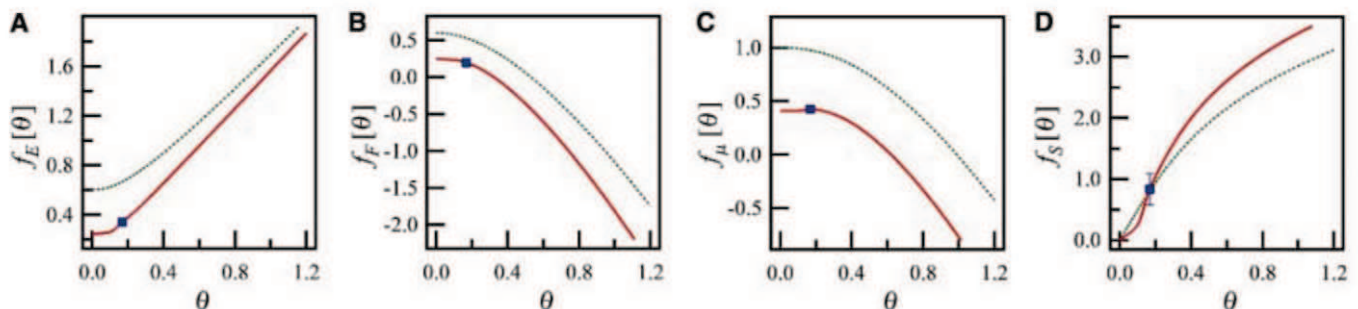
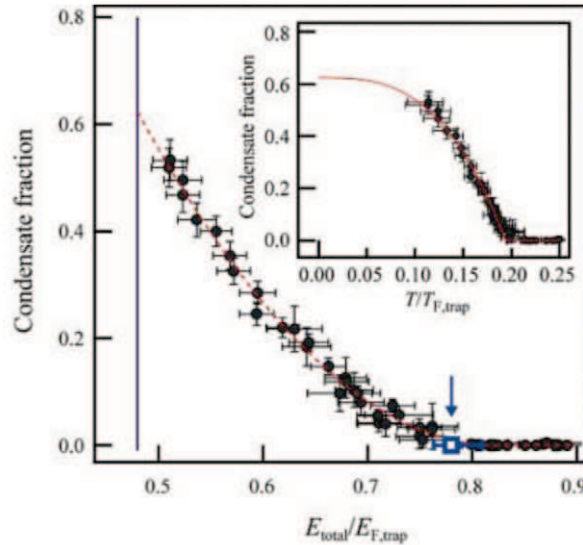


Fig. 3. Various universal functions. (A) Experimentally determined universal function of the internal energy and the derived universal functions for (B) Helmholtz free energy, (C) chemical potential, and (D)

entropy. The red solid (green dashed) curve shows the universal functions for a unitary Fermi gas (ideal Fermi gas). The critical points are shown by blue squares with error bars, respectively.



**Fig. 4.** Determination of the critical point and the condensate fraction curve. Condensate fraction plotted as a function of the reduced energy (black circles). The critical point is identified as the data point just before the emergence of the condensate fraction (blue open square indicated by the arrow). The purple vertical line corresponds to the ground-state of  $\sqrt{1 + \beta} \cdot 3/4 = 0.48$  at zero temperature in the trapped system (15). The red dashed curve is a fit to the function  $f(x) = B \cdot \{\text{Max}[1 - (x - x_0)/(C - x_0), 0]\}^A$  to estimate the maximum condensate fraction, where  $A$ ,  $B$ , and  $C$  are the fitting parameters and  $x_0$  is fixed at 0.48. The results of the fit are as follows:  $A = 2.0$  (0.3),  $B = 0.62$  (0.03), and  $C = 0.82$  (0.02). (Inset) Fraction curve as a function of  $T/T_{F,\text{trap}}$ , which is calculated from  $E_{\text{total}}/E_{F,\text{trap}}$  by using thermometry for the trapped unitary Fermi gas. The fraction curve is fitted to the function  $f(x) = F \cdot \text{Max}[1 - (x/E)^D, 0]$ , where  $D$  and  $E$  are the fitting parameters and the maximum condensate fraction  $F$  is fixed at 0.62. From the best fit (red solid line), we find  $D = 3.0$  (0.1) and  $E = 0.194$  (0.01). Error bars indicate standard errors of the mean.



Next, we applied our method to the unitary Fermi gas. We analyzed and averaged the data over some 800 profiles. We obtained  $f_E[\theta]$  for various trap geometries and temperatures (25) and confirmed that  $f_E[\theta]$  measured by our method is independent of the trap geometry. The red circles in Fig. 1 show the experimentally determined  $f_E[\theta]$  for the unitary Fermi gas. Each data point includes results from the profiles at different temperatures. Because of the effective attractive interaction at unitarity (3),  $f_E[\theta]$  for the unitary Fermi gas has lower values than  $f_E^{\text{ideal}}[\theta]$  for the ideal Fermi gas. By fitting the data points of  $f_E[\theta]$  with a smooth curve, we obtain the universal function for the unitary Fermi gas.

We tested the validity of the measured universal function of the internal energy in two ways. The first approach involves a comparison between the potential energy per particle,  $E_{\text{pot}}$ , and the internal energy per particle,  $E_{\text{int}}$ , for a unitary Fermi gas trapped in a harmonic potential. Here,  $E_{\text{pot}}$  is given by  $E_{\text{pot}} = E_{\text{total}}/2$ , whereas  $E_{\text{int}}$  is given by the integration of the local internal energy over the volume, that is,  $E_{\text{int}} = \int n E_F(n) f_E[\theta] dV/N$ . Because  $E_{\text{pot}} = E_{\text{int}}$  from the virial theorem (11), we can verify the obtained  $f_E[\theta]$  by comparing the two energies at various temperatures. They are in close agreement (Fig. 2A), which indicates that the  $f_E[\theta]$  determined from our measurement gives the correct internal energy. In Fig. 2A, we find a deviation of about 5% between the data and the line  $E_{\text{pot}} = E_{\text{int}}$ , which gives an estimate of error for  $f_E[\theta]$ .

The second approach involves the measurement of the velocity of the first sound. The unitary Fermi gas exhibits hydrodynamic behavior because lo-

cal thermal equilibrium is achieved due to a large collision rate (6). According to hydrodynamic theory,  $\bar{u}_1 = \sqrt{\int \int n dx dy / m \int \int n (\partial p / \partial n)^{-1} dx dy} \Big|_{z=0}$  is the effective speed of the first sound propagating along the axial direction at the center of an elongated unitary Fermi gas (26). Under the isentropic condition,  $\theta$  should be held constant (11); thus,  $(\partial p / \partial n)_S = (2/3) \cdot (\partial \mathcal{E} / \partial n)_S = 10 E_F(r) f_E[\theta(r)]/9$ . Therefore, the speed of sound,  $\bar{u}_1$ , can be calculated from  $f_E[\theta]$ . In this study, we directly measured  $\bar{u}_1$  by applying density modulation at the center of the cloud, as demonstrated in (27), and we compared the result thus obtained with the  $\bar{u}_1$  calculated from  $f_E[\theta]$ . The measured and calculated sound velocities are compared in Fig. 2B, showing close agreement at all temperatures, and once again proving the validity of our universal function.

We can now determine the other universal functions for the unitary Fermi gas. The universal functions of the Helmholtz free energy, chemical potential, and entropy are derived from the standard thermodynamic relations, that is,  $f_E[\theta] = f_F[\theta] - \theta f'_F[\theta]$ ,  $f_\mu[\theta] = \{5 f_F[\theta] - 2 \theta f'_F[\theta]\}/3$  and  $f_S[\theta] = -f'_F[\theta]$ , respectively. The obtained thermodynamic functions are plotted in Fig. 3.

The critical point for the superfluid transition was determined experimentally by detecting the emergence of the zero center-of-mass momentum component of the paired fermions with use of a rapid field-sweep technique (8–10). We found the critical energy to be  $E_{\text{total}}/E_{F,\text{trap}} = 0.78$  (0.03) (blue open square in Fig. 4). This critical energy corresponds to the critical temperature of  $T/T_{F,\text{trap}} = 0.21$  (0.02), as calculated

using the thermometry in (15), which agrees with the values of 0.21 (0.01) and 0.185 (0.015) obtained from the measurement of entropy (15), 0.20 from the measurement of heat capacity (15), and 0.19 (0.02) using the rapid field-sweep technique with temperature calibration (8). At the critical point, the reduced temperature is found to be  $\theta_c = 0.17$  (0.01) from the peak atomic density and the cloud temperature, and consequently the universal functions have the values  $f_E[\theta_c] = 0.34$  (0.02),  $f_F[\theta_c] = 0.20$  (0.02),  $f_\mu[\theta_c] = 0.43$  (0.01), and  $f_S[\theta_c] = 0.8$  (0.3). For comparison, we list here some theoretical predictions of the values of the thermodynamic functions at the critical point:  $\theta_c = 0.225, 0.152$  (0.07), 0.16, 0.15 (0.01);  $f_E[\theta_c] = 0.4, 0.31$  (0.01), 0.304, 0.27 (0.01);  $f_\mu[\theta_c] = 0.459, 0.493$  (0.014), 0.394, 0.43 (0.01); and  $f_S[\theta_c] = 0.91, 0.2$  (0.2), 0.71, 0.19 [from (28), (29), (30), and (31), respectively].

From the universal function for entropy,  $f_S[\theta]$ , we estimated the critical entropy per particle for the trapped system to be  $S_c/k_{B,\text{trap}} \sim 2.0$  by integrating the local entropy over the volume with the density distribution at the critical temperature. This value is consistent with the value of 1.99 (0.15) that is obtained from the critical energy of 0.78 (0.03) through the relationship between energy and entropy for a trapped unitary Fermi gas (14, 15), and it also agrees with the values of 2.2 (0.1) and 1.6 (0.3) obtained in earlier studies (14, 15). This consistency strongly confirms the validity of the measured thermodynamic functions and critical parameters.

Lastly, we note that the chemical potential shows a plateau below the critical temperature (Fig. 3C) and that the critical exponent of the condensate fraction curve is found to be 3.0 (0.1) (Fig. 4 inset). This behavior is reminiscent of that of an ideal Bose gas below the critical temperature, even though the system is strongly interacting.

## References and Notes

- C. J. Pethick, D. G. Ravenhall, *Annu. Rev. Nucl. Part. Sci.* **45**, 429 (1995).
- G. A. Baker, *Phys. Rev. C Nucl. Phys.* **60**, 054311 (1999).
- H. Heiselberg, *Phys. Rev. A* **63**, 043606 (2001).
- E. Shuryak, *Prog. Part. Nucl. Phys.* **53**, 273 (2004).
- Q. Chen, J. Stajic, S. Tan, K. Levin, *Phys. Rep.* **412**, 1 (2005).
- K. M. O'Hara, S. L. Hemmer, M. E. Gehm, S. R. Granade, J. E. Thomas, *Science* **298**, 2179 (2002); published online 7 November 2002 (10.1126/science.1079107).
- T. Bourdel *et al.*, *Phys. Rev. Lett.* **91**, 020402 (2003).
- C. A. Regal, M. Greiner, D. S. Jin, *Phys. Rev. Lett.* **92**, 040403 (2004).
- M. W. Zwierlein *et al.*, *Phys. Rev. Lett.* **92**, 120403 (2004).
- M. W. Zwierlein, C. H. Schunck, C. A. Stan, S. M. F. Raupach, W. Ketterle, *Phys. Rev. Lett.* **94**, 180401 (2005).
- J. E. Thomas, J. Kinast, A. Turlapov, *Phys. Rev. Lett.* **95**, 120402 (2005).
- J. Kinast *et al.*, *Science* **307**, 1296 (2005); published online 27 January 2005 (10.1126/science.1109220).

13. G. B. Partridge, W. Li, R. I. Kamar, Y.-A. Liao, R. G. Hulet, *Science* **311**, 503 (2006); published online 22 December 2005 (10.1126/science.1122876).
14. L. Luo, B. Clancy, J. Joseph, J. Kinast, J. E. Thomas, *Phys. Rev. Lett.* **98**, 080402 (2007).
15. L. Luo, J. E. Thomas, *J. Low Temp. Phys.* **154**, 1 (2009).
16. S. Riedl *et al.*, *Phys. Rev. A* **78**, 053609 (2008).
17. J. T. Stewart, J. P. Gaebler, C. A. Regal, D. S. Jin, *Phys. Rev. Lett.* **97**, 220406 (2006).
18. W. Ketterle, M. W. Zwierlein, *Riv. Nuovo Cimento* **31**, 247 (2008).
19. T.-L. Ho, *Phys. Rev. Lett.* **92**, 090402 (2004).
20. T.-L. Ho, E. J. Mueller, *Phys. Rev. Lett.* **92**, 160404 (2004).
21. S. Inoue *et al.*, *Nature* **392**, 151 (1998).
22. M. Bartenstein *et al.*, *Phys. Rev. Lett.* **94**, 103201 (2005).
23. H. Hu, P. D. Drummond, X.-J. Liu, *Nat. Phys.* **3**, 469 (2007).
24. A. Bulgac, J. E. Drut, P. Magierski, *Phys. Rev. Lett.* **99**, 120401 (2007).
25. Materials and methods are available as supporting material on Science Online.
26. P. Capuzzi, P. Vignolo, F. Federici, M. P. Tosi, *Phys. Rev. A* **73**, 021603 (2006).
27. J. Joseph *et al.*, *Phys. Rev. Lett.* **98**, 170401 (2007).
28. H. Hu, X.-J. Liu, P. D. Drummond, *Phys. Rev. A* **73**, 023617 (2006).
29. E. Burovski, N. Prokof'ev, B. Svistunov, M. Troyer, *Phys. Rev. Lett.* **96**, 160402 (2006).
30. R. Haussmann, W. Rantner, S. Cerrito, W. Zwerger, *Phys. Rev. A* **75**, 023610 (2007).
31. A. Bulgac, J. E. Drut, P. Magierski, *Phys. Rev. A* **78**, 023625 (2008).
32. We thank Y. Inada and S. Pradhan for experimental assistance. S.N. acknowledges support from the Japan Society for the Promotion of Science.

**Supporting Online Material** [www.sciencemag.org/cgi/content/full/327/5964/442/DC1](http://www.sciencemag.org/cgi/content/full/327/5964/442/DC1) Materials and Methods  
Fig. S1  
References

7 October 2009; accepted 24 November 2009  
10.1126/science.1183012

# Direct Measurements of Island Growth and Step-Edge Barriers in Colloidal Epitaxy

Rajesh Ganapathy,\*† Mark R. Buckley, Sharon J. Gerbode, Itai Cohen

Epitaxial growth, a bottom-up self-assembly process for creating surface nano- and microstructures, has been extensively studied in the context of atoms. This process, however, is also a promising route to self-assembly of nanometer- and micrometer-scale particles into microstructures that have numerous technological applications. To determine whether atomic epitaxial growth laws are applicable to the epitaxy of larger particles with attractive interactions, we investigated the nucleation and growth dynamics of colloidal crystal films with single-particle resolution. We show quantitatively that colloidal epitaxy obeys the same two-dimensional island nucleation and growth laws that govern atomic epitaxy. However, we found that in colloidal epitaxy, step-edge and corner barriers that are responsible for film morphology have a diffusive origin. This diffusive mechanism suggests new routes toward controlling film morphology during epitaxy.

Epitaxy, which is the layer-by-layer growth of a crystalline film on a substrate (1), plays a pivotal role in the fabrication of solid-state and organic semiconductor devices, the creation of strain relief nanostructured arrays, and the design of coatings with novel optical and mechanical properties (2). Understanding the microscopic details of the various growth processes at work continues to be a central focus of surface- and materials-science research (1–6). More recently, this area of research has also branched out to include the self-assembly of nano- and microscale particles into crystalline thin films for the purpose of creating tailor-made metamaterials and photonic band-gap structures (7–11). A variety of experimental techniques have been developed to study atomic homoepitaxy (1, 12), but these tools are

not appropriate for investigating kinetic pathways in epitaxy of nano- and microscale particles. Without knowledge of these kinetic pathways, kinetic Monte Carlo (KMC) simulations cannot

predict accurate growth laws. In fact, at present, it is unclear whether the same kinetic barriers that govern nucleation and growth in atomic systems also govern nano- and microscale particle epitaxy.

We developed and integrated techniques in colloid science to study the epitaxy of microscale particles with an attractive short-range depletion interaction (13). Because colloidal particles can be studied and manipulated at the single-particle level, they are particularly well-suited for investigating such phenomena. Our experiments show that the two-dimensional (2D) growth laws for atoms and colloids are remarkably similar. In addition, we found that for colloids, there exists an analog of the atomic Ehrlich-Schwoebel barrier (ESB), the energetic cost for moving a particle over a step edge or around an island corner (14, 15). In atoms, this barrier is thought to arise from interparticle interactions that are comparable to the atomic spacing. We show that in colloids, the barrier originates from the diffusive nature of the particle dynamics. Nevertheless, this effective barrier leads to similar nonuniformities in the 2D and 3D island morphol-

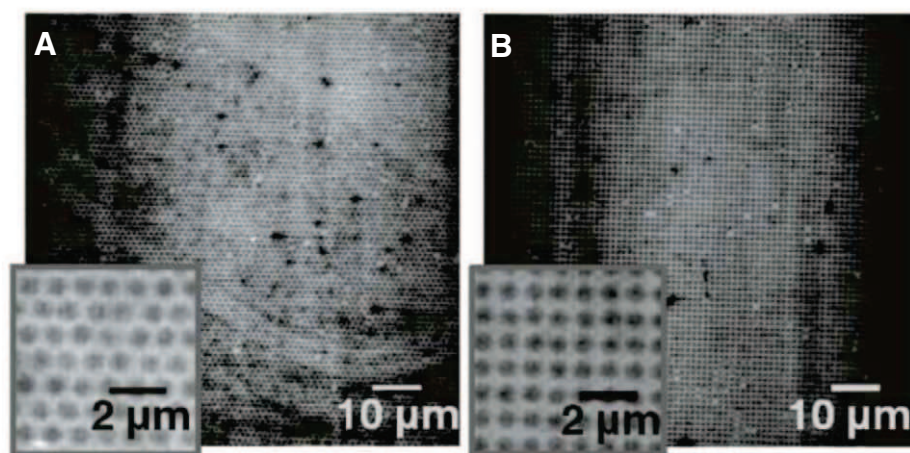


**Fig. 1.** Confocal micrographs of silica colloid monolayers. The particles are seen as dark circles in a bright fluorescent background. (A) Triangular lattice with lattice spacing of 1.05  $\mu\text{m}$ . (B) Square lattice with lattice spacing of 1.04  $\mu\text{m}$ .

Department of Physics, Cornell University, Ithaca, NY 14853, USA.

\*To whom correspondence should be addressed. E-mail: rajeshg@jncasr.ac.in

†Present address: International Centre for Materials Science, Jawaharlal Nehru Center for Advanced Scientific Research, Bangalore, Karnataka 560064, India.



ogies. These results demonstrate that key concepts derived from extensive studies on atomic epitaxial growth are directly applicable to film growth of larger-scale particles. In addition, because colloids act as good model systems for studying statistical-mechanics phenomena (9, 10, 16–18), concepts gleaned from these colloidal deposition experiments should offer insights into atomic and nanoparticle epitaxy.

Our systems consist of charge-stabilized silica or polystyrene colloids with diameters of 1.0 or 1.3  $\mu\text{m}$ , respectively, and sodium polystyrene sulfonate or sodium carboxyl methyl cellulose polymers with a radius of gyration of about 50 nm. The polymers act as depletants that induce an effective attraction between the particles (13) [supporting online material (SOM) text]. Each colloidal epitaxy experiment consists of sedimenting particles onto a substrate at a fixed flux  $F$ , which was determined by measuring the area fraction occupied by monomers and islands with time, and with units of monolayers/s (12). To make contact with atomic epitaxy experiments, a single crystalline colloidal monolayer, formed by binding particles to a lithographically patterned template, was used as the substrate (Fig. 1) (19). The sedimented particles perform a 2D random walk on the substrate by thermally activated hops and coalesce into crystalline islands (movie S1). We found that the monomer surface diffusion constant  $D$  is about 0.01 (lattice constants)<sup>2</sup>/s, which is 100 times smaller than the diffusion constant for a free particle in liquid (SOM text). This decrease arises from depletion-induced bonds with the underlying substrate, creating an energetic barrier that must be overcome for particles to hop from one interstitial

site to another. The ratio of  $D/F$  determines the size of the region explored by the particle before it meets another particle, island, or step edge, and this ratio is a key parameter that governs thin-film growth (1, 12).

To compare epitaxy of colloids and atoms, a significant overlap in  $D/F$  values is essential. The expression for  $D$  has an activated form  $D = D_0 \exp(-U/k_B T)$ , where  $D_0$  is the attempt frequency,  $U$  is the activation barrier,  $k_B$  is Boltzmann's constant, and  $T$  is temperature (1, 12). In colloid experiments,  $U$  can be made arbitrarily small by tuning the depletant concentration. Thus, even though  $D_0$  is approximately  $10^{-8}$  times as large as in atoms, by careful control over the deposition flux,  $D/F$  can be tuned from  $10^{-1}$  to  $10^4$ . For atomic deposition,  $10^{-1} < D/F < 10^9$  (12). This significant overlap in  $D/F$  values allows for quantitative comparison of the mechanisms governing film growth in these two systems.

Snapshots of nucleation and island growth on a square lattice with  $D/F = 1300 \pm 100$  are shown in Fig. 2A, 1 to 4. In our experiments, dimers act as stable nucleation sites. Therefore, we define an island as a cluster equal to or greater than two particles. With time, we observed nucleation of numerous disconnected islands that grew and eventually coalesced to form a single monolayer. The number of disconnected islands per unit area,  $n$ , versus area fraction of islands,  $\Theta$ , for this  $D/F$  ratio is shown by the solid blue squares in Fig. 2B. Initially, the monomer density on the substrate rises and leads to a linear increase in  $n$  (Fig. 2A, 1 and 2, and movie S2). With further increase in the monomer density,  $n$  saturates at a critical density  $n_c$ , because arriving monomers diffuse to nearby islands before encountering

other monomers. At later times, existing islands grow in size, leading to coalescence and a decrease in  $n$ . By varying the substrate symmetry (movie S3), depletant concentration, and bulk colloid volume fraction, we were able to tune  $D$  and  $F$  independently. This allows for conducting epitaxy experiments at different  $D/F$  ratios (Fig. 2B).

We compared the measured  $n_c$  versus  $D/F$  for our colloid experiments (Fig. 2C, solid symbols) with those from atomic experiments (inverted open triangles) (20), atomic KMC simulations (open squares) (12), rate equation with post deposition mobility (brown line), and the rate equation for stable islands (green line) (20). We found quantitative agreement between the colloid and atom data. At a high  $D/F$  ratio, our data approach the  $n_c \propto (D/F)^{-1/3}$  scaling predicted by classical nucleation theory for systems where dimers form stable islands (12, 20). At  $D/F \approx 50$ ,  $n_c$  reaches a maximum and decreases for lower  $D/F$  ratios (green line), because diffusion becomes slow and fewer islands nucleate and grow during deposition (20, 21). We found that the measured saturation value for  $n_c$  agrees with the atomic experiments and the theoretical prediction for systems with stable dimer islands. Finally, we found that the average size of 2D islands increases with increasing  $D/F$  (SOM text), and this behavior is consistent with the trend observed in atomic epitaxy (12). These data indicate that scaling laws that are relevant for atoms carry over to 2D film growth of larger-scale particles with attractive interactions.

In addition to controlling island growth, controlling island morphology is of central importance in the growth of high-quality crystalline films (1, 22). In atoms, the fundamental parameters that determine island morphology in two

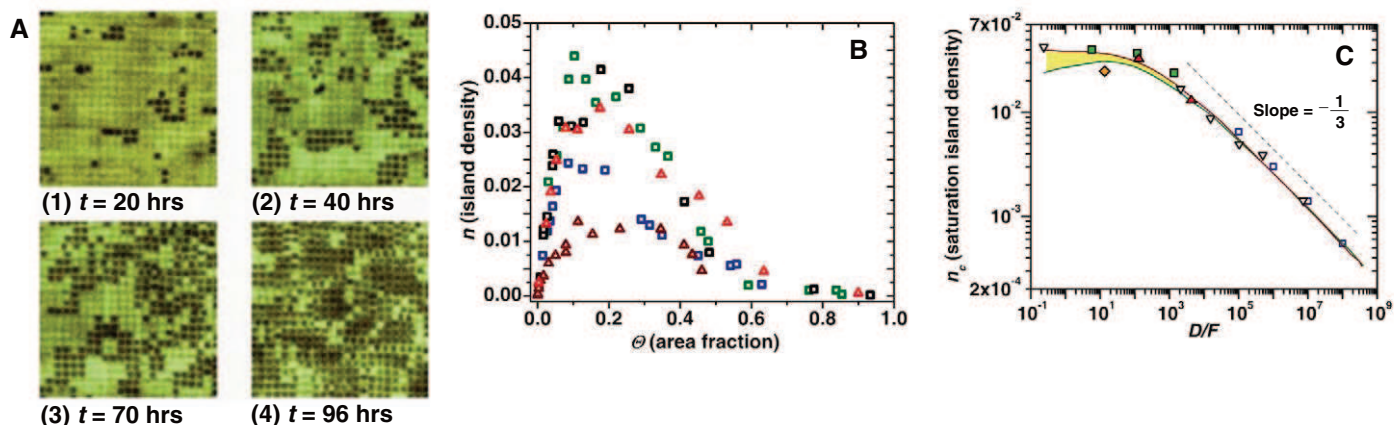


**Fig. 2.** (A) Four images from an island nucleation and growth experiment on a square template with  $D/F = 1300 \pm 100$ . (B) Island density measurements at various  $D/F$  values for square and triangular lattices. Square lattice data for  $D/F = 1300 \pm 100$  (blue squares),  $D/F = 116 \pm 8$  (black squares),  $D/F = 5.7 \pm 0.6$  (green squares). Triangular lattice data for  $D/F = 4200 \pm 233$  (brown triangles),  $D/F = 130 \pm 10$  (red triangles). (C)  $n_c$  versus  $D/F$  for atomic deposition experiments (inverted black triangles); for KMC simulations (blue open squares) [from (12)]; rate equation with post-deposition

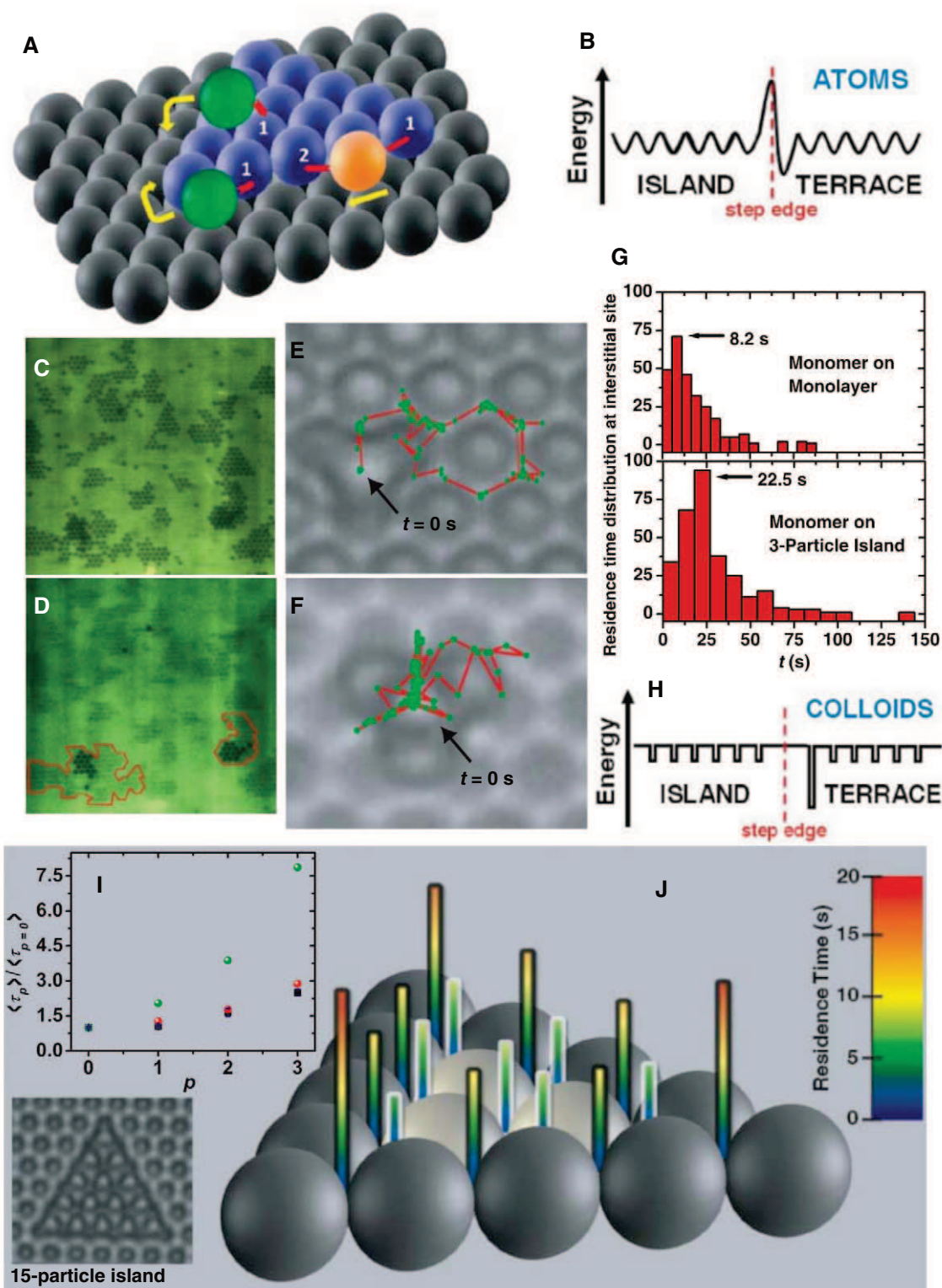
mobility is represented by the brown line; rate equation for stable islands is represented by the green line [from (20, 21)]. The colloid epitaxy experiments with silica particles on the square lattice are shown by green solid squares, whereas those on the triangular lattice are shown by red solid triangles.  $n_c$  is obtained from fitting a cubic polynomial to the  $n$  versus  $\Theta$  data. An experiment with polystyrene particles on a square lattice is shown by the orange solid diamond. The data correspond to systems where dimers form stable island nuclei.

and three dimensions are the island-corner and the ESB step-edge kinetic barriers (1, 14, 15, 23), respectively. Such barriers are thought to arise from the interactions between the atoms and their neighbors. Specifically, as an atom hops from one interstitial site to another on the same island, it must break bonds with its nearest neighbors and form bonds at the new site.

Because the range of the interaction in atomic systems extends beyond the size of an atom, new bonds are able to form as the old ones are broken. This minimizes the energetic cost for going through the lower coordination number state during the hop. The distances between sites straddling a step edge or corner are longer than those between other adjacent sites on the

island; therefore, the energetic barriers for hopping over step edges and corners are substantially larger (Fig. 3, A and B). Because depletion interactions in our colloidal epitaxy experiments are very short-ranged, extending to only 1/20 of the particle diameter, these arguments do not hold for our system. Nevertheless, in our experiments on colloids, we did find evidence of

**Fig. 3.** (A) Schematic of an adatom diffusing near an island step edge. (B) Energy landscape for atoms near a step edge. (C) Image of islands growing on the monolayer substrate. (D) Image of islands nucleating on top of islands shown in (C) (red outline). The separation between islands in (C) is  $\approx 8.0$  lattice constants, whereas the radius of the islands in (D) is  $\approx 2.5$  lattice constants. Such features in atomic systems are associated with a step-edge barrier. (E) Polystyrene colloid diffusing on a colloidal monolayer with triangular symmetry. The trajectory of the colloid during a 180-s interval is shown in red with green dots. (F) Trajectory of a polystyrene colloid diffusing on a three-particle island over 180 s. Island rearrangements in our experiments are rare. (G) Interstitial residence time distribution for a colloidal particle diffusing on a monolayer (top) and for a particle diffusing on a three-particle island (bottom). (H) Energy landscape for colloids near a step edge. (I) Residence time ratios  $\langle \tau_p \rangle / \langle \tau_{p=0} \rangle$  versus  $p$ . Experiments are shown as black squares. Error bars are on the order of the symbol size and show SEM. Simulations in the strong interaction limit (red circles) and weak interaction limit (green circles) are shown. (J) Experimental mean interstitial residence times on a 15-particle island. Color bars indicate residence time.





such barriers. For example, we observed nucleation on top of islands even when the separation between them was larger than the average island size. Furthermore, our data are consistent with a decrease in the fractal dimension of 2D islands with  $D/F$  (SOM text). These phenomena in atomic epitaxy are associated with ESB step-edge and island-corner barriers (Fig. 3, C and D) (1).

To determine unambiguously whether a step-edge barrier exists for colloidal particles with short-ranged interactions, it is necessary to compare hopping dynamics of particles moving from one island interstitial site to another with those of particles descending island step edges. To quantify these dynamics, we used holographic optical tweezers (Arryx) (24) to place individual colloids on islands consisting of different numbers of particles (SOM text and movie S4). We then turned the tweezers off and tracked the colloids as they moved to different island sites (movies S5 and S6). Particle trajectories of 180-s duration are shown for a large triangular island, where the diffusing colloid explores only interior interstitial sites (Fig. 3E), and a three-particle triangular island, where all excursions are over step edges (Fig. 3F). The trajectories show that island step edges significantly confine the space explored by a diffusing monomer. By repeating these experiments a total of 600 times, we quantified the difference in residence times between interstitial sites away from step edges and those at a step edge. The peak values of the interstitial residence time for a monomer at a step edge is substantially larger than the residence time for a monomer in the island interior (Fig. 3B). This increase indicates that despite the short-range nature of the particle interactions, step-edge barriers also exist in colloidal epitaxy.

The particle trajectories in Fig. 3, E and F, show that once a bond is broken with the underlying lattice, colloid monomers predominantly diffuse along local 1D trajectories corresponding to the valleys formed by the underlying particles (Fig. 3H). Because particles on islands with triangular symmetry must diffuse 2.8 times farther to descend a step edge (SOM text), the diffusion time and the probability of returning to the origin (25) and reforming the original bond increases. Thus, we expect that the mean residence time will increase with the number of longer pathways  $p$ . To test this prediction, we conducted 100 independent experiments with a total of 1089 monomer moves on a 15-particle triangular island, where different perimeter sites have different  $p$  (movie S7). We combined these data with measurements on the large triangular island (Fig. 3E) and three-particle island (Fig. 3F). We plotted the ratios of the mean residence times for sites with  $p = 0, 1, 2$ , or 3 to the mean residence time on an interior site (Fig. 3I) and the mean residence

times for all sites on the 15-particle island (Fig. 3J). In accordance with the prediction, we found that the mean residence time increases with  $p$ .

Depending on the strength of the depletion interaction, there are two limiting regimes. In the weak-interaction limit, the bond breaking time is small and the time taken to diffuse between sites is the dominant contribution to the mean residence time. For diffusion, the mean-squared displacement increases linearly with time. Therefore, the mean residence time scales as the square of the path length. In the strong interaction limit, the bond-breaking time dominates. For a 1D random walker between partially absorbing boundaries, the number of returns to the origin grows linearly with the path length (26). Because the particle re-forms the bonds upon each return, the mean residence time increases linearly with the path length. To determine whether either limit is appropriate for describing our experiment, we modeled the process of moving from one interstitial site to another as a 1D random walk on three line segments that share a common origin and are terminated by absorbing boundaries (27) (SOM text). We have numerically implemented this model and calculated the mean residence time ratios in both the diffusive and strong-interaction limits. The experimentally observed mean residence time ratios are consistent with the strong interaction limit (Fig. 3I).

Collectively, these results indicate that epitaxy in colloidal systems is remarkably similar to epitaxy in atoms. We have shown that, as with atoms, the  $D/F$  ratio dictates the 2D growth laws. In addition, we have uncovered a novel dynamic mechanism that leads to step-edge and corner barriers even in systems with short-range interactions. Implementing techniques that use gravity or electromagnetic fields to bias the diffusion of particles down step edges would lower the step-edge barrier and lead to substantially smoother films. Such techniques might also be applicable for tuning barriers in nanoparticle and molecular systems. The powerful array of tools that we have brought together to investigate colloidal epitaxy may also be helpful in elucidating mechanisms that have proven difficult to study in atoms, such as dynamic stress relaxation mechanisms in strained layer heteroepitaxy (6). Finally, given the rapid advances in synthesizing micro- and nanoscale colloidal particles with directional interactions (28) and anisotropic shapes (29), we expect that future epitaxy experiments with such particles will lead to a valuable exchange of ideas among the fields of microparticle, nanoparticle, and atomic epitaxy.

#### References and Notes

1. Z. Zhang, M. G. Lagally, *Science* **276**, 377 (1997).
2. J. V. Barth, G. Costantini, K. Kern, *Nature* **437**, 671 (2005).
3. B. Lewis, D. S. Campbell, *J. Vac. Sci. Technol.* **4**, 209 (1967).
4. T. Michely, J. Krug, *Islands, Mounds, and Atoms: Patterns and Processes in Crystal Growth Far from Equilibrium* (Springer-Verlag, Berlin, 2004).
5. J. A. Venables, *Philos. Mag.* **27**, 697 (1973).
6. C. Teichert, *Phys. Rep.* **365**, 335 (2002).
7. A. van Blaaderen, R. Ruel, P. Wiltzius, *Nature* **385**, 321 (1997).
8. Z. Cheng, W. B. Russel, P. M. Chaikin, *Nature* **401**, 893 (1999).
9. P. Schall, I. Cohen, D. A. Weitz, F. Spaepen, *Science* **305**, 1944 (2004).
10. M. E. Leunissen *et al.*, *Nature* **437**, 235 (2005).
11. E. V. Shevchenko, D. V. Talapin, N. A. Kotov, S. O'Brien, C. B. Murray, *Nature* **439**, 55 (2006).
12. H. Brune, *Surf. Sci. Rep.* **31**, 121 (1998).
13. S. Asakura, F. Oosawa, *J. Chem. Phys.* **22**, 1255 (1952).
14. G. Ehrlich, F. G. Hudda, *J. Chem. Phys.* **44**, 1039 (1966).
15. R. L. Schwoebel, E. J. Shipsey, *J. Appl. Phys.* **37**, 3682 (1966).
16. A. M. Alsayed, M. F. Islam, J. Zhang, P. J. Collings, A. G. Yodanis, *Science* **309**, 1207 (2005).
17. J. R. Savage, D. W. Blair, A. J. Levine, R. A. Guyer, A. D. Dinsmore, *Science* **314**, 795 (2006).
18. P. Schall, I. Cohen, D. A. Weitz, F. Spaepen, *Nature* **440**, 319 (2006).
19. Materials and methods are available as supporting material on Science Online.
20. H. Brune, G. S. Bales, J. Jacobsen, C. Borgano, K. Kern, *Phys. Rev. B* **60**, 5991 (1999).
21. In atomic epitaxy, scanning tunneling microscope measurements are conducted after deposition. Thus the remaining monomers continue to diffuse, and this leads to further island growth and/or nucleation. In our colloidal epitaxy measurements, we measured the instantaneous number density of stable islands, and we expect our data to follow the rate equation that ignores post-growth and/or nucleation.
22. J. W. Evans, P. A. Thiel, M. C. Bartelt, *Surf. Sci. Rep.* **61**, 1 (2006).
23. G. Hlawacek *et al.*, *Science* **321**, 108 (2008).
24. E. R. Dufresne, D. G. Grier, *Rev. Sci. Instrum.* **69**, 1974 (1998).
25. G. Polya, *Math. Ann.* **83**, 149 (1921).
26. S. Redner, *A Guide to First Passage Processes* (Cambridge Univ. Press, Cambridge, 2001).
27. M. A. El-Shewhawy, *J. Phys. Math. Gen.* **33**, 9005 (2000).
28. L. Hong, S. Jiang, S. Granick, *Langmuir* **22**, 9495 (2006).
29. V. N. Manoharan, M. T. Elsesser, D. J. Pine, *Science* **301**, 483 (2003).
30. We thank L. Ristorph, J. Savage, T. Arias, J. Machta, and A. Woll for useful discussions. We would like to especially thank J. Sethna for helping us set up the numerical calculations for residence times. This research was supported by grants from the NSF Division of Materials Research, the Cornell NanoScale Science and Technology Facility, and in part by award no. KUS-C1-018-02 from King Abdullah University of Science and Technology (KAUST).

**Supporting Online Material** [www.sciencemag.org/cgi/content/full/327/5964/445/DC1](http://www.sciencemag.org/cgi/content/full/327/5964/445/DC1) Materials and Methods  
SOM Text  
Figs. S1 to S6  
Movies S1 to S7  
References

30 July 2009; accepted 24 November 2009  
10.1126/science.1179947

# $^{238}\text{U}/^{235}\text{U}$ Variations in Meteorites: Extant $^{247}\text{Cm}$ and Implications for Pb-Pb Dating

G. A. Brennecke,<sup>1\*</sup> S. Weyer,<sup>2†</sup> M. Wadhwa,<sup>1</sup> P. E. Janney,<sup>1</sup> J. Zipfel,<sup>3</sup> A. D. Anbar<sup>1,4</sup>

The  $^{238}\text{U}/^{235}\text{U}$  isotope ratio has long been considered invariant in meteoritic materials (equal to 137.88). This assumption is a cornerstone of the high-precision lead-lead dates that define the absolute age of the solar system. Calcium-aluminum-rich inclusions (CAIs) of the Allende meteorite display variable  $^{238}\text{U}/^{235}\text{U}$  ratios, ranging between  $137.409 \pm 0.039$  and  $137.885 \pm 0.009$ . This range implies substantial uncertainties in the ages that were previously determined by lead-lead dating of CAIs, which may be overestimated by several million years. The correlation of uranium isotope ratios with proxies for curium/uranium (that is, thorium/uranium and neodymium/uranium) provides strong evidence that the observed variations of  $^{238}\text{U}/^{235}\text{U}$  in CAIs were produced by the decay of extant curium-247 to uranium-235 in the early solar system, with an

Meteorites can provide a wealth of information about the formation and evolution of the solar system. In chondritic meteorites, calcium-aluminum-rich inclusions (CAIs) represent the first solids to condense from the cooling protoplanetary disk during the birth of the solar system (1); therefore, the ages of CAIs are generally considered to date the solar system's origin (2–4). High-precision Pb-Pb dating studies, which rely on a known ratio of parent U isotopes, assume that the  $^{238}\text{U}/^{235}\text{U}$  ratio is invariant in meteoritic material (equal to 137.88) (5). Uranium isotope variations in meteorites may be produced by many mechanisms, including the decay of extant  $^{247}\text{Cm}$  to  $^{235}\text{U}$ , nucleosynthetic anomalies in U isotopes, or fractionation of U isotopes during chemical reactions, as recently observed on Earth (6, 7). Any or all of these mechanisms may play some role in  $^{238}\text{U}/^{235}\text{U}$  variability in early solar system materials; however, the existence and effect of  $^{247}\text{Cm}$  on the  $^{238}\text{U}/^{235}\text{U}$  ratio can be studied using geochemical proxies for Cm.

$^{247}\text{Cm}$  is only created in certain types of supernovae during *r*-process nucleosynthesis. It decays to  $^{235}\text{U}$  with a half-life of 15.6 million years (My) (8–13). If  $^{247}\text{Cm}$  was present during the formation of the solar system, it would be detected by variations of  $^{238}\text{U}/^{235}\text{U}$  in ancient meteoritic materials in which the original solar system Cm/U ratio may have been substantially fractionated by processes associated with the formation of the meteoritic materials. The CAIs in chondritic meteorites are likely to be such materials, because many of them experienced ele-

mental fractionation during condensation and evaporation processes that were involved in their formation and because Cm is more refractory than U (14).

Quantification of the abundance of extant  $^{247}\text{Cm}$  has the potential to provide new constraints on the origin of short-lived radionuclides in the early solar system. If the  $^{247}\text{Cm}$  in the early solar system was predominantly inherited from galactic chemical evolution (13), then it should be possible for us to determine the time interval of free decay ( $\Delta$ ) between the last *r*-process nucleosynthetic event and the formation of the solar system (5, 11, 15, 16). Supposed claims of large variations in the  $^{238}\text{U}/^{235}\text{U}$  ratio that were caused by the decay of  $^{247}\text{Cm}$  (8, 9) were refuted in subsequent studies (5, 10, 11, 17). Here we present high-precision  $^{238}\text{U}/^{235}\text{U}$  ratios obtained from 13 CAIs of the Allende meteorite to quantify the amount of  $^{247}\text{Cm}$  present in the early solar sys-

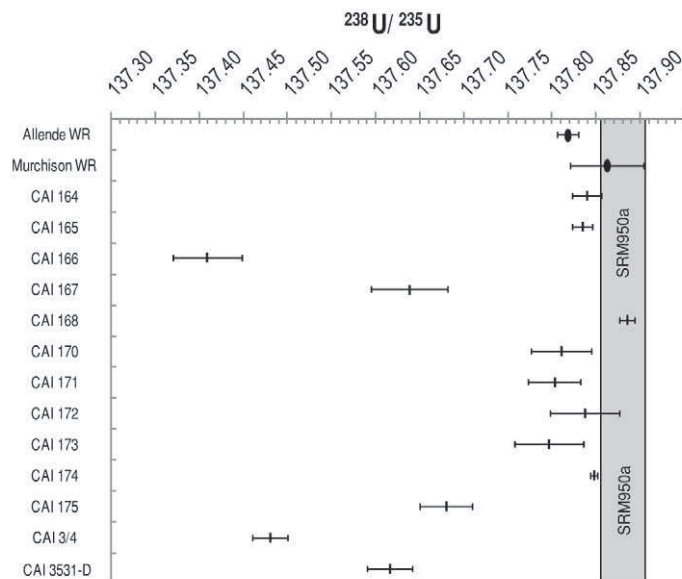
tem and to determine the extent of potential offsets in the calculated Pb-Pb ages of early solar system materials (18).

The  $^{238}\text{U}/^{235}\text{U}$  ratios of the two bulk meteorites (Allende and Murchison) are  $137.818 \pm 0.012$  and  $137.862 \pm 0.042$ , respectively (Fig. 1). The 13 CAIs show a large range of U isotope compositions, with  $^{238}\text{U}/^{235}\text{U}$  ratios varying from  $137.409 \pm 0.039$  to  $137.885 \pm 0.009$ . All but two CAIs differ outside uncertainties from the standard value, and five CAIs have significantly lower  $^{238}\text{U}/^{235}\text{U}$  values than that of bulk Allende.

If  $^{247}\text{Cm}$  decay is the primary mechanism for  $^{238}\text{U}/^{235}\text{U}$  variability, then materials with a high initial Cm/U value would contain a higher relative amount of  $^{235}\text{U}$  than those with lower initial Cm/U values. However, because Cm has no long-lived stable isotope, the initial Cm/U ratio of a sample cannot be directly determined. Because Th and Nd have similar geochemical behavior to Cm, Th/U and Nd/U ratios can serve as proxies for the initial Cm/U ratio in the sample (9, 11). Our sample set spans a large range of Th/U and Nd/U, and both these ratios correlate with the U isotopic composition (Fig. 2).

Because of the higher volatility of U, thermodynamic calculations suggest that substantial fractionation of Cm (and other geochemically similar elements such as Th and Nd) from U is possible in the early solar nebula (19). Large variations in the Th/U and Nd/U ratios seen in our CAI data set (table S1) support this claim. A special group of CAIs, called group II CAIs, are distinguished by a unique abundance pattern of the rare earth elements (REEs). Group II CAIs are highly depleted in the most refractory (that is, heavy REEs, except Tm and Yb) and the most volatile (that is, Eu and Yb) REEs, yet the moderately refractory light REEs (including Nd) are only present in chondritic relative abundances (20). This REE pattern, which is characteristic of

**Fig. 1.**  $^{238}\text{U}/^{235}\text{U}$  isotope values for the samples of this study. The box represents the measured value and analytical precision of replicate analyses of 20- to 100-parts per billion solutions of the SRM950a standard. Error bars are calculated as 2 times the standard deviation (2SD) of multiple runs of each sample, when possible. In samples with extremely limited uranium, for which fewer than three runs were possible, the reported errors are conservatively represented by the long-term reproducibilities (2SD) based on multiple runs of SRM950a measured over the course of this study at the same concentration as the sample.



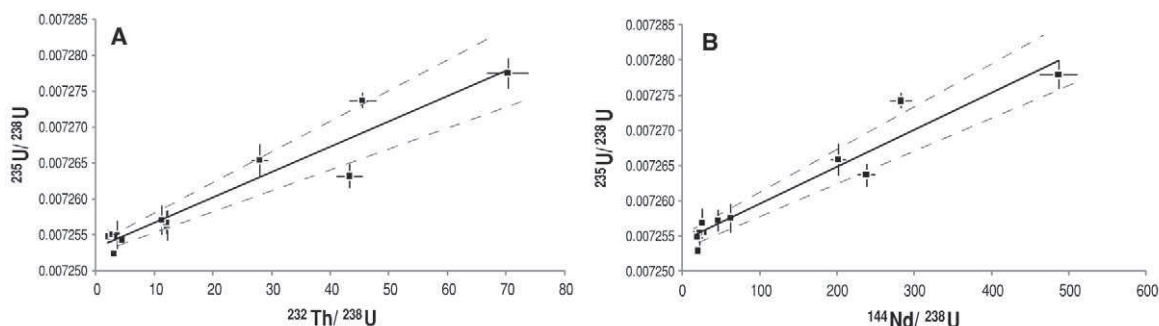
<sup>1</sup>School of Earth and Space Exploration, Arizona State University, Tempe, AZ 85287 USA. <sup>2</sup>Institut für Geowissenschaften, Goethe-Universität, Frankfurt, Germany. <sup>3</sup>Senckenberg Forschungsinstitut und Naturmuseum, Frankfurt, Germany. <sup>4</sup>Department of Chemistry and Biochemistry, Arizona State University, Tempe, AZ 85287, USA.

\*To whom correspondence should be addressed. E-mail: brennecke@asu.edu

†Present address: Institut für Geologie und Mineralogie, Universität zu Köln, Cologne, Germany.



**Fig. 2. (A)**  $^{232}\text{Th}/^{238}\text{U}$  and  $^{144}\text{Nd}/^{238}\text{U}$  ratios plotted versus  $^{235}\text{U}/^{238}\text{U}$  ratios, the reciprocal values of our measured  $^{238}\text{U}/^{235}\text{U}$  ratios. The gray dashed lines represent the 2SD errors on the best-fit line (solid black). Errors on the y-axis data are  $\pm 2\text{SD}$ ; x-axis error bars are  $\pm 5\%$  of the determined value of the elemental ratio.



group II CAIs, suggests a complex condensation history involving fractional condensation (21, 22). The four CAIs of this study that have the highest Nd/U and Th/U ratios (as well as the lowest  $^{238}\text{U}/^{235}\text{U}$  ratios) are all classified as group II CAIs by their REE patterns (Fig. 3). Because of the lower condensation temperature of U relative to Nd and Th (23), the fractional condensation history that resulted in the characteristic group II REE pattern in these objects is likely to have produced the relatively high Nd/U and Th/U ratios.

The correlation of both Th/U and Nd/U with U isotope ratios in the CAIs indicates that the  $^{238}\text{U}/^{235}\text{U}$  variations do not arise from nucleosynthetic anomalies or U isotope fractionation, neither of which easily give rise to such a trend, and instead provide evidence for the presence of extant  $^{247}\text{Cm}$  in the early solar system. Under this interpretation, deviations from the best-fit lines in Fig. 2 could be caused by heterogeneity of  $^{238}\text{U}/^{235}\text{U}$  in the solar nebula, Th and Nd acting as imperfect proxies for Cm, or  $^{238}\text{U}/^{235}\text{U}$  fractionation following Allende CAI formation, possibly from variable redox during secondary alteration processes (7).

In contrast to our findings, a recent study did not detect deviations in the  $^{238}\text{U}/^{235}\text{U}$  ratio among a variety of bulk meteorite samples, including Allende and Murchison (11). Given the reported precision of the study's U isotope analysis, the  $^{144}\text{Nd}/^{238}\text{U}$  ratios should have been sufficient to reveal detectable variations in  $^{238}\text{U}/^{235}\text{U}$  from  $^{247}\text{Cm}$  decay. Although the  $^{238}\text{U}/^{235}\text{U}$  value of bulk Murchison samples agrees within error with our observed values, those for bulk Allende differ well outside of reported errors. The reason for this disagreement is unclear at this time.

The initial  $^{247}\text{Cm}/^{235}\text{U}$  ratio in the early solar system can be estimated by using the slopes of the best-fit lines in Fig. 2 (11). Using Th and Nd as proxies for Cm, we estimate the initial solar system  $^{247}\text{Cm}/^{235}\text{U}$  ratio to be  $2.4 \times 10^{-4} \pm 0.6 \times 10^{-4}$  and  $1.1 \times 10^{-4} \pm 0.2 \times 10^{-4}$ , respectively. The difference between the estimates may be due to slight differences in the geochemical behavior of Th and Nd or possibly because of uncertainties in the assumed solar system Nd/U or Th/U ratios. Nevertheless, these values are, on average, higher than the upper limit derived previously using analyses of the U isotope com-

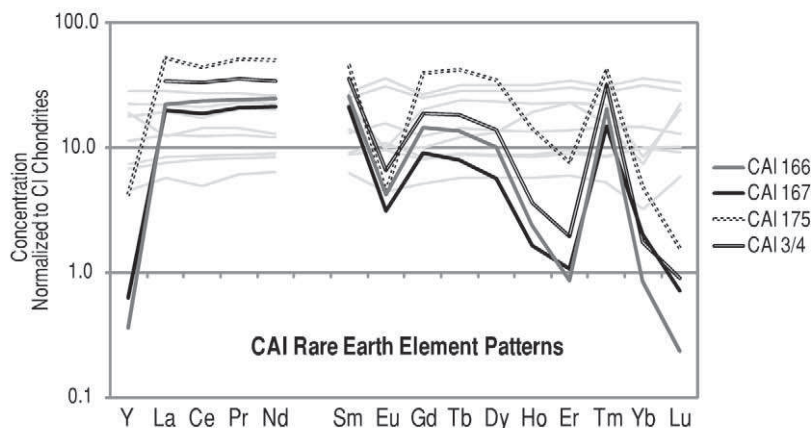


**Fig. 3.** REE patterns of four group II CAIs analyzed in this study, normalized to CI chondrites. All other CAI samples studied here (except 3531-D, for which the REE abundances were not measured) display flat REE patterns, indicating chondritic relative abundances of these elements (light gray lines).

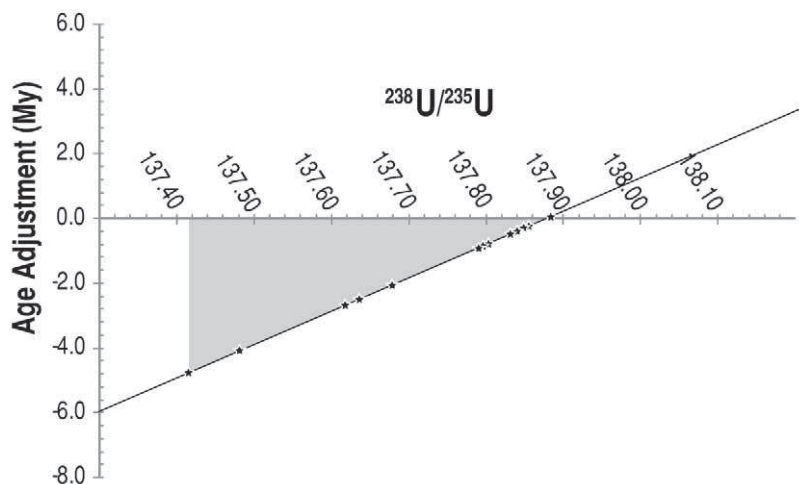


**Fig. 4.** Age adjustment required for samples found not to have a  $^{238}\text{U}/^{235}\text{U}$  value of 137.88, as assumed in the Pb-Pb age equation (Eq. 1). The shaded region represents the range of U isotope compositions reported in this study, and the asterisks represent the specific  $^{238}\text{U}/^{235}\text{U}$  ratios measured in these samples.

positions of bulk chondritic meteorites (11). Our estimates are, however, in agreement with the upper limit of  $\sim 4 \times 10^{-3}$  that was determined previously based on analyses of CAIs (12). If  $^{247}\text{Cm}$  is inherited from galactic chemical evolution, the range of initial solar system  $^{247}\text{Cm}/^{235}\text{U}$  ratios estimated here translates to  $\Delta \sim 110$  to 140 My. This value is similar to, but more precise than, previous estimates of  $\Delta$  based on the inferred initial solar system abundances of

other *r*-process-only radionuclides such as  $^{244}\text{Pu}$  and  $^{129}\text{I}$ , but does not match the significantly shorter estimate of  $\Delta$  ( $\sim 30$  My) derived from the initial abundance of  $^{182}\text{Hf}$  (16). However, because  $^{182}\text{Hf}$  was overabundant in the early solar system compared with its expected abundance from galactic chemical evolution, it may have been injected into the presolar molecular cloud or the solar nebula by a nearby supernova event [for example, (13)].

Our findings also have implications for precise dating of early events in the history of the solar system. The Pb-Pb age equation (Eq. 1) has been used for decades to calculate the absolute ages of both meteoritic and terrestrial materials (24). This equation assumes that  $^{238}\text{U}/^{235}\text{U}$  is invariant at any given time, and that the present-day value is 137.88.

$$\frac{{}^{206}\text{Pb}^*}{{}^{206}\text{Pb}} = \frac{{}^{235}\text{U}e^{\lambda_{235}t} - 1}{{}^{238}\text{U}e^{\lambda_{238}t} - 1} = \frac{1}{137.88} \frac{e^{\lambda_{235}t} - 1}{e^{\lambda_{238}t} - 1} \quad (1)$$

Here,  $\lambda$  is the decay constant for the specific isotope and  $t$  is the age. Any deviation from this assumed  $^{238}\text{U}/^{235}\text{U}$  would cause miscalculation in the determined Pb-Pb age of a sample. A difference of up to 3.5 per mil (‰) implies that a correction of up to -5 My would be required if the Pb-Pb ages of these CAIs were obtained using the previously assumed  $^{238}\text{U}/^{235}\text{U}$  value (Fig. 4).

Because  $^{238}\text{U}/^{235}\text{U}$  variations in solar system materials are not restricted to CAIs, this requirement may extend to high-precision Pb-Pb dating of other materials as well. It is possible, however, that the  $^{238}\text{U}/^{235}\text{U}$  values of bulk chondrites are controlled to a substantial degree by CAIs, which may be heterogeneously distributed at the scale at which these analyses were made.

The Pb-Pb dating technique is the only absolute dating technique able to resolve age differences of <1 My in materials formed in the early solar system. Whereas the full range of  $^{238}\text{U}/^{235}\text{U}$  ratios reported here would result in an overestimation of the ages of these CAIs by up to 5 My, the largest excesses (>3.5‰) in  $^{235}\text{U}$  occur in the group II CAIs that appear to have

experienced the largest Cm/U fractionation. For non-group II CAIs, the age overestimation is  $\leq 1$  My. The apparent discrepancies between absolute Pb-Pb ages and relative (for example,  $^{26}\text{Al}$ - $^{26}\text{Mg}$ ,  $^{53}\text{Mn}$ - $^{53}\text{Cr}$ , and  $^{182}\text{Hf}$ - $^{182}\text{W}$ ) ages (2, 4, 25, 26) may therefore place limits on the uncertainty of the age of the solar system.

## References and Notes

- C. M. Gray, D. A. Papanastassiou, G. J. Wasserburg, *Icarus* **20**, 213 (1973).
- Y. Amelin, A. N. Krot, I. D. Hutcheon, A. A. Ulyanov, *Science* **297**, 1678 (2002).
- A. Bouvier, J. Blichert-Toft, F. Moynier, J. D. Vervoort, F. Albarede, *Geochim. Cosmochim. Acta* **71**, 1583 (2007).
- B. Jacobsen et al., *Earth Planet. Sci. Lett.* **272**, 353 (2008).
- J. Chen, G. J. Wasserburg, *Geophys. Res. Lett.* **7**, 275 (1980).
- C. H. Stirling, M. B. Anderson, E.-K. Potter, A. Halliday, *Earth Planet. Sci. Lett.* **264**, 208 (2007).
- S. Weyer et al., *Geochim. Cosmochim. Acta* **72**, 345 (2008).
- J. W. Arden, *Nature* **269**, 788 (1977).
- M. Tatsumoto, T. Shimamura, *Nature* **286**, 118 (1980).
- G. W. Lugmair, S. J. G. Galer, *Geochim. Cosmochim. Acta* **56**, 1673 (1992).
- C. H. Stirling, A. N. Halliday, D. Porcelli, *Geochim. Cosmochim. Acta* **69**, 1059 (2005).
- J. Chen, G. J. Wasserburg, *Earth Planet. Sci. Lett.* **52**, 1 (1981).
- L. R. Nittler, N. Dauphas, *Meteorites and the Early Solar System II*, D. S. Lauretta, H. Y. McSweeney Jr., Eds. (Univ. of Arizona Press, Tucson, AZ, 2006), pp. 127–146.
- W. V. Boynton, *Earth Planet. Sci. Lett.* **40**, 63 (1978).
- G. J. Wasserburg, M. Busso, R. Gallino, *Astrophys. J.* **466**, L109 (1996).
- G. J. Wasserburg, M. Busso, R. Gallino, K. M. Nollet, *Nucl. Phys.* **777**, 5 (2006).
- T. Shimamura, G. W. Lugmair, *Lunar Planet. Sci.* **XII**, 976 (1981).
- Materials and methods are available as supporting material on Science Online.
- J. B. Blake, D. N. Schramm, *Nature* **289**, 138 (1973).
- G. J. MacPherson, *Treatise on Geochemistry, Volume 1* A. M. Davis, Ed. (Elsevier, Amsterdam, 2003), pp. 201–246.
- W. V. Boynton, *Geochim. Cosmochim. Acta* **39**, 569 (1975).
- A. M. Davis, L. Grossman, *Geochim. Cosmochim. Acta* **43**, 1611 (1979).
- B. Mason, S. R. Taylor, *Contributions to the Earth Sciences*, vol. 25 (Smithsonian Institution Scholarly Press, Washington, DC, 1982).
- C. C. Patterson, *Geochim. Cosmochim. Acta* **10**, 230 (1956).
- G. W. Lugmair, A. Shukolyukov, *Geochim. Cosmochim. Acta* **62**, 2863 (1998).
- C. Burkhardt et al., *Geochim. Cosmochim. Acta* **72**, 6177 (2008).
- We thank the Center for Meteorite Studies at Arizona State University and the Senckenberg Museum in Frankfurt for providing the samples. We thank the W. M. Keck Laboratory for Environmental Biogeochemistry and R. Hines for technical assistance. We are grateful to H. Palme for helpful discussions and to R. Williams and L. Borg for assistance with the double spike. We also thank G. Wasserburg, S. Galer, and an anonymous reviewer for thoughtful comments that greatly improved the manuscript. This work was partially supported by NASA Origins of Solar Systems grant NNX07AF49G to M.W., as well as NASA Astrobiology Institute grant NNA09DA79A and NASA Exobiology Program grant NNX07AU15G to A.D.A.

**Supporting Online Material** www.sciencemag.org/cgi/content/full/science.1180871/DC1 Materials and Methods  
Fig. S1  
Tables S1 and S2  
References

20 August 2009; accepted 11 December 2009  
Published online 31 December 2009;  
10.1126/science.1180871  
Include this information when citing this paper.

# Contribution of Semi-Arid Forests to the Climate System

Eyal Rotenberg and Dan Yakir\*

Forests both take up  $\text{CO}_2$  and enhance absorption of solar radiation, with contrasting effects on global temperature. Based on a 9-year study in the forests' dry timberline, we show that substantial carbon sequestration (cooling effect) is maintained in the large dry transition zone (precipitation from 200 to 600 millimeters) by shifts in peak photosynthetic activities from summer to early spring, and this is counteracted by longwave radiation ( $L$ ) suppression (warming effect), doubling the forestation shortwave ( $S$ ) albedo effect. Several decades of carbon accumulation are required to balance the twofold  $S + L$  effect. Desertification over the past several decades, however, contributed negative forcing at Earth's surface equivalent to ~20% of the global anthropogenic  $\text{CO}_2$  effect over the same period, moderating warming trends.

The need to generate measurement-based estimates of biosphere-atmosphere carbon and energy exchange on land (1, 2) led to

global observational efforts to measure the carbon, water, and radiation fluxes at the canopy scale (www.fluxnet.ornl.gov). Obtaining primary data from semi-arid regions is important principally because of their size [2.4 billion ha or ~17.7% of total land surface area (3)] coupled with their low clouds-high solar radiation conditions: 18 to 21 and 10 to 13  $\text{MJ m}^{-2} \text{day}^{-1}$  in

semi-arid and temperate regions, respectively (4). These regions have potentially large impacts on local climate (5–7) and the global radiation budget and represent climatic conditions predicted for large areas of currently wetter regions (8). We used the concept of “radiative forcing” as a metric for comparing changes in surface energy balance with carbon uptake and storage associated with semi-arid forestation.

We used a field research site with continuous flux measurements of  $\text{CO}_2$ , water vapor, and energy established in 2000 in a 2800-ha pine forest (Yatir) in southern Israel, using methodology established in the Euroflux network (9). The forest represents a low-stature (10 m), low-density [leaf area index (LAI) ~ 1.3] woody vegetation ecosystem at the dry timberline (285 mm mean precipitation). The forest maintains relatively high productivity, with a mean annual net ecosystem  $\text{CO}_2$  exchange ( $NEE$ ) of 2.3  $\text{ton C ha}^{-1}$  for the study period (10), compared with ~2.0  $\text{ton C ha}^{-1}$  in European pine forests and a Fluxnet mean of ~2.5  $\text{ton C ha}^{-1}$  (Table 1). This reflects moderate mean annual gross primary productivity ( $GPP$ ) coupled with low mean annual

Environmental Sciences and Energy Research, Weizmann Institute of Science, Rehovot 76100, Israel.

\*To whom correspondence should be addressed. E-mail: dan.yakir@weizmann.ac.il



carbon loss in respiration ( $R_e$ ), resulting in a high  $NEE/GPP$  ratio (Table 1).

The indicators of high carbon use efficiency are associated with a range of eco-physiological adjustments (11), as well as potential increase in fire hazard (12). The most fundamental adjustment is the “homeostatic-like” stability in ambient conditions during time of peak activity reported in Fig. 1. Moving from the northern (Finland) to the southern (Israel) pine forest sites, time of peak GPP shifts from July and August to mid-March, narrowing down substantially the climatic gradient, such as in air temperature from 17.4°C (annual mean) to 4.6°C (time of peak GPP, when mean temperature is  $17.0^\circ \pm 1.5^\circ\text{C}$ , excluding one outlier maritime site), or in incoming global irradiance ( $E_g$ , from  $150\text{ W m}^{-2}$  annual mean to  $67\text{ W m}^{-2}$  for time of peak GPP). For a first approximation, the change in day of year of peak GPP ( $DOY_{GPP}$ ) is best described by the gradient in annual mean  $E_g$ :  $DOY_{GPP} = -0.71(E_g) + 263.1$  ( $R^2 = 0.87$ ), or 7 days advance for each increase of  $10\text{ W m}^{-2}$  in annual mean global radiation. The trend depicted in Fig. 1 is for European pine forests, reflecting plasticity within a single vegetation type rather than changes in species composition along geographical and climatic gradients (13). This homeostatic-like ecosystem-scale behavior also provides an alternative perspective to the proposed leaf-level “homeostatic” temperature reconstructed from oxygen isotopic records in plant matter (14).

The adjustments in timing and productivity noted above provide a contrasting and more optimistic long-term view of forest productivity and carbon uptake than those based on episodic droughts in temperate climates. For example, signature drought years like 2003 in Europe (15) indicated massive losses of carbon from forest ecosystems, but the results here indicate that long-term management of forestation can result in productive forests that can sustain seasonal drought permanently (10).

In addition to carbon, we must consider the direct effects of vegetation cover on the surface radiation balance (2, 16, 17), where the semi-arid forest also indicates large effects. From a global perspective, the characteristics of energy fluxes over a semi-arid forest such as Yatir are unique (Fig. 2). The incoming solar radiation approaches that of the Sahara, but owing to an albedo as low as in other forests the net radiation ( $R_n$ ) is higher than that in any of the other eco-regions (35% greater than in the Sahara). The high net radiation coupled with the dry environment (small latent heat flux; Fig. 2 inset) results in a sensible heat flux,  $H$ , larger than that of any of the other eco-regions (30% larger than the Sahara and 1.6 and 2.4 times greater than tropical and temperate forests, respectively). Two important implications are, first, that the albedo change associated with forestation in the low-cloud high-radiation environment results in a large increase in surface radiation load. We observed

(18) a 0.1 change (decrease) in mean albedo ( $\delta_\alpha$ ) above the forest compared with that above the sparse background shrubland [compare with (19–21)]. Combined with the high global radiation, this  $\delta_\alpha$  yields a large increase in annual shortwave radiation load of  $\delta_S = +23.8\text{ W m}^{-2}$ . Second, we report that this relatively large shortwave albedo effect (16, 17, 22) is essentially doubled by a longwave radiation effect.

With suppressed latent heat flux ( $LE$ ) because of lack of water, the forest is transformed into an effective “convector” that exploits the low tree density and open canopy and, consequently, high canopy-atmosphere aerodynamic coupling. Indeed, low aerodynamic resistance ( $r_a$ ) was estimated [ $\sim 16\text{ s m}^{-1}$  annual mean midday value (23)] supporting the massive  $H$  (Fig. 2 inset). This is associated with a large increase in surface roughness in going from shrubland to forest, resulting in changes in buoyancy and increasing efficiency of heat convection, with potential implications on local circulation.

The effective convector effect of the canopy-atmosphere coupling resulted in annual mean cooling of the canopy surface temperature of about 5°C, compared with that of the back-

ground shrubland (and as much as a 30°C cooling in summer midday). This was associated with high Bowen ratio ( $\beta = H/LE$ ), which was on average 5.2 ( $>10$  in summer). In contrast, in temperate and tropical forests the albedo-related increased radiation load is typically compensated for by evapotranspiration, reducing temperature differences between forest and nonforest surfaces and maintaining  $\beta$  around 1.

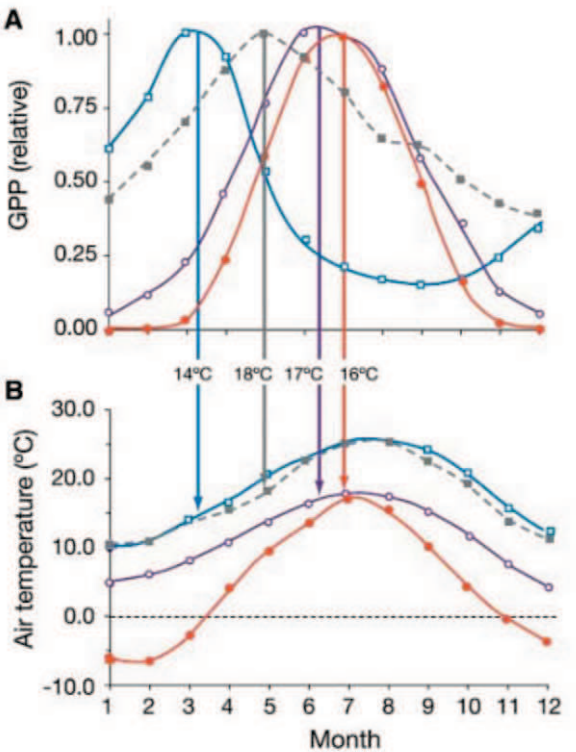
Longwave radiation is of great importance in the semi-arid system (20, 24). And a consequence of the surface cooling in the forested area is a suppression of the upwelling longwave radiation flux,  $L$ . In fact, the annual mean longwave radiation suppression that we observed (18) in our forest-shrubland comparison is  $\delta_L \sim 25\text{ W m}^{-2}$  (up to  $100\text{ W m}^{-2}$  in summer midday) and is equivalent in magnitude to the shortwave albedo effect ( $\sim 23.8\text{ W m}^{-2}$ ; Table 2). Therefore, in dry vegetation ecosystems the increase in surface radiation load is twice as large when both the shortwave, albedo, and the longwave radiation effects are considered (balanced by heat transfer to the overlaying boundary layer).

The surface energy characteristics in the semi-arid regions have at least two important global

**Table 1.** Indicators of carbon use efficiency in pine forests:  $GPP$ ,  $R_e$ , and  $NEE$  of carbon for the 12 European pine forest sites [62 data years (36)], for the entire global Fluxnet network (43), and for semi-arid forest [Yatir (44)].

Pine forest	$GPP$	$R_e$	$NEE$	$NEE/GPP$
European (Carboeurope)	1142	944	200	0.17
Global (FluxNet)	1540	1280	260	0.17
Semi-arid (Yatir)	820	600	220	0.27

**Fig. 1.** Annual patterns in (A)  $GPP$ , monthly means based on 0.5-hour values from Carboeurope database (36) and normalized as  $GPP/GPP_{max}$ , and (B) air temperature (monthly mean) in 4 representative European pine forest sites (out of the 12 Carboeurope pine forest sites examined; other sites omitted for clarity but are within same range). Vertical lines indicate the air temperature at time of peak activity. Sites are Yatir, Israel (blue); El Salar, Spain (gray); Brasschaat, Belgium (purple); and Hyttiala, Finland (orange).



implications when considering the large land surface areas involved. First, the success of afforestation and the associated carbon sequestration potential must also be linked to the consequences in surface energy balance. Secondly, the results provide a basis for a first approximation of the impact of the large-scale desertification process that took place in the semi-arid region over the past several decades.

We used the observed albedo-derived shortwave radiative forcing ( $RF$ ) of the forest,  $\delta_S = +23.8$ , together with the calculated  $RF$  associated with carbon sequestration, using (17) and (25) and the observed semi-arid forest productivity [ $-2.3 \text{ ton C ha}^{-1}$  annually (10) and  $\sim 100 \text{ ton C ha}^{-1}$  over the past 40 years (26)] to estimate the time required to achieve balance between the two  $RF$  values (27). The  $RF$  values in this context should be interpreted with caution (28) and are used here as a convenient way to compare the

magnitude of biogeophysical and biogeochemical forcing (24). The estimated time required to reach this balance in the semi-arid environment is  $\sim 40$  years. Such calculation traditionally considers only the shortwave radiation effect. Explicitly introducing the observed longwave radiation suppression effect in this calculation doubles the time needed to achieve the  $RF$  balance, considering that  $\delta_S$  and  $\delta_L$  are similar ( $23.8$  and  $25 \text{ W m}^{-2}$ ).

Such estimates indicate that a net negative (cooling)  $RF$  is reached only after  $\sim 80$  years of forestation, but we note that the data used here provide a “worst-case scenario” by considering results from the dry timberline and ignoring the possibly greater climate sensitivity to  $\text{CO}_2$  removal than to land surface changes (28). Obtaining the full range of  $RF$ -C sequestration tipping points across the climate transition zone is important, will likely indicate much shorter mean time to reach a net cooling effect, and should

also consider that afforestation of only  $\sim 12\%$  of dry, carbon-neutral areas (3, 29) can produce a carbon sink of  $\sim 1 \text{ Pg C year}^{-1}$  for a minimum 50 years of forest growth. This is equivalent to one “wedge” to address potential anthropogenically derived climate change (30).

Lastly, we address the implications of our results for long-term desertification trends in the semi-arid region. From the atmospheric and surface radiation perspective, the Yatir forest provides a generic representation of vegetation of similar LAI in the semi-arid region [ $2.1 \pm 1.6$  and  $1.3 \pm 0.9$  for shrubland and deserts (31)]. Such vegetation types underwent large-scale desertification over the past several decades, estimated at  $\sim 5.8 \text{ Mha year}^{-1}$  (3, 32). We estimated that the total organic carbon released from a fully degraded land surface is  $\sim 2.2 \text{ kg C m}^{-2}$  (3, 29, 33) and that the degradation period (DP) for the release of carbon to the atmosphere is about 50 years. We consider the albedo effect, however, to peak in about half that time ( $\sim 25$  years) because it is associated only with live vegetation, whereas carbon degradation in litter and soil organic matter is not. Using the approach of (17) for the shortwave radiation ( $S$ ) albedo effect but expanded to explicitly include the thermal radiation ( $L$ ) suppression discussed above, we estimated the potential  $RF$  of the transition from vegetation cover with LAI of  $\sim 1.3$  to near zero under semi-arid conditions as:

$$RF_{S+L}(y) = A(y)(\delta_\alpha \cdot E_g + \delta_L)/A_E \quad (1)$$

where  $A(y)$  is the annually degraded area accumulated to year  $y$  (calculated as a time series with full degradation in 25 years),  $\delta_\alpha = 0.1$ ,  $E_g = 240 \text{ W m}^{-2}$ ,  $\delta_L = 25$  (Table 2), and  $A_E$  is Earth surface area ( $5.1 \times 10^{14} \text{ m}^2$ ). This estimate indicates a negative (cooling) radiative forcing at the surface over a 35-year degradation process (say, 1970–2005 when data quoted above apply) of  $-0.145 \text{ W m}^{-2}$  ( $-0.075$  plus  $-0.070 \text{ W m}^{-2}$  associated with  $S$  and  $L$ , respectively).

The radiative forcing resulting from the  $\text{CO}_2$  released from biomass degradation associated with desertification can be estimated according to (25):

$$RF_{\text{CO}_2}(y) = \eta \cdot L_n \left[ 1 + \frac{C(y)}{C_0} \right] \quad (2)$$

where  $\eta$  is the  $\text{CO}_2$  radiative forcing efficiency ( $5.35 \text{ W m}^{-2}$ );  $C_0$  is a reference  $\text{CO}_2$  concentration (360 ppm);  $C(y) = A(y)C\kappa/\zeta$  sums the total  $\text{CO}_2$  emitted over  $y$  years [35 years of desertification in this case (3)];  $A(y)$  is as above with degradation period of 50 years, acknowledging the delay in degradation effects between surface radiation and  $\text{CO}_2$  release;  $C$  is the total degradable carbon per unit land area (see above);  $\kappa$  converts kg of C to ppmv [ $2.13 \times 10^{12} \text{ kg C per part per million by volume (ppmv}^{-1})$ ]; and  $\zeta$  is the airborne fraction [ $0.5$  (34)]. The results indicate that the releases of  $\text{CO}_2$  to the atmosphere

**Table 2.** Annual mean values (6 years) of radiation fluxes, albedo, and surface (skin) temperature in the semi-arid forest (Yatir) and in the shrubland background.

Variable	Forest	Shrubland
Global radiation ( $E_g$ , $\text{W m}^{-2}$ )	238	238
Albedo (unit-less)	0.11	0.21
Net solar radiation ( $S_n$ , $\text{W m}^{-2}$ )	212	188
Net longwave radiation ( $L_n$ , $\text{W m}^{-2}$ )	-96	-121
Net radiation ( $R_n = S_n + L_n$ , $\text{W m}^{-2}$ )	115	67
Skin temperature ( $^{\circ}\text{C}$ )	19	24*

\* (27)

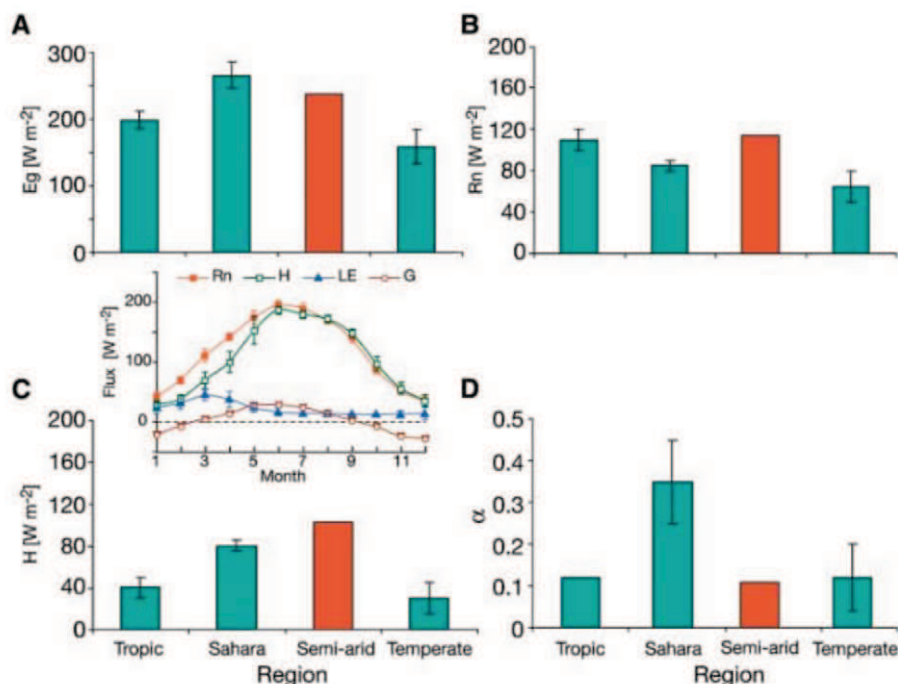


**Fig. 2.** Annual means of energy flux components in forests (except Sahara) in globally representative regions: (A)  $E_g$ , (B)  $R_n$ , (C)  $H$ , and (D) surface albedo,  $\alpha$ . Values for tropical forests include Africa and South America; temperate forests are represented by forests around latitude  $45^{\circ}\text{N}$  in North America and Europe; semi-arid forests are represented by Yatir (mean for the study period); the Sahara represents hot deserts. Error bars indicate the range in literature-reported values. Albedo values for tropical forests, the Sahara, and temperate forests are from (37–41). Values for  $E_g$  are from (4), and for  $R_n$  and  $H$  from (42). (Inset) The mean seasonal cycle in energy fluxes in the semi-arid Yatir forest during the study period.



during the above desertification period had radiative forcing of  $+0.006 \text{ W m}^{-2}$ , a factor of 24 smaller and in the opposite direction than the combined radiative effects [compare with (28)].

On the basis of our estimates, the total desertification in the semi-arid regions had a combined  $RF$  of about  $-0.14 \text{ W m}^{-2}$ . This counteracts the equivalent of  $\sim 20\%$  of the global

$RF$  associated with the 44-ppmv increase in atmospheric  $\text{CO}_2$  over the same period [(35)]

e.g.,  $(0.145-0.006)/0.62$ ; see Eqs. 1 and 2], moderating the potential warming trend. This moderating effect adds to that assigned to the low  $\text{CO}_2$  airborne fraction resulting from ocean and land carbon sinks (34). These are clearly first approximations, but the large effects and the large area involved with generally stable high-radiation low-cloud conditions make these estimates relatively robust and demonstrate again the importance of research in the semi-arid regions.

# References and Notes

1. D. Baldocchi *et al.*, *Bull. Am. Meteorol. Soc.* **82**, 2415 (2001).
2. G. B. Bonan, *Science* **320**, 1444 (2008).
3. R. Lal, *Environ. Manage.* **33**, 528 (2004).
4. National Climatic Data Center, "Mean daily solar radiation, monthly and annual" (U.S. Department of Commerce, Washington, DC, 1964).
5. J. Otterman, *Science* **186**, 531 (1974).
6. J. Charney, W. J. Quirk, S. H. Chow, J. Kornfield, *J. Atmos. Sci.* **34**, 1366 (1977).
7. Y. K. Xue, Q. J. R. *Meteorol. Soc.* **123**, 1483 (1997).
8. Intergovernmental Panel on Climate Change (IPCC), *Fourth Assessment Report, Climate Change 2007: Synthesis Report*, available at [www.ipcc.ch/publications\\_and\\_data/publications\\_ipcc\\_fourth\\_assessment\\_report\\_synthesis\\_report.htm](http://www.ipcc.ch/publications_and_data/publications_ipcc_fourth_assessment_report_synthesis_report.htm).
9. M. Aubinet *et al.*, *Adv. Ecol. Res.* **30**, 113 (1999).
10. K. Maseyk, J. M. Grunzweig, E. Rotenberg, D. Yakir, *Glob. Change Biol.* **14**, 1553 (2008).
11. K. S. Maseyk *et al.*, *New Phytol.* **178**, 603 (2008).
12. D. M. J. S. Bowman *et al.*, *Science* **324**, 481 (2009).

16. G. Bala *et al.*, *Proc. Natl. Acad. Sci. U.S.A.* **104**, 6550 (2007).
17. R. A. Betts, *Nature* **408**, 187 (2000).
18. Four pairs of shortwave (0.29 to 4.0  $\mu\text{m}$ , Kipp and Zonen CM21) and longwave (4.0 to 100  $\mu\text{m}$ , Eppley precision infrared radiometer) radiation sensors were used, two (multiple positions) for measuring down- and upwelling radiation  $\sim 5 \text{ m}$  above the canopy (and  $\sim 4 \text{ m}$  away from the flux tower) and two (multiple positions) below the canopy  $\sim 1.5 \text{ m}$  above bare soil surface. The L sensors output (precision mode) was corrected for solar radiation by using the companion S sensor. Albedo was estimated, in addition, from Moderate Resolution Imaging Spectroradiometer (MODIS) data for the forest and surrounding area using a full-year dark and white sky in the visible and near-infrared (NIR) spectral ranges ([www.modis.bu.edu/bdrl/userguide/albedo.html](http://www.modis.bu.edu/bdrl/userguide/albedo.html)).
19. J. Charney, Q. J. R. *Meteorol. Soc.* **101**, 193 (1975).
20. G. L. Smith, A. C. Wilber, S. K. Gupta, P. W. Stackhouse Jr., *J. Clim.* **15**, 1175 (2002).
21. K. Fraedrich, A. Kleidon, F. Lunkeit, *J. Clim.* **12**, 3156 (1999).
22. M. Schaeffer *et al.*, *Global Biogeochem. Cycles* **20**, GB2020 (2006).
23. Aerodynamic resistance,  $r_a$ , was estimated as  $r_a = \frac{H}{\Delta T_a} C_p$ .  $C_p$  and  $p$  are the air heat capacity and density;  $H$  was continuously measured; canopy-to-air temperature gradient,  $\Delta T_a$ , was estimated from continuous sonic anemometer measurements 9 m above the canopy; and canopy "skin" temperature was estimated from upwelling longwave radiation measurements both above the soil and the canopy. For comparing forest and surrounding shrubland, surface temperatures were based on soil temperature measurements in the forest and at the shrubland (only 1 year for the latter), as well as MODIS surface temperature products for the forest and the surrounding region (at 10 km-by-10 km grids, 8-days mean at 10 AM, January through August 2005). Comparing roughness height was based on (45).
24. M. Claussen, V. Brovkin, A. Ganopolski, *Geophys. Res. Lett.* **28**, 1011 (2001).
25. G. Myhre, E. J. Highwood, K. P. Shine, F. Stordal, *Geophys. Res. Lett.* **25**, 2715 (1998).
26. A. Bar Massada, Y. Carmel, G. E. Tzur, J. M. Grünzweig, D. Yakir, *Can. J. For. Res.* **36**, 2585 (2006).
27. The time ( $y$ , years) required for a semi-arid forest to achieve balance between the surface positive  $RF$  and the carbon sequestration negative  $RF$  is approximated based on (17) as  $y = \left( \frac{RF_{\text{surface}} \cdot \kappa \cdot C_0}{A_E \cdot NEE \cdot \eta \cdot \zeta} \right)$ , where  $RF_{\text{surface}}$  is either the albedo or the combined albedo-longwave effect,

- $RF_{\text{surface}}$ ,  $A_E$  the Earth surface area ( $\text{m}^2$ ),  $\kappa$  converts parts per million (ppm)  $\text{CO}_2$  to  $\text{kg C}$ ,  $C_0$  the reference atmospheric  $\text{CO}_2$  concentration (370 ppm),  $\eta$  is the  $\text{CO}_2$  radiative forcing efficiency ( $\text{W m}^{-2}$ ),  $\zeta$  is the airborne fraction, and  $NEE$  is the observed annual net carbon uptake of the semi-arid forest ( $\text{kg C m}^{-2} \text{ year}^{-1}$ ).
28. E. L. Davin, N. de Noblet-Ducoudre, P. Friedlingstein, *Geophys. Res. Lett.* **34**, L13702 (2007).
29. H. N. Le Houérou, *J. Arid Environ.* **34**, 133 (1996).
30. S. Pacala, R. Socolow, *Science* **305**, 968 (2004).
31. G. P. Asner, J. M. O. Scurlock, J. A. Hicke, *Glob. Ecol. Biogeogr.* **12**, 191 (2003).
32. J. F. Reynolds *et al.*, *Science* **316**, 847 (2007).
33. Food and Agriculture Organization (FAO), *Carbon Sequestration in Dryland Soils* (World Soils Resources Reports 102, FAO, Rome, 2004).
34. J. G. Canadell *et al.*, *Proc. Natl. Acad. Sci. U.S.A.* **104**, 18866 (2007).
35. [www.esrl.noaa.gov/gmd/ccgg](http://www.esrl.noaa.gov/gmd/ccgg)
36. <http://gaia.agraria.unitus.it/database/carboeuropeip/>
37. W. J. Shuttleworth *et al.*, *Q. J. R. Meteorol. Soc.* **110**, 1163 (1984).
38. W. Knorr, K. G. Schnitzler, Y. Govaerts, *Geophys. Res. Lett.* **28**, 3489 (2001).
39. T. T. Warner, *Desert Meteorology* (Cambridge Univ. Press, Cambridge, 2004).
40. G. S. Campbell, J. M. Norman, *An Introduction to Environmental Biophysics* (Springer-Verlag, New York, ed. 2, 1998).
41. V. Masson, J. L. Champeaux, F. Chauvin, C. Meriguet, R. Lacaze, *J. Clim.* **16**, 1261 (2003).
42. J. Peixoto, A. Oort, *Physics of Climate* (Springer-Verlag, New York, 1992).
43. S. Luyssaert *et al.*, *Glob. Change Biol.* **13**, 2509 (2007).
44. T. Afik, thesis, Hebrew University of Jerusalem (2009).
45. R. H. Shaw, A. R. Pereira, *Agric. Meteorol.* **26**, 51 (1982).
46. We thank the students, postdocs, and technicians of the Yatir team for making this project possible. The long-term operation of the Yatir Forest Research Field Site is supported by the Cathy Wills and Robert Lewis Program in Environmental Science. Financial support from the Israel Science Foundation, Global Change and the Hydrological Cycle—Jordan River (GLOWA-JR), Keren Kayemet L'Israel (KKL), Jewish National Fund (JNF), the Minerva-Avron Center, and the Weizmann Institute is gratefully acknowledged.

31 July 2009; accepted 28 December 2009

## Modeled Impact of Anthropogenic Warming on the Frequency of Intense Atlantic Hurricanes

Morris A. Bender,<sup>1\*</sup> Thomas R. Knutson,<sup>1</sup> Robert E. Tuleya,<sup>2</sup> Joseph J. Sirutis,<sup>1</sup> Gabriel A. Vecchi,<sup>1</sup> Stephen T. Garner,<sup>1</sup> Isaac M. Held<sup>1</sup>

Several recent models suggest that the frequency of Atlantic tropical cyclones could decrease as the climate warms. However, these models are unable to reproduce storms of category 3 or higher intensity. We explored the influence of future global warming on Atlantic hurricanes with a downscaling strategy by using an operational hurricane-prediction model that produces a realistic distribution of intense hurricane activity for present-day conditions. The model projects nearly a doubling of the frequency of category 4 and 5 storms by the end of the 21st century, despite a decrease in the overall frequency of tropical cyclones, when the downscaling is based on the ensemble mean of 18 global climate-change projections. The largest increase is projected to occur in the Western Atlantic, north of  $20^\circ\text{N}$ .

Rising sea-surface temperatures (SSTs) and a possible increase in Atlantic basin hurricane activity since 1950 have raised concern that human-caused climate change may

be increasing Atlantic hurricane activity. Increasing amounts of greenhouse gases are a likely factor in the recent warming of tropical Atlantic SSTs (1–3), although internal variability

(4) and reduced aerosol or dust forcing (5, 6) may have also contributed. Some statistical analyses suggest a link between warmer Atlantic SSTs and increased hurricane activity (6–8), although other studies contend that the spatial structure of the SST change may be a more important control on tropical cyclone frequency and intensity (9–11). A few studies (6, 8, 12) suggest that greenhouse warming has already produced a substantial rise in Atlantic tropical cyclone activity, but others question that conclusion (9, 11, 13).

Dynamical models that can reproduce certain aspects of the observed frequency, structure, and intensity of hurricanes bring an important perspective to these questions (9, 10, 14–16). A recent modeling study (16) at the National Oceanic and

<sup>1</sup>National Oceanic and Atmospheric Administration/Geophysical Fluid Dynamics Laboratory, 201 Forrestal Road, Princeton, NJ, 08540, USA. <sup>2</sup>Center for Coastal Physical Oceanography, Old Dominion University, 4111 Monarch Way, Norfolk, VA 23508, USA.

\*To whom correspondence should be addressed. E-mail: [Morris.Bender@noaa.gov](mailto:Morris.Bender@noaa.gov)

Atmospheric Administration's (NOAA) Geophysical Fluid Dynamics Laboratory (GFDL) using an 18-km grid regional atmospheric model (ZETAC) has demonstrated success in reproducing the trend and year-to-year variability in August-through-October Atlantic tropical cyclone frequency during 1980 to 2005 [supporting online material (SOM) text]. The modeled interannual variability of hurricane counts was well-correlated with observed counts ( $r = 0.86$ ) and exhibited an increasing trend during 1980 to 2005, although the modeled count was somewhat larger than what was observed.

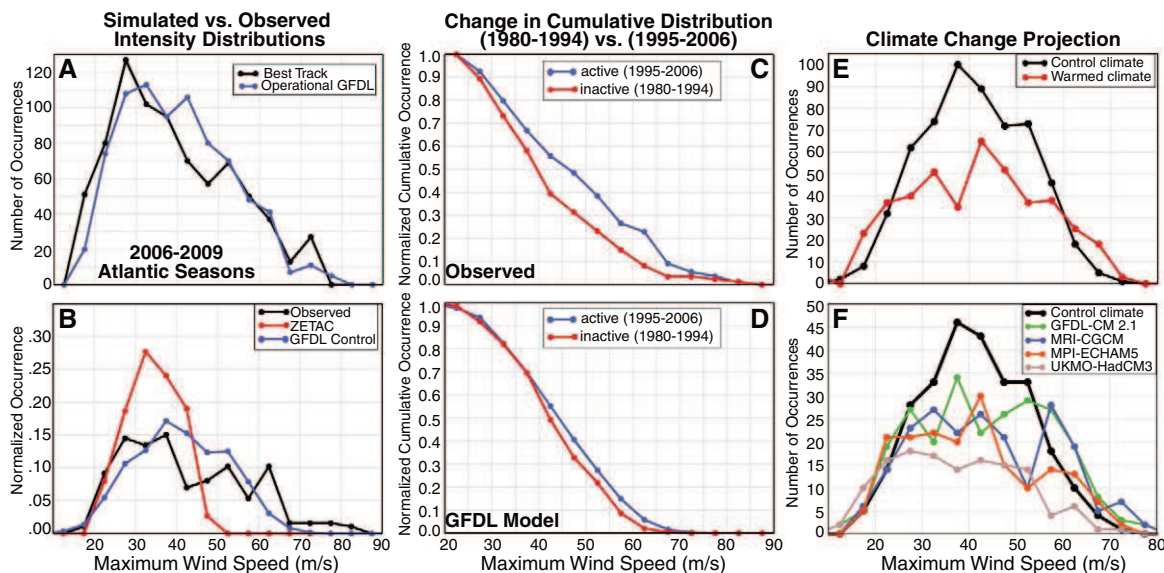
Hurricane frequency in a globally warmed, late-21st-century climate was investigated in a subsequent study (9) by perturbing the mean atmospheric state and SSTs given in (16) by an

ensemble-mean (18 models) late-21st-century climate change projection. The 18 models are from the World Climate Research Program coupled model intercomparison project 3 (CMIP3) (17) and use the Intergovernmental Panel on Climate Change (IPCC) A1B emissions scenario. The frequencies of both tropical storms and hurricanes in the ZETAC model were significantly reduced (−27% and −18%, respectively) in the warm climate relative to the control. However, the model was unable to simulate major hurricanes (category 3 to 5) with maximum winds greater than 50 m/s (Fig. 1B).

To improve the simulations of intensity, we extend the modeling approach of (9) by downscaling each individual model storm from that

study with two different operational versions of the GFDL hurricane model (18). The National Weather Service (NWS) version of the model (termed here GFDL) has been used operationally since 1995, and since 2001, it has been coupled to a three-dimensional ocean model (19). The system has remained largely unchanged from 2006 through 2009 and has been run on a large sample of tropical cyclones of varying intensity. The second closely related version of this hurricane model (GFDN) has been run operationally by the U.S. Navy since 1996 for tropical cyclone activity globally. The GFDN model was upgraded in 2008 and uses modified surface physics compared with the GFDL version, providing a test of robustness of our results.

**Fig. 1.** Simulated and observed histograms of maximum surface wind speed (m/s) in the Atlantic basin. (A) Simulated versus observed maximum winds for every 120-hour forecast made (at 6-hour intervals) during the 2006 to 2009 hurricane seasons, using the GFDL operational model run by NOAA's NWS (excluding depressions). (B) Normalized intensity histogram (dividing by the total number of storms) for the ZETAC regional model (red), the combined GFDL (NWS) and GFDN (Navy) downscalings (blue), and the observed (black) for the 27 seasons (1980 to 2006) of the control simulations. (C and D) Observed (C) and simulated (D) cumulative maximum wind distribution (CDFs) comparing the period 1995 to 2006 (blue) to 1980 to 1994 (red). (E) Comparison of control (black) and warm climate (red) distributions (combined GFDL and GFDN models) based on the 18-member CMIP3



ensemble A1B scenario climate change. (F) Comparison of control (black) and warm climate (colors) distributions for the GFDL and GFDN models based on the four individual CMIP3 model A1B warming scenarios. To save computer resources, the four supplemental experiments (F) were only run for the 13 odd years during 1981 to 2005.

**Table 1.** Comparison of observed and control storm counts from the GFDL downscaling experiments for various categories of storm intensity and the percent change for each of the five warmed climate conditions. Results for all 27 years from 1980 through 2006 are shown in the leftmost three columns, with the columns indicated by asterisks computed for the 13 odd years only. The results are from the average of storm counts for the two versions of the operational

hurricane model (versions run by NOAA's National Weather Service and the U.S. Navy). The warmed climate perturbation runs are based on downscaling the same seasons but with the addition of the mean climate change difference field between the 2001 to 2020 and the 2081 to 2100 periods from the CMIP3 model ensemble or the linear trend over 2000 to 2100 for each model, scaled to 80-year magnitude, for each of the four individual CMIP3 models (SOM text).

Type of storm	Number of observed storms (average storms per year)	Number of storms in control (average storms per year)	Ensemble warmed climate (every year; percent change)	Ensemble warmed climate* (percent change)	GFDL-CM2.1 warmed climate* (percent change)	MRI-CGCM warmed climate* (percent change)	MPI-ECHAM5 warmed climate* (percent change)	UKMO-HADCM3 warmed climate* (percent change)
Tropical storms and hurricane	9.0	10.9	−28%	−28%	−4%	−22%	−33%	−49%
Hurricane (33 m/s or above)	5.3	8.0	−32%	−33%	−7.5%	−24%	−40%	−60%
Major hurricane	2.4	2.7	−18%	−18%	40%	8%	−30%	−60%
Category 4 and 5	1.4	0.59	81%	75%	110%	110%	21%	−53%
Winds greater than 65 m/s	0.52	0.11	250%	220%	160%	180%	80%	−60%



Operational forecasts from the GFDL hurricane model have a distribution of maximum winds that agrees well with observations (Fig. 1A and fig. S1), and the model simulates a much more realistic distribution of intense hurricane winds than the ZETAC regional model does (Fig. 1B). To evaluate the GFDL model's ability to simulate the interdecadal variability of Atlantic hurricane intensities, we compared the observed and simulated cumulative distribution functions (CDFs) of maximum wind for the relatively inactive and active eras of 1980 to 1994 and 1995 to 2006 (Fig. 1, C and D). The observed CDF (Fig. 1C) is shifted toward higher intensities in the more-active era. The GFDL model (Fig. 1D) reproduces this tendency toward higher intensities, but underpredicts the magnitude of the change. The intensity distributions in Fig. 1, A and B, and the qualitative simulation in Fig. 1, C and D, of the multidecadal increase of hurricane intensity raises our confidence in the model's ability to simulate the effects of changes in the storm environment on intensity. However, the model's underprediction of the magnitude of the multidecadal intensity signal provides a note of caution. Future studies with significantly increased model horizontal resolution and explicit treatment of convection could potentially alter sensitivities to wind shear and other environmental conditions.

Despite the reduced storm frequency that was simulated in ZETAC (9), the distribution of maximum winds of the downscaled storms from the hurricane model shows an increase in the number of the most intense storms for the warmer climate compared with the control climate (Fig. 1E). Focusing on the category 4 and 5 hurricanes with maximum winds greater than 60 m/s, the total number (GFDL plus GFDN) increased sharply from 24 to 46. Hurricanes with winds greater than 65 m/s increased from 6 to 21.

Four individual CMIP3 global models were also downscaled using the same two-step methodology as is used in the 18-model ensemble. These four individual CMIP3 models (17) are the GFDL-CM2.1, the Japanese Meteorological Research Institute MRI-CGCM, the Max Planck Institute MPI-ECHAM5, and the Hadley Centre UK Meteorological Office UKMO-HadCM3. Because we used a single realization of the late-21st-century climate scenario (A1B) from each global model, the simulation results may differ between models in part because of internal variability, as well as because of differences in the global model formulations or precise forcings, although our experimental design attempts to reduce the influence of internal variability on the results (SOM text).

Figure 1F shows the intensity distributions obtained from downscaling the four individual CMIP3 models. The substantial differences between the resulting projections of intense hurricane activity imply that there are important differences among the large-scale environment changes projected by the 18-model ensemble (fig. S2) and by the individual models (fig. S3).

The largest increase in category 4 and 5 hurricane numbers is simulated for the GFDL-CM2.1 and MRI-ECHAM5 models, with each

exhibiting an increase of over 100% (Table 1), despite simulated reductions in the total number of hurricanes by 8% and 24%, respectively. On

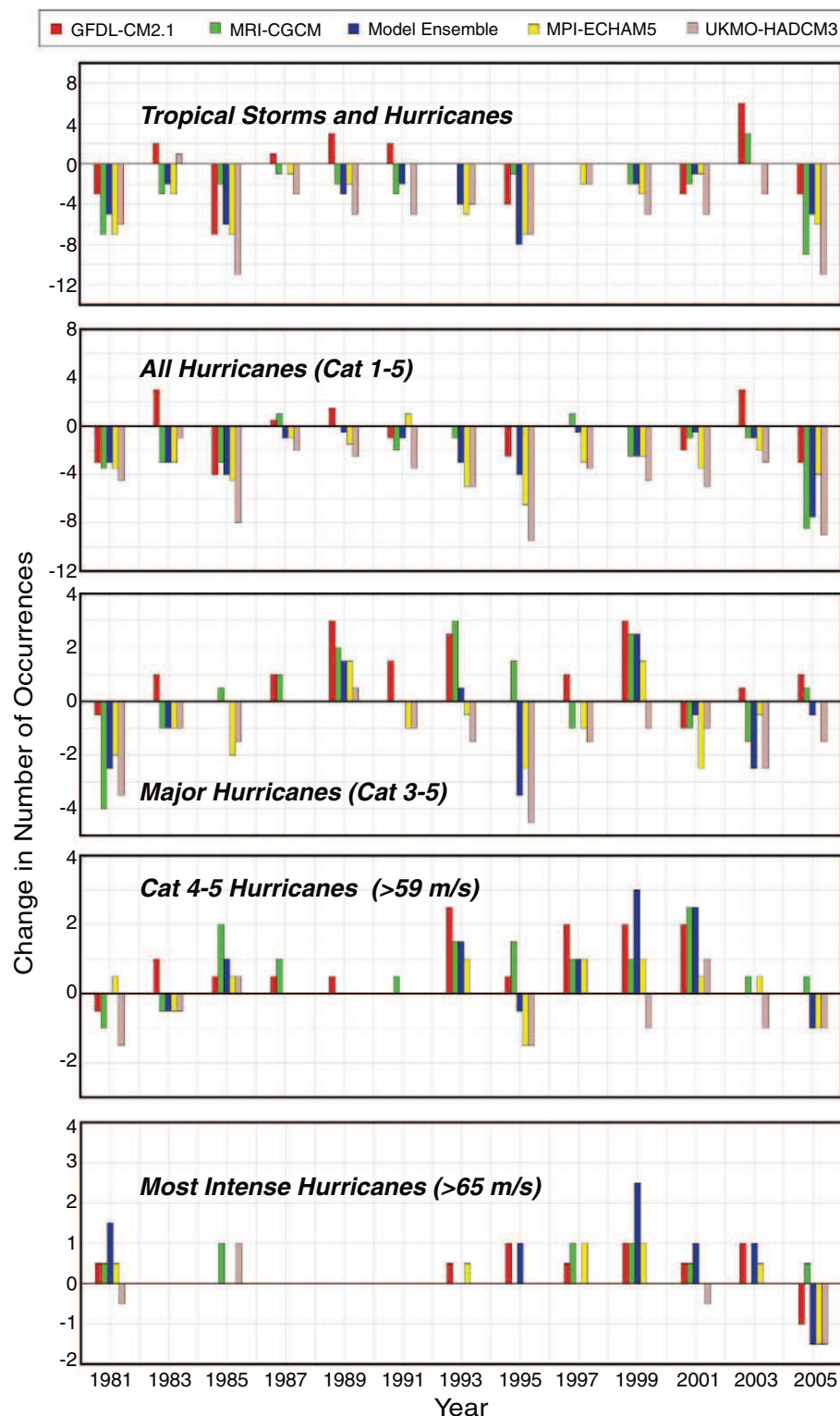


**Fig. 2.** Annual changes in storm counts for each odd year (1981 to 2005) warm minus control, for each of the five warmed climate scenarios. Results are shown for five categories of storm intensity (tropical storms and hurricanes, hurricanes, major hurricanes, category 4 and 5 hurricanes, and strong category 4+ hurricanes with maximum winds greater than 65 m/s). The five warmed climate scenarios plotted are the 18-model CMIP3 ensemble (blue), the GFDL-CM2.1 (red), the MRI-CGCM 2.3.2 (green), the MPI-ECHAM5 (yellow), and the UKMO-HadCM3 (gray). The results are computed from the average of storm counts for the two versions of the operational hurricane prediction model (GFDL and GFDN).

the other hand, the downscaling of the UKMO-HadCM3 produces a decrease in all categories of tropical cyclones. For the odd years, the most-intense simulated hurricanes (>65-m/s winds) in four of the five model projections (including the 18-model ensemble) showed an increase, ranging from 80 to 220%.

The year-by-year changes (warm minus control) of storm counts for each of the five down-scaled climates were examined (Fig. 2). Results are presented separately for five different classes of storm intensity. Reduced numbers of both tropical storms and hurricanes are simulated nearly every year in the warm climate runs. For

major hurricanes (category 3 to 5), a mix of increases and decreases is simulated, whereas for very intense hurricanes (category 4 and 5), a more robust increase in frequency results. Finally, the most intense hurricanes (>65 m/s) showed either no change or an increase in every year except one.

**Fig. 3. (Left)** Tracks for all storms reaching category 4 or 5 intensity, for the control and the warmed 18-model ensemble conditions, as obtained using the GFDL/NWS hurricane model. **(Right)** The spatial distribution of category 4 and 5 occurrences (scaled by storm counts per decade) for the combined control (average of the GFDL and GFDN model versions, top right); the combined CMIP3 18-model ensemble warmed climate results (middle right); and the difference between the warmed climate and control intense hurricane occurrences (bottom right). (The tracks for both the GFDL and GFDN models are presented in fig. S7 for comparison.)

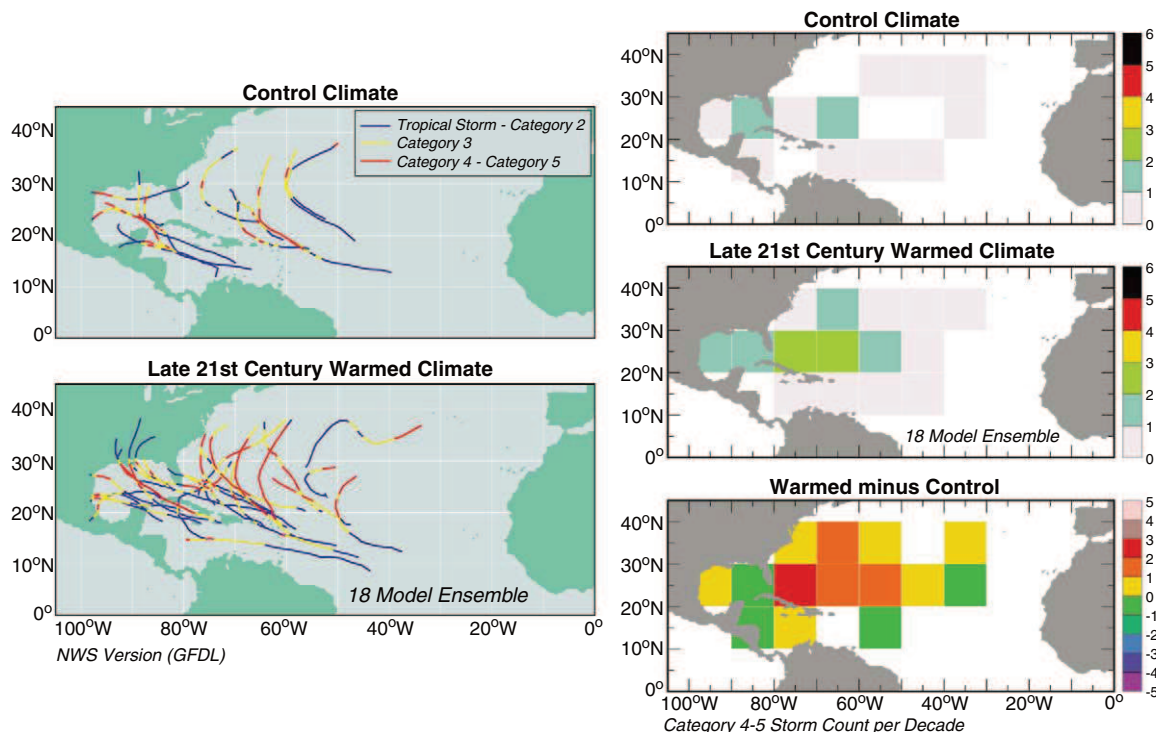
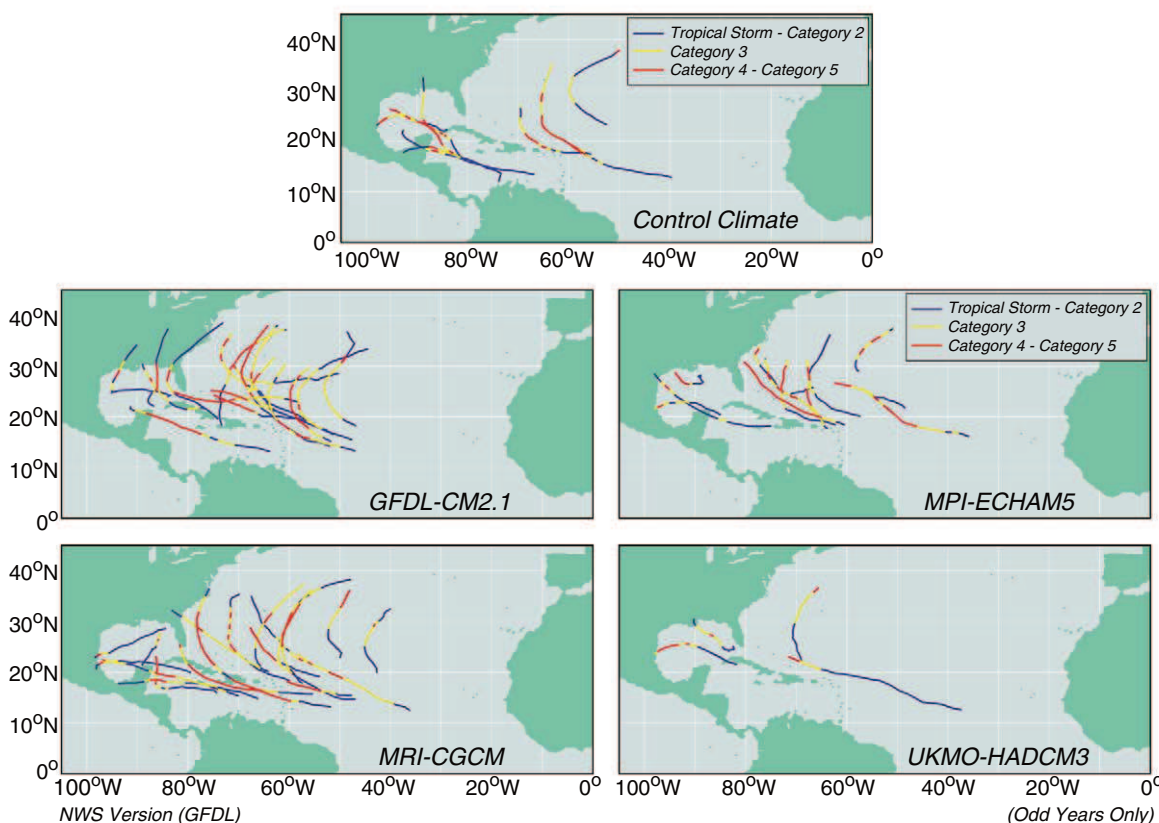


**Fig. 4. Model tracks** for all storms that eventually reached category 4 or 5 intensity, for the control (top) and the warm climate conditions provided by the four individual CMIP3 models. (The tracks shown are for the GFDL/NWS version of the hurricane model. For comparison, the results for the U.S. Navy's version of the model, GFDN, are presented in fig. S8).





The tracks and spatial distribution of category 4 and 5 hurricanes (Fig. 3) for the control and the warm climate (18-model ensemble) indicate that the largest increase of very intense hurricane activity is projected for the western Atlantic between 20°N and 40°N. This region corresponds fairly well with a region of increased potential intensity, reduced vertical wind shear, and increased SSTs (20) (fig. S2). In contrast, the ensemble mean exhibits an increase of shear in the Caribbean and mixed changes in the Gulf of Mexico (20) (fig. S2). The number of hurricane days for all categories, including category 4 and 5, decreases substantially in the Caribbean, with more modest decreases in the Gulf of Mexico (fig. S4).

The distribution of category 4 and 5 tracks and spatial distribution obtained from downscaling climate changes from the four individual CMIP3 models (Fig. 4 and fig. S6) show that for three of the four models, an increase of intense hurricane activity occurs in the region of the western Atlantic similar to the increase in the 18-model ensemble case. The decreased activity in the fourth model (UKMO-HadCM3) plausibly results from that model's relatively large projected increase in wind shear over much of the Atlantic south of 22°N (fig. S3), as well as a decrease in potential intensity in the western Atlantic equatorward of 25°N. In contrast, the GFDL-CM2.1 model projects reduced shear over most of the western Atlantic, whereas the MRI-CGCM and MPI-ECHAM5 models project shear changes (and simulated storm changes) between these two extremes. The differences between the individual GCM responses (fig. S3) and the ensemble-mean response (20) (fig. S2) give some indication of the uncertainty of the projected changes due to model formulation and/or forcing differences. Quantification of the relative influence of shear, potential intensity, or other environmental factors on these results is beyond the scope of this study.

The results in Figs. 3 and 4 used the GFDL/NWS version of the hurricane model. As a sensitivity test, the experiments were repeated using the alternative GFDN model. For both the 18-model CMIP3 ensemble (fig. S7) and the four individual CMIP3 models (fig. S8), the results are similar for the two operational models, increasing confidence in the robustness of our findings.

An analysis of normalized hurricane damage in the United States during 1900 to 2005 (21) indicates that major (category 3 to 5) and very intense (category 4 and 5) hurricanes at landfall accounted for 86% and 48% of all hurricane damage, respectively, despite accounting for only 24% and 6% of U.S. landfalls. Combining these findings with our model-based projections of the percent change in number of hurricanes for each category, we estimated changes in damage potential (table S1). For the CMIP3 ensemble mean and for two of four individual models, the increase in damage potential from the increase in very intense hurricanes outweighs the decrease in damage potential from the reduced occurrence of weaker systems. A damage potential increase of roughly 30% is pro-

jected for the CMIP3 18-model ensemble, with a range of roughly -50% to +70% among the four individual CMIP3 models. These estimates use projected storm changes over the entire North Atlantic basin. The estimate for the ensemble-mean CMIP3 model, in particular, would be increased if we took into account that the largest increase of intense hurricane frequency is projected for the western part of the basin.

For the downscaling of the 18-model CMIP3 ensemble-mean climate change, the frequency of category 4 and 5 hurricanes increased by 81% in 80 years (Table 1), corresponding to a linear trend of roughly +10% per decade. We estimate that the emergence time scale ( $p = 0.05$ ) for such a linear trend would be roughly 60 years, based on bootstrap resampling tests using noise characteristics from the observed category 4 and 5 hurricane time series since 1944 (SOM text).

The A1B scenario for the 21st century includes significant reductions in aerosols as well as increases in greenhouse gases; we have not attempted to separate the effects of these two forcings in our projections. To the extent that aerosol effects are significant, rescaling these projections to historical periods with a different mix of aerosol and greenhouse gas forcings is problematic. We refer to the mix of forcings in the A1B scenario as "A1B-like."

Assuming that we can rescale our model projections to the observed (~0.5°C) tropical Atlantic warming since 1944, the expected increase in category 4 and 5 hurricanes from 1944 to 2008 due to A1B-like anthropogenic effects is only about +20%, or about one-third of the projected change at our estimated time of signal emergence. Although our internal variability estimate is very uncertain, these results suggest that one would not expect to detect an A1B-like anthropogenic influence on Atlantic basin category 4 and 5 frequency at the present time.

The observed category 4 and 5 time series for 1944 to 2008 (fig. S9), which incorporates a downward adjustment of intensities for certain storm classes during 1944 to 1969 (22), shows a pronounced increase since the 1970s. The frequency also increases by more than a factor of two, in terms of the estimated linear trend, over the period 1944 to 2008. We suspect, however, that the trend since 1944 is biased high because of changes in the capabilities of observing systems during the record, although a quantitative evaluation of such a bias is beyond the scope of this study. In addition to data problems (13, 22), the potential influence on trends of Atlantic multidecadal variability (4) is cause for concern. If one has confidence in our downscaling results, and assumes that our A1B downscaling can be rescaled to apply to 1944 to 2008, this leads to a trend that is less than one-fifth of the observed magnitude. Such a small trend argues against the interpretation of the larger observed trend as resulting from a (rescaled) A1B-like anthropogenic forcing. On the other hand, our model's underestimate of the difference in intensity distributions between active and inactive periods (Fig. 1, C versus D) raises some note of caution

concerning our model's estimate of anthropogenic intensity trends.

Our results suggest that a significant anthropogenic increase in the frequency of very intense Atlantic hurricanes may emerge from the background climate variability in the latter half of the 21st century, despite a projected decrease in the overall number of hurricanes. These findings are dependent on the global climate models used to provide the environmental conditions for our downscaling experiments. Future studies should reassess our findings using both updated climate model projections and improved hurricane simulation models.

## References and Notes

1. S. Solomon et al., Eds., *Climate Change 2007: The Physical Science Basis. Contribution of Working Group I to the Fourth Assessment Report of the Intergovernmental Panel on Climate Change* (Cambridge Univ. Press, Cambridge, 2007).
2. B. D. Santer et al., *Proc. Natl. Acad. Sci. U.S.A.* **103**, 13905 (2006).
3. N. P. Gillett, P. A. Stott, B. D. Santer, *Geophys. Res. Lett.* **35**, L09707 (2008).
4. R. Zhang, T. L. Delworth, *Geophys. Res. Lett.* **33**, L17712 (2006).
5. A. T. Evan, D. J. Vimont, A. K. Heidinger, J. P. Kossin, R. Bennart, *Science* **324**, 778 (2009).
6. M. Mann, K. Emanuel, *Eos* **87**, 233 (2006).
7. J. B. Elsner, J. P. Kossin, T. H. Jagger, *Nature* **455**, 92 (2008).
8. K. A. Emanuel, *Nature* **436**, 686 (2005).
9. T. R. Knutson, J. J. Sirutis, S. T. Garner, G. A. Vecchi, I. M. Held, *Nat. Geosci.* **1**, 359 (2008).
10. M. Zhao, I. M. Held, S. J. Lin, G. A. Vecchi, *J. Clim.*, **22**, 6653 (2009).
11. G. A. Vecchi, K. L. Swanson, B. J. Soden, *Science* **322**, 687 (2008).
12. G. J. Holland, P. J. Webster, *Philos. Trans. R. Soc.* **365**, 2695 (2007).
13. G. A. Vecchi, T. R. Knutson, *J. Clim.* **21**, 3580 (2008).
14. L. K. Bengtsson et al., *Tellus* **59A**, 539 (2007).
15. S. Gualdi, E. Scoccimarro, A. Navarra, *J. Clim.* **21**, 5204 (2008).
16. T. R. Knutson, J. J. Sirutis, S. T. Garner, I. M. Held, R. E. Tuleya, *Bull. Am. Meteorol. Soc.* **88**, 1549 (2007).
17. G. A. Meehl et al., *Bull. Am. Meteorol. Soc.* **88**, 1383 (2007).
18. M. A. Bender, I. Ginis, R. E. Tuleya, B. Thomas, T. Marchok, *Mon. Weather Rev.* **135**, 3965 (2007).
19. M. A. Bender, I. Ginis, *Mon. Weather Rev.* **128**, 917 (2000).
20. G. A. Vecchi, B. J. Soden, *Geophys. Res. Lett.* **34**, L08702 (2007).
21. R. A. Pielke et al., *Nat. Hazards Rev.* **9**, 29 (2008).
22. K. Emanuel, *J. Clim.* **20**, 5497 (2007).
23. We wish to thank T. Marchok, R. Stouffer, A. Wittenburg, and three Science reviewers for their helpful comments and suggestions on earlier versions of the manuscript. We are also grateful to T. Marchok for his assistance in the preparation of several figures and to S. Sellars for assistance with some statistical calculations. Special appreciation goes to the current director of GFDL, V. Ramaswamy, for his support and encouragement. We thank the CMIP3 modeling groups, the Program for Climate Model Diagnosis and Intercomparison (PCMDI), and the World Climate Research Programme's (WCRP) Working Group on Coupled Modelling (WGCM) for their roles in making available the WCRP CMIP3 multi-model dataset. Support of this dataset is provided by the Office of Science, U.S. Department of Energy.

**Supporting Online Material** [www.sciencemag.org/cgi/content/full/327/5964/454/DC1](http://www.sciencemag.org/cgi/content/full/327/5964/454/DC1) Materials and Methods  
SOM Text  
Figs. S1 to S9  
Table S1  
References

13 August 2009; accepted 23 November 2009

# Requirement of Prorenin Receptor and Vacuolar H<sup>+</sup>-ATPase-Mediated Acidification for Wnt Signaling

Cristina-Maria Cruciati,<sup>1\*</sup> Bisei Ohkawara,<sup>1\*</sup> Sergio P. Acebron,<sup>1</sup> Emil Karaulanov,<sup>1</sup> Carmen Reinhard,<sup>1</sup> Dierk Ingelfinger,<sup>2</sup> Michael Boutros,<sup>2</sup> Christof Niehrs<sup>1†</sup>

Wnt/β-catenin signaling is important in stem cell biology, embryonic development, and disease, including cancer. However, the mechanism of Wnt signal transmission, notably how the receptors are activated, remains incompletely understood. We found that the prorenin receptor (PRR) is a component of the Wnt receptor complex. PRR functions in a renin-independent manner as an adaptor between Wnt receptors and the vacuolar H<sup>+</sup>-adenosine triphosphatase (V-ATPase) complex. Moreover, PRR and V-ATPase were required to mediate Wnt signaling during antero-posterior patterning of *Xenopus* early central nervous system development. The results reveal an unsuspected role for the prorenin receptor, V-ATPase activity, and acidification during Wnt/β-catenin signaling.

Wnt/β-catenin signaling is implicated in stem cell biology and human disease, including cancer, and has important roles during embryonic development, such as axis formation and patterning of the central nervous system (1–4). Wnt binding to its receptors,

low-density lipoprotein receptor-related protein 6 (LRP6) and frizzled (Fz), induces receptor aggregation in signalosomes (5) and phosphorylation of LRP6 by the kinases casein kinase 1γ (CK1γ) (6) and glycogen synthase kinase 3 (GSK3) (7). This requires the action of dishevelled (Dvl) and leads to recruitment of the negative regulator axin, thus stabilizing β-catenin (5, 8, 9).

To identify previously undescribed Wnt pathway components regulating Wnt receptors, we carried out a genome-wide small inhibitory RNA (siRNA) screen and identified the prorenin receptor gene (*PRR*) (10). In brief, human embryonic kidney (HEK293T) cells were transfected individually with siRNA pools targeting about

18,500 human genes, stimulated with Wnt3a, and analyzed for transcription of a Wnt-responsive luciferase reporter (11). The PRR is a single spanning transmembrane protein located at the plasma membrane that transmits renin and prorenin signals (12–16). Hypomorphic *PRR* mutation causes mental retardation and epilepsy in humans (17). PRR has a short cytoplasmic domain mediating renin signal transduction but contains no obvious motifs (18).

Three independent siRNAs targeting *PRR* inhibited luciferase reporter activity stimulated by Wnt3a but not by β-catenin, attesting to the specificity of the effect (Fig. 1A and fig. S1). Although Wnt1 or Wnt3a signaling was inhibited by *PRR* siRNA, signaling induced by downstream components of the Wnt pathway, including constitutively active LRP6 (LRP6ΔE1-4), Dvl, or β-catenin, remained unaffected (Fig. 1B). This indicates that PRR is required for Wnt/β-catenin signaling at the level of or upstream of the coreceptor LRP6, consistent with it being a transmembrane protein. Overexpressed PRR did not activate Wnt/β-catenin signaling by itself, but a C-terminally truncated construct (PRRΔC) synergized with Wnt3a in reporter activation (Fig. 1C), in causing duplication of the *Xenopus* embryonic axis (Fig. 1D), as well as in increasing transcription of the direct Wnt response gene *siamois* in *Xenopus* animal cap assays (Fig. 1E).

To analyze whether *PRR* is required for Wnt signaling in vivo, we studied its role in *Xenopus* embryos, where the gene shows weak expression in most tissues and prominent expression in the central nervous system (fig. S2A). Tadpoles that

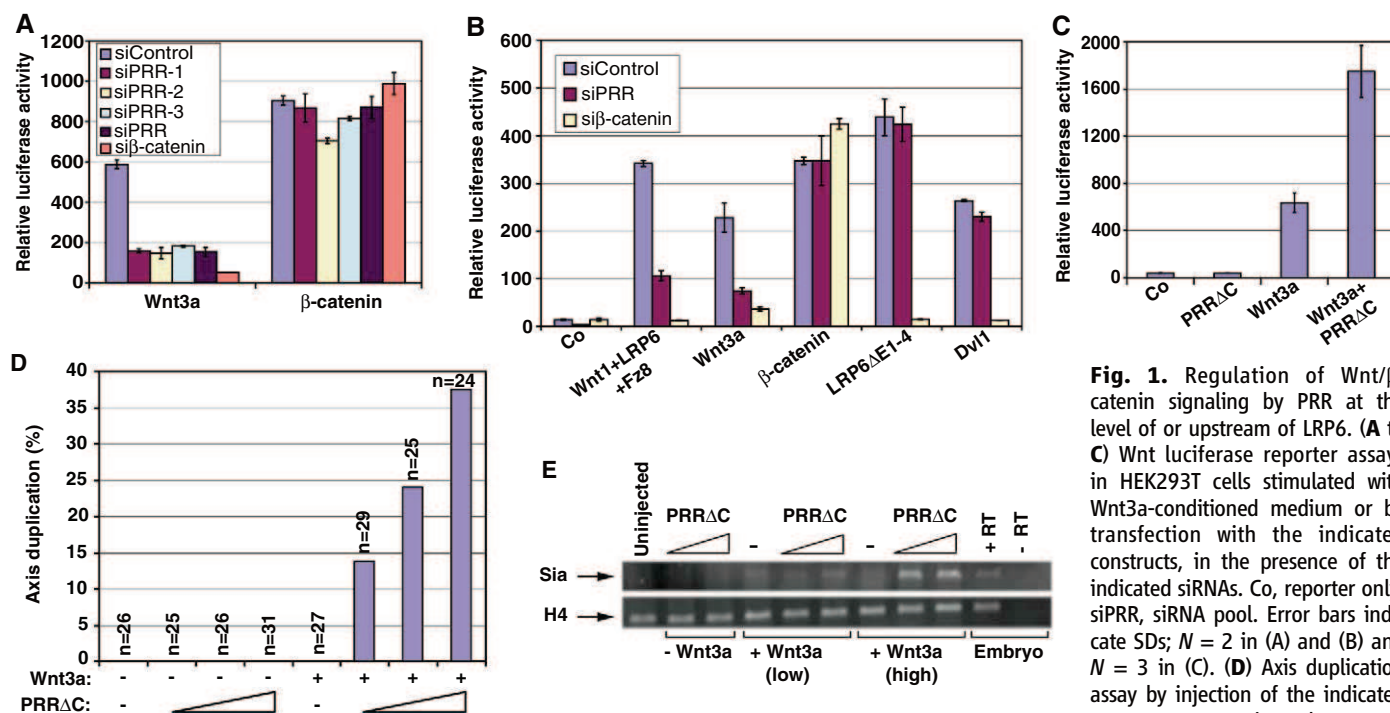


**Fig. 1.** Regulation of Wnt/β-catenin signaling by PRR at the level of or upstream of LRP6. (A to C) Wnt luciferase reporter assays in HEK293T cells stimulated with Wnt3a-conditioned medium or by transfection with the indicated constructs, in the presence of the indicated siRNAs. Co, reporter only; siPRR, siRNA pool. Error bars indicate SDs; *N* = 2 in (A) and (B) and *N* = 3 in (C). (D) Axis duplication assay by injection of the indicated *Xenopus* mRNAs into the ventral

blastomeres of *Xenopus* embryos at the four-cell stage. (E) Reverse transcription polymerase chain reaction (RT-PCR) analysis of animal caps from *Xenopus* embryos injected with the indicated mRNAs. Animal caps were excised from blastula embryos and cultivated until stage 10. Sia, siamois; H4, histone H4.



developed from cleavage-stage embryos injected with PRR antisense morpholino (Mo) oligonucleotides had small heads, shortened tails, and defects in melanocyte and eye pigmentation (Fig. 2, A and B). This phenotype appeared to be specific because it was efficiently rescued by co-injection of human *PRR* mRNA (Fig. 2, A and B). A very similar phenotype was observed for zebrafish *PRR* mutant embryos (19). Phenotypic rescue was also obtained by constructs with deletion in the intracellular domain ( $\Delta C$ ) but not those with deletions in the extracellular or transmembrane domain (Fig. 2B; see Fig. 3B for constructs), suggesting that PRR does not directly transduce a cytoplasmic signal in Wnt signaling.

In Wnt reporter assays in *Xenopus* embryos, PRR Mo inhibited both endogenous and Wnt3a-stimulated expression of luciferase (Fig. 2C). The requirement for PRR was specific for Wnt signaling. Nodal, fibroblast growth factor (FGF), and bone morphogenetic protein (BMP) signaling in *Xenopus* (fig. S3) and transforming growth factor- $\beta$  (TGF $\beta$ ), BMP, tumor necrosis factor- $\alpha$  (TNF $\alpha$ ), FGF, or phorbol myristyl acetate (PMA) signaling in HEK293T cells (fig. S4) were not affected by depletion of PRR.

Marker gene analysis in embryos depleted of PRR showed down-regulation of the forebrain marker *otx2* and the mid-hindbrain boundary marker *engrailed2* (*en2*), whereas the hind-brain marker *Krox20* was unaffected (Fig. 2D). Such embryos showed no changes in cell proliferation or apoptosis in the central nervous system (CNS) (fig. S5, A and B). They also showed no change in the mesodermal markers *Xbra* and *chordin* (fig. S5C). Taken together, these results indicate that loss of anterior marker gene expression represents a defect of antero-posterior neural patterning, wherein Wnt signaling is prominently involved (20). Injection of PRR Mo in the animal region, which gives rise to the neuroectoderm, reduced expression of *en2* and of the direct Wnt target gene *Axin2*, but not expression of *otx2*. Conversely, injection of PRR Mo in the vegetal region, thus targeting mesendodermal precursors, reduced expression of *otx2* but not that of *en2* (Fig. 2E). These results suggest an indirect PRR requirement for *otx2* expression and forebrain development through its effect to promote formation of dorsal mesoderm and a cell-autonomous requirement of PRR for *en2* expression and development of the mid-hindbrain. We conclude that PRR is required for Wnt signaling and anterior CNS patterning in *Xenopus* embryos.

Because *en2* is a well-characterized, direct Wnt target gene (21, 22), we focused on the requirement of PRR for *en2* expression. *Xenopus* animal caps were neuralized by injection with the BMP inhibitor chordin, which increased transcription of the gene encoding the pan-neural marker *NCAM* as well as the gene *en2* (Fig. 2F). PRR Mo specifically abolished expression of *en2* and *Axin2* but left *NCAM* unaffected. Expression of *en2* and *Axin2* was rescued by coinjection of human *PRR* mRNA as well as by  $\beta$ -catenin, but not

by *Wnt3a* DNA. These results (i) corroborate that PRR is essential for *en2* expression because of its requirement in Wnt signaling and (ii) indicate that PRR functions downstream of Wnts and upstream of  $\beta$ -catenin, consistent with the cell culture data, which placed PRR action at the level of Wnt receptors.

We therefore tested whether PRR bound to frizzled 8 (Fz8) or LRP6. In coimmunoprecipitation (CoIP) experiments with transfected cells,

PRR bound to both Fz8 and LRP6 but not to the control transmembrane protein FLRT3 (Fig. 3A). Deletion of the cytoplasmic domain ( $\Delta C$ ), which mediates renin signaling, had no effect on Wnt receptor binding (Fig. 3A) or the ability of the protein to rescue Wnt signaling in PRR siRNA-treated cells (Fig. 3C) or Mo-treated embryos (Fig. 2B). Although transmembrane domain-deleted protein ( $\Delta TMC$ ) also bound to the receptors, albeit weakly (Fig. 3A), it failed to rescue Wnt signaling

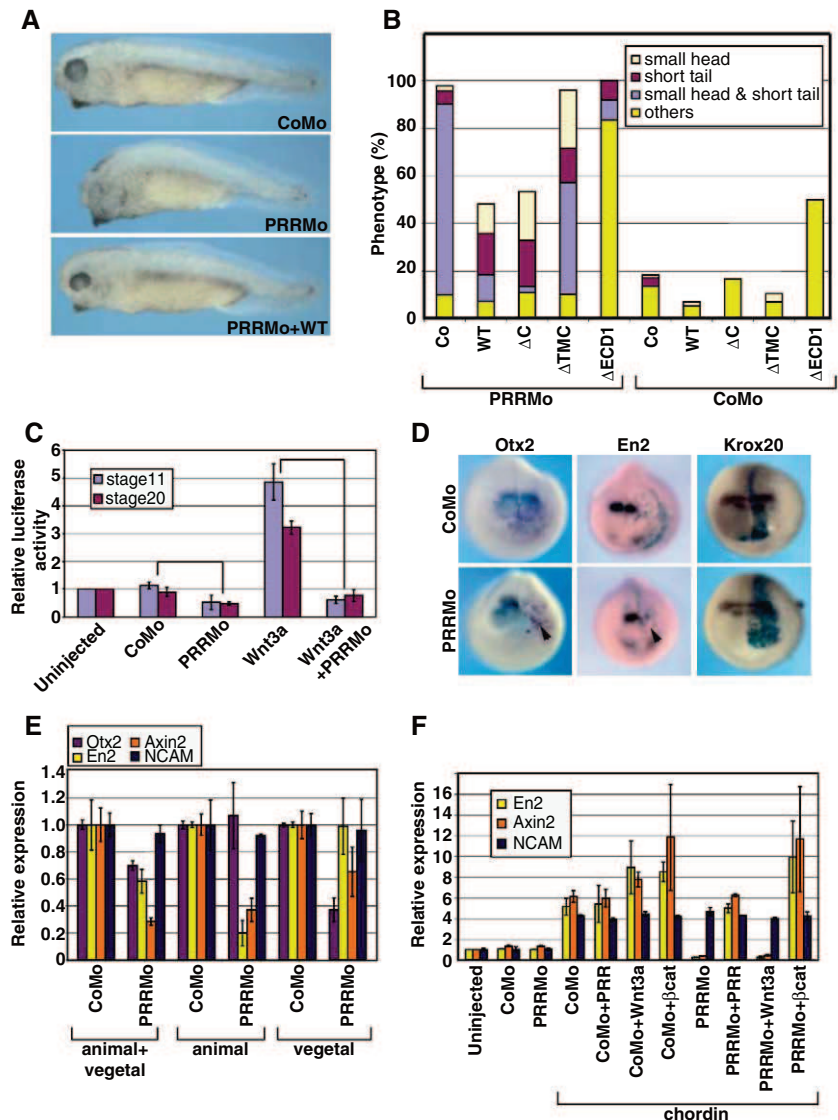


**Fig. 2.** Requirement of PRR for Wnt/ $\beta$ -catenin signaling and antero-posterior neural patterning in *Xenopus*. (A and B) Tailbud stage *Xenopus* embryos injected in all blastomeres of the animal hemisphere at the four-cell stage with PRR antisense Mo oligonucleotides in the absence or presence of wild-type or mutated human *PRR* mRNAs. (For *PRR* mutants, see Fig. 3B.) CoMo, control Mo; Co, PPL mRNA. (C) Wnt luciferase reporter assay of whole embryos at the indicated stages injected in all blastomeres at the animal pole with PRR Mo and/or Wnt3a mRNA. Luciferase activity in uninjected embryos was set to 1. Error bars indicate SDs;  $N = 3$ . (D) Whole-mount in situ hybridization of neurula-stage embryos injected in the animal blastomeres with the indicated Mo plus  $\beta$ -galactosidase mRNA lineage tracer (red or light blue), showing reduced expression (arrowheads) of *otx2* (65%,  $n = 26$ ) and *en2* (96%,  $n = 25$ ), but not of *Krox20* (0%,  $n = 24$ ). (E and F) Quantitative PCR (qPCR) analysis of indicated genes in neurulae (E) or animal caps cultured until neurula stage (F). Eight-cell-stage embryos were injected into indicated blastomeres (E) or animal 4 blastomeres (F) with PRRMo and the following mRNA and DNA: chordin mRNA, 250 pg; PRR mRNA, 200 pg; Wnt3a DNA, 50 pg; and  $\beta$ -catenin DNA, 100 pg. Error bars show SDs of biological triplicates. Gene expression in CoMo or uninjected explants was set to 1.

(Figs. 3C and 2B), suggesting that PRR transmembrane localization is essential. In contrast, the extracellular domain (ECD) was necessary for binding LRP6 or Fz8 and for Wnt signaling (Figs. 3A and 2B). These results corroborate the specificity of physical PRR-Wnt receptor interactions, which require the PRR ECD.

We confirmed these interactions in binding assays using soluble, recombinant proteins (fig. S6), as well as by CoIP of endogenous LRP6 and PRR (Fig. 3D). We also tested whether PRR binds Wnt but found no significant interaction. We conclude that both Wnt receptor binding and Wnt function require the PRR ECD but not the intracellular domain.

Prorenin is not expressed in early *Xenopus* embryos, and addition of renin had no effect in Wnt luciferase assays (fig. S7, A and B). Further, the PRR cytoplasmic domain, which mediates

renin signaling, is not required for its role in Wnt signaling. Moreover, there are PRR homologs in *Drosophila* and *Hydra* that have no renin. Thus, PRR may function in Wnt signaling in a renin-independent manner. Indeed, a PRR fragment, identified as adenosine triphosphatase (ATPase),  $H^+$ -transporting, lysosomal accessory protein 2 (ATP6AP2), interacts with the vacuolar  $H^+$ -ATPase (V-ATPase) (23). We confirmed that PRR binds (directly or indirectly) to the V-ATPase subunits ATP6V0C and ATP6V0D1 but not to control transmembrane proteins (Fig. 3, E and F). We mapped the interaction domain of PRR with ATP6V0C and show that the transmembrane and the ECD of PRR are required for binding ATP6V0C (fig. S8). The results indicate that PRR is associated with the V-ATPase, although the subunit directly contacting PRR remains to be determined.

The V-ATPase is a multiprotein complex localized in intracellular organelles and at the plasma membrane. It is involved in diverse processes such as phagocytosis, virus entry, metastasis, and embryonic left-right patterning. Its main mechanism is to pump protons and acidify vesicles, thereby promoting vesicular traffic, notably endocytosis (24, 25). Disruption of pH homeostasis in V-ATPase mutants leads to lethality in various organisms (26).

LRP6 signal transduction involves receptor aggregation in signalosomes and phosphorylation, for example at Thr<sup>1479</sup>, a process which requires Dvl (5). LRP6 phosphorylation is accompanied by receptor internalization in caveolin-containing vesicles, and endocytosis is essential for Wnt/ $\beta$ -catenin signaling (27, 28). This raised the possibility that PRR and V-ATPase may influence LRP6 endocytosis, phosphorylation, and  $\beta$ -catenin activation.

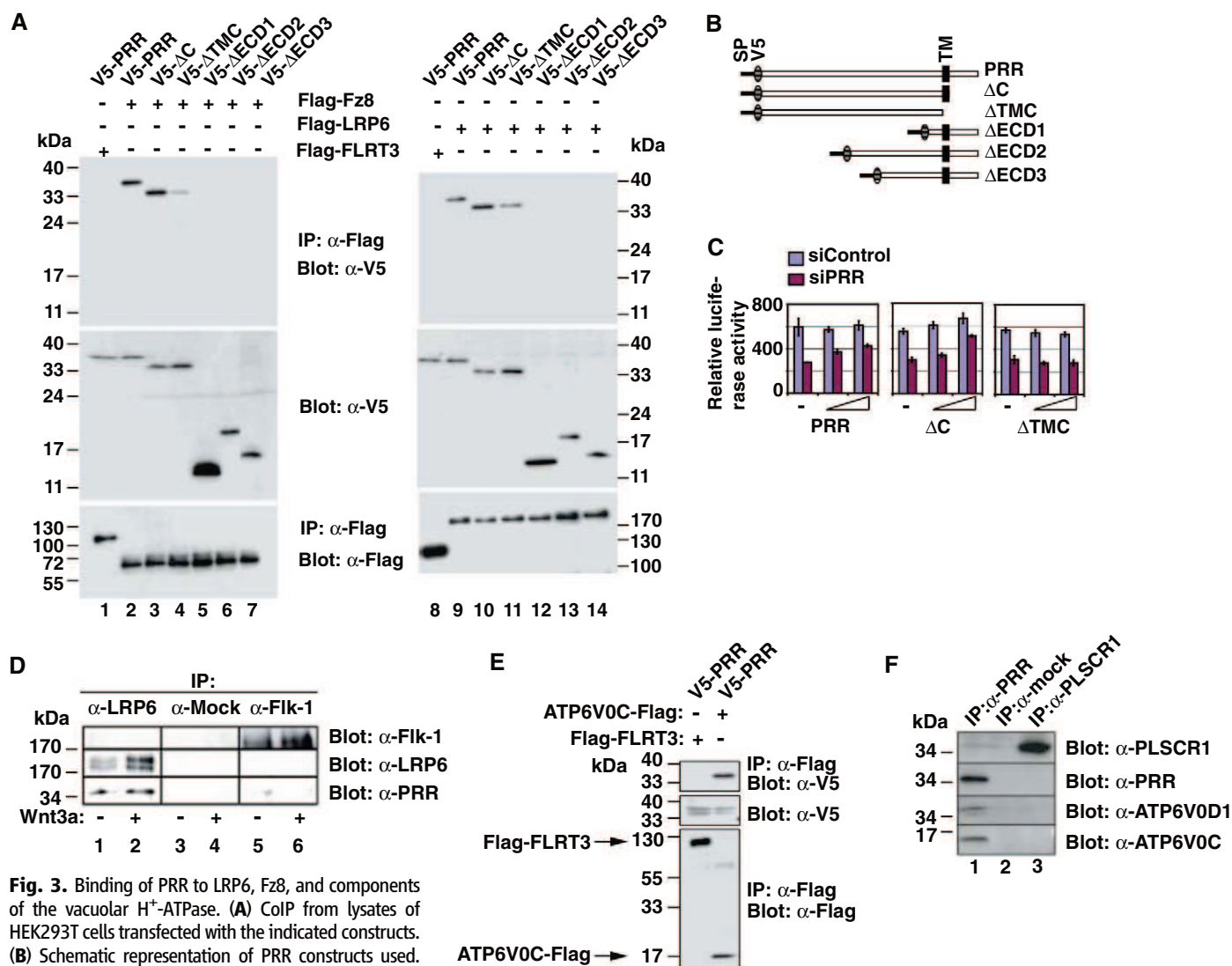


**Fig. 3.** Binding of PRR to LRP6, Fz8, and components of the vacuolar  $H^+$ -ATPase. (A) CoIP from lysates of HEK293T cells transfected with the indicated constructs. (B) Schematic representation of PRR constructs used. SP, signal peptide; TM, transmembrane domain; C, cytoplasmic domain; and TMC, cytoplasmic and transmembrane domains. (C) Wnt luciferase reporter assay in HEK293T cells transfected with control or PRR siRNA and stimulated with Wnt3a-conditioned medium in absence or presence of the indicated transfected Flag-tagged PRR constructs. Error bars indicate SDs;  $N = 3$ . (D) CoIP of endogenous PRR with endogenous LRP6 from lysates of

HEK293T cells in the presence or absence of Wnt3a. (E) CoIP of V5-PRR with Flag-tagged ATP6V0C from lysates of transfected HEK293T cells. Flag-FLRT3 serves as negative control. (F) CoIP of endogenous ATP6V0D1 and endogenous ATP6V0C with endogenous PRR from HEK293T lysates using antibody against PRR (anti-PRR). Anti-PLSCR1 serves as negative control.



Loss of function and pharmacological inhibition of V-ATPase in vitro and in vivo showed that this enzyme is required for Wnt/ $\beta$ -catenin signaling. In reporter assays, treatment of HEK293T cells with

siRNAs targeting two subunits of V-ATPase (ATP6V1C2 and ATP6V0C) inhibited Wnt signaling (Fig. 4A). Likewise, two pharmacologic V-ATPase inhibitors, apicaren and bafilomycin (29),

inhibited Wnt signaling (Fig. 4B). Neither V-ATPase siRNAs nor the pharmacologic inhibitors affected Wnt signaling stimulated by Dvl1, constitutively active LRP6 (LRP6 $\Delta$ E1-4), or  $\beta$ -catenin (Fig. 4A and fig. S9), consistent with a specific requirement for Wnt receptor activation. Furthermore, in *Xenopus* embryos, injection of mRNA encoding YCHE78, a well-characterized dominant-negative V-ATPase subunit E (30), elicited a very similar phenotype to that observed by treatment with PRR Mo. It inhibited expression of *otx2* and *en2* but not that of *Krox20* (Fig. 4C). In Wnt reporter assays in *Xenopus* embryos, YCHE78 inhibited both endogenous as well as Wnt3a-stimulated reporter activity, and low YCHE78 doses synergized with PRR Mo in Wnt inhibition, indicative of functional interaction (fig. S10). Lastly, in chordin-neuritized animal caps, YCHE78 inhibited expression of *en2* and *Axin2*, and this was rescued specifically by  $\beta$ -catenin but not by Wnt3a (Fig. 4D).

Our data indicate that V-ATPase activity is required for activation of the Wnt receptor. To test this, we treated mouse P19 embryonal carcinoma cells with Wnt3a and monitored phosphorylation of LRP6 by immunofluorescence microscopy (6). Phosphorylation of LRP6 was inhibited in cells treated with PRR/V-ATPase siRNA (fig. S11). Immunoblotting also showed that Wnt-stimulated phosphorylation of LRP6 in human teratocarcinoma (NTERA2) cells was inhibited by depletion of PRR, Dvl1-3, or ATP6V0C (Fig. 4E) or by treatment of NTERA2 and P19 cells with apicaren and bafilomycin (fig. S12). Similarly, Wnt3a-induced expression of *Axin2* was inhibited upon treatment of neuroblastoma SHEP cells with apicaren (fig. S12).

These results demonstrate that phosphorylation of LRP6 (which correlates with LRP6 activation) requires V-ATPase activity, suggesting that the receptor may need to enter an acidic intracellular compartment to become phosphorylated. To analyze acidification directly, we fused the extracellular domain of full-length LRP6 with the green fluorescent protein (GFP) pH-sensor variant pHluorin, which can be monitored by ratiometric imaging (31) (fig. S13, A and B). Fluorometric analysis of ratiometric-LRP6 (Ra-LRP6) in cell lysates indicated that the protein shows a higher fluorescence at the excitation wavelength of 488 nm than at 405 nm, when the pH is below pH  $\sim$  6.5 (fig. S13, C and D). In unstimulated live cells, fluorescence of transfected Ra-LRP6 was mostly undetectable. However, within minutes of Wnt treatment, Ra-LRP6 fluorescence was observed in intracellular vesicles (movie S1). The signal plateaued after 1 hour and was inhibited by apicaren treatment (Fig. 4F and fig. S13E). We also tested a fusion protein between pHluorin and constitutively active LRP6 (Ra-LRP6 $\Delta$ E1-4). LRP6 $\Delta$ E1-4 is spontaneously aggregating, is constitutively phosphorylated, and resides in signalosomes (5). Consistent with this, Ra-LRP6 $\Delta$ E1-4 showed punctate fluorescence even in unstimulated cells, indicating that it enters acidic vesicles spontaneously (Fig. 4F). Ra-LRP6 may also be a useful tool to monitor acute Wnt signaling in living cells.

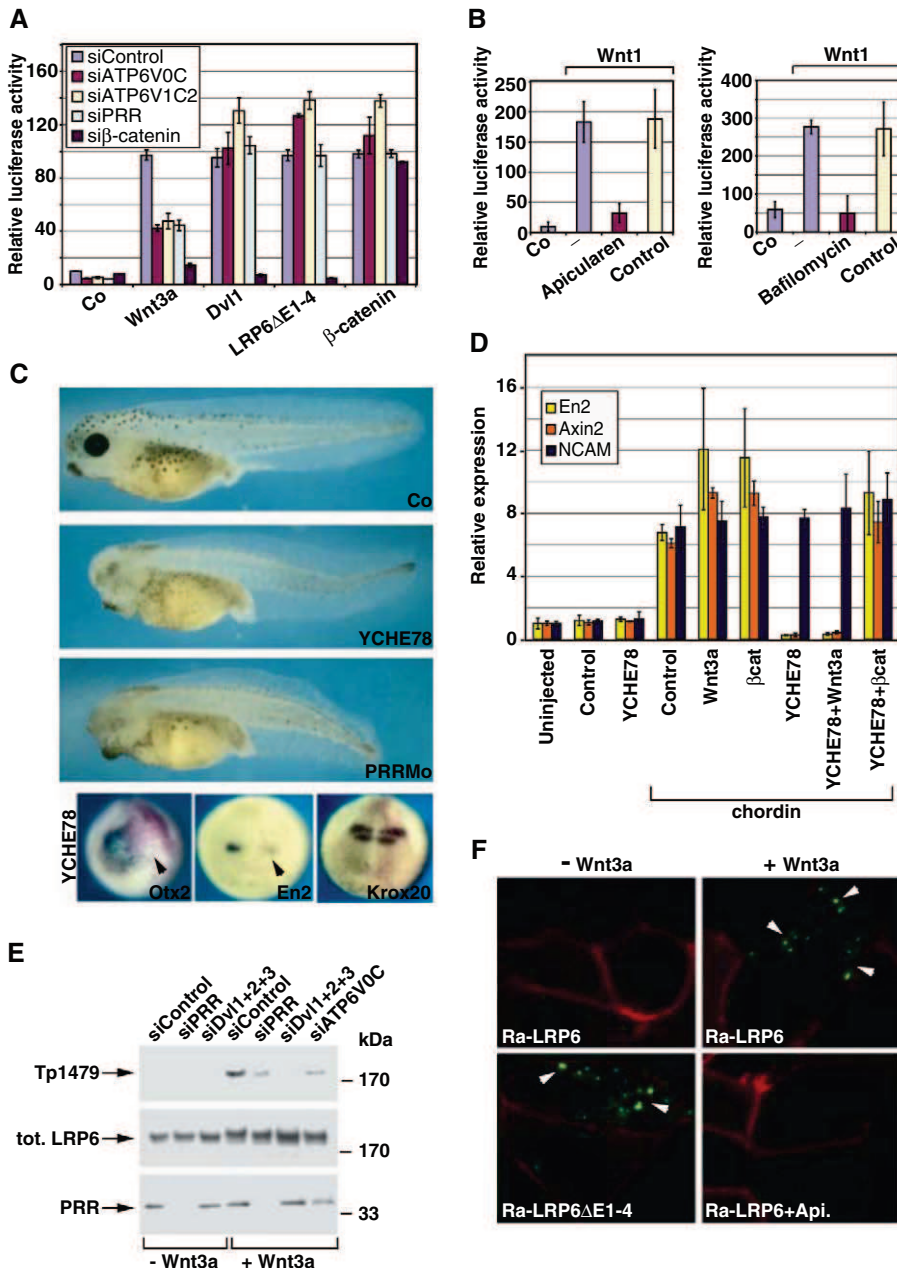


**Fig. 4.** Requirement of V-ATPase and acidification for Wnt/ $\beta$ -catenin signaling. **(A and B)** Wnt luciferase reporter assays in HEK293T cells stimulated with Wnt3a-conditioned medium or by transfection with Wnt1 and the indicated constructs in the presence of the indicated siRNAs or the V-ATPase inhibitors apicaren and bafilomycin A1. Error bars indicate SDs;  $N = 2$  and  $N = 3$ , respectively. **(C)** Tadpole-stage *Xenopus* embryos that had been injected in all animal blastomeres at the four-cell stage as indicated. (Bottom) In situ hybridization of *otx2*, *en2*, and *Krox20* at neurula stage. Injection of YCHE78 mRNA unilaterally reduced expression of *otx2* (67%,  $n = 60$ ) and *en2* (70%,  $n = 27$ ) but not significantly *Krox20* (11%,  $n = 27$ ), as indicated by arrowheads. Co-injected  $\beta$ -galactosidase mRNA was used as lineage tracer (red). **(D)** qPCR analysis of the indicated mRNAs was performed as described in Fig. 2F. **(E)** Western blot of endogenous LRP6 and PRR from NTERA2 cells treated with the indicated siRNAs and stimulated for 1 hour with Wnt3a-conditioned medium or control medium. tot. LRP6, total LRP6. **(F)** Live-cell confocal microscopy of ratiometric LRP6 in acidic compartments. HEK293T cells were transfected with Ra-LRP6 or Ra-LRP6 $\Delta$ E1-4 and membrane-anchored RFP (red) and treated for 1 hour with control or Wnt3a-conditioned medium, respectively, in the absence or presence of apicaren (Api). Images were acquired by excitation at 405 and 488 nm and subtracting frames ( $f_{488} - f_{405}$ ) to monitor reporter proteins in acidic compartments (green).

Our data reveal an unsuspected role of the prorenin receptor PRR in Wnt/ $\beta$ -catenin signaling and provide evidence that this multifunctional protein interacts with V-ATPase. We propose a mechanism wherein PRR is part of the Wnt receptor complex, acting as a specific adaptor between LRP6 and V-ATPase. Upon Wnt stimulation, this signaling complex is endocytosed, and across the vesicle membrane V-ATPase generates a proton gradient that is essential for LRP6 phosphorylation and hence  $\beta$ -catenin activation. Our results raise intriguing questions about the role of PRR in renin signaling and mental retardation and the immediate consequence of acidification in Wnt receptor signaling. The  $\text{Na}^+\text{-H}^+$  exchanger Nhe2 is required for Fz-planar cell polarity signaling in *Drosophila* (32), suggesting that electrochemical regulation may have multiple roles in Wnt receptor signaling. The V-ATPase may also provide a therapeutic target to modulate Wnt signaling in a disease context.

#### References and Notes

1. P. Polakis, *Genes Dev.* **14**, 1837 (2000).
2. C. Y. Logan, R. Nusse, *Annu. Rev. Cell Dev. Biol.* **20**, 781 (2004).
3. R. T. Moon, A. D. Kohn, G. V. De Ferrari, A. Kaykas, *Nat. Rev. Genet.* **5**, 691 (2004).
4. H. Clevers, *Cell* **127**, 469 (2006).
5. J. Bilic *et al.*, *Science* **316**, 1619 (2007).
6. G. Davidson *et al.*, *Nature* **438**, 867 (2005).
7. X. Zeng *et al.*, *Nature* **438**, 873 (2005).
8. X. Zeng *et al.*, *Development* **135**, 367 (2008).
9. J. Mao *et al.*, *Mol. Cell* **7**, 801 (2001).
10. Materials and methods are available as supporting material on Science Online.
11. V. Korinek *et al.*, *Science* **275**, 1784 (1997).
12. G. Nguyen *et al.*, *J. Clin. Invest.* **109**, 1417 (2002).
13. J. J. Saris *et al.*, *Hypertension* **48**, 564 (2006).
14. Y. Huang, N. A. Noble, J. Zhang, C. Xu, W. A. Border, *Kidney Int.* **72**, 45 (2007).
15. M. Sakoda *et al.*, *Hypertens. Res.* **30**, 1139 (2007).
16. A. Contrepas *et al.*, *Am. J. Physiol. Regul. Integr. Comp. Physiol.* **297**, R250 (2009).
17. J. Ramser *et al.*, *Hum. Mol. Genet.* **14**, 1019 (2005).
18. D. J. Campbell, *Hypertension* **51**, 1259 (2008).
19. A. Amsterdam *et al.*, *Proc. Natl. Acad. Sci. U.S.A.* **101**, 12792 (2004).
20. C. Kiecker, C. Niehrs, *Development* **128**, 4189 (2001).
21. A. P. McMahon, A. L. Joyner, A. Bradley, J. A. McMahon, *Cell* **69**, 581 (1992).
22. L. L. McGrew, K. Takemaru, R. Bates, R. T. Moon, *Mech. Dev.* **87**, 21 (1999).
23. J. Ludwig *et al.*, *J. Biol. Chem.* **273**, 10939 (1998).
24. M. Forgac, *Nat. Rev. Mol. Cell Biol.* **8**, 917 (2007).
25. V. Marshansky, M. Futai, *Curr. Opin. Cell Biol.* **20**, 415 (2008).
26. K. W. Beyenbach, H. Wiecek, *J. Exp. Biol.* **209**, 577 (2006).
27. J. T. Blitzer, R. Nusse, *BMC Cell Biol.* **7**, 28 (2006).
28. H. Yamamoto, H. Komekado, A. Kikuchi, *Dev. Cell* **11**, 213 (2006).
29. A. George, H. Leahy, J. Zhou, P. J. Morin, *Neurobiol. Dis.* **26**, 125 (2007).
30. M. Lu *et al.*, *J. Biol. Chem.* **277**, 38409 (2002).
31. G. Miesenböck, D. A. De Angelis, J. E. Rothman, *Nature* **394**, 192 (1998).
32. M. Simons *et al.*, *Nat. Cell Biol.* **11**, 286 (2009).
33. We thank H. Clevers, R. Grosschedl, X. He, R. Moon, J. Nathans, R. Nusse, M. Levin, G. Miesenböck, Y. M. Chan, M. A. Skinner, and M. Lorizate for reagents; Y. L. Huang for confocal microscopy; A. Glinka for recombinant Wnt3a-V5; and T. Büchling and K. Bartscherer for sharing data before publication and discussion. This work was supported by the Deutsche Forschungsgemeinschaft and the European Commission (Endotrack and Marie-Curie Program). S.P.A. is a recipient of a fellowship from Gobierno Vasco.

**Supporting Online Material** www.sciencemag.org/cgi/content/full/327/5964/459/DC1 Materials and Methods  
Figs. S1 to S13  
Table S1  
References  
Movie S1

28 July 2009; accepted 4 December 2009  
10.1126/science.1179802

# Identification of RACK1 and Protein Kinase C $\alpha$ as Integral Components of the Mammalian Circadian Clock

Maria S. Robles,\*† Cyril Boyault,\* Darko Knutti,\*‡ Kiran Padmanabhan, Charles J. Weitz§

At the core of the mammalian circadian clock is a negative feedback loop in which the dimeric transcription factor CLOCK-BMAL1 drives processes that in turn suppress its transcriptional activity. To gain insight into the mechanisms of circadian feedback, we analyzed mouse protein complexes containing BMAL1. Receptor for activated C kinase-1 (RACK1) and protein kinase C- $\alpha$  (PKC $\alpha$ ) were recruited in a circadian manner into a nuclear BMAL1 complex during the negative feedback phase of the cycle. Overexpression of RACK1 and PKC $\alpha$  suppressed CLOCK-BMAL1 transcriptional activity, and RACK1 stimulated phosphorylation of BMAL1 by PKC $\alpha$  in vitro. Depletion of endogenous RACK1 or PKC $\alpha$  from fibroblasts shortened the circadian period, demonstrating that both molecules function in the clock oscillatory mechanism. Thus, the classical PKC signaling pathway is not limited to relaying external stimuli but is rhythmically activated by internal processes, forming an integral part of the circadian feedback loop.

Circadian clocks are oscillators that drive daily biological rhythms. In mammals, circadian clocks are intrinsic to most tissues (1, 2). At the core of the clock is a negative feedback loop (3) in which the dimeric transcription factor CLOCK-BMAL1 (4) drives transcription of *Period* (*Per*) and *Cryptochrome* (*Cry*) genes. PER and CRY proteins in turn enter the nucleus and suppress CLOCK-BMAL1 activity

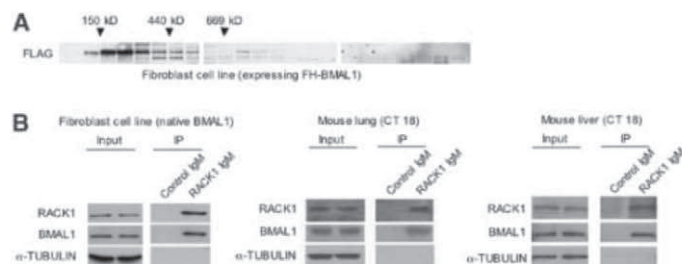
by an unknown mechanism. Phosphorylation of CLOCK and BMAL1 appears to be important in circadian feedback, affecting CLOCK-BMAL1

activity and/or stability (5–8). Degradation of PERs and CRYs (9–12) derepresses CLOCK-BMAL1 activity, initiating a new cycle.

To gain insight into circadian clock negative feedback, we searched for proteins in a complex with BMAL1 at the time when CLOCK-BMAL1 activity was suppressed. BMAL1 complexes, extracted from mouse fibroblasts [BLi cells (13)] or tissues collected during the phase of negative feedback, were initially characterized by sucrose density gradient centrifugation. The majority of BMAL1 was in complexes of 200 to 400 kD, but some was in larger complexes, particularly in the liver (fig. S1A).

For isolation of BMAL1 complexes, we used FH-BMAL1, a tagged BMAL1 with a FLAG-hemagglutinin (FH) tandem epitope (14) at the N terminus (fig. S1B). Stably expressed FH-BMAL1 [EFH cells (13)] was similar to BMAL1 in transcriptional activity and in suppression by CRY1 (fig. S2A), and it was mostly in complexes of 200 to 400 kD (Fig. 1A). FH-BMAL1 thus preserved the basic transcriptional and biochemical properties of BMAL1.

**Fig. 1.** Identification of RACK1 as a component of a BMAL1 protein complex by proteomics analysis. (A) Sucrose density gradient sedimentation (5 to 45% sucrose, from left to right) of FH-BMAL1 protein complexes from mouse fibroblasts stably expressing FH-BMAL1. Image shows a Western blot probed with anti-FLAG. (B) Immunoprecipitation of endogenous BMAL1 with endogenous RACK1. Extracts from fibroblasts, liver, or lung (input) and proteins immunoprecipitated (IP) with antibody to RACK1 or control IgG were probed with antibodies to RACK1, BMAL1, and  $\alpha$ -TUBULIN, as indicated. CT, circadian time.



Department of Neurobiology, Harvard Medical School, Boston, MA 02115, USA.

\*These authors contributed equally to this work.

†Present address: Proteomics and Signal Transduction, Max Planck Institute for Biochemistry, D-82152 Martinsried, Germany.

‡Present address: DSM Nutritional Products, Basel 4002, Switzerland.

§To whom correspondence should be addressed. E-mail: cweitz@hms.harvard.edu



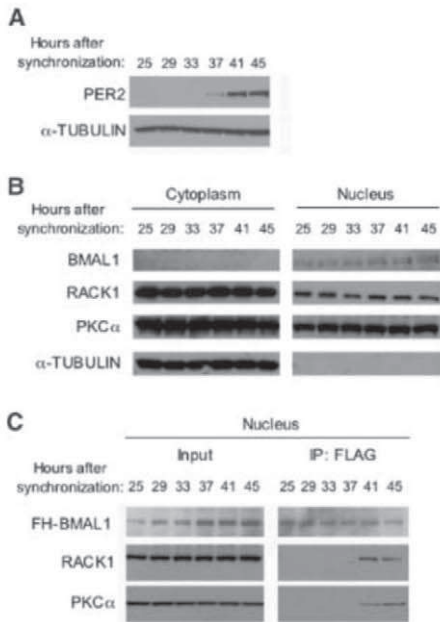


**Fig. 2.** Circadian association of RACK1 and PKCα with BMAL1 in cell nuclei. **(A)** Coherent circadian rhythms in cultured mouse fibroblasts after synchronization with forskolin. Shown are Western blots analyzing PER2 or α-TUBULIN in extracts of whole cells harvested at 4-hour intervals across a circadian cycle (harvest times indicated at the top). **(B)** Western blot analyzing subcellular and temporal regulation of the indicated proteins. α-TUBULIN, a cytoplasmic marker, serves as control for fractionation. **(C)** Immunoprecipitation (IP) showing a circadian rhythm of association of RACK1 and PKCα with BMAL1 in the nucleus.

To identify BMAL1-associated proteins by mass spectrometry, we infected *Bmal1*<sup>-/-</sup> fibroblasts [MLi cells (13)] with either an adenovirus expression vector with no insert (control) or a vector encoding FH-BMAL1. The cells were synchronized, harvested during the phase of negative feedback, and processed for affinity purification of FH-BMAL complexes and subsequent mass spectrometry (fig. S2B). After removing background proteins found in the control, the two proteins from which the most numerous peptides were identified were FH-BMAL1 and CLOCK. Next was RACK1 (receptor for activated C kinase-1), a signaling protein best known for recruiting activated, Ca<sup>2+</sup>-sensitive protein kinase C (PKC) isoforms, particularly PKCβII but also PKCα and others, to their substrates (15–17).

To determine whether endogenous BMAL1 and RACK1 are in a complex, we harvested mouse fibroblasts, lung, and liver during the negative feedback phase, immunoprecipitated RACK1, and probed for BMAL1. Endogenous BMAL1 from all sources coimmunoprecipitated with endogenous RACK1 (Fig. 1B), indicating that the two proteins are associated in multiple tissues.

**Fig. 3.** Inhibition of CLOCK-BMAL1 transcriptional activity by RACK1. **(A)** Effect of RACK1 on CLOCK-BMAL1 transactivation of a luciferase reporter from *Per1* E-boxes (mean ±SD; *N* ≥ 3). Mean luciferase activity after transfection of expression vector without inserts was set to 1 (dashed line). **(B)** Effect of RACK1 or ID on MYOD-E12 transactivation of a luciferase reporter from *Mck* gene E-boxes. Data displayed as in (A). **(C)** Antagonization of the inhibitory effect of RACK1 on CLOCK-BMAL1 transcriptional activity by C2 peptide. Displayed as in (A). +, transfection of expression plasmid with insert encoding the indicated protein. **(D)** Partial inhibition of CLOCK-BMAL1 transcriptional activity by RACK1 enhanced by PKCα. Displayed as in (A).

on CLOCK-BMAL1 transcriptional activity by C2 peptide. Displayed as in (A). +, transfection of expression plasmid with insert encoding the indicated protein. **(D)** Partial inhibition of CLOCK-BMAL1 transcriptional activity by RACK1 enhanced by PKCα. Displayed as in (A).

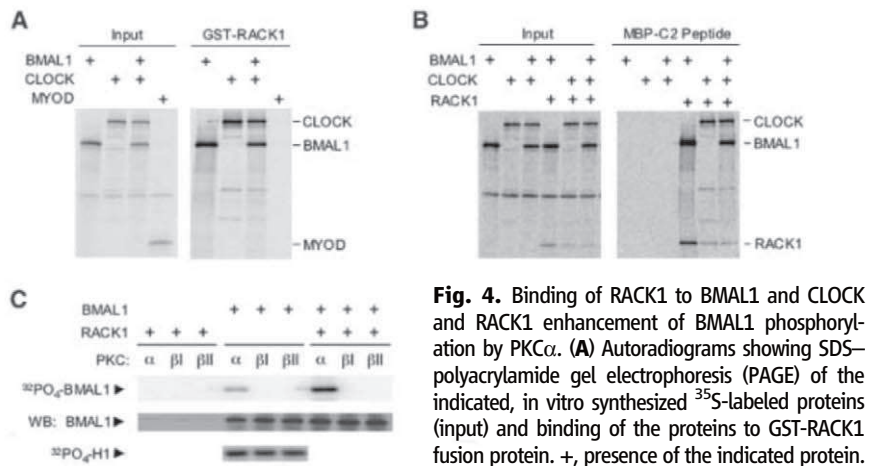


**Fig. 4.** Binding of RACK1 to BMAL1 and CLOCK and RACK1 enhancement of BMAL1 phosphorylation by PKCα. **(A)** Autoradiograms showing SDS-polyacrylamide gel electrophoresis (PAGE) of the indicated, in vitro synthesized <sup>35</sup>S-labeled proteins (input) and binding of the proteins to GST-RACK1 fusion protein. +, presence of the indicated protein. **(B)** Autoradiograms showing SDS-PAGE of the indicated, in vitro synthesized <sup>35</sup>S-labeled proteins (input) and binding of the proteins to MBP-C2 fusion protein. Data displayed as in (A). **(C)** Top: Autoradiogram showing in vitro transfer of <sup>32</sup>P-labeled phosphate to BMAL1 by the indicated activated PKCs. +, addition of the indicated protein. Middle: Control Western blot documenting BMAL1 in the samples. Bottom: Control autoradiogram showing phosphorylation of histone 1 (H1) by all PKCs.

We monitored BMAL1, RACK1, and PKCα expression across the circadian cycle, the latter because of its role in resetting the suprachiasmatic nucleus (SCN) clock (18). After synchronization, fibroblasts exhibited the expected circadian rhythm of PER2 (Fig. 2A). The cells were harvested at six time points and separated into cytoplasmic and nuclear fractions, which were then analyzed by Western blotting (Fig. 2B). BMAL1 was mostly nuclear, and RACK1 and PKCα were present in the cytoplasm and nucleus, with little or no circadian variation.

To examine circadian association of the proteins, we harvested synchronized fibroblasts stably expressing FH-BMAL1 at six circadian time points and immunoprecipitated FH-BMAL1 from nuclear fractions (Fig. 2C). BMAL1, RACK1, and PKCα were constitutively present in the

nucleus (Fig. 2C, input), but coimmunoprecipitation of RACK1 and PKCα with BMAL1 was detected only during part of the cycle (Fig. 2C), the time corresponding to the phase of negative feedback (see Fig. 2A). Thus, RACK1 and PKCα are components of BMAL1 nuclear complexes, and the formation and/or dissociation of these complexes is under circadian control. Further analysis indicated that RACK1 and PKCα were present in ~400-kD BMAL1 complexes (fig. S3) (13).

To test whether RACK1 and PKCα might be negative feedback regulators of CLOCK-BMAL1, as suggested by the time of their association with BMAL1, we assayed the transcriptional activity of CLOCK-BMAL1 (4). Cotransfection of increasing amounts of RACK1 expression plasmid negatively correlated with CLOCK-BMAL1 activity

**Fig. 5.** Short circadian period length caused by depletion of endogenous RACK1 or endogenous PKC $\alpha$ . (A to C) RACK1; (D to F) PKC $\alpha$ . (A) Western blot showing the effect of control shRNA (R3 Mut, three point mutations in 22-nucleotide core sequence) or RACK1 shRNA (R3) on steady-state level of endogenous RACK1.  $\alpha$ -TUBULIN, loading control. (B) Real-time circadian oscillations of bioluminescence in synchronized circadian reporter fibroblasts after adenoviral delivery of R3 shRNA against RACK1 (blue) or R3 Mut control shRNA (yellow). Traces from three independent cultures are shown for each shRNA. (C) Circadian period of fibroblasts expressing R3 Mut control or R3 RACK1 shRNA (mean  $\pm$  SEM;  $N = 3$  for each;  $t$  test, two-tailed). [(D) to (F)] Data for electroporation of control siRNA (P2 Mut, three point mutations in 22-nucleotide core sequence) or effective PKC $\alpha$  siRNA (P2) into fibroblasts displayed as in (A) to (C).

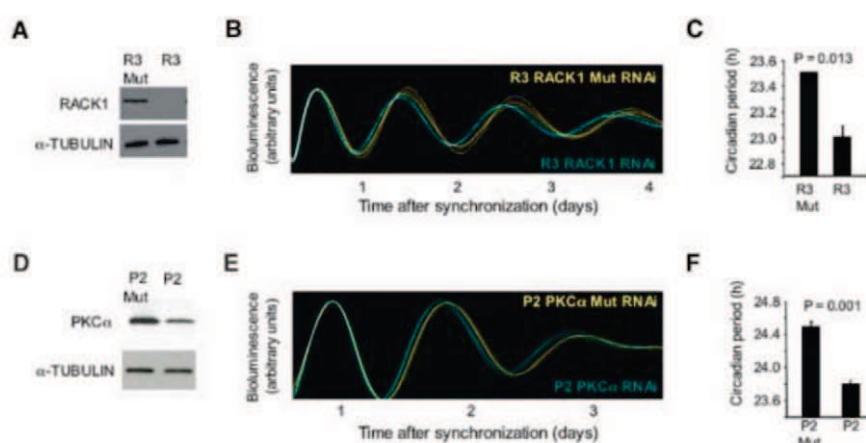


(Fig. 3A). RACK1 produced no inhibition of the activity of MYOD-E12, a transcription factor related to CLOCK-BMAL1 (Fig. 3B).

We tested whether this effect of RACK1 likely involved PKC. C2 is a loop of PKC $\beta$ II (nearly identical to PKC $\alpha$ ) that interacts with RACK1; binding of C2 to RACK1 antagonizes PKC-dependent functions of RACK1 (19). Expression of C2 had no effect on either baseline transcription or CLOCK-BMAL1 activity, but C2 reversed the inhibitory action of RACK1 (Fig. 3C). Thus, inhibition of CLOCK-BMAL1 activity by RACK1 likely requires binding of PKC. In addition, expression of PKC $\alpha$  produced no effect on baseline transcription or CLOCK-BMAL1 activity, but it enhanced a partial inhibitory action of RACK1 (Fig. 3D). These results suggest that RACK1 inhibits CLOCK-BMAL1 activity by recruiting PKC $\alpha$ .

RACK1 targets the transcription factor hypoxia-inducible factor-1 $\alpha$  (HIF-1 $\alpha$ ) for degradation (20). But from our results (fig. S4) (13), it appears that any effect of RACK1 on the steady-state abundance of CLOCK or BMAL1 is unlikely to account for its inhibition of CLOCK-BMAL1 activity.

We analyzed in vitro binding of [ $^{35}$ S] methionine-labeled BMAL1, CLOCK, or MYOD to glutathione-S-transferase (GST)-RACK1. Both BMAL1 and CLOCK bound to RACK1 fusion protein, whereas the related transcription factor MYOD showed no detectable binding (Fig. 4A). We also examined [ $^{35}$ S]methionine-labeled BMAL1, CLOCK, or RACK1, alone or in combination, for binding to a fusion protein of maltose binding protein (MBP) with C2. BMAL1 and CLOCK associated with C2 fusion protein only if RACK1 was present (Fig. 4B). This result suggests that RACK1 promotes assembly of activated PKC $\alpha$  and CLOCK-BMAL1 into a complex.

To determine whether RACK1 might enhance phosphorylation of BMAL1 by PKC $\alpha$ , we synthesized BMAL1 and RACK1 by in vitro transcription-translation and tested the ability of several activated classical PKCs to phosphorylate BMAL1 in vitro with or without RACK1. PKC $\alpha$ , but not PKC $\beta$ I or PKC $\beta$ II, phosphorylated

BMAL1, and this activity was increased by the presence of RACK1 (Fig. 4C).

If RACK1 has a nonredundant role in the clock, then depletion of endogenous RACK1 should alter circadian period length. We introduced small hairpin RNA constructs (shRNAs) into circadian bioluminescence reporter fibroblasts (13) to deplete RACK1. Three nonoverlapping shRNAs each caused depletion of endogenous RACK1 relative to their respective mutated controls (Fig. 5A and fig. S5, A and D), and each caused a shortening of circadian period length observable in individual bioluminescence traces: At the outset, all traces were aligned, but by the second circadian cycle all blue traces (effective RACK1 shRNA) were running ahead of all yellow traces (ineffective mutated shRNA) (Fig. 5B and fig. S5, B and E). The short-period phenotype was significant in all cases (Fig. 5C and fig. S5, C and F).

If a major function of RACK1 in the clock is to recruit PKC $\alpha$  to CLOCK-BMAL1, then depleting PKC $\alpha$  should cause a short-period phenotype like that caused by depletion of RACK1. Three nonoverlapping small interfering double-stranded RNAs (siRNAs) (P1, P2, and P3) were electroporated separately into circadian reporter fibroblasts, and each caused moderate depletion of endogenous PKC $\alpha$  and a significant shortening of circadian period (Fig. 5, D to F, and fig. S6). Thus, RACK1 and PKC $\alpha$  function in the oscillatory mechanism of the clock, and the similar effect of depletion of the two proteins supports the hypothesis that they act in concert.

RACK1 has been identified as a PER1-interacting protein in a yeast two-hybrid screen (21), but the in vivo relevance of this finding is unknown. One or more classical PKCs contributes to light-dependent resetting of the SCN clock (18, 22, 23) and to serum shock resetting of the fibroblast clock (24). Mutant mice lacking PKC $\alpha$  have impaired light-dependent resetting of circadian behavioral rhythms, but they exhibit no change in circadian period (18). This difference from our results could reflect developmental compensation in the mutant mice, differences between

the circadian clocks of the fibroblast and SCN, or, perhaps most likely, the ability of the SCN multi-oscillator network to compensate for mutations that alter clock function in individual cells (25).

Our results indicate that a classical, Ca $^{2+}$ -sensitive signaling pathway is not limited to relaying external stimuli but is triggered by internal processes, forming an integral part of the circadian clock feedback loop. We do not know how this pathway is rhythmically activated, but it is intriguing that circadian oscillations of free Ca $^{2+}$  have been widely observed (26, 27).

## References and Notes

1. A. Balsalobre, F. Damiola, U. Schibler, *Cell* **93**, 929 (1998).
2. S. Yamazaki *et al.*, *Science* **288**, 682 (2000).
3. J. S. Takahashi, H. K. Hong, C. H. Ko, E. L. McDearmon, *Nat. Rev. Genet.* **9**, 764 (2008).
4. N. Gekakis *et al.*, *Science* **280**, 1564 (1998).
5. T. Tamaru *et al.*, *Genes Cells* **8**, 973 (2003).
6. H. Dardente, E. E. Fortier, V. Martineau, N. Cermakian, *Biochem. J.* **402**, 525 (2007).
7. T. Tamaru *et al.*, *Nat. Struct. Mol. Biol.* **16**, 446 (2009).
8. H. Yoshitane *et al.*, *Mol. Cell. Biol.* **29**, 3675 (2009).
9. L. Busino *et al.*, *Science* **316**, 900 (2007); published online 26 April 2007 (10.1126/science.1141194).
10. S. M. Siepka *et al.*, *Cell* **129**, 1011 (2007).
11. S. I. H. Godinho *et al.*, *Science* **316**, 897 (2007); published online 26 April 2007 (10.1126/science.1141138).
12. G. Asher *et al.*, *Cell* **134**, 317 (2008).
13. See supporting material on Science Online.
14. Y. Nakatani, V. Ogryzko, *Methods Enzymol.* **370**, 430 (2003).
15. D. Schechtman, D. Mochly-Rosen, *Oncogene* **20**, 6339 (2001).
16. H. S. Lee *et al.*, *Osteoarthritis Cartilage* **10**, 890 (2002).
17. E. H. Sklan, E. Podoly, H. Soreq, *Prog. Neurobiol.* **78**, 117 (2006).
18. V. Jakubcakova *et al.*, *Neuron* **54**, 831 (2007).
19. E. G. Stebbins, D. Mochly-Rosen, *J. Biol. Chem.* **276**, 29644 (2001).
20. Y. V. Liu, G. L. Semenza, *Cell Cycle* **6**, 656 (2007).
21. L. Hu *et al.*, *J. Mol. Neurosci.* **29**, 55 (2006).
22. K. M. Schak, M. E. Harrington, *Brain Res.* **840**, 158 (1999).
23. B. Lee, A. Almad, G. Q. Butcher, K. Obrietan, *Eur. J. Neurosci.* **26**, 451 (2007).
24. H. S. Shim *et al.*, *EMBO Rep.* **8**, 366 (2007).
25. A. C. Liu *et al.*, *Cell* **129**, 605 (2007).
26. T. Imaizumi, J. I. Schroeder, S. A. Kay, *Sci. STKE* **2007**, pe32 (2007).



27. M. C. Harrisingh, Y. Wu, G. A. Lnenicka, M. N. Nitabach, *J. Neurosci.* **27**, 12489 (2007).  
 28. We thank P. Nakatani (Dana-Farber Cancer Institute) for the FH cassette; P. Sassone-Corsi (University of California, Irvine) for BMAL1 antiserum; M. J. Weber (University of Virginia), D. Mochly-Rosen (Stanford University), P. Blumberg (National Cancer Institute), and M. Grossi (University of Rome), respectively, for RACK1, C2, PKC $\alpha$ , and MYOD cDNAs; M. Liu for expert

technical assistance; N. Vujovic for help with transactivation assays; and L. Lande-Diner for comments on the manuscript. Supported by grants from the Edward R. and Anne G. Lefler Center and the G. Harold and Leila Y. Mathers Charitable Foundation (C.J.W.), an Edward R. and Anne G. Lefler Center postdoctoral fellowship (M.S.R.), a Swiss National Science Foundation grant (D.K.), and an EMBO postdoctoral fellowship (C.B.).

**Supporting Online Material** [www.sciencemag.org/cgi/content/full/327/5964/463/DC1](http://www.sciencemag.org/cgi/content/full/327/5964/463/DC1) Materials and Methods  
 SOM Text  
 Figs. S1 to S6  
 References

3 August 2009; accepted 7 December 2009  
 10.1126/science.1180067

# Tuberculous Granuloma Induction via Interaction of a Bacterial Secreted Protein with Host Epithelium

Hannah E. Volkman,<sup>1\*</sup> Tamara C. Pozos,<sup>2,\*†</sup> John Zheng,<sup>2</sup> J. Muse Davis,<sup>3</sup> John F. Rawls,<sup>4,5</sup> Lalita Ramakrishnan<sup>6,7,8‡</sup>

Granulomas, organized aggregates of immune cells, are a hallmark of tuberculosis and have traditionally been thought to restrict mycobacterial growth. However, analysis of *Mycobacterium marinum* in zebrafish has shown that the early granuloma facilitates mycobacterial growth; uninfected macrophages are recruited to the granuloma where they are productively infected by *M. marinum*. Here, we identified the molecular mechanism by which mycobacteria induce granulomas: The bacterial secreted protein 6-kD early secreted antigenic target (ESAT-6), which has long been implicated in virulence, induced matrix metalloproteinase-9 (MMP9) in epithelial cells neighboring infected macrophages. MMP9 enhanced recruitment of macrophages, which contributed to nascent granuloma maturation and bacterial growth. Disruption of MMP9 function attenuated granuloma formation and bacterial growth. Thus, interception of epithelial MMP9 production could hold promise as a host-targeting tuberculosis therapy.

**T**uberculous infection begins with recruitment of monocytes to a peripheral infection site where they engulf mycobacteria and migrate to deeper tissues (1, 2). Additional macrophages and other immune cells then aggregate with the infected cells to form granulomas (3). Granulomas, recognized as pathological hallmarks of tuberculosis for over a century, were thought to curtail infection by encasing mycobacteria (4). However, visualization of granuloma formation in transparent zebrafish larvae infected with *Mycobacterium marinum* (Mm) has revealed that the early granuloma serves to expand bacterial numbers (5, 6). An infected macrophage induces granuloma formation by promoting recruitment of additional phagocytes

(6). Upon its death, multiple newly arriving macrophages phagocytose it and thereby become infected. Concerted iteration of these processes makes the early granuloma a site for bacterial expansion (6). Mycobacteria direct these granuloma-forming processes via their region of difference-1 (RD1) virulence locus that encodes the ESAT-6 secretion system-1 (ESX-1) secretion system (5, 6). The host factors coopted in RD1-mediated granuloma formation remain unknown.

In a host gene expression survey comparing zebrafish larvae infected with wild-type Mm (WT) or RD1-deleted Mm ( $\Delta$ RD1) (5, 6), we identified *matrix metalloproteinase 9* (*mmp9*) and *tissue inhibitor of metalloproteinase 2b* (*timp2b*) as being RD1-induced during granuloma formation at 5 days post infection (5 dpi) (Fig. 1, A and B; tables S1 to 4; and fig. S1, A and B). To control for  $\Delta$ RD1's attenuated infection at 5 dpi (5), we confirmed RD1-dependent gene induction using higher  $\Delta$ RD1 inoculations that produced similar bacterial burdens at 5 dpi with the expected paucity of  $\Delta$ RD1 granulomas (5, 6) (Fig. 1, A and C, and fig. S1C). At 1 dpi, only *mmp9* was induced, suggesting that *timp2b* induction at 5 dpi was a compensatory response to increased *mmp9* (Fig. 1D). *Mmp9* is a gelatinase, and gelatin zymography confirmed that RD1-dependent *mmp9* mRNA expression resulted in increased *Mmp9* gelatinase activity (Fig. 1E). In contrast, mRNA expression and activity of another gelatinase *Mmp2* were not altered by infection (fig. S1A and Fig. 1E).

MMP9 is implicated in the pathogenesis of several inflammatory conditions (7, 8) and is highly expressed in human tuberculosis as well as in the mouse model of tuberculosis (9–12) (table S1). In mice, MMP9 activity correlates to increased macrophage migration and granuloma formation; however, it is reported to be a host resistance factor, perhaps because its expression is associated with variable effects on infection in different genetic backgrounds (10). In humans, MMP9 clearly mediates susceptibility as its increased activity is correlated with worse outcomes (9). To test *mmp9*'s role in promoting granuloma formation and virulence, we knocked down its expression transiently with three modified antisense oligonucleotides (morpholinos) (1, 13) (fig. S2). The morpholinos, singly or in combination, reduced gelatinase activity reliably up to 4 dpi with activity returning to control levels by 5 dpi (fig. S2). WT infection of morpholino-injected embryos (morphants) resulted in attenuated infection sharing several features of  $\Delta$ RD1 infection of control embryos. First, morphants displayed reduced numbers of bacteria and granulomas, as well as increased host survival (Fig. 2, A to C). Second, kinetic analyses of granuloma formation in the morphants confirmed a specific granuloma-forming deficit (Fig. 2, D to F). We found a dynamic link between *Mmp9* activity, granuloma formation, and bacterial expansion: Bacterial burdens and granuloma formation differed only up to 4 dpi, returning to control levels by 5 dpi contemporaneous with restoration of *Mmp9* activity (Fig. 2, A to E, and fig. S2). Finally, although the RD1 locus promotes macrophage recruitment to nascent granulomas, it is not required for initial phagocyte migration to infecting bacteria when they are still extracellular (5, 6). Similarly, *mmp9* morphants displayed normal macrophage migration to extracellular bacteria when injected into the hindbrain ventricle (fig. S3).

RD1 probably contributes to granuloma expansion through pleiotropic effects that include inducing apoptosis of infected macrophages and recruiting new uninfected macrophages (5, 6, 14–16). In contrast, *Mmp9* was not required for RD1-induced cell death; morphant and control granulomas in WT infection contained similar numbers of TUNEL (terminal deoxynucleotidyl transferase-mediated deoxyuridine triphosphate nick end labeling)-positive cells, whereas control granulomas in  $\Delta$ RD1 infection exhibited the expected reduction (13) (Fig. 2G). Thus RD1-induced apoptosis is *Mmp9* independent and cannot mediate bacterial ex-

<sup>1</sup>Molecular and Cellular Biology Graduate Program, University of Washington, Seattle, WA 98155, USA. <sup>2</sup>Department of Pediatrics, University of Washington, Seattle, WA 98155, USA. <sup>3</sup>Immunology and Molecular Pathogenesis Graduate Program, Emory University, Atlanta, GA 30322, USA. <sup>4</sup>Department of Cell and Molecular Physiology, University of North Carolina, Chapel Hill, NC 27599, USA. <sup>5</sup>Department of Microbiology and Immunology, University of North Carolina, Chapel Hill, NC 27599, USA. <sup>6</sup>Department of Microbiology, University of Washington, Seattle, WA 98155, USA. <sup>7</sup>Department of Medicine, University of Washington, Seattle, WA 98155, USA. <sup>8</sup>Department of Immunology, University of Washington, Seattle, WA 98155, USA.

\*These authors contributed equally to this work.

†Present address: Pediatric Infectious Diseases and Immunology, Children's Hospitals and Clinics of Minnesota, St. Paul, MN 55102, USA.

‡To whom correspondence should be addressed. E-mail: lalital@u.washington.edu

pansion in the absence of new macrophage recruitment, and Mmp9-mediated acceleration of macrophage recruitment to granulomas is an independent mediator of pathogenesis.

Multiple cell types express *MMP9* in many inflammatory conditions (7). In the context of tuberculosis, it is induced in cultured monocytes infected with *Mycobacterium tuberculosis*

(9, 17–19) and in epithelial cells (20). In advanced human tuberculosis, induced expression is reported in some monocytes and multinucleated giant cells abutting necrotic centers of

**Fig. 1.** RD1-dependent

Mmp9 induction. (A) Representative fluorescence images of 5-dpi embryos used for gene expression studies in (B and C). Embryos in the top and middle panels were injected with similar doses of WT and  $\Delta$ RD1, respectively (WT dose of  $193 \pm 36$  and  $\Delta$ RD1 dose of  $217 \pm 63$ ), where  $\Delta$ RD1 bacterial burdens are lower than those of WT at 5 dpi. Embryo in bottom panel was injected with  $\sim$  five times as much  $\Delta$ RD1 ( $\Delta$ RD1-high) to achieve bacterial burdens similar to those of WT at 5 dpi [5-dpi bacterial burdens were  $1601 \pm 1071$  for WT and  $1531 \pm 1011$  for  $\Delta$ RD1-high, not significant (NS)]. Arrows, granulomas; arrowheads, single infected macrophages. Scale bars, 400  $\mu$ m. (B and C) Relative gene expression levels (mean  $\pm$  SEM of at least three biological replicates) of 5-dpi (B) WT- and  $\Delta$ RD1-infected embryos and (C) WT and  $\Delta$ RD1-high-infected embryos. Although there appears to be a dose-dependent induction of *mmp9* by  $\Delta$ RD1 [compare induction in (B) and (C)], the difference is not significant ( $P = 0.2$ ). (D) Relative gene expression levels (mean  $\pm$  SEM of three biological replicates) 1 day after injection with  $721 \pm 39$  WT or  $484 \pm 147$   $\Delta$ RD1 (NS). \* $P < 0.05$ , \*\* $P < 0.01$  (Student's *t* test). (E) Gelatin zymography of embryos 5 dpi with 200 WT or 700  $\Delta$ RD1, or mock-infected. Controls are purified human MMP9 and MMP2.

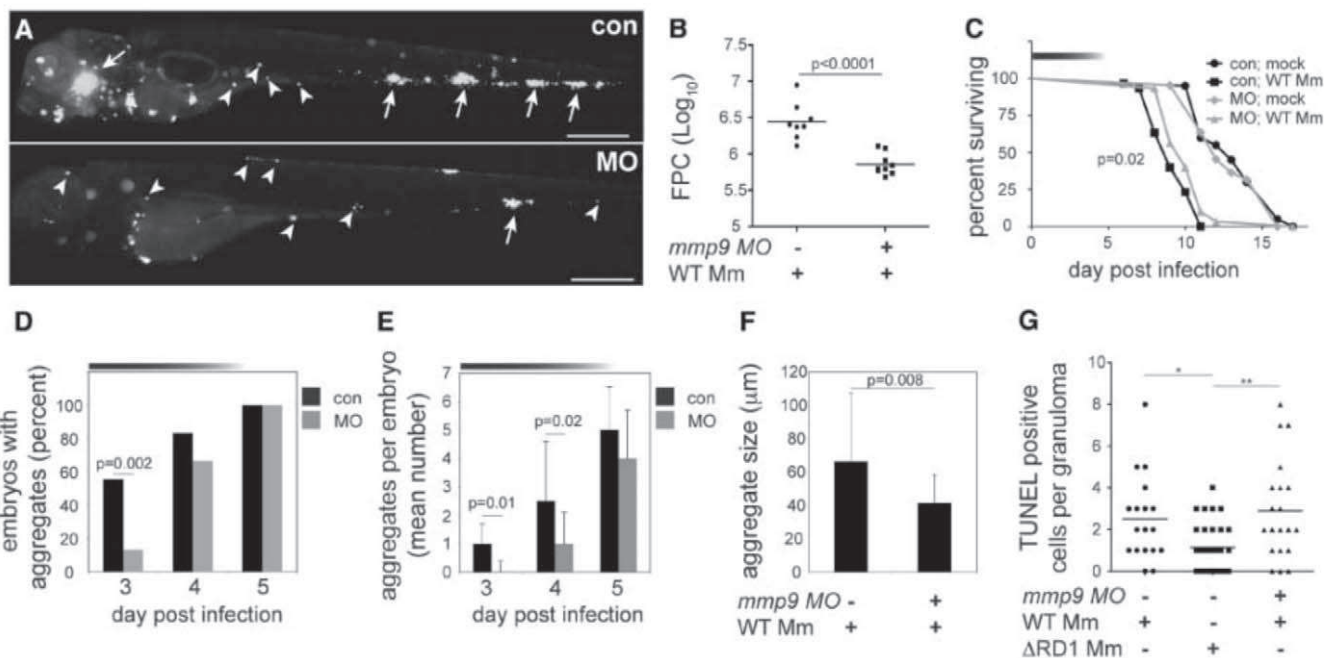
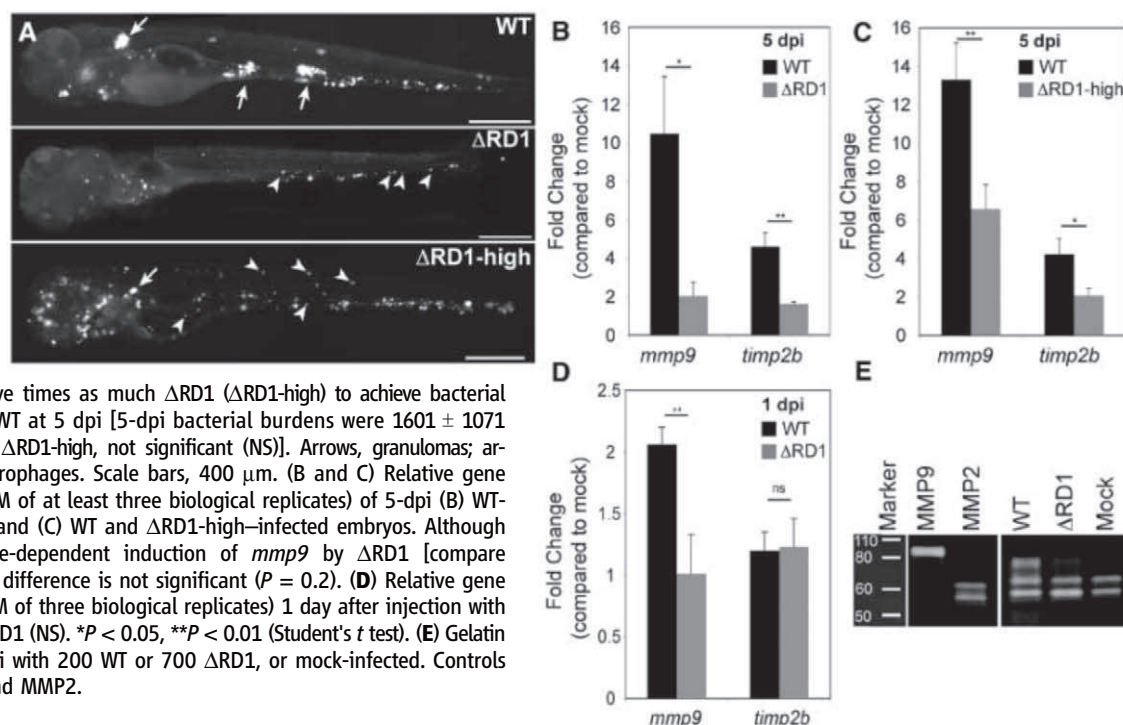


**Fig. 2.** Mmp9 promotes granuloma formation and virulence. (A) Fluorescence images of representative control (con) and *mmp9* morphant (MO) embryos 4 dpi with 116 WT. Arrows, granulomas; arrowheads, single infected macrophages. Scale bars, 400  $\mu$ m. (B) Bacterial burdens of all 4-dpi embryos determined by fluorescence pixel counts (FPC) (31). (C) Survival of con and MO embryos ( $n = 30$  each) infected with 150 colony-forming units (CFU) of WT or mock-infected ( $n = 20$  each). Median survival was 10 days for infected MO and 9 days for infected con ( $P = 0.02$ ; log-

rank test) and no different for uninfected MO and con. Top horizontal bar denotes duration of MO activity (fig. S2). (D to F) Kinetics of granuloma formation in con and MO embryos infected with 101 WT. Data in (D) were analyzed by Fisher's exact test of a contingency table. Bars in (E) and (F) represent the mean  $\pm$  SEM (Student's *t* test). (G) Median number of TUNEL-positive cells per con or MO granuloma 4 dpi with 37 CFU of WT and con granulomas 4 dpi with 585  $\Delta$ RD1 (one-way analysis of variance;  $P = 0.003$ , with Dunnett's multiple comparison test).



lymph node granulomas (18, 21) and in epithelial cells proximal to lung granulomas (20). To understand how the RD1-Mmp9 axis mediates granuloma formation, we assessed localization of *mmp9* expression during this process. Fluorescence whole-mount in situ hybridization (FISH) (1) revealed RD1-dependent *mmp9* induction in 5-dpi embryos in cells associated with granulomas as well as in distal single cells (Fig. 3A). Multiplex FISH combining the *mmp9* and macrophage-specific *fms* probes, or *mmp9* and neutrophil-specific *mpo* probes (1), showed that the distal single cells consisted largely of neutrophils with a minor macrophage contribution (figs. S4 and S5). However, *mmp9* expression by neutrophils and macrophages was unlikely to be relevant for granuloma formation because their *mmp9* expression induced by infection was RD1 independent, and most granulomas contained

few, if any, of these cells (Fig. 3B and figs. S4 and S5).

Differential interference contrast (DIC) and confocal microscopy revealed that granuloma-associated *mmp9* expression was localized to epithelial cells proximate to infected macrophages (22) (Fig. 3B and movie S1). Expression was restricted to specific epithelial cell types: Epidermal cells adjacent to the granuloma expressed *mmp9*, whereas immediately overlying peridermal cells did not (22) (movie S1). Epidermal cell-specific expression was highlighted in granulomas forming in muscle where *mmp9* was expressed not by the immediately surrounding myocytes but by their closest epidermal neighbors (Fig. 3C and movie S2). Every granuloma analyzed had proximate *mmp9*-expressing epithelial cells ( $n = 35$  granulomas in 9 fish), including the smallest identifiable macrophage aggregates (fig. S6 and

movie S3). Thus Mmp9 induction is critical for granuloma formation from the very earliest stages and probably in later stages as well, given RD1's continued influence on granuloma structure in chronic tuberculous infection (5, 23).

Bacteria residing in macrophages could induce epithelial cell *mmp9* in two ways: (i) RD1 might induce macrophage signals such as secreted cytokines (24, 25) that in turn elicit *mmp9* secretion by epithelial cells, or (ii) bacteria (26, 27) or bacterial products (28) released from macrophages might interact directly with epithelial cells. To distinguish between these mechanisms, we assessed *mmp9* induction in *pu.1* morphants that lack macrophages and in which infection results in extracellular mycobacterial growth (1). *pu.1* morphants exhibited RD1-dependent *mmp9* induction, suggesting that bacteria or their products interact directly with epithelial cells to induce

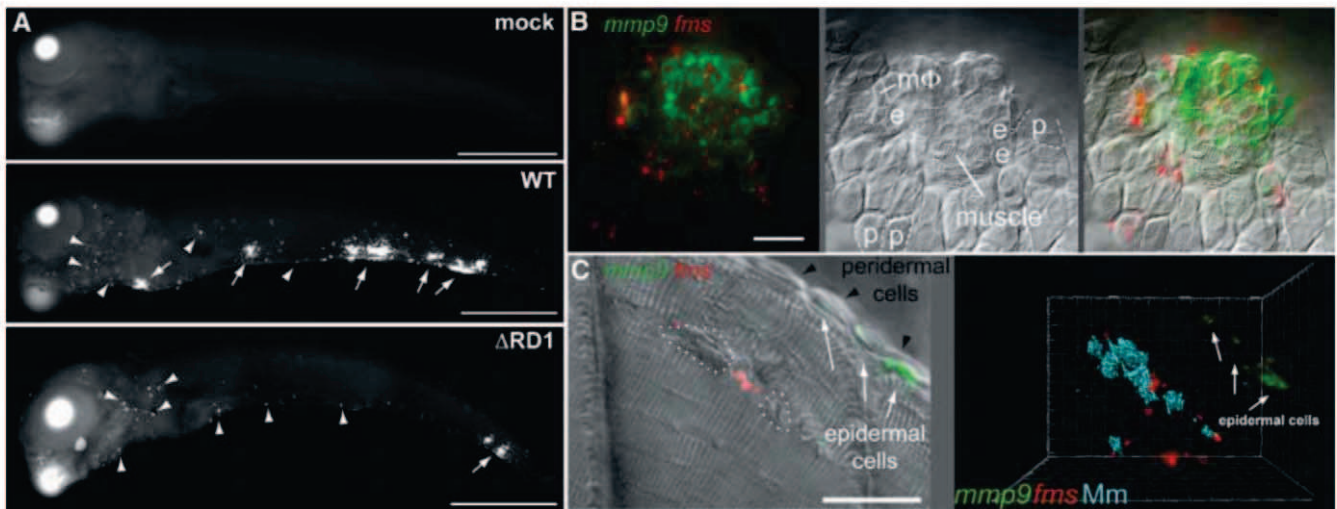
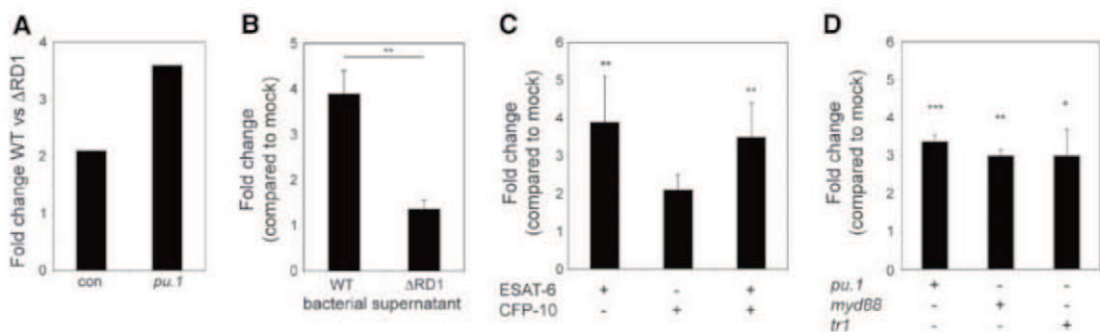


**Fig. 3.** *mmp9* is selectively induced in epithelial cells neighboring infected macrophages. (A) *mmp9* FISH images of embryos 5 days after mock infection or infection with 78 CFU of WT or 130 CFU of  $\Delta$ RD1. Arrows, *mmp9* expression corresponding to granulomas; arrowheads, single *mmp9*-expressing cells. Scale bars, 400  $\mu$ m. (B and C) Images of WT granulomas after dual *mmp9* and *fms* FISH. (B) Fluorescence (left), DIC (middle), and overlay (right) images. e, epidermal cell; p, peridermal cell; M $\Phi$ , macrophage. Scale bar, 20  $\mu$ m. Also see

movie S1. (C) Fluorescence and DIC overlay of nascent WT muscle granuloma (left). Dotted white circles outline bacterial clusters discerned by DIC microscopy. Fluorescence data have been deconvolved. Right panel represents three-dimensional reconstruction from fluorescence image of the same lesion with bacterial locations pseudocolored blue, showing complete absence of *mmp9* expression in adjacent muscle, and strong *mmp9* expression in nearest neighboring epidermal cells. Scale bar, 20  $\mu$ m. Also see movie S2.

**Fig. 4.** Mycobacterial ESAT-6 is sufficient to induce *mmp9* in epithelial cells independent of Myd88 and TNF signaling. (A to D) Relative *mmp9* expression analyzed by real-time quantitative reverse transcriptase-polymerase chain reaction of (A) con or *pu.1* morphant embryos 3 dpi with 84 WT or 126  $\Delta$ RD1 (represents one biological replicate), or (B) 34-hpf (hours post fertilization) embryos 4 hours after injection with WT or  $\Delta$ RD1 bacterial supernatant. Bars represent the means  $\pm$  SEM of three biological replicates. (C) Thirty-four-hpf con embryos 4 hours after injection with  $4.8 \times 10^{-17}$  mol of purified ESAT-6 or CFP-10, or  $4.9 \times 10^{-17}$  mol of ESAT-6 plus  $5.0 \times 10^{-17}$  mol of CFP-10. Bars represent the means



( $\pm$  SEM) of five biological replicates. (D) Thirty-four-hpf con embryos, *myd88* morphants, or *tr1* morphants 4 hours after injection with  $5.7 \times 10^{-17}$  mol of purified ESAT-6. Bars represent the means  $\pm$  SEM of four biological replicates (*pu.1* morphant), or three biological replicates (*myd88* and *tr1* morphants).

*mmp9* by a macrophage-independent mechanism (Fig. 4A).

The observation that uninfected epithelial cell *mmp9* induction can occur distant from infection foci (Fig. 3C and movie S3) implicated an RD1-dependent secreted determinant rather than direct bacterial contact with epithelial cells. Indeed, injection of WT but not  $\Delta$ RD1 bacterial supernatants rapidly induced *mmp9* expression (Fig. 4B). The ESX-1 secretion system secretes five proteins that are all mutually codependent for secretion, so distinguishing their individual roles in virulence has been difficult (14, 15). We pursued ESAT-6 as the lead candidate for inducing *mmp9* for two reasons: ESAT-6 mediates virulence independent of secretion (15), and its pore-forming activity (29, 30) could allow it direct access to epithelial cells. Injection of  $4.8 \times 10^{-17}$  mol of purified ESAT-6 was sufficient to induce *mmp9* within 4 hours (Fig. 4C). In contrast,  $5.0 \times 10^{-17}$  mol of 10-kD culture filtrate protein (CFP-10), thought to bind ESAT-6 and serve as its chaperone (15), failed to induce *mmp9* significantly (Fig. 4C). Moreover, coinjection of CFP-10 and ESAT-6 did not augment the induction observed with ESAT-6 alone, confirming an ESAT-6-specific effect (Fig. 4C). Finally, similar to RD1-competent bacteria (Fig. 4A), ESAT-6 induced *mmp9* in *pu.1* morphants (Fig. 4D), consistent with a direct interaction with epithelial cells. We next asked if epithelial cell *mmp9* induction was dependent on MyD88 and TNF (tumor necrosis factor) signaling, as each can enhance mycobacterial induction of *mmp9* in cultured cells under certain conditions (19, 20). ESAT-6 induced *mmp9* in *myd88* and *tnf-receptor 1* (*tr1*) morphants (Fig. 4D), suggesting a previously unknown pathway for this epithelial cell-specific interaction. Moreover, TNF-independent induction of *mmp9* is consistent with the finding that TNF does not mediate granuloma formation either in the presence or absence of bacterial RD1 (13).

Thus, ESAT-6 functions in virulence by promoting granuloma formation via interaction with epithelial cells, previously regarded as bystanders in the pathogenesis of tuberculosis (fig. S7). The cooption of epithelial cells may offer mycobacteria a means of amplifying MMP9 secretion in the vicinity of a single infected macrophage to establish the granuloma niche. In addition, the differential induction of inflammatory programs in macrophages and epithelial cells may generate a hospitable growth niche in macrophages while harnessing epithelial cells to facilitate the chemotaxis of additional macrophages for niche expansion (6) (fig. S7). Our work provides a mechanistic explanation for the implication of MMP9 in human susceptibility to tuberculosis (9, 11, 12) and suggests targeted inhibition of its expression as a host-directed antituberculous therapy. Because increased MMP9 is detrimental in both tuberculosis and a variety of noninfectious inflammatory conditions (7), interception of this pathway may have broad utility in treating a

variety of inflammatory conditions in addition to tuberculosis.

#### References and Notes

1. H. Clay *et al.*, *Cell Host Microbe* **2**, 29 (2007).
2. A. J. Wolf *et al.*, *J. Immunol.* **179**, 2509 (2007).
3. D. O. Adams, *Am. J. Pathol.* **84**, 164 (1976).
4. T. Ulrichs, S. H. Kaufmann, *J. Pathol.* **208**, 261 (2006).
5. H. E. Volkman *et al.*, *PLoS Biol.* **2**, e367 (2004).
6. J. M. Davis, L. Ramakrishnan, *Cell* **136**, 37 (2009).
7. P. E. Van den Steen *et al.*, *Crit. Rev. Biochem. Mol. Biol.* **37**, 375 (2002).
8. K. J. Greenlee, Z. Werb, F. Kheradmand, *Physiol. Rev.* **87**, 69 (2007).
9. N. M. Price *et al.*, *J. Immunol.* **166**, 4223 (2001).
10. J. L. Taylor *et al.*, *Infect. Immun.* **74**, 6135 (2006).
11. K. J. Park *et al.*, *Respiration* **72**, 166 (2005).
12. P. Sheen *et al.*, *Eur. Respir. J.* **33**, 134 (2009).
13. H. Clay, H. E. Volkman, L. Ramakrishnan, *Immunity* **29**, 283 (2008).
14. P. A. DiGiuseppe Champion, J. S. Cox, *Cell. Microbiol.* **9**, 1376 (2007).
15. R. Simeone, D. Bottai, R. Brosch, *Curr. Opin. Microbiol.* **12**, 4 (2009).
16. S. C. Derrick, S. L. Morris, *Cell. Microbiol.* **9**, 1547 (2007).
17. J. C. Chang *et al.*, *Thorax* **51**, 306 (1996).
18. N. M. Price, R. H. Gilman, J. Uddin, S. Recavarren, J. S. Friedland, *J. Immunol.* **171**, 5579 (2003).
19. S. Shi *et al.*, *J. Exp. Med.* **198**, 987 (2003).
20. P. T. Elkington *et al.*, *Am. J. Respir. Cell Mol. Biol.* **37**, 431–437 (2007).
21. X. W. Zhu, N. M. Price, R. H. Gilman, S. Recavarren, J. S. Friedland, *J. Infect. Dis.* **196**, 1076 (2007).
22. D. Le Guellec, G. Morvan-Dubois, J. Y. Sire, *Int. J. Dev. Biol.* **48**, 217 (2004).
23. D. R. Sherman *et al.*, *J. Infect. Dis.* **190**, 123 (2004).
24. I. C. Koo *et al.*, *Cell. Microbiol.* **10**, 1866 (2008).
25. S. A. Stanley, S. Raghavan, W. W. Hwang, J. S. Cox, *Proc. Natl. Acad. Sci. U.S.A.* **100**, 13001 (2003).
26. L. M. Stamm *et al.*, *J. Exp. Med.* **198**, 1361 (2003).
27. M. Hagedorn, K. H. Rohde, D. G. Russell, T. Soldati, *Science* **323**, 1729 (2009).
28. D. G. Russell, *Nat. Rev. Microbiol.* **5**, 39 (2007).
29. T. Hsu *et al.*, *Proc. Natl. Acad. Sci. U.S.A.* **100**, 12420 (2003).
30. M. I. de Jonge *et al.*, *J. Bacteriol.* **189**, 6028 (2007).
31. Materials and methods are available as supporting material on Science Online.
32. We thank J. I. Gordon, W. Parks, D. Raible, D. Sherman, K. Urdahl, and P. Elkington for advice and discussion; D. Beery and R. Kim for help with microinjections; and J. Cameron, L. Swaim, and H. Wiedenhoft for fish facility maintenance. We also thank K. Winglee for developing FPC analysis methods, R. Burmeister for graphic design, and D. Tobin, B. Cormack, W. Parks, D. Stetson, R. Berg, and F. Chu for review of the manuscript. This work was supported by the Burroughs Wellcome Fund (L.R.), the Pew Scholars Program (J.F.R.), the NIH (L.R. and J.F.R.), an American Heart Association predoctoral fellowship (H.E.V.), a Pediatric Infectious Diseases Society postdoctoral award, the Children's Health Research Center new investigator award, an NIH diversity supplement (T.C.P.), and a National Defense Science and Engineering predoctoral fellowship (J.M.D.).

**Supporting Online Material** [www.sciencemag.org/cgi/content/full/science.1179663/DC1](http://www.sciencemag.org/cgi/content/full/science.1179663/DC1) Materials and Methods

Figs. S1 to S7

Tables S1 to S4

References

Movies S1 to S3

24 July 2009; accepted 19 November 2009

Published online 10 December 2009;

10.1126/science.1179663

Include this information when citing this paper.

## Evolution of MRSA During Hospital Transmission and Intercontinental Spread

Simon R. Harris,<sup>1\*</sup> Edward J. Feil,<sup>2\*</sup> Matthew T. G. Holden,<sup>1</sup> Michael A. Quail,<sup>1</sup> Emma K. Nickerson,<sup>3,4</sup> Narisara Chantratita,<sup>3</sup> Susana Gardete,<sup>5,6</sup> Ana Tavares,<sup>5</sup> Nick Day,<sup>3,7</sup> Jodi A. Lindsay,<sup>8</sup> Jonathan D. Edgeworth,<sup>9,10</sup> Hermínia de Lencastre,<sup>5,6</sup> Julian Parkhill,<sup>1</sup> Sharon J. Peacock,<sup>3,4</sup> Stephen D. Bentley<sup>1†</sup>

Current methods for differentiating isolates of predominant lineages of pathogenic bacteria often do not provide sufficient resolution to define precise relationships. Here, we describe a high-throughput genomics approach that provides a high-resolution view of the epidemiology and microevolution of a dominant strain of methicillin-resistant *Staphylococcus aureus* (MRSA). This approach reveals the global geographic structure within the lineage, its intercontinental transmission through four decades, and the potential to trace person-to-person transmission within a hospital environment. The ability to interrogate and resolve bacterial populations is applicable to a range of infectious diseases, as well as microbial ecology.

The development of molecular typing techniques has been instrumental in studying the population structure and evolution of bacterial pathogens. Sequence-based approaches, such as multilocus sequence typing (MLST) (1), have resulted in large searchable databases of the most clinically important species. However, MLST defines variation within a very small sam-

ple of the genome and cannot distinguish between closely related isolates. Full-genome sequencing provides a complete inventory of microevolutionary changes, but this approach is impractical for large population samples. The use of next-generation sequencing technologies, such as Illumina Genome Analyzer, bridges this gap by mapping genome-wide single-nucleotide poly-



morphisms (SNPs) and insertions or deletions (indels) to a reference sequence. The use of index adapters to create individually tagged genomic libraries provides the means to generate data for multiple bacterial isolates on a single sequencer lane and makes it feasible to rapidly generate whole-genome DNA sequence data for large population samples of bacteria.

<sup>1</sup>The Wellcome Trust Sanger Institute, Wellcome Trust Genome Campus, Hinxton, Cambridge CB10 1SA, UK. <sup>2</sup>Department of Biology and Biochemistry, University of Bath, South Building, Claverton Down, Bath BA2 7AY, UK. <sup>3</sup>Faculty of Tropical Medicine, Mahidol University, Bangkok, Thailand. <sup>4</sup>Department of Medicine, University of Cambridge, Addenbrooke's Hospital, Cambridge CB2 0QQ, UK. <sup>5</sup>Laboratory of Molecular Genetics, Instituto de Tecnologia Química e Biológica, Universidade Nova de Lisboa, 2780-156 Oeiras, Portugal. <sup>6</sup>Laboratory of Microbiology, The Rockefeller University, New York, NY 10065, USA. <sup>7</sup>Centre for Clinical Vaccinology and Tropical Medicine, Nuffield Department of Clinical Medicine, University of Oxford, Oxford OX3 7LJ, UK. <sup>8</sup>Centre for Infection, Department of Cellular and Molecular Medicine, St. George's, University of London, Cranmer Terrace, London SW17 0RE, UK. <sup>9</sup>Department of Infectious Diseases, King's College London, Guy's, King's, and St. Thomas' Medical School, Guy's Hospital, London SE1 9RT, UK. <sup>10</sup>Directorate of Infection, Guy's and St. Thomas' National Health Service Foundation Trust, London SE1 7EH, UK.

\*These authors contributed equally to this work.

†To whom correspondence should be addressed. E-mail: sdb@sanger.ac.uk

Health care-associated, methicillin-resistant *Staphylococcus aureus* (HA-MRSA) is a globally important human pathogen. Current typing methods resolve the majority of HA-MRSA isolates into a small number of widely disseminated clonal lineages (2). One such clone, defined by MLST as sequence type 239 (ST239), is multiply antibiotic-resistant and accounts for at least 90% of HA-MRSA throughout China (3), Thailand (4), Turkey (5), and probably much of mainland Asia (6). ST239 has been detected in South America (7, 8) and is currently circulating in Eastern Europe (9–11). Variants of ST239 correspond to the epidemic MRSA(1)–1, -4, -11, Brazilian, Portuguese, Hungarian, and Viennese clones, which are distinguished on the basis of variation within the large type III SCCmec element, *spa* data, and subtle differences by pulsed-field gel electrophoresis (PFGE). Despite this variation, current typing methods provide little discriminatory power for subtyping ST239 isolates within a given region because single variants that undergo clonal expansion can dominate in hospitals throughout a large geographic area.

To investigate the utility of a second-generation DNA sequencing platform for high-resolution genotyping and investigation of the microevolutionary events within MRSA, we analyzed 63 ST239 isolates (table S1) from two distinct samples

(12). The first sample, consisting of 43 isolates from a global collection recovered between 1982 and 2003, provides a snapshot of the global ST239 population. One of these isolates (TW20) was sequenced to completion to provide a reference for analysis. The second sample of 20 isolates, derived from patients at the Sappasithiprasong hospital in northeast Thailand within a 7-month period, provides a very closely related group, potentially linked via a chain of transmission.

Mapping reads for each isolate against TW20 (table S2) identified 6714 high-quality SNPs. These SNPs had a markedly uneven distribution across the genome (fig. S1A), largely related to whether the SNP resided in the core (present in all sample isolates) or accessory regions of the genome. The accessory genome primarily comprised mobile genetic elements (MGEs) such as phage, transposons, SCCmec, and genomic islands that are known to constitute a major source of variation between *S. aureus* genomes (13). Because MGEs have an inherent potential for horizontal transfer between isolates, which could confound phylogenetic interpretations, we distinguished between the “core” and “noncore” genome for subsequent analysis.

The maximum likelihood phylogeny presented in Fig. 1 was reconstructed by using the 4310 variable sites in the core genome (table S3).

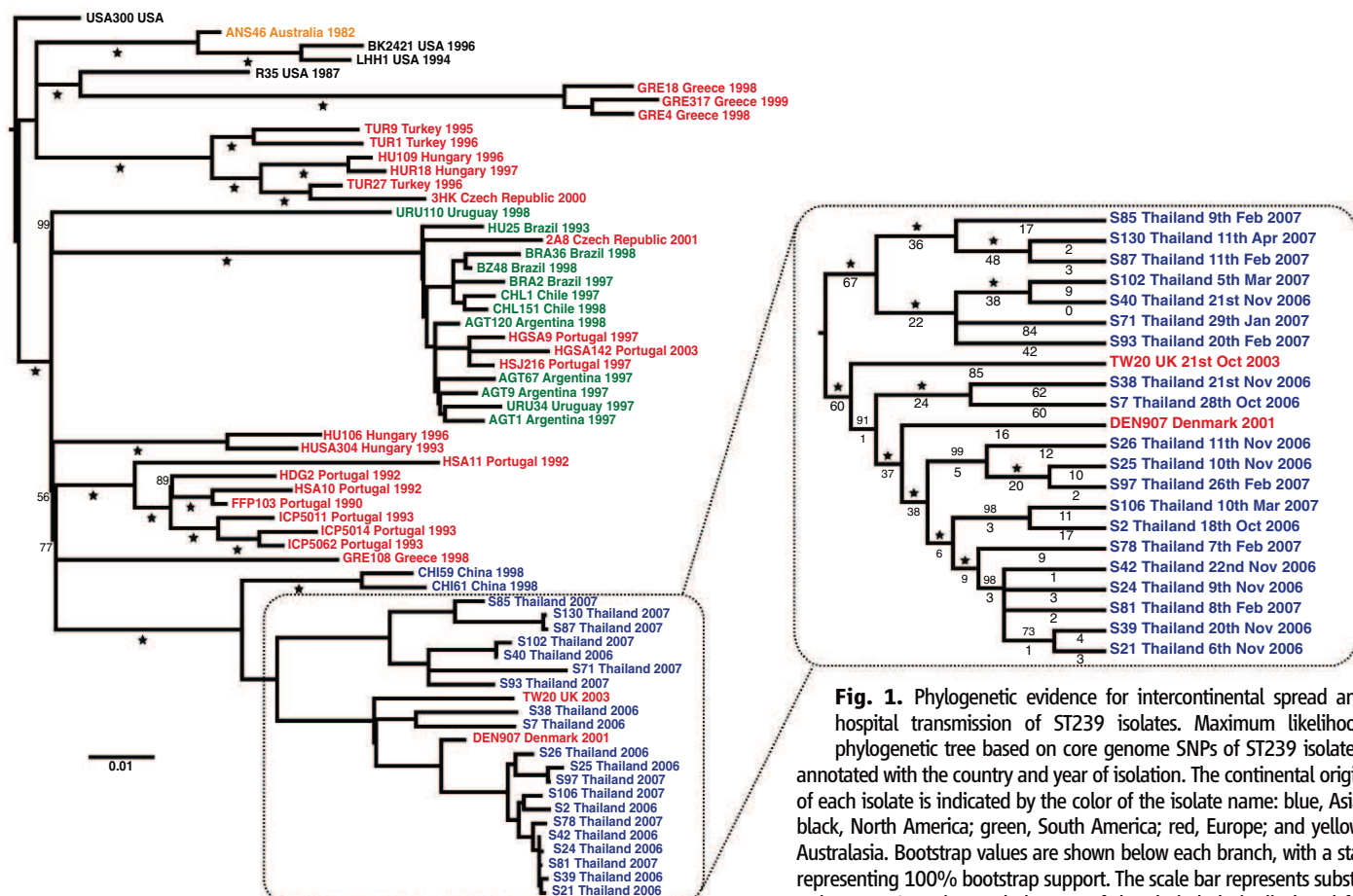


**Fig. 1.** Phylogenetic evidence for intercontinental spread and hospital transmission of ST239 isolates. Maximum likelihood phylogenetic tree based on core genome SNPs of ST239 isolates, annotated with the country and year of isolation. The continental origin of each isolate is indicated by the color of the isolate name: blue, Asia; black, North America; green, South America; red, Europe; and yellow, Australasia. Bootstrap values are shown below each branch, with a star representing 100% bootstrap support. The scale bar represents substitutions per SNP site. A cladogram of the Thai clade is displayed for

greater resolution with bootstrap values (above the branch), number of distinguishing SNPs (below the branch), and isolates labeled with date of isolation, where known.

We are confident that our approach has resulted in a robust tree. First, we noted little evidence of homoplasy (convergent evolution); of the 4310 sites that exhibited a SNP, only 38 (0.88%) were homoplastic (cannot be explained without convergence when mapped onto the tree) (Table 1). Notably, many of the homoplastic SNPs were in genes involved in drug resistance, with 10 corresponding to mutations known to confer resistance. Secondly, the tree showed a striking consistency with geographic source (Fig. 1). The South American isolates, with one exception, clustered tightly within a highly distinct and uniform clade, which may reflect a recent expansion of a single variant throughout the continent. Similarly, the Thai and

Chinese isolates formed a single, although more diverse, Asian clade. The European isolates were more diverse still, with most positioned basally on the tree, consistent with a possible European origin for ST239. Within the European isolates, there was also evidence of geographical clustering.

There were several exceptions to this geographical structure that illustrate the intercontinental spread of MRSA. Two PGFE-distinguishable clones of ST239 are known to have dominated in Portuguese hospitals during the 1990s: the Portuguese clone in the early 1990s and the Brazilian clone that appeared in 1997. All seven Portuguese clone isolates recovered between 1990 and 1993 clustered together, whereas the three Bra-

zilian clone isolates clustered within the South American clade, strongly supporting the hypothesis that this second wave in Portugal resulted from the introduction of a South American variant.

More intriguing were two European isolates that clustered within the Thai clade: DEN907, isolated in Denmark, and TW20, from a large 2-year outbreak at a London hospital (14). In addition to the core SNPs, both isolates contain the  $\phi$ SP $\beta$ -like (TW20) prophage characteristic of the Asian clade (fig. S1B). Records for the Danish isolate indicated that the patient was Thai, consistent with its position on the tree. The position of TW20 is less readily explained and potentially points to a single intercontinental transmission event, most likely from southeast Asia, that sparked the London outbreak.

Although the current isolate collection did not permit a robust temporal analysis, a linear regression of root-to-tip distances against the year of sampling showed a strong correlation, with older isolates positioned more basally (fig. S2). The estimated mutation rate for the isolate collection was  $3.3 \times 10^{-6}$  [95% confidence interval (CI) from  $2.5 \times 10^{-6}$  to  $4.0 \times 10^{-6}$ ] per site per year and would date the most recent common ancestor of ST239 to the mid to late 1960s, a period contemporaneous with the emergence of MRSA in Europe (15). This rate is about 1000 times faster than the canonical substitution rate estimate for *E. coli* (16) but more in line with recent rate estimates based on analyses of more closely related bacterial genomes (17, 18). Potential explanations for this could include a reduction in effective population size, leading to increased accumulation of mutations (although we have no evidence of this), or the possibility that some of the core SNPs were transferred by recombination, although the low level of homoplasy suggests that recombination has been rare. Alternatively, it may be that the greater resolution of our analysis allows us to determine the rate of mutation in the population before selection has had time to purify out those that are detrimental. This explanation implies that purifying selection acts on all mutations, including intergenic and synonymous sites, but over longer time periods, as suggested by Moran *et al.* (17) and shown for nonsynonymous mutations by Rocha *et al.* (19).

In addition to providing evidence for intercontinental transmission of ST239 variants, these data also hold the promise of revealing fine-scale transmission events between or within single hospitals. Our data included 20 isolates collected over 7 months at a single hospital in Thailand. These isolates were surprisingly divergent when compared with the South American clade (which encompasses isolates from Brazil, Chile, Argentina, and Uruguay). However, five isolates were differentiated by only 14 SNPs: four isolates (S21, S24, S39, and S42) obtained within a 16-day period and the remainder (S81) isolated 11 weeks later. These times of isolation are consistent with our estimated mutation rate of one core SNP every 6 weeks. We examined the possibility of

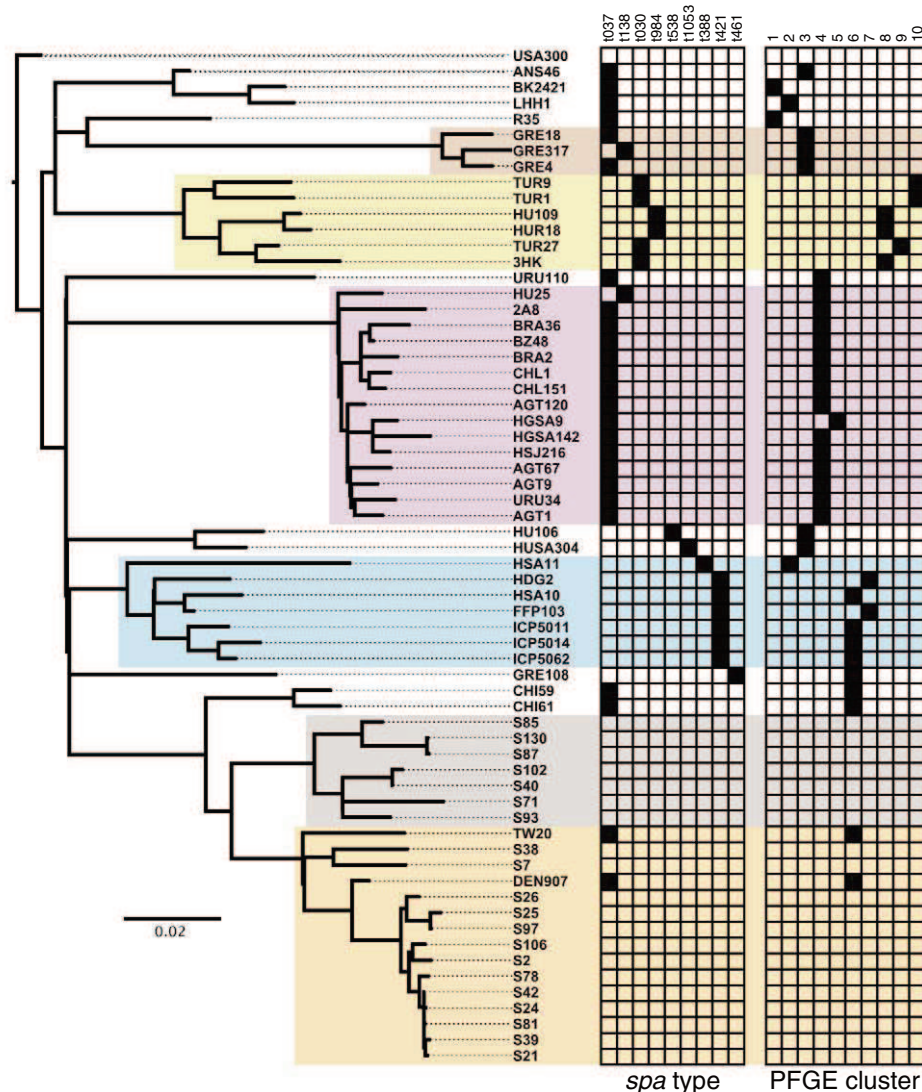


**Fig. 2.** Comparison of phylogeny with traditional typing techniques. Maximum likelihood phylogenetic tree based on core genome SNPs of ST239 isolates, annotated with *spa* typing databased on the RIDOM scheme (27), and PFGE typing databased on BioNumerics (version 4.0, Applied Maths, Ghent, Belgium) clustering (excluding the Thai hospital isolates and USA300, which had not been typed). The most common *spa* type was t037, which accounted for all but one of the isolates corresponding to the South American clade but was also represented among a scattering of isolates from Europe and Asia, suggesting that t037 represents the ancestral ST239 *spa* type (the plesiomorphic state). Solid boxes in the appropriate column indicate the respective *spa* type (left grid) and PFGE cluster (right grid) of the strain. Major clades in the tree are shaded for clarity.



**Table 1.** Homoplasies identified in the core regions of ST239 isolates. The SNP substitutions listed relate to the predicted forward strand of the TW20 chromosome. Isolates where homoplasies were detected are indicated, and where the isolates share the same node as illustrated in the phylogenetic tree in Fig. 1 they are in parentheses. bp indicates base pairs.

SNP position	Region	Isolates	SNP	Substitution	Antibiotic
7254	DNA gyrase subunit A (GyrA)	HUSA304, (S85, S130, S87)	T→G	Ser <sup>84</sup> →Ala <sup>84</sup> (Ser84Ala)*	
7255	GyrA	(BK2421, LHH1), (GRE18, GRE317, GRE4), (TUR9, TUR1), (TUR27, 3HK), (URU110, HU25, 2A8, BRA36, BZ48, BRA2, CHL1, CHL151, HGSA9, HGSA142, HSJ216, AGT67, AGT9, URU34, AGT1), HUSA304, GRE108, (CHI59, CHI61), (S102, S40, S71, S93, TW20, S38, S7, DEN907, S26, S25, S97, S106, S2, S78, S42, S24, S81, S39, S21)	C→T	Ser84Leu	Quinolone (23)
7266	GyrA	(HU109, HUR18), AGT120, HU106, (ICP5014, ICP5062)	G→A	Lys88Glu	Quinolone (23)
133864	Immunoglobulin G binding protein A precursor	HU25, GRE108	G→A	Synonymous	—
134787	92 bp upstream of immunoglobulin G binding protein A precursor	3HK, (HU25, BZ48, BRA2, CHL1, AGT120, HGSA142, HSJ216, AGT67, AGT9, AGT1)	G→T	Intergenic	—
278498	129 bp upstream of putative acetyl-coenzyme A transferase	(ANS46, BK2421, LHH1, R35, GRE18, GRE317, GRE4, TUR9, TUR1, HU109, HUR18, TUR27, 3HK), GRE108	T→C	Intergenic	—
436474	34 bp upstream of putative dioxygenase	(TUR9, TUR1, HU109, HUR18, TUR27, 3HK), HSA10	C→T	Intergenic	—
594883	Tetrapyrrole (corrin/porphyrin) methylase family protein	(BK24210, LHH1), TUR9	C→T	Pro49Ser	—
657696	DNA-directed RNA polymerase beta chain protein (RpoB)	GRE4, HSJ216, GRE108, HDG2	C→A	Asp471Glu	Rifampin (25)
657724	RpoB	(GRE18, GRE317, GRE4), (TUR9, TUR1, HU109, HUR18, TUR27, 3HK), (HU25, 2A8, BRA36, BZ48, BRA2, CHL1, CHL151, AGT120, HGSA9, HGSA142, HSJ216, AGT67, AGT9, URU34, AGT1), (HDG2, HSA10, FFP103), (S85, S87, S130, S93, S71, S102, S40)	C→A	His481Asn	Rifampin (25)
657869	DNA-directed RNA polymerase beta chain protein RpoB	AGT67, (S93, S71, S102, S40)	C→T	Ser529Leu	Rifampin (25)
666536	Translation elongation factor G (FusA)	(GRE18, GRE317, GRE4), GRE108	T→A	Leu461Lys <sup>†</sup>	Fusidic acid (20)
666537	FusA	(GRE18, GRE317, GRE4), GRE108	T→A		
681826	48 bp upstream of serine-aspartate repeat-containing protein C	CHI61, (S26, S97, S2, S78, S39)	C→A	Intergenic	—
862898	Putative membrane protein	GRE4, (S87, S130)	A→C	Ser160Ala	—
1130135	63 bp upstream of FOLD bifunctional protein	URU110, HGSA9	G→T	Intergenic	—
1138698	Phosphoribosylglycinamide formyltransferase (PurN)	(GRE18, GRE317, GRE4), (HUSA304, HU106), (HSA10, FFP103)	T→A	Leu174Met	—
1172434	50 bp upstream of probable manganese transport protein	(TUR27, 3HK), (HU25, 2A8, BRA36, BZ48, BRA2, CHL1, CHL151, AGT120, HGSA9, HGSA142, HSJ216, AGT67, AGT9, URU34, AGT1), (TW20, S38, S7, DEN907, S26, S97, S25, S2, S106, S78, S24, S81, S39)	T→G	Intergenic	—
1172436	52 bp upstream of probable manganese transport protein	(BK24210, LHH1), HSA11	T→C	Intergenic	—
1172444	60 bp upstream of probable manganese transport protein	(R35, GRE18, GRE317, GRE4), (HDG2, HSA10, FFP103, ICP5011, ICP5014, ICP5062)	C→G	Intergenic	—
1206826	ribonuclease HIII	(HU25, 2A8, BRA36, BZ48, BRA2, CHL1, CHL151, AGT120, HGSA9, HGSA142, HSJ216, AGT67, AGT9, URU34, AGT1), (TW20)	C→T	Glu199Lys	—
1261219	Isoleucyl-tRNA synthetase	CHI59, TW20	G→T	Val588Phe	Mupirocin (22)
1448063	Topoisomerase IV subunit A (GrlA)	ANS46, R35, (HDG2, HSA10, FFP103), ICP5011	T→C	Ser80Phe	Quinolone (23)

Continued on next page

SNP position	Region	Isolates	SNP	Substitution	Antibiotic
1524413	Dihydrofolate reductase type I (DfrB)	GRE18, (URU110, HU25, 2A8, BRA36, BZ48, BRA2, CHL1, CHL151, AGT120, HGSA9, HGSA142, HSJ216, AGT67, AGT9, URU34, AGT1)	T→C	His150Arg	Trimethoprim (24)
1524566	DfrB	(ANS46, BK2421, LHH1), (GRE18, GRE317, GRE4), (URU110, HU25, 2A8, BRA36, BZ48, BRA2, CHL1, CHL151, AGT120, HGSA9, HGSA142, HSJ216, AGT67, AGT9, URU34, AGT1), (HU106, HUSA304, HDG2, HSA10, FFP103, ICP5011, ICP5014, ICP5062)	A→T	Phe99Tyr	Trimethoprim (21)
1524789	DfrB	LHH1, 2A8	G→A	Synonymous	—
1525796	Thymidylate synthase (ThyA)	LHH1, 2A8, GRE108	G→A	Synonymous	—
1525817	ThyA	LHH1, 2A8, GRE108	G→A	Synonymous	—
1525832	ThyA	LHH1, 2A8, GRE108	G→A	Synonymous	—
1640281	Glyoxalase/bleomycin resistance protein/dioxygenase superfamily protein	ICP5014, (CHI59, CHI61)	T→G	Synonymous	—
1689862	Putative transcriptional repressor (CcpN)	(BK24210, LHH1), (HU106, HUSA304)	C→T	Synonymous	—
1755814	Probable cell wall amidase (Lyth)	HDG2, (S85, S87, S130, S93, S71, S102, S40, TW20, S38, S7, DEN907, S26, S25, S97, S106, S2, S78, S42, S24, S81, S39, S21)	A→G	Pro63Ser	—
1921379	Bifunctional riboflavin biosynthesis protein (RibD)	ANS46, URU110	G→T	Asn208Lys	—
2334865	Protein SprT-like	TUR1, S40	G→A	Ser43Phe	—
2753531	458 bp upstream of conserved hypothetical protein	(BK24210, LHH1), GRE18	A→T	Intergenic	—
2828688	200 bp downstream of putative exported protein	(TUR9, TUR1, HU109, TUR27, 3HK), GRE108, CHI59	T→C	Intergenic	—
2828714	226 bp downstream of putative exported protein	(TUR9, TUR1, HU109, TUR27, 3HK), GRE108, CHI59, (S38, DEN907, S26, S25, S97, S106, S2, S78, S42, S24, S81, S39, S21)	G→T	Intergenic	—
2859765	39 bp upstream of O-acetyltransferase (OatA)	3HK, S106	C→T	Intergenic	—

\*Change from serine to alanine occurs due to accompanying SNP (7255) within the same codon. †Change from leucine to lysine due to the presence of both SNPs (666536, 666537) within the same codon.

an epidemiological link between these five isolates and noted that the patients were located in wards in adjacent blocks of the hospital and that these wards were not represented in the more divergent isolates. This result has important implications for infection control and generates invaluable information for interventions to target MRSA transmission.

Typing methods, such as *spa* and PFGE, are routinely used for epidemiological studies of *S. aureus* and other bacteria and can distinguish between different ST239 variants. We explored the extent to which the variation assayed by these methods is consistent with the high-resolution SNP data. Overall, we found high levels of consistency between *spa* type and phylogenetic position (Fig. 2), with only a single example of a *spa* type being shared by unrelated isolates (GRE317 and HU25). This finding contrasts with the study of Nübel *et al.* (20), who noted inconsistencies between the *spa* data and SNP data for the ST5 lineage. One possible explanation for this discrepancy is that there has been insufficient time to accumulate numerous *spa* homoplasies within the younger ST239 clone.

PFGE data for the isolates (excluding the Thai isolates) divided the collection into 10

clusters (fig. S3). Again, there was a large degree of consistency between the PFGE clusters and the tree (Fig. 2). However, there were some incompatibilities. For example, cluster 6 was found in unrelated European and Asian isolates. Although certain prophage and MGEs are associated with specific clades [e.g.,  $\phi$ SP $\beta$ -like (TW20) prophage with the Asian clade], the inconsistencies here are likely to be due to the frequent gain and loss of MGEs, which can have dramatic effects on PFGE patterns.

By analyzing whole-genome data of a collection of MRSA ST239, we have gained new insights into fundamental processes of evolution in an important human pathogen. By creating a precise and robust phylogeny for the collection, we now have a highly informative perspective on the evolution of the clone.

These observations point to a limited number of successful intercontinental transmission events and expansion of subclonal variants that in some cases have become dominant in their new geographical region. The potential to detect these new introductions and target heightened infection control interventions, as occurred in the London TW20 outbreak, has clear public health implications and highlights the need for

more informed global surveillance strategies. Equally important is the achievement of absolute discrimination of isolates within a single clinical setting, even those recovered only days apart, and the ability to use this SNP data to inform epidemiological analysis. Multiple additional costly infection control interventions are often used to reduce MRSA transmission supported by patient, staff, and environmental screening programs. The estimated rate of core genome divergence (1 SNP per ~6 weeks) should provide sufficient diversity to separate recent from distant transmission events, thereby dramatically improving contact tracing in endemic and outbreak settings and allowing targeting of diagnostics and interventions according to need. The additional variation from noncore regions provides supplementary discriminatory power and may inform the design of bespoke typing schemes for specific clones and locales.

From these data, we have described an estimated time frame for the emergence of a bacterial pathogen clone and how it has subsequently evolved. Of particular importance is the observation that over a quarter (28.9%) of the homoplasies detected can be directly related to evolution of resistance to antibiotic drugs cur-



rently in use (21–26), confirming clinical practice as a major driver of pathogen evolution and lending heightened importance to understanding the relevance of other homoplasies. Such insights inform future surveillance strategies for the detection of emerging clones and management of epidemic spread. We fully anticipate that, as the technology and analytical methods improve, the approach described here will underpin the next wave of molecular data for epidemiological and microevolutionary studies in bacteria.

# References and Notes

- M. C. Maiden *et al.*, *Proc. Natl. Acad. Sci. U.S.A.* **95**, 3140 (1998).
- M. C. Enright *et al.*, *Proc. Natl. Acad. Sci. U.S.A.* **99**, 7687 (2002).
- B. L. Xu *et al.*, *J. Hosp. Infect.* **71**, 245 (2009).
- E. J. Feil *et al.*, *J. Clin. Microbiol.* **46**, 1520 (2008).
- E. Alp *et al.*, *J. Infect.* **58**, 433 (2009).
- K. S. Ko *et al.*, *J. Clin. Microbiol.* **43**, 421 (2005).
- D. C. Oliveira, A. Tomasz, H. de Lencastre, *Microb. Drug Resist.* **7**, 349 (2001).
- A. M. Vivoni *et al.*, *J. Clin. Microbiol.* **44**, 1686 (2006).
- M. D. Bartels *et al.*, *Eur. J. Clin. Microbiol. Infect. Dis.* **27**, 757 (2008).
- A. Szczepanik, M. Koziol-Montewka, Z. Al-Doori, D. Morrison, D. Kaczor, *Eur. J. Clin. Microbiol. Infect. Dis.* **26**, 29 (2007).
- O. Melter *et al.*, *J. Clin. Microbiol.* **41**, 4998 (2003).
- Materials and methods are available as supporting material on Science Online.
- J. A. Lindsay, M. T. G. Holden, *Trends Microbiol.* **12**, 378 (2004).
- J. D. Edgeworth *et al.*, *Clin. Infect. Dis.* **44**, 493 (2007).
- H. de Lencastre, A. Tomasz, in *Evolutionary Biology of Bacterial and Fungal Pathogens*, F. Baquero, C. Nombela, G. H. Cassell, J. A. Gutierrez, Eds. (American Society for Microbiology, Washington, DC, 2008), pp. 333–346.
- H. Ochman, S. Elwyn, N. A. Moran, *Proc. Natl. Acad. Sci. U.S.A.* **96**, 12638 (1999).
- N. A. Moran, H. J. McLaughlin, R. Sorek, *Science* **323**, 379 (2009).
- D. Falush *et al.*, *Proc. Natl. Acad. Sci. U.S.A.* **98**, 15056 (2001).
- E. P. Rocha *et al.*, *J. Theor. Biol.* **239**, 226 (2006).
- U. Nübel *et al.*, *Proc. Natl. Acad. Sci. U.S.A.* **105**, 14130 (2008).
- S. Besier, A. Ludwig, V. Brade, T. A. Wichelhaus, *Mol. Microbiol.* **47**, 463 (2003).
- G. E. Dale *et al.*, *J. Mol. Biol.* **266**, 23 (1997).
- J. G. Hurdle, A. J. O'Neill, I. Chopra, *J. Antimicrob. Chemother.* **53**, 102 (2004).
- M. Tanaka, T. Wang, Y. Onodera, Y. Uchida, K. Sato, *J. Infect. Chemother.* **6**, 131 (2000).
- A. A. Vickers, N. J. Potter, C. W. Fishwick, I. Chopra, A. J. O'Neill, *J. Antimicrob. Chemother.* **63**, 1112 (2009).
- T. A. Wichelhaus *et al.*, *Antimicrob. Agents Chemother.* **46**, 3381 (2002).
- D. Harmsen *et al.*, *J. Clin. Microbiol.* **41**, 5442 (2003).
- The Sanger Institute is core funded by the Wellcome Trust. We thank C. Milheirico and J. D. Cockfield for preparation of genomic DNA and G. Dougan and the Sanger Institute Sequencing and Informatics groups for general support. S.G. and A.T. were supported by grants SFRH/BPD/25403/2005 and SFRH/BD/44220/2008, respectively, from Fundação para a Ciência e Tecnologia, Portugal. E.K.N., N.C., N.D., and S.J.P. were funded by the Wellcome Trust. Funding for the sequencing of the TW20 genome was provided by Guy's and St. Thomas' Charity. J.D.E. receives funding from the Department of Health via the National Institute for Health Research's comprehensive Biomedical Research Centre award to Guy's and St. Thomas' National Health Service Foundation Trust in partnership with King's College London. The Illumina Genome Analyzer reads are deposited in the Short Read Archive (National Center for Biotechnology Information) under the accession no. ERA000102. The annotated chromosome of TW20 has been submitted to European Molecular Biology Laboratory with the accession number FN433596.

**Supporting Online Material** [www.sciencemag.org/cgi/content/full/327/5964/469/DC1](http://www.sciencemag.org/cgi/content/full/327/5964/469/DC1) Materials and Methods  
Figs. S1 to S4  
Tables S1 to S4

24 September 2009; accepted 25 November 2009  
10.1126/science.1182395

## Impact of Spikelets on Hippocampal CA1 Pyramidal Cell Activity During Spatial Exploration

Jérôme Epsztein,<sup>†</sup> Albert K. Lee,<sup>‡</sup> Edith Chorev, Michael Brecht

In vivo intracellular recordings of hippocampal neurons reveal the occurrence of fast events of small amplitude called spikelets or fast prepotentials. Because intracellular recordings have been restricted to anesthetized or head-fixed animals, it is not known how spikelet activity contributes to hippocampal spatial representations. We addressed this question in CA1 pyramidal cells by using in vivo whole-cell recording in freely moving rats. We observed a high incidence of spikelets that occurred either in isolation or in bursts and could drive spiking as fast prepotentials of action potentials. Spikelets strongly contributed to spiking activity, driving ~30% of all action potentials. CA1 pyramidal cell firing and spikelet activity were comodulated as a function of the animal's location in the environment. We conclude that spikelets have a major impact on hippocampal activity during spatial exploration.

Spikelets are voltage fluctuations of small amplitude with a spike-like waveform. They were initially described in vivo intracellular recordings from the hippocampus and inferior olive of anesthetized animals (1, 2). Further in vitro experimental work using paired

recordings has shown that spikelets can result from direct action potential transmission via electrical coupling between principal cells (3, 4) and interneurons (5–12). In the hippocampus, it has been suggested that such coupling can occur between the axons of principal neurons (13, 14). However, it has also been suggested that spikelets could reflect the occurrence of ectopic axonal spikes (15–17) or dendritic spikes (1), and the exact origin of spikelet activity remains to be clarified. Because spikelets are difficult to detect with extracellular techniques classically used to record neuronal activity in freely moving animals, nothing is known about how these events contribute to hippocampal spatial representations (18, 19). To address this question, we

used head-anchored whole-cell recording in freely moving rats (20–23) and analyzed spikelet activity during spatial exploration (22).

Recordings were performed in current clamp mode while the animal freely explored an O-shaped maze. We first characterized the properties of hippocampal spikelets (Fig. 1). In an identified CA1 pyramidal cell (Fig. 1A), we observed fast all-or-none events of small amplitude (Fig. 1B, upper trace) that occurred at high frequency (mean = 4.96 Hz) while the rat ran around the maze (Fig. 1B, lower trace). In 10 neurons, these events had electrophysiological characteristics (Fig. 1C) matching those of previously described spikelets such as a fast rise time (mean ± SEM = 0.56 ± 0.08 ms), a biphasic decay ( $\tau_1 = 0.87 \pm 0.11$  ms;  $\tau_2 = 17.3 \pm 5.2$  ms), a small amplitude (mean = 7.03 ± 1.00 mV), and all-or-none behavior. Spikelets had much faster kinetics and higher amplitude ( $P < 0.01$ ) than did excitatory postsynaptic events recorded in the same cells (Fig. 1, D and E, and fig. S1). On the other hand, they were much slower and smaller ( $P < 0.001$ ) than action potentials (APs) (Fig. 1F and fig. S1).

Spikelets were found in a majority of recorded CA1 pyramidal cells (10 out of 16 cells) and occurred with a mean frequency of  $4.8 \pm 1.6$  Hz. Spikelets could be observed either isolated or in the form of short bursts (mean burst duration =  $19 \pm 1$  ms; Fig. 2, A and B). Bursts consisted of three to six spikelets (mean =  $3.2 \pm 0.4$ ) at high frequency (mean =  $138 \pm 9$  Hz, Fig. 2C) often embedded with APs (in five cells with spikelet bursts).

How are spikelets related to the neuron's subthreshold activity? To address this, we first

Bernstein Center for Computational Neuroscience, Humboldt University, 10115 Berlin, Germany.

\*These authors contributed equally to this work.

<sup>†</sup>Present address: Institut de Neurobiologie de la Méditerranée, Institut National de la Santé et de la Recherche Médicale U901, Parc scientifique et technologique de Luminy, Boîte Postale 13, 13273 Marseille Cedex 9, France. To whom correspondence should be addressed. E-mail: epsztein@inmed.univ-mrs.fr

<sup>‡</sup>Present address: Howard Hughes Medical Institute, Janelia Farm Research Campus, Ashburn, VA 20147, USA.

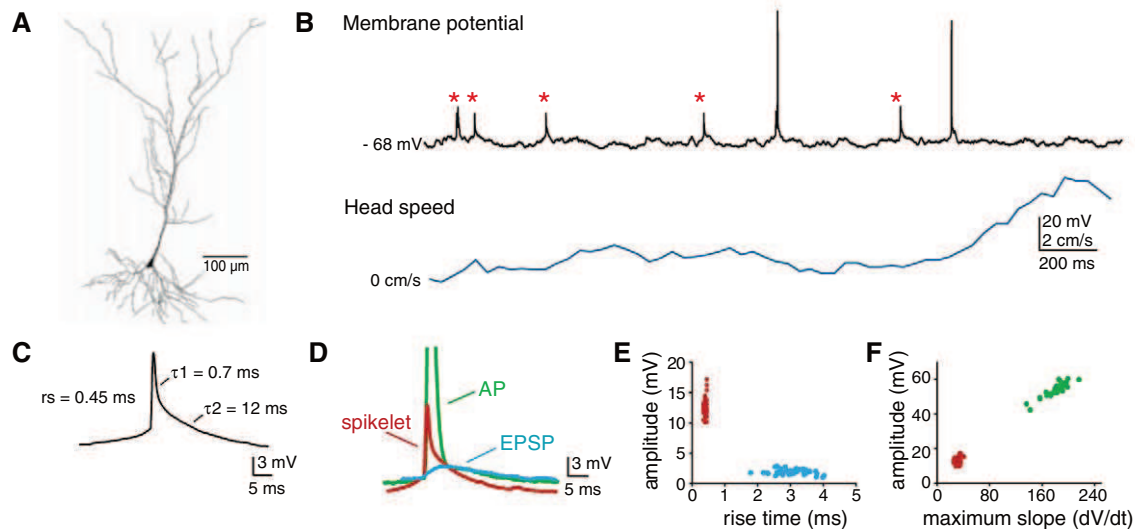
analyzed whether spikelets contribute to AP activity. Spikelets could be recorded as fast prepotentials of APs as previously described (1, 2, 24) (Fig. 3A). Close examination (Fig. 3B) revealed two populations of APs in our data set: some starting abruptly from a slowly rising baseline membrane potential (we refer to them as full-blown APs, fb-APs) and some starting with a faster initial rising phase (we refer to this second class of APs as shoulder APs, sh-APs). When the first derivative ( $dV/dt$ ) of the AP was computed (Fig. 3C), a characteristic initial rising phase (shoulder potential) was seen before the threshold for sh-APs, whereas no such shoulder was observed for fb-APs or APs evoked by current step injection. The distinction between fb-APs and sh-APs became much clearer when the rate of rise of the membrane potential in the 1 ms immediately preceding the AP threshold (50 V/s) was computed (fig. S2).

A number of observations suggest that sh-APs are actually APs initiated by spikelets: Spikelets and shoulder potentials had (i) similar rates of rise ( $12.5 \pm 2.4$  versus  $13.1 \pm 2.6$  V/s;  $P = 0.78$ ), (ii) similar peak  $dV/dt$  ( $15.1 \pm 3.6$  versus  $19.1 \pm 7.5$  V/s;  $P = 0.90$ ), and (iii) sh-APs were never seen in cells that had no spikelet activity ( $n = 6$  out of 6) (fig. S3). That spikelets are sufficient to trigger spikes is strongly supported by the temporal correlation of all spikelet (including shoulder potentials) and AP activity. As shown in the spikelet-AP crosscorrelation (Fig. 3, D and E), APs were tightly time-locked to spikelets, suggesting that it is the occurrence of the spikelet rather than other inputs that ultimately drives those APs. In addition to the sharp millisecond time scale locking of spikelets and AP activity, we also observed a broader temporal correlation on the 10-ms time scale. As stated above, spikelets often occurred in the form of high fre-

quency bursts with interspikelet intervals in that range (range from 6.1 to 9 ms,  $n = 5$ ). The modulation of the spikelet-AP crosscorrelation with similar intervals is in line with the idea that a large proportion of APs are driven by spikelets. To further test that sh-APs are driven by spikelets, we also performed current injection experiments in four neurons with spikelets in anesthetized animals and computed the spikelet-to-AP transfer ratio (the ratio of shoulder potentials to all spikelets, including both isolated spikelets and the ones in the form of shoulder potentials). We observed a significant increase in the spikelet-to-AP transfer ratio during depolarization by current injection in two of these neurons (we could not assess the effect of current injection in a statistically meaningful way in the two remaining cells) (fig. S4).

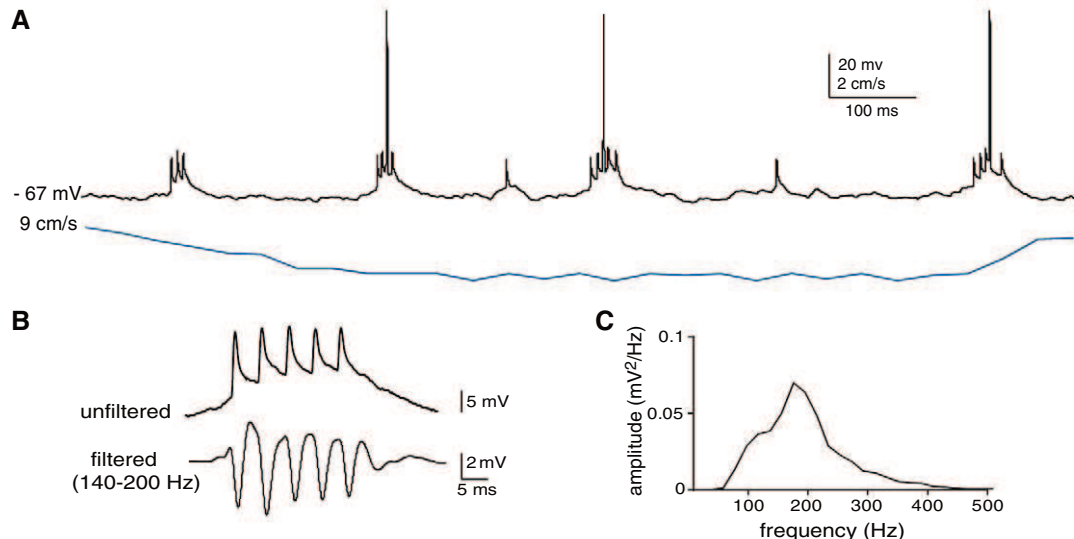
We then quantified the occurrence of sh-APs in CA1 pyramidal cells. Sh-APs could be ob-

**Fig. 1.** Spikelets from an identified hippocampal CA1 pyramidal cell in a freely moving rat. (A) Reconstruction of the morphology of the recorded CA1 pyramidal neuron filled with biocytin during recording. (B) (Top) Membrane potential trace recorded during spatial exploration. Fast events of small amplitude (red stars) are present in addition to action potentials (APs). (Bottom) Corresponding speed of the animal's head. (C) Averaged spikelet ( $n = 35$ ). Mean spikelet has a fast rise time (rs) and a decay time best fitted by the sum of two exponentials. (D) Superimposition of averaged APs (green), spikelets (red), and excitatory postsynaptic potentials (EPSPs, blue). (E) Scatterplot of EPSP (blue) and spikelet (red) amplitude versus rise time. Spikelets represent an independent population of events with faster rise times and larger



amplitudes than EPSPs. (F) Scatterplot of AP (green) and spikelet (red) amplitude versus maximum rising slope ( $dV/dt$ ). Spikelets represent an independent population of events with slower rising slopes and smaller amplitudes than APs.

**Fig. 2.** Temporal pattern of spikelets. (A) (Top) Membrane potential trace of a CA1 pyramidal cell during spatial exploration. Spikelets often occur as high frequency bursts. (Bottom) Corresponding speed of the animal's head. (B) Example of a spikelet burst recorded in this cell. (Top) Unfiltered. (Bottom) Filtered in the ripple frequency band. (C) Mean power spectrum of spikelet bursts recorded in this cell ( $n = 49$  bursts, mean interspikelet interval =  $6.1 \pm 1.5$  ms).





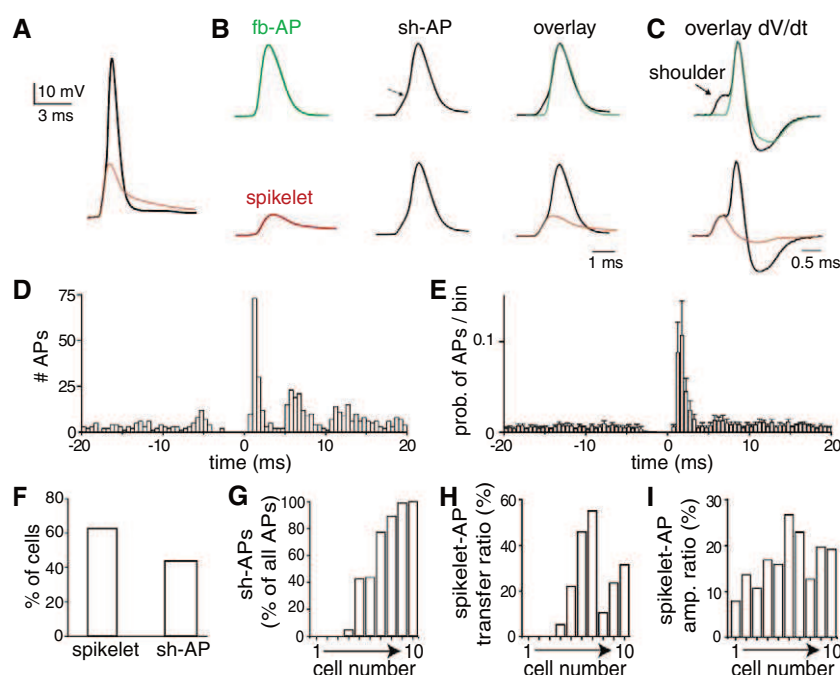


**Fig. 3.** Spikelets drive spiking in CA1 pyramidal cells in freely moving rats. **(A)** Overlay of mean AP (black) and spikelet (red) waveforms. **(B)** (Top) Mean waveforms of fb-APs (green) as evoked by current injection and sh-APs (black, shoulder break marked by an arrow), overlaid on the right. (Bottom) Mean waveforms of spikelets (red) and sh-APs (black), overlaid on the right. **(C)** (Top) Overlay of first derivative ( $dV/dt$ ) of mean fb-AP as evoked by current injection (green) and sh-AP (black). (Bottom) Overlay of first derivative ( $dV/dt$ ) of mean sh-AP (black) and spikelet (red). The shoulder potential corresponds to the spikelet waveform. **(D)** Spikelet-AP crosscorrelogram for the cell shown in Fig. 2. The start time of all spikelets (including the ones in the form of shoulder potentials) is cross-correlated with the peak time of all APs (fb-APs and sh-APs). **(E)** Same as in (D) for all cells with spikelets ( $n = 10$ ). Error bars indicate SEM. **(F)** Fraction of cells with spikelets and sh-APs. **(G)** Fraction of sh-APs out of all APs (fb-APs and sh-APs) for each cell with spikelets. **(H)** Fraction of spikelets that drive spiking (in the form of shoulder potentials) out of all spikelets (isolated spikelets and shoulder potentials) for each cell with spikelets. **(I)** Spikelet amplitude expressed as a percentage of AP amplitude for each cell with spikelets.

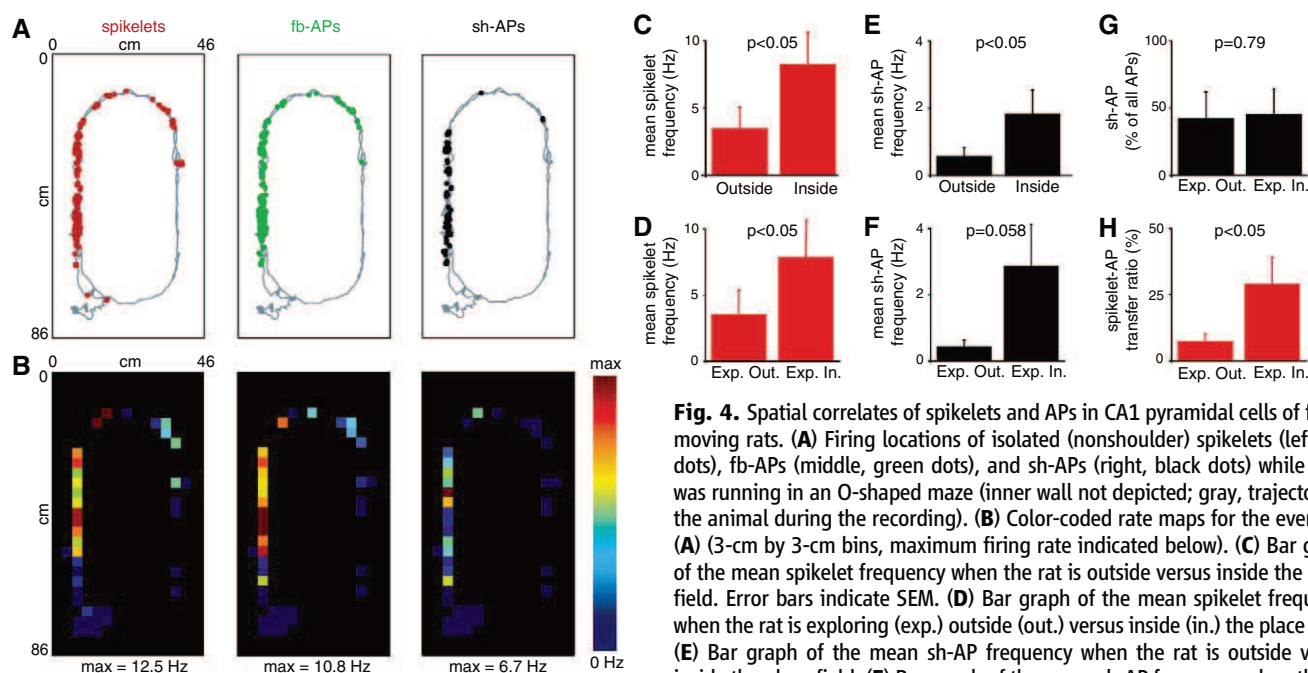


**Fig. 4.** Spatial correlates of spikelets and APs in CA1 pyramidal cells of freely moving rats. **(A)** Firing locations of isolated (nonshoulder) spikelets (left, red dots), fb-APs (middle, green dots), and sh-APs (right, black dots) while a rat was running in an O-shaped maze (inner wall not depicted; gray, trajectory of the animal during the recording). **(B)** Color-coded rate maps for the events in **(A)** (3-cm by 3-cm bins, maximum firing rate indicated below). **(C)** Bar graph of the mean spikelet frequency when the rat is outside versus inside the place field. Error bars indicate SEM. **(D)** Bar graph of the mean spikelet frequency when the rat is exploring (exp.) outside (out.) versus inside (in.) the place field. **(E)** Bar graph of the mean sh-AP frequency when the rat is outside versus inside the place field. **(F)** Bar graph of the mean sh-AP frequency when the rat is exploring (exp.) outside (out.) versus inside (in.) the place field. **(G)** Bar graph of the mean proportion of sh-APs (out of all APs) when the rat is exploring (exp.) outside (out.) versus inside (in.) the place field. **(H)** Bar graph of the mean spikelet-AP transfer ratio when the rat is exploring (exp.) outside (out.) versus inside (in.) the place field.

is exploring (exp.) outside (out.) versus inside (in.) the place field. **(G)** Bar graph of the mean proportion of sh-APs (out of all APs) when the rat is exploring (exp.) outside (out.) versus inside (in.) the place field. **(H)** Bar graph of the mean spikelet-AP transfer ratio when the rat is exploring (exp.) outside (out.) versus inside (in.) the place field.

served in a large proportion of recordings (7 out of 16 cells, Fig. 3F) and in these cells represented a large fraction of spiking activity (mean =  $65 \pm 13\%$  of all APs; Fig. 3G). Across all cells (including those without spikelets), we found that spikelets triggered  $28 \pm 10\%$  of the spiking activity of CA1 pyramidal cells in the awake behaving animal. As shown in Fig. 3G, the proportion of sh-APs varied greatly between cells with spikelets. We computed the spikelet-to-AP transfer ratio, which represents the efficiency with which spikelets drive APs, for individual cells (Fig. 3H) and observed that it could be predicted in part from the amplitude of the respective spikelets (Fig. 3I). Although in several cells close to 100% of APs were sh-APs, we never observed a cell where all spikelets resulted in sh-APs.

Lastly we analyzed the behavioral correlates of spikelets. Extracellular recordings have revealed a strong spatial modulation of hippocampal CA1 pyramidal cell firing (18, 19). In our data set, there were seven cells in which the animal completed multiple laps around the maze and which we analyzed for such place cell activity (23, 25). Of these, three (~40%) were place cells, showing spatial modulation of their firing rate. Figure 4 shows an example of such a cell where spikelet and sh-AP activity were detected. The cell showed an increase in AP firing rate during two successive passes through the same location (i.e., its place field). The frequency of both fb-APs and spikelets was specifically increased in this location (Fig. 4, A and B, and fig. S5A). The sh-AP rate was also specifically increased in the same location, indicating that spikelet activity contributed to spiking activity

recorded inside the place field (Fig. 4, A and B). In two out of the three recorded place cells, AP and spikelet activity were spatially comodulated, whereas the remaining cell showed no spikelet activity.

We also analyzed spiking and spikelet spatial modulation in four additional cells where the rat's spatial exploration was sufficient (i.e., a single lap around the maze) for spatial modulation analysis but which we could not unambiguously classify as place cells [because of the absence of data across multiple laps (25)]. The AP firing rate was spatially modulated in all four of these cells, and the spikelet rate in two. Remarkably, three of these cells showed significant spatial comodulation of spike and spikelet rate ( $P < 0.05$ , figs. S5B and S6). Overall, out of six spatially modulated cells with spikelets (two of which were classified as place cells), five showed significant ( $P < 0.05$ ) comodulation. We conclude that, like spiking activity, spikelet activity can be spatially modulated in CA1 pyramidal cells and that both types of cellular activity are spatially aligned.

We then analyzed spikelet activity in the non-place-modulated cells. In these cells, the overall spiking activity was very low, as previously described (26). Interestingly, only one out of four non-place-modulated cells showed spikelet activity, and in this cell spikelet frequency was low (0.12 Hz). Furthermore, this cell showed no spatial modulation of spikelet activity.

Further analysis was done to investigate the specific functional contribution of spikelets to in-field spiking during spatial exploration. The animal's behavior was classified into periods of exploratory versus resting (but awake) behavior and separately into periods inside versus outside the AP firing rate field (25) for the six spatially modulated cells with spikelets. The mean spikelet firing rate was higher inside compared with outside the field (Fig. 4C), consistent with the spatial comodulation of AP and spikelet firing rates. This difference was preserved when considering only periods of exploratory behavior (7.82 Hz inside versus 3.50 Hz outside,  $P < 0.05$ ; Fig. 4D). The in-field spikelet rate was not different between exploration and rest ( $P = 0.53$ ), as was also the case for the out-of-field rate ( $P = 0.98$ ) (Fig. 4D and fig. S7A). Thus, the spikelet rate depends on the animal's location

with respect to the AP field regardless of behavioral state. What about the sh-APs, which represent the direct effect of spikelets on spiking? The mean sh-AP rate was higher inside versus outside the AP field (Fig. 4E), and this relation held during both exploration (2.86 Hz versus 0.43 Hz,  $P = 0.058$ ; Fig. 4F) and rest (fig. S7B). However, the proportion of all APs that was driven by spikelets was not different inside versus outside the field during exploration (0.45 versus 0.42,  $P = 0.79$ , Fig. 4G) or rest (fig. S7C). In contrast, the spikelet-AP transfer ratio was higher inside versus outside the field during exploration (0.29 versus 0.07,  $P < 0.05$ , Fig. 4H) and similarly so, but by a lesser amount, during rest (fig. S7D). Thus, spikelets have their maximum impact on spiking within the place field during exploratory behavior. On the basis of the findings from our current injection experiments, we suggest that the increased efficacy of spikelets results from membrane potential depolarization inside the place field (23, 27).

Spikelets have been observed in intracellular recordings of a variety of neuronal types both in vivo and in vitro. In the hippocampus, in vitro slice recordings as well as computational simulations suggest an important synchronizing role for spikelets during spontaneous high-frequency oscillations (28) and acute pharmacologically induced epileptiform activity (29–33). Here, intracellular recordings in freely behaving animals allowed us to assess the role of spikelet activity during spatial exploration. In hippocampal CA1 pyramidal cells with spatially modulated spiking, the frequency of spikelets was elevated within the place field; however, in those cells lacking clear spatial modulation of spiking, spikelet as well as spike frequency were both low. Together with the observation that spikelets can powerfully influence the spiking behavior of CA1 pyramidal cells, these results provide new insights into why hippocampal place cells fire where they fire.

#### References and Notes

1. E. R. Kandel, W. A. Spencer, *J. Neurophysiol.* **24**, 272 (1961).
2. R. Llinas, R. Baker, C. Sotelo, *J. Neurophysiol.* **37**, 560 (1974).
3. B. A. MacVicar, F. E. Dudek, *Science* **213**, 782 (1981).
4. A. Mercer, A. P. Bannister, A. M. Thomson, *Brain Cell Biol.* **35**, 13 (2006).
5. M. Galarreta, S. Hestrin, *Nature* **402**, 72 (1999).

6. J. R. Gibson, M. Beierlein, B. W. Connors, *Nature* **402**, 75 (1999).
7. P. Mann-Metzer, Y. Yarom, *J. Neurosci.* **19**, 3298 (1999).
8. G. Tamás, E. H. Buhl, A. Lörincz, P. Somogyi, *Nat. Neurosci.* **3**, 366 (2000).
9. C. E. Landisman et al., *J. Neurosci.* **22**, 1002 (2002).
10. A. Simon, S. Oláh, G. Molnár, J. Szabadics, G. Tamás, *J. Neurosci.* **25**, 6278 (2005).
11. V. Zsiros, G. Maccaferri, *J. Neurosci.* **25**, 8686 (2005).
12. G. P. Dugué et al., *Neuron* **61**, 126 (2009).
13. D. Schmitz et al., *Neuron* **31**, 831 (2001).
14. F. Hamzei-Sichani et al., *Proc. Natl. Acad. Sci. U.S.A.* **104**, 12548 (2007).
15. S. F. Stasheff, M. Hines, W. A. Wilson, *J. Neurophysiol.* **70**, 961 (1993).
16. R. D. Traub, S. B. Colling, J. G. R. Jefferys, *J. Physiol.* **489**, 127 (1995).
17. M. Avoli, M. Methot, H. Kawasaki, *Eur. J. Neurosci.* **10**, 2714 (1998).
18. J. O'Keefe, J. Dostrovsky, *Brain Res.* **34**, 171 (1971).
19. R. Müller, *Neuron* **17**, 813 (1996).
20. A. K. Lee, I. D. Manns, B. Sakmann, M. Brecht, *Neuron* **51**, 399 (2006).
21. A. K. Lee, J. Epszstein, M. Brecht, *Nat. Protoc.* **4**, 385 (2009).
22. J. Epszstein, A. K. Lee, M. Brecht, *Soc. Neurosci. Abstr.* **2008**, 690.21 (2008).
23. A. K. Lee, J. Epszstein, M. Brecht, *Soc. Neurosci. Abstr.* **2008**, 690.22 (2008).
24. S. Crochet, P. Fuentealba, I. Timofeev, M. Steriade, *Cereb. Cortex* **14**, 1110 (2004).
25. Materials and methods are available as supporting material on Science Online.
26. L. T. Thompson, P. J. Best, *J. Neurosci.* **9**, 2382 (1989).
27. C. D. Harvey, F. Collman, D. A. Dombeck, D. W. Tank, *Nature* **461**, 941 (2009).
28. A. Draguhn, R. D. Traub, D. Schmitz, J. G. Jefferys, *Nature* **394**, 189 (1998).
29. J. G. Jefferys, H. L. Haas, *Nature* **300**, 448 (1982).
30. C. P. Taylor, F. E. Dudek, *Science* **218**, 810 (1982).
31. J. L. Perez-Velazquez, T. A. Valiante, P. L. Carlen, *J. Neurosci.* **14**, 4308 (1994).
32. T. A. Valiante, J. L. Perez Velazquez, S. S. Jahromi, P. L. Carlen, *J. Neurosci.* **15**, 6946 (1995).
33. R. D. Traub, R. Bibbig, A. Piechotta, R. Draguhn, D. Schmitz, *J. Neurophysiol.* **85**, 1246 (2001).
34. We would like to thank B. Geue, R. Karpinski, and A. Stern at Humboldt University for technical assistance and D. Schmitz for comments on the manuscript. This work was supported by NeuroCure, Bernstein Center for Computational Neuroscience (BMBF), Humboldt University, and Neuro-behavior European Research Council grants (M.B.), a European Molecular Biology Organization Long Term Fellowship (A.K.L.), and a Human Frontier Science Program Long Term Fellowship (J.E.).

**Supporting Online Material** www.sciencemag.org/cgi/content/full/327/5964/474/DC1 Materials and Methods  
Figs. S1 to S7

2 October 2009; accepted 3 December 2009  
10.1126/science.1182773



## NEW PRODUCTS



## FT-IR SYSTEM

The Atlas FT-IR System for in situ reaction monitoring combines the technology of the Atlas automated reactor with Bruker Optics' Matrix-MF, a process-ready Fourier transform infrared (FT-IR) spectrometer. Available in a wide range of vessel sizes, from 50 ml to 5 L, this compact system fits easily into fume cupboards, making it suitable for any laboratory performing real-time analysis of chemical reactions and processes. With the ability to perform real-time, in situ quantitative analysis, this system can be used to examine product yields, impurities, reaction kinetics, end points, and more. The system is easily upgradable to provide functionality such as reaction calorimetry, pH control, gravimetric or volumetric reagent addition, and crystallization control. The robust system combines a chemically resistant reactor and an attenuated total reflection probe with vibration-resistant optics.

**Syrris** For info: 617-803-6655 | [www.syrris.com](http://www.syrris.com)

## CLONAL AMPLIFICATION

cBot is a plug-and-play, user-installable system for clonal amplification of sequencing libraries capable of four-hour clonal amplification with less than 10 minutes of hands-on time. Its innovations include ready-to-use, prepackaged reagents; simple touch-screen operation; and browser-based remote monitoring. High-quality results are ensured by smart sensors that monitor instrument performance, combined with new chemistry protocols that deliver higher density clusters and improve sequencing accuracy. Illumina's proprietary cluster generation process offers advantages over competing emulsion polymerase chain reaction-based methods in terms of simplicity and hands-on time. cBot improves those advantages by minimizing user touch points, improving chemistry for higher quality results, and decreasing hands-on time.

**Illumina**

For info: 800-809-4566 | [www.illumina.com](http://www.illumina.com)

## DNA ISOLATION KITS

The PowerWater and RapidWater DNA isolation kits are for extraction of genomic DNA from a variety of water samples. The PowerWater DNA Isolation Kit makes use of patented Inhibitor Removal Technology to provide high-quality DNA from even the most turbid water. For nonturbid water, the RapidWater DNA Isolation Kit provides pure genomic DNA in less than 15 minutes. These next generation kits contain several improvements, including a novel bead tube with an optimized bead mix and reformulated buffers that streamline the protocol and reduce processing volumes. Both kits are compatible with a range of filter membrane types and are available with or without sterile, disposable 0.45  $\mu$ m and 0.22  $\mu$ m filter funnels.

**Mo Bio Laboratories**

For info: 800-606-6246 | [www.mobio.com/water](http://www.mobio.com/water)

## LIQUID CHROMATOGRAPHY SYSTEM

The ÄKTAmicro liquid chromatography system is designed for small sample volumes and concentrations, providing reproducible high-resolution purification and enabling characterization of target molecules. The system includes a microfraction collections kit for collection of minute fraction volumes and an adapted Unicorn wizard control system for improved ease of use. With an optional degasser and the ability to connect to light-scattering detectors, the system is suitable for molecular characterization. It is a completely bioinert system that can be used for purification of target molecules from a range of sources, such as intact proteins, protein complexes, and nucleotides. It is also well suited for rapid purity/recovery analysis in method development and drug discovery. It offers application flexibility, including reversed-phase and ion-exchange chromatography techniques, as well as gel filtration.

**GE Healthcare**

For info: 800-526-3593 | [www.gelifesciences.com](http://www.gelifesciences.com)

## PHOTONICS WORKSTATION

The Optometronic 4000 photonics workstation is designed to address nano/micro-photonics characterization. Photonic and plasmonic characterization requires multiple functionality in one platform. This platform integrates Nanonics' multiprobe nearfield optical and atomic force capabilities with its state-of-the-art lensed fibers and highly compact lensed fiber nanomanipulators. Applications of the instrument include analysis of plasmonic waveguides and plasmonic structures, analysis of light in waveguides and optical resonators, profiling of lensed fiber, measurement of a refractive index profile, nanomanipulation of plasmonic particles with multiple probes, and more.

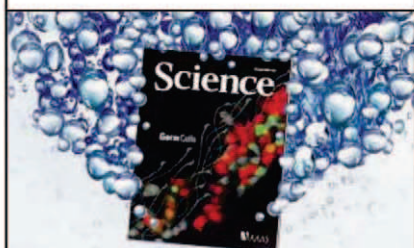
**Nanonics Imaging**

For info: +972-2-678-9573. | [www.nanonics.co.il](http://www.nanonics.co.il)

Electronically submit your new product description or product literature information! Go to [www.sciencemag.org/products/newproducts.dtl](http://www.sciencemag.org/products/newproducts.dtl) for more information.

Newly offered instrumentation, apparatus, and laboratory materials of interest to researchers in all disciplines in academic, industrial, and governmental organizations are featured in this space. Emphasis is given to purpose, chief characteristics, and availability of products and materials. Endorsement by *Science* or AAAS of any products or materials mentioned is not implied. Additional information may be obtained from the manufacturer or supplier.

## Release **The Power of Science**



### **Science Careers** **Classified Advertising**

For full advertising details, go to [ScienceCareers.org](http://ScienceCareers.org) and click For Employers, or call one of our representatives.

#### **Tracy Holmes**

Worldwide Associate Director  
Science Careers  
Phone: +44 (0) 1223 326525

#### **UNITED STATES & CANADA**

E-mail: [advertise@sciencecareers.org](mailto:advertise@sciencecareers.org)  
Fax: 202-289-6742

#### **Daryl Anderson**

US Sales Manager  
Phone: 202-326-6543

#### **Tina Burks**

Midwest/Canada  
Phone: 202-326-6577

#### **Alexis Fleming**

East Coast  
Phone: 202-326-6578

#### **Nicholas Hintibidze**

West Coast/South Central  
Phone: 202-326-6533

#### **Online Job Posting Questions**

Phone: 202-326-6577

#### **EUROPE & REST OF WORLD**

E-mail: [ads@science-int.co.uk](mailto:ads@science-int.co.uk)  
Fax: +44 (0) 1223 326532

#### **Alex Palmer**

Phone: +44 (0) 1223 326527

#### **Dan Pennington**

Phone: +44 (0) 1223 326517

#### **Susanne Kharraz Tavakol**

Phone: +44 (0) 1223 326529

#### **Lisa Patterson**

Phone: +44 (0) 1223 326528

#### **JAPAN**

#### **ASCA Corporation**

Jie Chin  
Phone: +81-3-6802-4616  
Fax: +81-3-6802-4615  
E-mail: [careerads@sciencemag.jp](mailto:careerads@sciencemag.jp)

#### **To subscribe to Science:**

In US call 866 434-2227  
In the rest of the world call +1 202 326-6417

All ads submitted for publication must comply with applicable US and non-US laws. *Science* reserves the right to refuse any advertisement at its sole discretion for any reason, including without limitation for offensive language or inappropriate content, and all advertising is subject to publisher approval. *Science* encourages our readers to alert us to any ads that they feel may be discriminatory or offensive.

**Science Careers**

From the journal *Science* **MAAAS**

## POSITIONS OPEN



**PROFESSOR, PRACTICE IN ENVIRONMENTAL SCIENCE, Tulane University.** The Department of Earth and Environmental Sciences seeks to fill a nontenure-track, Professor of Practice position to teach introductory courses in environmental science, to supervise introductory environmental science laboratory courses, and to teach other courses related to the candidate's field of expertise. We seek an individual possessing an enthusiastic dedication to teaching who is willing to make a long-term commitment to the Department and the University. A Ph.D. is required at the time of appointment. The initial appointment will be for three years with the possibility of renewal after a performance review at the end of the second year. The deadline for applications is March 1, 2010, but the position will remain open until filled. Applications should include curriculum vitae, a statement of teaching interests and goals, and the names and contact information of at least three references sent to: **Dr. Stephen Nelson, Department of Earth and Environmental Sciences, Tulane University, 6823 St. Charles Avenue, New Orleans, LA 70118-5698. E-mail: [snelson@tulane.edu](mailto:snelson@tulane.edu)** (e-mail preferred). Further information about the Department and University can be obtained at **website: <http://tulane.edu/sse/cens>**. *Tulane University is an Affirmative Action/Equal Opportunity Employer. Women and minorities are encouraged to apply.*

For more than 130 years, Lilly has been dedicated to meeting the health care needs of people in the United States and around the world. We address these needs primarily by developing innovative medicines, investing a higher percentage of our sales in research and development than any other major pharmaceutical company. If you are interested in being considered for employment with a Best in Class pharmaceutical company, please review the following opportunity: **Job I.D. 50364226.** Lilly seeks a **RESEARCH SCIENTIST** in Indianapolis, Indiana, for its Protein Optimization Team to lead enzymological studies for prelead through lead-optimization chemical research phases for the efficient production of research reagents. Specific duties include: lead research projects within established timelines and departmental parameters, guide project direction to meet research goals, and effectively analyze and summarize enzymology projects' progress; oversee the design and implementation of research projects within our Protein Optimization Team and direct laboratory experiments in support of such projects; provide scientific results that support the generation of patents, regulatory submissions, and high-level publications; present experimental data at internal and external meetings; review literature, patents, and technologies in the field of enzymology to ensure that the Team stays abreast of new developments in the field; coordinate with cross-functional research groups within our Biotherapeutic Discovery area, as well as other groups such as Drug Disposition and Bioproduct Research and Development, in order to ensure that research projects progress as planned. Salary starting at \$92,712 per year. Please submit resume to **website: <http://www.lilly.com/careers>** and cite the relevant job title and job I.D. number in your submission. *Lilly is an Equal Opportunity Employer that values the strength diversity brings to the workplace.*

### **POSTDOCTORAL OR RESEARCH ASSOCIATE** **University of Toronto/Seoul National University**

Postdoctoral or Research Associate position in neurobiology of memory and pain. Available immediately for recent Ph.D. trained in neuroscience. Working in two great cities, Toronto and Seoul. Research focuses on basic mechanisms of synaptic plasticity and behaviour. Excellent opportunity for collaboration and travel. Please electronically send a cover letter and curriculum vitae to **Dr. Min Zhuo, e-mail: [min.zhuo@utoronto.ca](mailto:min.zhuo@utoronto.ca)**.

## POSITIONS OPEN



### **ASSISTANT and ASSOCIATE PROFESSOR** **Center of Excellence in Cancer Research**

The newly created Center of Excellence in Cancer Research at the Paul L. Foster School of Medicine at El Paso is seeking highly qualified applicants for tenure-track faculty positions at the Assistant and Associate Professor levels in the Department of Biomedical Sciences. Successful candidates are expected to develop an independently funded research program in cancer research or a related field. The positions report to the Director of Basic Science Research of the Center of Excellence in Cancer Research.

Minimum qualifications: M.D., Ph.D., or M.D.-Ph.D. degree in a field related to cancer, three years of post-doctoral experience, and a strong publication record.

Preferred qualifications: Candidates with experience in cancer research, experience using the latest technologies, and funded grant support are particularly encouraged to apply. (Only candidates with funded grant support will be considered for Associate Professor rank.)

A competitive salary, startup package, and comprehensive benefits are available. Interested candidates must apply online at **website: <http://jobs.texastech.edu>**, **requisition# 80343**. For further information, potential applicants may inquire confidentially to: **Rajkumar Lakshmanaswamy Ph.D., e-mail: [rajkumar.lakshmanaswamy@ttuhsc.edu](mailto:rajkumar.lakshmanaswamy@ttuhsc.edu)**, **Director of Basic Science Research of the Center of Excellence in Cancer Research.**

The position is open until filled. Application review will begin immediately.

*Texas Tech University Health Sciences Center is an Equal Opportunity/Affirmative Action Employer.*

### **POSTDOCTORAL OR CLINICAL FELLOW**

to work on mechanistic studies understanding the physiological regulation of the cerebral circulation with respect to understanding the neurovascular unit in matching blood flow to neuronal metabolic activity.

The successful candidate would be supported by a NIH T32 Training Program directed by **Dr. David Harder**, and would be affiliated with the Cardiovascular Research Center, Center for Translational Studies, the Department of Physiology, and the appropriate basic or clinical department related to the candidate's training.

Research will relate to the biochemical, ionic, genetic, molecular, cellular, and whole animal regulation and integration of neurons, astrocytes, and microvasculature studying mechanisms by which multiple cell types function in an integrated manner to meet neuronal metabolic demand. Studies will also examine regulation of the blood-brain barrier and mechanisms of blood flow autoregulation. Expertise in molecular/cellular biology of excitable cells, patch clamp analysis of ion channel kinetics, in vivo and in vitro genetic manipulation, and whole animal physiology related to neuro- and vascular biology will be required.

Training in any of the above areas will be provided if necessary. Studies will be translational in nature, related to a variety of disease states. Please direct curriculum vitae and any pertinent information (a letter outlining career goals would be helpful, but not required) to:

**David R. Harder, Ph.D.**  
**Professor of Physiology**  
**Kohler Company Endowed**  
**Professor of Cardiovascular Science**  
**Associate Dean for Research**  
**Medical College of Wisconsin**  
**8701 Watertown Plank Road**  
**Milwaukee, WI 53226**  
**Telephone: 414-456-5611**  
**Fax: 414-456-6515**  
**E-mail: [dharder@mcw.edu](mailto:dharder@mcw.edu)**



**march 8-9, 2010**

Arizona Biltmore | Phoenix, Arizona



# personalized medicine in the clinic:

policy, legal, and ethical implications

This national conference with top experts will examine the impact of personalized medicine on the delivery of healthcare in the future. Conference highlights:

**patient rights**  
**medical privacy and confidentiality**  
**ethics**  
**individualized medical care**  
**economics**  
**liability issues for physicians**

For CLE and CME information and to register, visit  
[www.law.asu.edu/personalizedmedicine2010](http://www.law.asu.edu/personalizedmedicine2010).  
To become a conference supporter, call 480.965.2465.

Conference co-sponsors:

CENTER FOR THE STUDY OF  
**LAW, SCIENCE, & TECHNOLOGY**

**ASU** Sandra Day O'Connor  
College of Law  
ARIZONA STATE UNIVERSITY



**MAYO CLINIC**

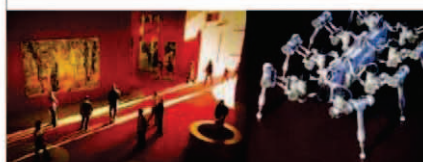
**AAAS**  
AMERICAN ACADEMY OF  
SCIENCE





# Discover Research in Germany

[www.research-in-germany.de](http://www.research-in-germany.de)



Find out about

- Research institutions
- Latest research findings
- Funding opportunities
- Practical hints for your research stay

... and much more.



**Research in  
Germany**  
Land of Ideas

## SYRACUSE UNIVERSITY

### Department of Biology Tenure-Track Position - Plant Molecular Biologist (025862)

The Department of Biology invites applications for a tenure-track Assistant Professor position to be filled by fall 2010 (contingent upon availability of funds) in plant cell molecular biology, with emphasis on biofuels. The areas of research include, but are not limited to, energy storage in plants, cell walls, metabolic pathways, biomass, biotic and abiotic stress resistance, etc. The applicant's interests should augment existing Biology Department strengths (see department website (<http://biology.syr.edu/>)). Candidates are expected to develop an independent, sustainable research program and contribute to departmental teaching at the undergraduate and graduate levels. Competitive salary, start-up funds and new laboratory space will be provided.

The individual filling this position will be part of an interdisciplinary initiative in biofuels currently underway at Syracuse University. There will be a concurrent faculty hire in the area of biofuels by the Department of Biomedical and Chemical Engineering. Thus, this position offers an outstanding opportunity for collaboration with colleagues in Biology, Biomedical and Chemical Engineering, Chemistry, Physics, as well as those at the State University of New York-Environmental Science & Forestry (<http://www.esf.edu/>). These two institutions (Syracuse University and SUNY-ESF) form one nearly contiguous campus. The Syracuse University Biology Department recently moved to the new 110,000 net sq. ft. Life Sciences Complex (LSC), which we share with the Department of Chemistry. The LSC features generous, well-appointed research laboratories designed to promote interaction, and the option to customize a component of research space. In addition, LSC has a brand new 5000 sq. ft. state-of-the-art greenhouse on the roof.

To apply, candidates should visit [www.sujobopps.com](http://www.sujobopps.com) (0258620) to complete a Dean/Senior Executive/Faculty application form and attach a current curriculum vitae plus (1) a cover letter outlining the candidate's qualifications, (2) a brief statement of research interests and future goals, and (3) a summary of teaching experience and teaching interests as a single PDF file. We ask that interested candidates have at least three letters of reference sent directly either to the electronic address above or to the mailing address below. Please include the name, address, phone number and e-mail address of each of your references in your cover letter. Personal inquiries may be directed to:

#### Plant Molecular Biologist Faculty Search

**Ramesh Raina, Ph.D.**  
Department of Biology  
107 College Place  
Syracuse University  
Syracuse, NY 13244  
E-mail: [raraina@syr.edu](mailto:raraina@syr.edu)



Priority will be given to full applications received prior to January 31, 2010.

*Syracuse University is an Affirmative Action/Equal Opportunity Employer.*



### Tenure Track Position: Stem Cell/Tissue Engineering Department of Bioengineering, University of Washington, Seattle

The UW Department of Bioengineering is recruiting a tenure-track faculty member in the area of **tissue engineering and regenerative medicine**. Relevant expertise includes, but is not limited to, adult and pluripotent stem cell biology, stem cell engineering, biomaterials for stem cell and tissue engineering, bioreactors, growing replacement tissues and whole organs, animal models of disease (including physiology and imaging), and drug delivery strategies to improve stem cell and tissue engineered construct performance.

The Department of Bioengineering is a joint venture between the College of Engineering and the School of Medicine. The successful candidate will work within an established collaborative environment at the University. Further, the candidate will have the opportunity to partner with highly successful programs in tissue engineering and investigators in the Institute for Stem Cell and Regenerative Medicine (<http://depts.washington.edu/iscrm/>).

Applications are sought at Assistant, Associate and Full Professor levels, but those at the Assistant Professor level are particularly encouraged. Ph.D. or M.D. degrees are required, and prior post-doctoral or higher level experience is highly valued. The successful candidate will be expected to develop an internationally recognized research program and to participate in the teaching and service missions of the department. Scientists and engineers who apply should show evidence of excellence, originality and productivity in research and potential for excellent teaching. Candidates who are likely to attract strong interest from other departments will be particularly sought after because of the UW's and Department of Bioengineering's long tradition of collaboration across disciplinary boundaries. Candidates whose research may lead to improvements in clinical medicine are also of interest, and she or he will be able to take advantage of our active Coulter Translational Research Partnership.

More information can be found at <http://depts.washington.edu/bioe>. Applications must be submitted electronically at <http://www.engr.washington.edu/facsearch/?dept=BioE>. Applicant review will begin **January 22, 2010** and continue until the position is filled. All positions are contingent on the availability of funding.

*The University of Washington is building a culturally diverse faculty and strongly encourages applications from women, minorities, individuals with disabilities and covered veterans. Faculty engage in teaching, research and service. The University of Washington is the recipient of a 2006 Alfred P. Sloan Award for Faculty Career Flexibility and a 2001 National Science Foundation ADVANCE Institutional Transformational Award to increase the advancement of women faculty in science, engineering and math. The University is an Equal Opportunity, Affirmative Action Employer.*



A woman with short dark hair, wearing a black blazer over a white collared shirt and a red beaded necklace, is smiling and looking towards the camera. She is positioned in the foreground of a large, ornate, circular dome with intricate architectural details and a balcony with a white railing. The lighting is warm and golden, highlighting the woman and the architectural features.

AAAS is here.

**Science & Technology  
Policy Fellows**

The science and engineering challenges that society faces today are far more complex than those of 40 to 50 years ago. The best available scientific, technical, and economic information is required to establish priorities, make decisions, and develop best practices. AAAS manages the Science & Technology Policy Fellowships in four areas to provide the opportunity for accomplished scientists and engineers to contribute to the federal policymaking process while learning firsthand about the intersection of science and policy. And this is just one of the ways that AAAS is committed to advancing science to support a healthy and prosperous world. Join us. Together we can make a difference. [aaas.org/plusyou/fellows](http://aaas.org/plusyou/fellows)



[www.storemags.com](http://www.storemags.com) & [www.aaas.org](http://www.aaas.org)





## UNIVERSITY OF OSLO



The University of Oslo is Norway's largest university with 6000 employees and 33000 students. We offer interesting career opportunities and a good work environment.

### Position as Department Head and Professor I / Associate Professor of Medicine (Clinical Molecular Biology)

at the Department of Clinical  
Epidemiology and Molecular Biology  
(Epi-Gen), Faculty Division Akershus  
University Hospital.

**Closing date for applications:**  
**28.02.2010**

**Reference no: 2009/16372**

[www.uio.no](http://www.uio.no)



## Vice President for Research

Stony Brook University invites nominations and applications for the position of Vice President for Research. The successful candidate will lead the ongoing campuswide expansion of the University's research mission and will manage the research administration activities, including compliance, technology transfer, and grants administration.

Home to many highly ranked graduate research programs, Stony Brook is located 60 miles from New York City on Long Island's scenic North Shore. Our 1,000-acre campus is home to 24,000 undergraduate, graduate, and doctoral students and more than 15,000 faculty and staff, including those employed at Stony Brook University Medical Center, Suffolk County's only academic medical center and tertiary care provider. The University is a member of the prestigious Association of American Universities and co-manager of nearby Brookhaven National Laboratory (BNL). Major resources at BNL include the Relativistic Heavy Ion Collider, the National Synchrotron Light Source, and the Center for Functional Nanomaterials, and the New York Center for Computational Sciences. Founded in 1957, Stony Brook is one of the four University Centers of the State University of New York. Long Island's largest single-site employer, Stony Brook generates an estimated \$4.7 billion annually in regional economic impact. Stony Brook University has three campuses: the main campus in Stony Brook, Stony Brook Manhattan, and the new Stony Brook Southampton campus. The main campus includes a Medical Center, a Health Sciences Center, and a Graduate School as well as the Colleges of Arts and Sciences, Business, and Engineering and Applied Sciences, and Schools of Medicine, Dental Medicine, Health Technology and Management, Journalism, Marine and Atmospheric Sciences, Nursing, Professional Development, and Social Welfare.

The new Vice President for Research will hold a key leadership role across the entire university and report directly to the President Dr. Samuel L. Stanley, Jr. MD. Since taking the helm 2009, President Stanley has identified the growth of Stony Brook's research enterprise as one of his top priorities. Primary responsibilities for the Vice President for Research include, but are not limited to: encouraging and facilitating excellence in research and providing leadership and oversight for sponsored research programs, compliance, intellectual property management, and economic development. Candidates should have earned a Ph.D., M.D., or the equivalent, and have a distinguished record of leadership in research. We seek someone with vision for the research enterprise, preferably with experience in research administration at the operations level and a strong relationship with government agencies and industry.

Interested individuals are encouraged to visit [www.stonybrook.edu/sb/vpresearch](http://www.stonybrook.edu/sb/vpresearch) for a detailed position description and for information about Stony Brook University and the application and nomination procedures.

Deadline for applications is March 15, 2010. All candidate information will be held in strict confidence.

Qualified applicants should submit their curriculum vitae and a letter of interest to: [vpresearch@notes.cc.sunysb.edu](mailto:vpresearch@notes.cc.sunysb.edu)

Equal Opportunity/Affirmative Action Employer. Women, people of color, individuals with disabilities, and veterans are encouraged to apply.



## TEXAS TECH UNIVERSITY TEXAS TECH UNIVERSITY HEALTH SCIENCES CENTER Institute for Comparative & Experimental Medicine

### Professor of Comparative Medicine

Texas Tech University (TTU) and the Texas Tech University Health Sciences Center (HSC) have collaborated to form a new Institute for Comparative and Experimental Medicine (ICEM). This new Institute will support the One Health National Initiative to study and provide solutions to human and animal health concerns. The institute will recruit a number of new faculty, assign and remodel new space suited to this line of research, and provide competitive start up funds in areas of comparative medicine including, but not limited to: • Infectious disease, vaccine development, immunology, or allergy • Inflammation • Bone health • Cardiovascular health • Diabetes and Obesity • Neuroscience • Imaging and Image Processing • Addiction • Cancer • Biomedical Engineering • Genomics and Metabolomics • Bioinformatics, Modeling and Advanced Biomedical Computing • Basic, translational and clinical studies

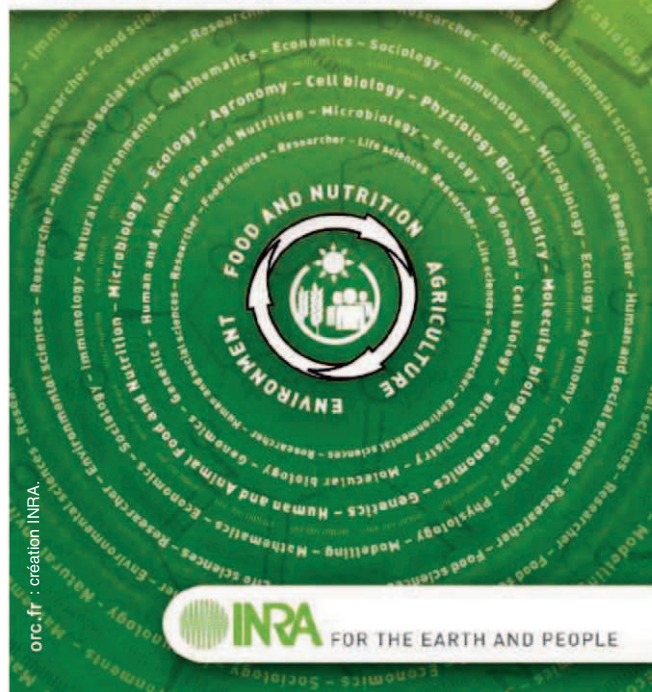
Collaboration with existing and newly hired ICEM faculty members in both computational and experimental research and interaction in a team environment are expected. Funds are available to remodel and equip shell space in our Experimental Sciences Building (ESB) for faculty who will be affiliated with TTU. Opportunities exist to collaborate on human clinical studies in the Texas Tech System. New faculty hires will have current competitive grant funding and a distinguished record of research productivity. Graduate teaching and advising are expected in areas of interest to the faculty. Service to the institutions and the profession are important aspects of successful faculty candidates. The primary appointment may be in any academic department at either institution. The level of academic appointment is open to all ranks though there is a preference for positions at the Associate/Full Professor level.

Applicants must submit a letter of interest expressing their vision for research contributions and interactions, graduate education goals, a complete resume/CV, the names of five references, and start-up requirements to: **Institute for Comparative and Experimental Medicine, Texas Tech University, Experimental Sciences Building, Lubbock, TX 79409-3132.** For more information visit <http://www.icem.ttu.edu>. Applications should be submitted to [icem@ttu.edu](mailto:icem@ttu.edu). These positions shall remain open until filled.

*Texas Tech University System is an Equal Opportunity Institution.*

## THE LEADING AGRICULTURAL RESEARCH INSTITUTE IN EUROPE IS RECRUITING 62 SCIENTISTS

Applications from 19 January to 26 February 2010  
Information: [www.international.inra.fr](http://www.international.inra.fr)







AAAS is here.

**Entry Point!  
Students with Disabilities**

To meet the challenge of the competitive economy in the new millennium, private industry and government research agencies must expand the pool of technical talent. AAAS started Entry Point!, a program that offers students with disabilities competitive internship opportunities in science, engineering, mathematics, computer science, and some fields of business. And this is just one of the ways that AAAS is committed to advancing science to support a healthy and prosperous world. Join us. Together we can make a difference. [aaas.org/plusyou/entrypoint](http://aaas.org/plusyou/entrypoint)



**AAAS + U =  $\Delta$**





## THE UNIVERSITY OF CHICAGO

The University of Chicago's Institute for Biophysical Dynamics, an interdisciplinary research institute at the interface of the physical and biological sciences, invites applications for the Institute's **Yen Fellowship**. This fellowship is for recent Ph.D. graduates and seeks to support outstanding individuals to undertake interdisciplinary research in the area of subcellular transport of macromolecules, using a combination of biophysical, genetic, computational, biochemical and cell biological tools. Yen Fellows are given considerable latitude in defining their research direction and will conduct their research in the laboratories of Institute faculty. A description of the Institute faculty and their research interests can be found at <http://ibd.uchicago.edu/directory.shtml>.

We encourage applicants to contact Institute faculty directly about potential projects. Applicants should send their curriculum vitae, three reference letters and a short research proposal to [jfeder@uchicago.edu](mailto:jfeder@uchicago.edu). Review of applications will start on **15 January 2010**.

*The University of Chicago is an Affirmative Action/Equal Opportunity Employer.*



## HARVARD UNIVERSITY Assistant/Associate Professors Department of Genetics and Complex Diseases

The Department of Genetics and Complex Diseases (GCD) at the Harvard School of Public Health (HSPH) invites applications for tenure-track positions at the level of assistant professor. Exceptional associate professor candidates will also be considered. Successful applicants will hold a PhD and/or MD degree and will have a record of outstanding productivity. Individuals are sought particularly in the following areas to complement the existing research and training goals of the department: signal transduction related to energy and nutrient sensing pathways, regulation of metabolic homeostasis, inflammatory and stress response pathways related to chronic metabolic diseases and aging, cancer metabolism, and epigenetic regulation of metabolism. Individuals using systems and/or computational approaches applied at a mechanistic level to problems of metabolic homeostasis, gene-environment interactions and/or adaptive responses are also encouraged to apply. The candidate should possess the ability to work collaboratively with other scientists and the scholarly qualities required to mentor doctoral students in the graduate program in the Division of Biological Sciences. Generous start-up packages and state-of-the-art research facilities are available.

Please send a letter of application, including a statement of current and future research interests, curriculum vitae, sample publications, and the names of four references to the following address. Applicants should ask their four references to write independently to this address:

**Chair, GCD Search, c/o Audrey Harmon**  
**Department of Genetics & Complex Diseases**  
**Harvard School of Public Health**  
**655 Huntington Avenue, Building II, 113**  
**Boston, MA 02115**  
[gcddept@hsph.harvard.edu](mailto:gcddept@hsph.harvard.edu)

*The Harvard School of Public Health is committed to increasing the representation of women and minorities in its faculty, and encourages applications from such candidates.*

## Immunotherapy Tenure Track Faculty Positions

### Texas Tech University Health Sciences Center Abilene, Texas

Applications are requested for two tenure track faculty positions at the Assistant Professor, Associate Professor, or Professor levels within the newly established Center for Immunotherapeutic Research, in the Department of Biomedical Sciences at Texas Tech University Health Sciences Center School of Pharmacy, Abilene, Texas. Successful candidates are expected to develop and maintain funded research program in immunology/immunotherapy and to teach in graduate (Ph.D.) and professional (Pharm.D.) courses and collaborate with other researchers within the Center and University. Candidates should have a Ph.D. and postdoctoral training in immunology, immunotherapy, or related discipline. Preference will be given to candidates with established research programs in translational/clinical immunology and immunotherapy, especially in personalized cancer immunotherapy. Nationally competitive salary and startup packages are available.

Interested applicants should submit documents online at <http://jobs.texasstate.edu> (Job Requisition #76713 or 77313). Please include a curriculum vitae, a summary of research and teaching interests, and names and addresses of three references. For questions, contact the search committee chair, **Dr. Jon Weidanz, Texas Tech University HSC, School of Pharmacy, 1718 Pine, Abilene, TX 79601. Email: [jon.weidanz@ttuhsc.edu](mailto:jon.weidanz@ttuhsc.edu)**. These positions will remain open until suitable candidates are identified.

*TTUHSC is an Equal Opportunity/Affirmative Action Institution. Minorities and Women are encouraged to apply.*



UNIVERSITY OF  
OXFORD

[www.ox.ac.uk/jobs](http://www.ox.ac.uk/jobs)

## Directorship of the Oxford University Museum of Natural History

in association with Kellogg College

The University of Oxford intends to make an appointment to the Directorship of the Oxford University Museum of Natural History from 1 October 2010, or as soon as possible thereafter, in succession to Professor W.J. Kennedy who retires on 30 September 2010. The primary role of the Director is to lead the development of the museum's research, stewardship, curation, educational, access, and fundraising profiles. A major challenge for the Director will be to sustain the collections at the centre of the University's teaching and research at the same time as maintaining the museum's commitment to public education. The successful candidate will have an international research reputation in any area of life sciences or earth sciences relevant to the museum's role and collections. Experience of fundraising, collections management, and education/outreach activities would be desirable.

Please see the further particulars at [www.admin.ox.ac.uk/fp/](http://www.admin.ox.ac.uk/fp/) for more details about the post and for full instructions before making an application. Applications, including a covering letter and full CV, and naming three referees should be received no later than Monday 22 March 2010, by Dr Gwen Booth, Personnel Officer, Senior Appointments at: [professorships@admin.ox.ac.uk](mailto:professorships@admin.ox.ac.uk) If you have a query about how to apply, please contact Mrs Elaine Eastgate at: [professorships@admin.ox.ac.uk](mailto:professorships@admin.ox.ac.uk) or telephone: +44 (0) 1865 280189.

**Committed to equality and valuing diversity**





AAAS is here.

Rwanda

A country devastated by genocide and a crippling AIDS epidemic. Together with the Rwandan Ministry of Education, AAAS, the world's largest multidisciplinary scientific society and publisher of *Science* magazine, is working to ensure that local children gain skills in science, technology, math, and engineering. And this is just one of the ways that AAAS is committed to advancing science to support a healthy and prosperous world. Join us. Together we can make a difference. [aaas.org/plusyou/rwanda](http://aaas.org/plusyou/rwanda)

 AAAS + U = Δ





**CASE WESTERN RESERVE  
UNIVERSITY**  
SCHOOL OF MEDICINE

**Full/Associate/Assistant Professor Case Western Reserve  
University School of Medicine**

**Case Center for Proteomics and Bioinformatics and  
Department of Molecular Biology and Microbiology**

The Center for Proteomics and Bioinformatics and Department of Molecular Biology and Microbiology in the School of Medicine at Case Western Reserve University invite applications for an open tenure-track faculty position at the Full, Associate or Assistant Professor level. The successful candidate will establish a vigorous research program, participate in teaching activities, and interact productively with the strong team of basic and clinical scientists interested in the overall areas of HIV/AIDS and host-pathogen interactions, and drug abuse in the context of HIV/AIDS at our institution. We are especially interested in candidates who are undertaking epigenetic, proteomic, systems biology, and/or bioinformatics studies of HIV/AIDS. In addition to newly refurbished laboratory space and generous start-up packages, we offer a highly interactive environment with exceptional intellectual, infrastructural, and administrative support. The candidate will be an active participant in the expansion of HIV/AIDS research conducted by the Center for Proteomics and Bioinformatics and the Center for AIDS Research. The successful candidate will receive a primary appointment in either the Center for Proteomics and Bioinformatics or the Department of Molecular Biology and Microbiology and a secondary appointment in the collaborating department, depending on the candidate's research focus. All candidates should have a Ph.D. and relevant post-doctoral experience. Candidates for the rank of associate professor or above must have a record of funding, active research program and a national reputation. Rank commensurate with experience. Interested candidates should apply by **February 28, 2010** by sending a cv, a plan of research, and the names of 3 references to: **Joan Schenkel, Case Center for Proteomics and Bioinformatics, CWRU, 10900 Euclid Ave, Cleveland, OH 44106-4988 or joan.schenkel@case.edu.**

*In employment as in education, Case Western Reserve University is committed to Equal Opportunity and World Class Diversity. Case is a recipient of a National Science Foundation ADVANCE Institutional Transformation Grant to increase the participation of women in Science and Engineering.*



**CASE WESTERN RESERVE  
UNIVERSITY**  
SCHOOL OF MEDICINE

**Associate Professor  
Case Center for Proteomics and Bioinformatics**

The Center for Proteomics and Bioinformatics in the School of Medicine at Case Western Reserve University invites applications for a tenure track faculty position at the Associate Professor level. The areas of research interest are any areas in sequence based or structural bioinformatics for nucleic acids or proteins. Candidates interested in translational approaches, such as biomarker discovery or drug design, are also encouraged to apply. The candidate will also have the opportunity to collaborate with other Medical School faculty in a large number of NIH funded center and program project grants affiliated with the Center. These funded programs emphasize research in protein-protein interaction networks, integration of genomics and proteomics data, and high-throughput structure modeling, using a variety of methods. Overall, the candidate will be an active participant in shaping the expansion of bioinformatics and/or macromolecular structure programs of the Center. Candidates should have a Ph.D. and relevant academic or industrial experience suitable for appointment at an Associate Professor level.

Interested candidates should apply by **February 28, 2010** by sending a cv including funded grants, a plan of research and teaching, and the names of 3 references to: **Joan Schenkel, Case Center for Proteomics and Bioinformatics, CWRU, 10900 Euclid Ave, Cleveland, OH 44106-4988 or joan.schenkel@case.edu.**

*In employment as in education, Case Western Reserve University is committed to Equal Opportunity and World Class Diversity. Case is a recipient of a National Science Foundation ADVANCE Institutional Transformation Grant to increase the participation of women in Science and Engineering.*



**University of Connecticut  
Department of Physiology  
and Neurobiology**

Applications are invited for a tenure track faculty position at the **Assistant Professor** level in **Bioinformatics and Systems Biology**. We seek individuals who will establish an outstanding research program using systems and genomics approaches to the study of complex neural and physiological questions. The successful candidate will receive dedicated laboratory space in a newly constructed building and a start-up package to establish an active independent research program. This individual is expected to develop collaborations within the Department of Physiology and Neurobiology as well as other programs such as the University of Connecticut Stem Cell Institute and the Center for Regenerative Biology.

The candidate's primary academic appointment, laboratory and teaching responsibilities will be within the Department of Physiology and Neurobiology at the main campus in Storrs, CT. The University of Connecticut is a Research I public university and has campuses at Avery Point, Hartford, Stamford, Torrington, Waterbury and West Hartford.

**Minimum Qualifications:** Ph.D. or M.D. in related field and have completed at least two years of postdoctoral training.

**Preferred Qualifications:** We encourage applicants with a research focus on bioinformatics and collection, management, integration and analyses of large datasets with particular emphasis on physiology and neurobiology. The preferred candidate will demonstrate an ability to provide leadership in developing pedagogical techniques designed to meet the needs of diverse learning styles.

Review of applications will begin immediately with preference given to those received before **March 15, 2010**. Applications should be submitted electronically as a single PDF document containing the following information: curriculum vitae, a brief summary of current research with a statement of research directions, a statement of teaching interests, and the names of at least three referees to: **Andrew Moiseff@uconn.edu, Andrew Moiseff, Chair, PNB Bioinformatics and Systems Biology Search Committee, UConn PNB, Box U-3156, 75 North Eagleville Road, Storrs, CT 06269-3156, (Search #2010 233).**

*An Equal Opportunity Employer.  
Minority and women scientists are especially encouraged to apply.*

**Neutron Scattering  
Instrument Scientist**

Neutron Sciences Directorate at Oak Ridge National Laboratory invites applications for an Extended Q-Range Small-Angle Neutron Scattering (EQ-SANS) Instrument Scientist.

The successful candidate will be a team member providing operational support for the new EQ-SANS instrument at the Spallation Neutron Source and developing a vigorous scientific program associated with the instrument.

An extensive record of research accomplishments using small angle neutron and/or x-ray scattering is required. A Ph.D. and a minimum of 10 years of experience as a research scientist in material science, physics, chemistry, or related fields (or equivalent combination of training and experience) are also required.

For more information about the position or to apply visit:  
[http://jobs.ornl.gov/neutron\\_science.shtml](http://jobs.ornl.gov/neutron_science.shtml)


**neutrons.ornl.gov**

10-G00054gim



**Real Science. Real Life.**



A man with short dark hair, wearing a white textured sweater, is seated at a wooden desk, looking at a laptop. The desk is cluttered with various items including a white hard hat, a small sailboat model, a red container, and several small figurines. In the background, a large periodic table of elements is pinned to a light-colored wall, along with several smaller papers and a framed portrait. The scene is dimly lit, with the primary light source being the laptop screen.

AAAS is here.

**HBCU-UP National  
Research Conference**

Historically Black Colleges and Universities (HBCUs) increase the number of underrepresented ethnic minorities qualified for education and research in science, technology, engineering, and mathematics (STEM). AAAS partners with NSF to host a national gathering that highlights undergraduate student research to enhance the quality of STEM education. And this is just one of the ways that AAAS is committed to advancing science to support a healthy and prosperous world. Join us. Together we can make a difference. [aaas.org/plusyou/hbcuup](http://aaas.org/plusyou/hbcuup)





# 35<sup>TH</sup> FEBS CONGRESS MOLECULES OF LIFE



Welcome to FEBS 2010, jointly organised by the  
Swedish Society for Biochemistry and Molecular  
Biology and the Norwegian Biochemical Society

June 26–July 1, 2010 • Gothenburg, Sweden • at Gothenburg Convention Centre (Svenska Mässan)

## Programme highlights

**Nobel Laureate lectures:** Roger Tsien (UCSD; Nobel Prize 2008)  
Venki Ramakrishnan (MRC-LMB; Nobel Prize 2009)  
Elizabeth Blackburn (UCSF; Nobel Prize 2009)  
John Walker (MRC-MBU; Nobel Prize 1997)  
**Datta lecture:** Juleen Zierath (Karolinska Institute)  
**Krebs lecture:** Harald Stenmark (Norwegian Radium Hospital)  
**Bücher lecture:** Svante Pääbo (MPI Leipzig)  
**EMBO lecture:** Uri Alon (Weizmann Institute)  
**IUBMB lecture:** Susan Lindquist (Whitehead Institute)

## Congress symposia

- A - Molecules in Health and Disease**
- B - Molecular Networks**
- C - Molecules at Work**
- D - Cellular Compartments**
- E - Biomolecular Design and Function**

## Important dates

Early registration	February 26, 2010
Deadline for support application	February 26, 2010
Abstract deadline	March 31, 2010
Congress starts	June 26, 2010 at 17.00

## Workshops on technology developments

- Sequencing technology
- Proteomics technologies
- Metabolomics
- Protein structures
- Life imaging
- Dynamic modelling
- Protein interactions
- Molecular imaging
- Protein expression
- Lipidomics
- Network modelling
- Bioinformatics

## Activities by FEBS committees and working groups

- Science & Society
- Education
- Women in Science

YOUNG SCIENTIST FORUM  
**LIFE OF MOLECULES**  
June 23–26 2010 Gothenburg



[www.febs2010.org](http://www.febs2010.org)



UPPSALA  
UNIVERSITET

## Assistant professor/ Research Associate in Molecular Systems Biology

at the Department of Cell  
and Molecular Biology.

The research area ranges from  
experimental biophysics with  
applications in living cells to  
theoretical approaches for intra-  
cellular kinetics.

For further information about the  
position, please contact Johan Elf,  
phone +46 18 471 4678, e-mail  
[johan.elf@icm.uu.se](mailto:johan.elf@icm.uu.se).

A full advertisement will be found at  
[www.uu.se/job](http://www.uu.se/job).  
Reference number is UFV-PA  
2009/3303.

[www.uu.se](http://www.uu.se)

## CONFERENCE

4<sup>th</sup> ANNUAL INTERNATIONAL PARTNERING CONFERENCE

# BIO-EUROPE SPRING<sup>®</sup> 2010

March 8–10, 2010  
Barcelona, Spain  
[www.ebdgroup.com/bes](http://www.ebdgroup.com/bes)

BIO-Europe Spring brings together companies  
from across the biotechnology value chain  
in a forum specifically designed to facilitate  
partnering.

Join your colleagues for three days of shared  
insights and productive partnering – all in one  
place!

## POSITIONS OPEN

### FACULTY POSITIONS in Molecular Cancer Research

The Department of Biochemistry and Molecular Biology at The George Washington University Medical Center invites applications for tenure-track **ASSISTANT/ASSOCIATE PROFESSORS**. We seek outstanding candidates with demonstrated excellence in cancer research. Areas of research interest include nuclear and growth factor receptors, signal transduction, transcription, and chromatin remodeling. The Medical Center is located on the main campus of The George Washington University. The presence of basic and applied science departments and the proximity of the NIH, Children's National Research Institute, and other medical centers in the Washington, D.C., metropolitan area offers ample opportunities for collaborations. The GW University will provide a competitive startup package to successful candidates. Basic qualifications: Applicants must hold a Ph.D. and/or M.D. degree in an appropriate discipline and shall have extramural funding for consideration of Associate Professorship.

Application process: Interested applicants must send a complete curriculum vitae, a statement of current and future research interests (limited to three pages), and the names and addresses of three references to: **Rakesh Kumar, Ph.D., Professor and Chair, Department of Biochemistry and Molecular Biology, Faculty Search, The George Washington University Medical Center, Suite 530, 2300 Eye Street N.W., Washington, DC 20037. Or via e-mail: bcmrag@gwumc.edu.** Review of applications by the Search Committee will continue until positions are filled. Only complete applications will be considered.

*The George Washington University is an Affirmative Action/Equal Opportunity Employer.*

### LEAD INSTRUCTOR AND DIRECTOR OF LABORATORIES

The Kenyon College Biology Department seeks applicants with broad training in biological sciences for a nontenure-track, continuing full-time position as Lead Instructor and Director of Introductory Laboratories. The Lead Instructor has overall responsibility for An Introduction to Experimental Biology (biology 109-110), a yearlong, stand-alone introductory laboratory course with an emphasis on experimental design, data analysis, and scientific writing.

Responsibilities include teaching two sections of the course per semester, coordinating and organizing instructional materials for all sections of the course, developing and implementing course curriculum with input from fellow faculty, managing course enrollments, and supervising student teaching assistants. Strong organizational skills, creativity, and a commitment to working closely with students and faculty colleagues on a residential campus are important qualifications. Master's in biology is required; Ph.D. and/or teaching experience preferred. This is a nine-month position. Please visit **website: <http://biology.kenyon.edu>** for more information.

To apply, please go to **website: <https://employment.kenyon.edu>**. A completed application will include: cover letter, curriculum vitae, contact information for three references, and a statement of teaching philosophy. Review of applications will begin February 15, 2010, and continue until the position is filled.

### POSTDOCTORAL POSITION Cancer Research

The laboratory of **Gary Kruh** at University of Illinois at Chicago Cancer Center is seeking a highly motivated Postdoctoral Fellow with a Ph.D. and more than four years in biochemistry, molecular biology, or closely related biological sciences to conduct cancer research. Experience in molecular genetic techniques and cell culture systems is desirable. Send resume, cover letter with a statement of research interests, and names of three references by February 15, 2010, to: **Ms. Dorothy Sholcen-Modrzyk, UIC Cancer Center MC 700, 914 South Wood Street, Chicago, IL 60612. Or e-mail: [cancer@uic.edu](mailto:cancer@uic.edu).** UIC is an Affirmative Action/Equal Opportunity Employer.

## POSITIONS OPEN

### QUANTITATIVE DISEASE ECOLOGIST

The Department of Biology and the Emerging Pathogens Institute (EPI), University of Florida, seek a tenure-track **FACULTY MEMBER** working on emerging infectious diseases. The position is open in rank. We seek applicants with strong quantitative skills who can advance our understanding of the dynamics and control of emerging infectious diseases. Broad experience with mathematical and computational models of emerging pathogens of humans, animals, or plants is highly desirable, as is a demonstrable ability to work in a multidisciplinary environment. The primary appointment will be in the Department of Biology, and some teaching will be required, but the position is expected to emphasize scientific research, and the successful candidate is expected to establish a strong, externally funded research program. The Department of Biology fosters a collegial, collaborative, interdisciplinary environment with strong ties to EPI, the Florida Museum of Natural History, the UF Genetics Institute, and other UF centers in biomedical, veterinary, environmental, and agricultural sciences. For more information and to submit an electronic application consisting of a cover letter, curriculum vitae, statements of research and teaching interests, three reprints, and names of three references, please go to **website: <http://www.biology.ufl.edu/Administration/Jobs.aspx>**. Ph.D. or equivalent in a relevant discipline is required; postdoctoral research experience is preferred. Review of applications will begin on March 1, 2010, and will continue until the position is filled. *The selection process will be conducted under Florida's Government in the Sunshine and Public Records laws. Our Department is committed to diversity as a component of excellence. Women, minorities, and members of other underrepresented groups are encouraged to apply. The University of Florida is an Equal Opportunity Institution.*

### FACULTY POSITION IN IMMUNOLOGY Boston University School of Medicine

The Department of Microbiology (**website: <http://www.bumc.bu.edu/microbiology>**) is seeking outstanding investigators with an innovative record in research for an immunology faculty position(s). Applications in all areas of immunology will be considered, but investigators specializing in basic aspects of adaptive immune responses or the immunology of infectious diseases are especially encouraged to apply. Candidates appropriate for any faculty level position will be considered.

Interested individuals should submit their curriculum vitae, summary of research accomplishments, future research plans, and the names of at least three references to **e-mail: [kfurness@bu.edu](mailto:kfurness@bu.edu)** no later than March 1, 2010.

*Boston University School of Medicine is an Equal Opportunity/Affirmative Action Employer.*

## POSITIONS OPEN

### POSTDOCTORAL POSITIONS Viruses, Telomeres, and Drug Discovery The Wistar Institute

Positions for Postdoctoral trainees are available in several areas, both in mammalian cells and human tumor-associated viruses.

(1) Telomere and cell growth regulation by telomeric repeat-containing RNA. The role of noncoding telomere RNA in regulating telomere chromatin and cell growth (*Mol. Cell* **35**,4:403-413, 2009; *Cell Cycle* **9**,1:69-74, 2010).

(2) Viral and cellular genome maintenance. Mechanisms regulating genome stability and chromosome organization, including factors controlling chromatin insulators and origins of DNA replication (*J. Virol.* **2009a**, 2009b, 2009c; *EMBO J.* **2008**).

(3) Small molecule inhibitors of latent viral infection. Identification of natural and synthetic inhibitors of viral regulatory proteins at the newly established Center for Chemical Biology and Translational Medicine at Wistar Institute.

Applicants should have a Ph.D. and experience in molecular biology, virology, and/or biochemistry. Highly competitive salary and benefits package. Forward curriculum vitae to: **Paul M. Lieberman, Ph.D., Gene Expression and Regulation Program, The Wistar Institute, 3601 Spruce Street, Philadelphia, PA 19104. E-mail: [lieberman@wistar.org](mailto:lieberman@wistar.org).**

**POSTDOCTORAL POSITION** available in the laboratory of **Dr. Venigalla Rao**, Biology Department, The Catholic University of America, Washington, D.C., to work on developing immunogens for HIV vaccine formulations (**website: <http://faculty.cua.edu/rao/>**). Research involves bacteriophage T4 assembly, recombinant DNA construction, protein purification, and mutagenesis. Candidate will have Ph.D. in biological sciences and strong background in molecular biology and biochemistry. Electronically send curriculum vitae and names of three references to **e-mail: [rao@cua.edu](mailto:rao@cua.edu)**. *Catholic University is an Equal Opportunity Employer.*

We  
deliver  
customized  
job alerts  
and more...



[www.ScienceCareers.org](http://www.ScienceCareers.org)

## MARKETPLACE

Promab Biotechnologies Inc.  
**Custom Monoclonal  
Antibody \$4,200**

>3,000 CLONES WILL BE SCREENED

1-866-339-0871

[www.promab.com](http://www.promab.com) [info@promab.com](mailto:info@promab.com)

Get your  
career questions  
answered.  
**Careers  
Forum**



[www.ScienceCareers.org](http://www.ScienceCareers.org)





### Everything is in one place!

"You can find what you need scientifically in the technical program, and in the exposition, you can find interesting new apparatus. Pittcon is a very good meeting place for analytical scientists—so you'll also find interesting colleagues from all over the world."

**STAFFAN NILSSON, Ph.D.** | *Professor of Technical Analytical Chemistry, Lund University, Sweden*



### At Pittcon, I was able to meet face-to-face with the people I needed to see.

"This was my first Pittcon and it was a memorable event. It proved to be a great opportunity to meet one-on-one with researchers and companies about GreenCentre Canada, and I was able to connect with new people who will certainly become professional colleagues in the future. For anyone looking to network with industry and academia from around the world for an entire week, Pittcon is the place to be."

**HASSAN JAFERI, M.Sc.** | *Analyst, Commercial Development, PARTEQ Innovations*



### At first, it was like entering a new universe.

"It really is the biggest event in the instrumentation field. It took a little while to find my way, but it was a good opportunity to learn about new theoretical subjects during seminars, and to see practical applications on the exhibition area. My lab presented a poster on a new instrument we developed, and we had many opportunities to share ideas with other researchers."

**VÉRONIQUE PERES** | *Maître de Recherche, Ecole Nationale Supérieure des Mines, Saint Etienne*

#### Write your own Pittcon story.

See all the newest scientific innovations and the latest products. Explore new applications and techniques. Meet one-on-one with technical experts. Exchange ideas with colleagues from all over the world. Be part of it all—at Pittcon 2010. To read more scientists' stories, or write your own, visit [www.pittcon.org/story](http://www.pittcon.org/story)

**ORLANDO, FLORIDA, USA • FEBRUARY 28 – MARCH 5, 2010 • [WWW.PITTCON.ORG](http://WWW.PITTCON.ORG)**

**PITTCON**  
CONFERENCE & EXPO **2010**